

# Particle-size-dependent chemistry in ultrafine aerosol particles

Online size-selected particle measurements  
using a custom-built aerosol inlet and nitrate CI-Orbitrap  
high-resolution mass spectrometry

## Dissertation

Zur Erlangung des akademischen Grades

„Doktor der Naturwissenschaften“

im Promotionsfach Chemie

am Fachbereich Chemie, Pharmazie,

Geographie und Geowissenschaften

der Johannes Gutenberg-Universität Mainz

vorgelegt von

**Marcel Douverne**

Geboren in Koblenz

Mainz, 2026

Dekanin:

1. Gutachter:

2. Gutachter:

Tag der mündlichen Prüfung:

D77 Dissertation der Johannes Gutenberg-Universität Mainz

CC-BY-4.0

## **Eigenständigkeitserklärung**

Hiermit erkläre ich Marcel Douverne,  
dass ich die vorliegende Arbeit mit dem Titel:

*“Particle-size-dependent chemistry in ultrafine aerosol particles: Online size-selected particle measurements using a custom-built aerosol inlet and nitrate CI-Orbitrap high-resolution mass spectrometry”*

selbstständig verfasst und keine anderen als die angegebenen Quellen und Hilfsmittel (dazu zählen auch KI-basierte Anwendungen oder Werkzeuge\*) benutzt habe. Sämtliche wörtlichen oder sinngemäßen Übernahmen und Zitate sind kenntlich gemacht und nachgewiesen (dies gilt auch für Texte, die durch generative KI, wie Chat GPT erzeugt wurden). Ich versichere, dass ich keine Hilfsmittel verwendet habe, deren Nutzung die Prüferin oder der Prüfer explizit ausgeschlossen hat.

Im Anhang „Use of AI Tools“ habe ich die verwendeten KI-Tools dokumentiert.

Mit Abgabe der vorliegenden Leistung übernehme ich die Verantwortung für das eingereichte Gesamtprodukt. Ich verantworte damit auch jegliche KI-generierten Inhalte, die ich in meine Arbeit übernommen habe. Die Richtigkeit übernommener (KI-generierter) Aussagen und Inhalte habe ich nach bestem Wissen und Gewissen geprüft.

Mir ist bekannt, dass ein Verstoß gegen die genannten Punkte prüfungsrechtliche Konsequenzen hat und insbesondere dazu führen kann, dass die Promotionsleistung als mit „nicht bestanden“ bewertet wird. Die Einschreibung kann für bis zu zwei Jahre widerrufen werden, wenn Studierende zweimal oder häufiger bei Prüfungsleistungen täuschen (§ 69 Abs. 4 und 5 HochSchG).

---

Ort, Datum und Unterschrift

\*Weiterführende Informationen zu KI-basierte Anwendungen oder Werkzeuge unter: <https://digitalelehre.uni-mainz.de/ki-in-der-hochschulbildung/>



*"It has long been an axiom of mine that the little things are infinitely the most important."*

Sherlock Holmes



# Zusammenfassung

Organische Aerosole üben einen wichtigen Einfluss auf das Erdklima aus, indem sie Strahlung streuen und absorbieren, sowie als Wolkenkondensationskeime (cloud condensation nuclei, CCN) wirken können. Um zu CCNs zu werden, müssen neu gebildete Partikel zunächst auf relevante Größen anwachsen. Da dieses Wachstum in Konkurrenz zur Entfernung durch Koagulation mit größeren Partikeln steht, benötigen frisch gebildete ultrafeine Aerosolpartikel hinreichend hohe Wachstumsraten, um in der Atmosphäre zu bestehen. Die Mechanismen, die ein derart schnelles Wachstum antreiben, sind bislang nur unvollständig verstanden. Atmosphärische Aerosolpartikel stellen zudem eine besondere Mikroumgebung für chemische Reaktionen dar. Das hohe Oberfläche-zu-Volumen-Verhältnis, größenabhängige thermodynamische Eigenschaften und Phasenzustandseffekte können Reaktionskinetiken und Produktverteilungen verändern. Insbesondere krümmungsabhängige Phänomene wie der Laplace-Druck dürften für Partikel im Nanometerbereich zunehmend an Bedeutung gewinnen, was potenziell Auswirkungen auf die Bildung von Verbindungen mit geringer Flüchtigkeit und das Partikelwachstum haben könnte. Während chemische Prozesse in atmosphärischen Aerosolen bereits umfassend untersucht wurden, gibt es vergleichsweise wenige Studien, die die Rolle der Partikelgröße, insbesondere im Nanometerbereich, explizit untersuchen. In dieser Arbeit wird daher untersucht, ob und wie chemische Reaktionen in nanometergroßen Aerosolpartikeln von der Partikelgröße abhängen und die physikalisch-chemischen Mechanismen eingeordnet, die das beobachtete Verhalten erklären könnten.

Hierzu wurden Reaktionslösungen zu Aerosolen zerstäubt und mittels eines differentiellen Mobilitätsanalysators monodisperse Aerosolpartikel mit definierten Durchmessern im Nanometerbereich isoliert. Heterogene Reaktionen und Partikelphasenreaktionen wurden anschließend bei kontrollierter relativer Luftfeuchte initiiert und über variierbare Aufenthaltszeiten mithilfe mehrerer Flowtubes mit definierten Volumina untersucht. Die entstehenden Partikelphasenbestandteile wurden online analysiert, indem eine thermische Verdampfung mit einer nitratbasierten chemischen Ionisation und einem Orbitrap-Massenspektrometer ( $\text{NO}_3\text{-CI-Orbitrap}$ ) über ein speziell entwickeltes Aerosolinlet gekoppelt wurde. Das Inlet kombiniert einen Partikelverdampfer mit einer nachgeschalteten Gaskühleinheit, um verdampfte Analyten schnell in die Ionenquelle zu überführen und dabei thermische Zersetzung sowie Wandverluste zu reduzieren. Die Instrumentenperformance wurde anhand von Modellaerosolen in kontrollierten Transmissions- und Verdampfungsexperimenten evaluiert.

Mit dem so etablierten experimentellen Versuchsaufbau wurden drei Modellreaktionssysteme auf partikelgrößenabhängige chemische Prozesse in Partikeln mit Mobilitätsdurchmessern von 30-110 nm untersucht. Zunächst wurde die heterogene

Ozonolyse von 5-Norbornen-2-endo,3-exo-dicarbonsäure als Modellsystem für zyklische Monoterpene untersucht. Kleinere Partikel zeigten höhere relative Signalbeiträge hochoxidierter Produkte und Dimere sowie geringere relative Signalbeiträge von Fragmentierungsprodukten. Unter trockenen Bedingungen näherte sich die Reaktion rasch einem Plateau an, wobei der Umsatz in kleineren Partikeln deutlich höher ausfiel. Außerdem wurde die heterogene Reaktion von Ascorbinsäurepartikeln mit Ozon untersucht, wobei ausgenutzt wurde, dass Ascorbinsäure in dem Reaktionssystem sowohl über Ozonolyse- als auch Oxidationspfade mit Ozon reagieren kann. Kleinere Partikel wiesen einen erhöhten relativen Beitrag von Ozonolyseprodukten und eine verstärkte Dimerbildung auf. Zusätzlich wurden zwei bislang nicht berichtete Ozonolyseprodukte beobachtet, und ein Dimer-Zwischenprodukt, das in der Literatur als möglicher Weg zur direkten Bildung hydratisierter bicyclischer Dehydroascorbinsäure diskutiert wird, konnte detektiert werden. Zuletzt wurde eine reine Partikelphasenreaktion, die Bildung von Borat-Tartrat-Esterkomplexen, in Tartrat-Aerosolpartikeln untersucht. Dabei zeigten sich ausgeprägt höhere Signale der Komplexe in kleineren Partikeln. Die beobachtete Größenabhängigkeit stimmt mit einem drucksensitiven Gleichgewicht überein, das potenziell durch den Laplace-Druck beeinflusst wird.

Insgesamt etabliert diese Arbeit ein experimentelles Rahmenkonzept für die molekulare online Analyse nanometergroßer Aerosolpartikel und zeigt, dass die Partikelgröße nicht nur Reaktionsgeschwindigkeiten, sondern auch Reaktionspfade und Produktverteilungen beeinflussen kann. Die Ergebnisse stützen die Vorstellung, dass krümmungsbedingte Effekte zur chemischen Alterung und zum Wachstum ultrafeiner atmosphärischer Partikel beitragen können.

# Abstract

Organic aerosols exert an important influence on Earth's climate by scattering and absorbing radiation, as well as by acting as cloud condensation nuclei (CCN). To become CCNs, newly formed particles must grow to relevant sizes. Because this growth competes with removal by coagulation with larger particles, freshly formed ultrafine aerosols require sufficiently rapid growth to persist. The mechanisms driving such rapid growth are still incompletely understood. Atmospheric aerosol particles provide a unique microenvironment for chemical reactions. High surface-to-volume ratios, size-dependent thermodynamics, and phase-state effects can modify reaction kinetics and product distributions. In particular, curvature-related phenomena such as Laplace pressure are expected to become increasingly relevant for nanometer-sized particles, with potential implications for the formation of low-volatility compounds and particle growth. While chemical processing in atmospheric aerosols has been studied extensively, comparatively few studies explicitly disentangle the role of particle size, particularly in the nanometer regime. This thesis therefore investigates whether and how chemical reactions in nanometer-sized aerosol particles depend on particle size and relates the physicochemical mechanisms that may account for the observed behavior.

For this purpose, reaction solutions were atomized into aerosols and monodisperse aerosol particles with defined diameters in the nanometer range were isolated using a differential mobility analyzer. Heterogeneous and particle-phase reactions were then initiated at controlled relative humidity and probed at variable residence times using a set of flow tubes with defined volumes. The resulting particle-phase constituents were analyzed online by coupling thermal evaporation to nitrate chemical-ionization Orbitrap mass spectrometry ( $\text{NO}_3\text{-CI-Orbitrap}$ ) via a custom-built aerosol inlet. The inlet design combines a particle evaporator with a dedicated gas-cooling unit to enable rapid transfer of volatilized analytes into the ion source while mitigating thermal decomposition and wall losses. Instrument performance was evaluated using model aerosols in controlled transmission and vaporization experiments.

The resulting experimental setup was applied to three model reaction systems to investigate particle-size-dependent chemical reactions at mobility diameters of 30–110 nm. First, the heterogeneous ozonolysis of 5-norbornene-2-endo,3-exo-dicarboxylic acid was investigated as a proxy for cyclic monoterpenes. Smaller particles exhibited higher relative signal contributions of highly oxidized products and dimers and lower relative contributions of fragmentation products. Under dry conditions, the reaction rapidly approached a plateau, with substantially higher conversions in smaller particles. Second, the heterogeneous reaction of ascorbic acid particles with ozone was examined, leveraging the dual reactivity of ascorbic acid via ozonolysis and oxidation pathways. Smaller particles showed an increased

relative contribution of ozonolysis products and enhanced dimer formation. In addition, two previously unreported ozonolysis products were observed and a dimer intermediate previously proposed in the literature to enable direct formation of hydrated bicyclic dehydroascorbic acid was detected. Third, a purely condensed-phase reaction, the borate-tartrate ester complex formation was studied in tartrate aerosol particles, revealing pronounced enhancements of complex signals in smaller particles. The observed size dependence is consistent with a pressure-sensitive equilibrium potentially influenced by Laplace pressure.

Overall, this work establishes an experimental framework for online molecular-level analysis of nanometer-sized aerosol particles and demonstrates that particle size can affect not only reaction rates but also chemical reaction pathways and product distributions. These findings support the concept that curvature-related effects may contribute to chemical processing and growth of ultrafine atmospheric particles.

# Table of Contents

Zusammenfassung.....	1
Abstract.....	3
Abbreviations .....	9
1 Theoretical Introduction and Motivation.....	11
1.1 Atmospheric Aerosol.....	11
1.1.1 Particle Size Distribution.....	11
1.1.2 Environmental Impacts.....	13
1.1.3 New Particle Formation .....	14
1.2 Nanoparticles as a Unique Reaction Medium .....	14
1.2.1 Kelvin Effect .....	15
1.2.2 Laplace Pressure .....	15
1.2.3 Tolman Length .....	16
1.2.4 Partial Solvation and Enhanced Interfacial Concentration.....	17
1.3 Chemical Foundations of the Studied Reactions .....	18
1.3.1 Pressure Dependence of Reactions in the Condensed Phase .....	18
1.3.2 Heterogeneous Ozonolysis of Unsaturated Compounds .....	19
1.4 Particle Measurement Instrumentation.....	21
1.4.1 Particle Concentrations.....	21
1.4.2 Particle Size Selection .....	23
1.4.3 Molecular Composition .....	24
1.5 Thesis Objective and Outline .....	29
2 Design and Characterization of an Aerosol Inlet for a CI-Orbitrap Mass Spectrometer .	31
2.1 Introduction.....	32
2.2 Materials and Methods.....	34
2.2.1 Setup .....	34
2.2.2 Experiments.....	36
2.3 Results and Discussion.....	38

2.3.1	Performance of the In-House Built Gas-Cooling Unit .....	38
2.3.2	Particle Transmission .....	39
2.3.3	Evaporation Efficiency.....	41
2.3.4	Particle-Size Dependent Sensitivity .....	42
2.3.5	Decomposition.....	44
2.3.6	Thermograms from $\alpha$ -pinene Ozonolysis.....	46
2.4	Conclusion .....	49
3	Size-Dependent Ozonolysis of Norbornene-Dicarboxylic-Acid-Aerosol Particles .....	51
3.1	Abstract .....	52
3.2	Introduction.....	52
3.3	Materials and Methods.....	55
3.3.1	Flow Tube Experiments .....	55
3.3.2	Particle Evaporation .....	56
3.3.3	CI-Orbitrap Measurements.....	57
3.4	Results and Discussion.....	59
3.4.1	Characterization of Reaction Products .....	59
3.4.2	Particle Evaporation Efficiency .....	64
3.4.3	Humidity Dependence of the Reaction Rate.....	67
3.4.4	Particle-Size-Dependent Chemistry .....	68
3.4.5	Influence of Relative Humidity on the Product Distribution .....	70
3.5	Conclusion .....	73
4	Size-Dependent Ozonolysis of Ascorbic Acid Aerosol Particles.....	75
4.1	Introduction.....	75
4.2	Materials and Methods.....	76
4.2.1	Aerosol Generation .....	76
4.2.2	Flow Tube Experiments.....	77
4.2.3	Aerosol Measurement.....	77
4.2.4	Data Evaluation .....	77
4.3	Results and Discussion.....	78

4.3.1	Kinetics of the Heterogeneous Reaction .....	78
4.3.2	Reaction Mechanism.....	80
4.3.3	Equilibrium between DHA and Cyclic aqDHA.....	83
4.3.4	Size-Dependent Reaction Pathways.....	85
4.3.5	Size-Dependent Dimer Formation.....	87
4.4	Conclusion .....	88
5	Size-Dependent Borate Cluster Formation in Tartrate Aerosol Particles .....	89
5.1	Introduction.....	89
5.2	Materials and Methods.....	90
5.2.1	Aerosol Generation .....	90
5.2.2	Flow Tube Experiments .....	91
5.2.3	Aerosol Measurement.....	91
5.2.4	Data Evaluation.....	92
5.3	Results and Discussion.....	92
5.3.1	Particle-Size-Dependent Complexation.....	92
5.3.2	Particle-Size Dependent Stoichiometry Distribution.....	94
5.3.3	Source Attribution.....	95
5.3.4	Dry Conditions .....	97
5.3.5	Discrepancy in the Educt Signal.....	99
5.4	Conclusion .....	101
6	Conclusion and Outlook .....	103
7	References.....	107
8	Appendix.....	125
8.1	Use of AI tools .....	125
8.2	Supplementary Materials Chapter 3.....	125
8.3	Supplementary Materials Chapter 4.....	141
8.4	Supplementary Materials Chapter 5.....	144
8.5	List of related publications and presentations.....	146
8.6	Curriculum Vitae.....	147



# Abbreviations

A <sup>-</sup>	ascorbate
AA	ascorbic acid
AAC	aerodynamic aerosol classifier
aqDHA	hydrated bicyclic dehydroascorbic acid
AAHP	$\alpha$ -acyloxyalkyl hydroperoxides
AMS	aerosol mass spectrometer
AHP	$\alpha$ -alkoxyalkyl hydroperoxides
APCI	atmospheric pressure chemical ionization
BTA	1,2,3,4- butanetetracarboxylic acid
CCN	cloud condensation nuclei
CHARON	Chemical Analysis of Aerosols Online
CI	chemical ionization
CI*	excited Criegee intermediate
CIMS	Chemical ionization mass spectrometry
CPC	condensation particle counter
DHA	dehydroascorbic acid
DMA	differential mobility analyzer
ELVOC	extremely low-volatility organic compound
ESI	electrospray ionization
EESI	extractive electrospray ionization
FIGAERO	Filter Inlet for Gases and Aerosols
HAHP	$\alpha$ -hydroxyalkyl hydroperoxide
HOM	highly oxidized molecule
HPLC	high performance liquid chromatography
HR-ToF-CIMS	high-resolution time-of-flight chemical ionization mass spectrometer
LVOC	low-volatility organic compound
MS	mass spectrometry

NDA	5-norbornene-2-endo,3-exo-dicarboxylic acid
NPF	new particle formation
OA	organic aerosol
OPC	optical particle counter
POZ	primary ozonide
PTR-MS	proton-transfer-reaction mass spectrometer
RH	relative humidity
SCI	stabilized Criegee intermediate
SOA	secondary organic aerosol
SOZ	secondary ozonide
SMPS	scanning mobility particle sizer
SVOC	semi-volatile organic compounds
TA	tricarballic acid
THR	threonic acid
UHRMS	ultrahigh-resolution mass spectrometry
VOC	volatile organic compound

# 1 Theoretical Introduction and Motivation

## 1.1 Atmospheric Aerosol

Earth's atmosphere is not composed solely of gas-phase molecules (primarily nitrogen, oxygen, argon, and carbon dioxide); rather, it is commonly a two-phase system in which numerous microscopic particles, which are present as solids or liquids, are suspended within the gas phase, forming an aerosol (Pöschl, 2005; Seinfeld and Pandis, 2006). Their particle number concentrations vary widely in space, ranging from fewer than 10 particles  $\text{cm}^{-3}$  in the stratosphere to up to  $10^6$  particles  $\text{cm}^{-3}$  in urban environments or coastal regions (O'Dowd et al., 2002; Curtius et al., 2005; Curtius, 2006). Aerosols can exhibit a high degree of chemical complexity. Even the smallest particles, with diameters of only a few nanometers, may contain thousands of distinct molecular species within volumes below one attoliter ( $10^{-18}$  L) (Riemer et al., 2019). This complexity reflects the diversity of sources contributing to atmospheric particulate matter. Natural sources include volcanic emissions, resuspended mineral dust, sea spray, pollen, biomass burning, and the emission of volatile organic compounds (VOCs) from vegetation and soils. In addition, anthropogenic sources such as fossil-fuel combustion and industrial emissions contribute substantially (Shrivastava et al., 2017; Curtius, 2006; Pöschl, 2005; Stolzenburg et al., 2023; Seinfeld and Pandis, 2006).

Depending on their origin, aerosol particles may be emitted directly into the atmosphere, as in the case of sea spray or pollen, and are then referred to as primary aerosols. Alternatively, aerosols can form in situ via gas-to-particle conversion processes. Such secondary organic aerosol (SOA) is produced, for example, when VOC oxidation generates lower-volatility products that subsequently nucleate to form new particles (new particle formation, NPF) or condense onto pre-existing particles (Seinfeld and Pandis, 2006; Curtius, 2006; Shrivastava et al., 2017; Stolzenburg et al., 2023; Kroll and Seinfeld, 2008).

### 1.1.1 Particle Size Distribution

After their formation, aerosol particles can further evolve in size through condensation or evaporation of gas-phase species and through coagulation with other particles (Seinfeld and Pandis, 2006). Depending on the definition, aerosol particle diameters span approximately five to six orders of magnitude, from  $<10$  nm up to  $\sim 100$   $\mu\text{m}$ . The lower limit is set by the transition to molecular clusters, whereas the upper limit is constrained by rapid gravitational settling (Alemán et al., 2007; Hinds, 1999; Seinfeld and Pandis, 2006). This size range is

commonly divided into fine particles (<2.5 μm) and coarse particles (>2.5 μm; see Figure 1.1) (Seinfeld and Pandis, 2006).

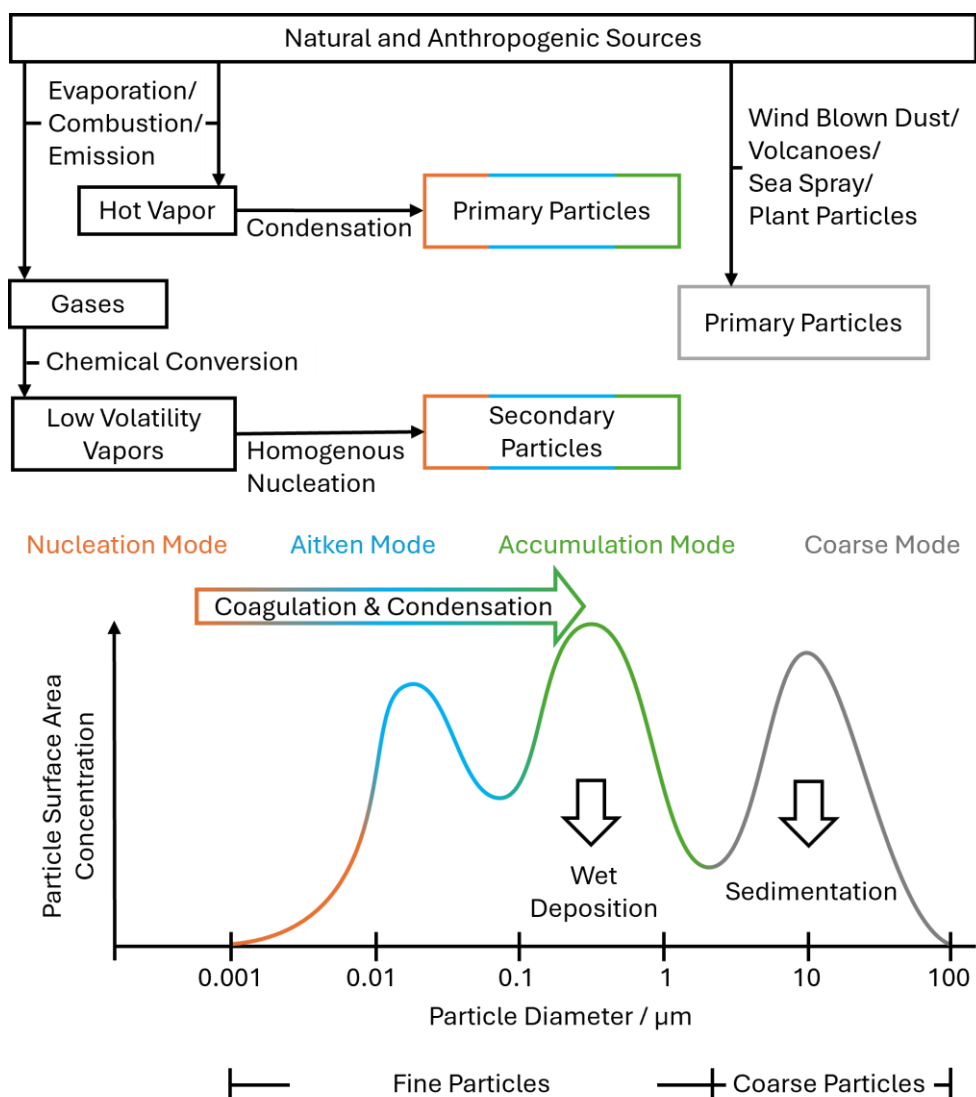


Figure 1.1: Schematic overview of the sources, transformation processes, and removal mechanisms of atmospheric aerosol, and the resulting multimodal distribution of particle surface area as a function of particle diameter. Modified after Whitby (1978) and Seinfeld and Pandis (2006).

The distinction between fine and coarse particles reflects fundamentally different sources, sinks, and chemical composition (Seinfeld and Pandis, 2006). Consequently, atmospheric aerosol size distributions are typically non-Gaussian and exhibit multiple modes as shown in Figure 1.1. Coarse particles are predominantly primary and are emitted via mechanical processes. Owing to their large mass, they are removed relatively rapidly from the atmosphere by sedimentation. Fine particles, in contrast, are often described by three modes: the nucleation, Aitken, and accumulation modes. Particles in the nucleation mode (approximately 3-12 nm) form via nucleation of gas-phase molecules followed by stabilization of the newly

formed clusters and growth through condensation of oxidized organic compounds (Kulmala et al., 2013; Stolzenburg et al., 2023). Through subsequent coagulation and condensational growth, these freshly formed particles can grow into the Aitken mode (12-100 nm) (Stier et al., 2005). The lifetimes of particles in the nucleation and Aitken modes are short because their high diffusivities promote rapid coagulation with larger particles, contributing to the formation and growth of the accumulation mode (Tomasi, 2017). In the accumulation mode, coagulation and sedimentation are comparatively less efficient removal pathways, resulting in longer atmospheric lifetimes (Seinfeld and Pandis, 2006). Instead, wet deposition, uptake of aerosol particles into cloud or rain droplets followed by precipitation, constitutes the dominant sink for accumulation-mode particles (Tomasi, 2017).

### 1.1.2 Environmental Impacts

Atmospheric aerosols can absorb and scatter both incoming solar radiation and outgoing terrestrial radiation, thereby exerting a direct influence on Earth's radiative balance. Whether this direct radiative effect results in net warming or cooling depends on particle size, chemical composition, and the albedo of the underlying surface beneath the aerosol-containing air mass (Bellouin et al., 2020; Szopa et al., 2023). For example, black carbon (soot) efficiently absorbs radiation and contributes to warming, whereas sulfate and organic aerosol (OA) predominantly scatter radiation and thus tend to produce a cooling effect. Overall, atmospheric aerosols are commonly assessed to exert a net cooling influence through their combined absorption and scattering of radiation (Szopa et al., 2023).

In addition to these direct effects, aerosols influence climate indirectly by acting as cloud condensation nuclei (CCN). Particles in the accumulation-mode size range provide surfaces onto which water vapor can condense, ultimately forming cloud droplets. Under otherwise comparable meteorological conditions, cloud droplet number concentrations typically increase with CCN abundance, while mean droplet sizes decrease (Twomey, 1977; McNeill, 2017). This microphysical response affects the radiative properties of clouds. Clouds composed of smaller droplets generally exhibit higher albedo and can therefore enhance planetary cooling (Albrecht, 1989; McNeill, 2017).

A substantial fraction of CCN-relevant particles originates from secondary organic aerosol produced via NPF followed by growth to climatically relevant sizes. Beyond their role in the radiative budget, ultrafine particles may also affect human health because their small size enables deep penetration into the respiratory tract (Kwon et al., 2020; Stolzenburg et al., 2023). NPF events have also been reported in large urban areas, where elevated emissions of anthropogenic VOCs can contribute to ultrafine particle production and thereby increase potential health risks.

### 1.1.3 New Particle Formation

New particle formation begins with collisions among very low-volatility gas-phase species that, in the initial step, assemble into a molecular cluster. This first step is commonly referred to as nucleation (Stolzenburg et al., 2023). The compounds most frequently implicated in forming and growing these embryonic clusters include sulfuric acid and ammonia. To prevent rapid evaporation back to the gas phase, these clusters must be stabilized, which can occur through acid-base chemistry and through additional condensation of amines and other organic vapors (Almeida et al., 2013; Kulmala et al., 2013).

Once a cluster has been stabilized, its subsequent growth rate becomes the key determinant of whether it can eventually reach sizes at which it may act as a CCN. This is because the smallest particles are particularly susceptible to removal by coagulation with pre-existing aerosol. Growth proceeds via continued condensation of low-volatility compounds, and highly oxidized molecules (HOMs) produced during gas-phase oxidation of VOCs often play a central role (Bianchi et al., 2019; Stolzenburg et al., 2023). However, more volatile species can also contribute to particle growth. VOC oxidation generates compounds that partition between the gas and particle phases. These semivolatile organic compounds (SVOCs) can condense onto particles according to their volatility. The particle-phase fraction of SVOCs increases with increasing particle mass, implying that their contribution to growth becomes more important as particles grow larger (Pankow, 1994). In addition, particle-phase reactions that convert SVOCs into lower-volatility products can further enhance growth by shifting the gas-particle partitioning equilibrium toward the condensed phase (Stolzenburg et al., 2023).

## 1.2 Nanoparticles as a Unique Reaction Medium

Transforming a liquid from the bulk phase into an aerosol particle or a microdroplet with diameters ranging from nanometers to a few micrometers changes not only the physical state of the system but can also substantially alter the chemical processes that occur within it. A central distinction between particles and bulk phases is the greatly increased surface-to-volume ratio in aerosols. This strongly affects heterogeneous reactivity because gas-phase species can access and interact with particle-bound reactants more efficiently. Moreover, reactions occurring at the particle-gas interface can be enhanced because a much larger fraction of molecules resides at or near the surface compared with bulk liquids or solids (Donaldson and Valsaraj, 2010; George and Abbatt, 2010; George et al., 2015).

However, the distinctive behavior of very small particles extends beyond their high surface-to-volume ratio. Because aerosol particles are approximately spherical, their surfaces are

curved rather than planar. This curvature influences the thermodynamics of the system. In particular, it modifies the chemical potential of molecules at the particle surface (Seinfeld and Pandis, 2006; Elliott, 2021). As surface curvature increases with decreasing particle diameter, such effects become especially relevant for particles below  $\sim 50$  nm, including freshly formed particles produced via NPF.

### 1.2.1 Kelvin Effect

A first curvature-driven effect is described by the Kelvin equation, which relates the equilibrium vapor pressure  $p_A$  above a pure liquid to the particle radius  $R_P$  (see Equation 1.1) (Seinfeld and Pandis, 2006).

$$p_A = p_A^\circ \cdot \exp\left(\frac{2\sigma M}{RT\rho_t R_P}\right) \quad 1.1$$

Here,  $p_A^\circ$  denotes the vapor pressure above a flat surface,  $\sigma$  is the surface tension, and  $M$  and  $\rho_t$  are the molar mass and density of the liquid, respectively. The Kelvin equation implies that the equilibrium vapor pressure above a curved surface is higher than that above a flat surface (Seinfeld and Pandis, 2006). Conceptually, this arises because molecules at a curved particle surface have fewer neighboring molecules than molecules on a planar interface, leading to weaker net cohesive interactions in the condensed phase. Consequently, less energy is required for a molecule to escape into the gas phase (Seinfeld and Pandis, 2006).

At equilibrium (i.e., in a saturated gas phase), the corresponding gas-phase concentration of a condensable species is therefore higher above small particles than above a flat surface. Because the effect increases with decreasing particle radius, any undersaturation in the surrounding gas phase promotes net evaporation, which reduces particle size and further elevates the equilibrium vapor pressure, thereby reinforcing evaporation. Conversely, if the ambient gas-phase concentration exceeds the Kelvin-adjusted equilibrium concentration, the particle will undergo net condensation and continuous growth (Hinds, 1999).

### 1.2.2 Laplace Pressure

The cohesive (attractive) interactions between molecules in the liquid phase described above imply that molecules in the bulk gain more interaction energy than molecules at the surface, simply because they have a larger number of neighboring interaction partners. As a result, the system experiences an effective pressure that tends to pull surface molecules into the bulk in order to maximize cohesive interactions. The counteracting force that maintains the interface is the surface tension. This balance also explains why liquids tend to form droplets. For a given

volume, a sphere minimizes surface area and thus minimizes the energetic cost associated with the interface (Mugele and Heikenfeld, 2018).

In small particles, this effect is enhanced by surface curvature, analogous to the Kelvin effect. The corresponding excess internal pressure relative to the surrounding gas phase is referred to as the Laplace pressure  $\Delta p$ , and is described by the Young–Laplace equation (see Equation 1.2) (Adamson and Gast, 1997).

$$\Delta p = \frac{2\sigma}{R_p} \quad 1.2$$

While Laplace pressure is negligible compared with atmospheric pressure for large particles, nanometer-sized particles can reach internal pressures comparable to those encountered in medium to high-pressure chemistry (see Figure 1.2) (Benito-López et al., 2008; Petters, 2022). The chemical composition strongly influences the magnitude of  $\Delta p$ . For particles of the same size, aqueous particles typically exhibit higher internal pressures than pure, dry organic particles because water has a higher surface tension (Petters, 2022; Gennes et al., 2009; Hritz et al., 2016).

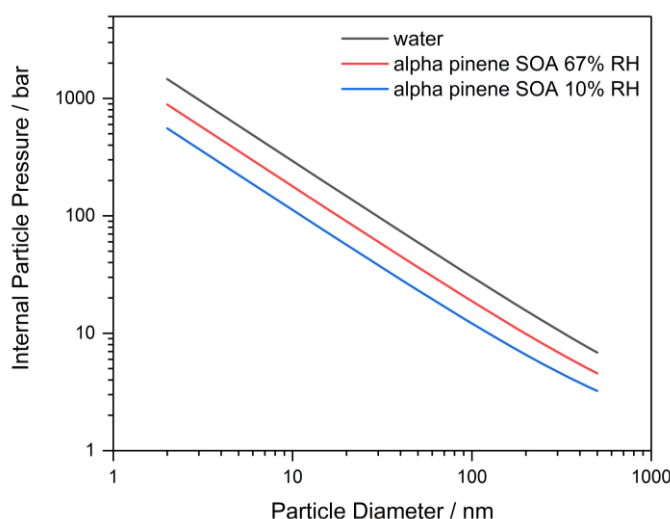


Figure 1.2: Resulting internal particle pressures as a function of particle diameter for pure water ( $\sigma = 73 \text{ mN m}^{-1}$  (Gennes et al., 2009)) and  $\alpha$ -pinene SOA at relative humidities of 67% and 10% ( $\sigma = 44.4 \text{ mN m}^{-1}$  and  $\sigma = 27.8 \text{ mN m}^{-1}$ , respectively (Hritz et al., 2016)).

### 1.2.3 Tolman Length

As indicated above, surface tension is a key parameter in curvature-induced effects. However, because surface tension itself originates from intermolecular interactions at an interface, it can in turn depend on interfacial geometry (Tolman, 1949; El Haber et al., 2024). This concept is commonly captured by the Tolman length, which characterizes the radius scale below which the surface tension of a curved interface deviates measurably from the macroscopic value.

When particle radii approach this scale, intermolecular interactions at the surface are reduced so sufficiently that the effective surface tension decreases (El Haber et al., 2024; Lu and Jiang, 2005). A reduction in surface tension would, in principle, counteract both the Kelvin effect and the Laplace pressure, which both scale with  $\sigma$ .

For most substances, reported Tolman lengths are on the order of  $< 1$  nm. It is therefore commonly assumed that Kelvin and Laplace effects remain relevant for particles larger than  $\sim 1$  nm, whereas curvature-induced changes in surface tension become significant only at still smaller length scales (Xue et al., 2011; Lu and Jiang, 2005).

#### 1.2.4 Partial Solvation and Enhanced Interfacial Concentration

In addition to curvature-driven thermodynamic effects, surface-specific kinetic effects have been discussed for microdroplets that could, in principle, also be relevant in smaller particles. Since the late 2000s, numerous studies have reported that a wide range of organic reactions proceeds substantially faster in aqueous microdroplets than in bulk solution (Augusti et al., 2006; Ismael Cotte-Rodríguez et al., 2006; Enami et al., 2008; Girod et al., 2011). The origin of these rate enhancements remains an active area of research, and multiple mechanisms have been proposed (Wei et al., 2020; Lacour et al., 2025; Chan et al., 2026). Unlike the curvature-induced effects discussed above, which are expected to become most pronounced at nanometer scales, microdroplet rate enhancements have primarily been observed for droplets larger than  $\sim 1$   $\mu\text{m}$ . Nevertheless, it is plausible that at least some of the underlying mechanisms may also influence nanometer-sized particles, as many explanations emphasize the unique physicochemical environment at the interface. Two commonly discussed hypotheses are briefly outlined below.

One explanation builds on the established observation that Diels–Alder reactions between hydrophobic dienes and dienophiles can proceed much faster in aqueous media than in organic solvents (Breslow, 1991; Narayan et al., 2005). This acceleration has been attributed to the accumulation of hydrophobic reactants at the water-air interface, leading to interfacial enrichment and thus higher effective local concentrations (Xiong et al., 2020; Ruiz-López and Martins-Costa, 2022). In addition, “dangling” OH groups at the water surface have been proposed to stabilize transition states of interfacial organic reactions (Jung and Marcus, 2007). By analogy, aqueous microdroplets may promote interfacial enrichment of relatively hydrophobic organic reactants, increasing collision frequencies and thereby accelerating reactions. This framework implies that rate enhancements should be most pronounced for bimolecular processes, which benefit directly from increased encounter rates, an expectation that is broadly consistent with the literature (Wei et al., 2020; Qiu et al., 2021).

A second explanation, also linked to the high surface-to-volume ratio, treats the interface as a distinct reaction environment intermediate between gas and condensed phases (Yan et al., 2016; Qiu et al., 2021). Gas-phase reactions are typically faster than reactions in solution, whereas reactions in the condensed phase can yield higher absolute product amounts because reactants encounter each other more frequently at higher density. One reason solution-phase reactions can be slower is that reactants are often solvated, such that solvent reorganization and partial desolvation may be required before reaction can occur (Olmstead and Brauman, 1977; Chandrasekhar et al., 1984). The particle surface may provide an environment in which reactants remain comparably densely packed, as in the bulk, while being less fully solvated at the boundary to the gas phase. This reduced solvation can lower the effective energetic barrier to react and thereby enhance reactivity at interfaces (Wei et al., 2020; Narendra et al., 2020).

## 1.3 Chemical Foundations of the Studied Reactions

### 1.3.1 Pressure Dependence of Reactions in the Condensed Phase

Whereas in the gas phase the effect of pressure on reaction rates is often directly linked to number density and collision frequency, pressure can also influence the kinetics and thermodynamics of chemical processes in the condensed phase. In solution, these effects can be described consistently in terms of the pressure derivatives of equilibrium constants  $K$  and rate constants  $k$  which lead to the key quantities reaction volume  $\Delta V$  and activation volume  $V^\ddagger$  (see Equations 1.3 and 1.4) (van Eldik et al., 1989).

$$\Delta V = -RT \cdot \left( \frac{\partial \ln K}{\partial p} \right)_T \quad 1.3$$

$$\Delta V^\ddagger = -RT \cdot \left( \frac{\partial \ln k}{\partial p} \right)_T \quad 1.4$$

According to Equation 1.3, increasing pressure shifts a chemical equilibrium toward products when the reaction volume is negative ( $\Delta V < 0$ ). Conversely, a positive reaction volume implies that higher pressure disfavors product formation. An analogous relationship holds for the kinetics. An increased pressure accelerates a reaction when the activation volume is negative ( $\Delta V^\ddagger < 0$ ), whereas it slows the reaction when the activation volume is positive ( $\Delta V^\ddagger > 0$ ).

The conceptual basis for  $\Delta V$  and  $\Delta V^\ddagger$  is illustrated in Figure 1.3. Each reactant is characterized by a molar volume  $V_R$ , and the molar volume of the products,  $V_P$ , may differ from that of the reactants. This difference is quantified by the reaction volume  $\Delta V$ . Chemical reactions typically proceed via a transition state ( $\ddagger$ ), which is associated with its own molar volume  $V^\ddagger$ .

The difference between  $V_R$  and  $V^\ddagger$  defines the activation volume  $\Delta V^\ddagger$  (van Eldik et al., 1989; Klärner and Wurche, 2000).

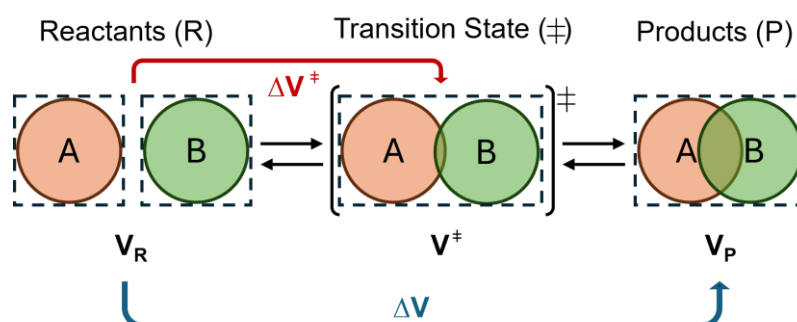


Figure 1.3: Schematic representation of reaction volume  $\Delta V$  activation volume  $V^\ddagger$ . Modified after Klärner and Wurche (2000).

Bond formation is often accompanied by a decrease in molar volume, as longer-range electrostatic and dispersion interactions are replaced by shorter-range interactions associated with increased orbital overlap in the bonded state (van Eldik, 2008; Petters, 2022). Consequently, addition reactions such as esterifications and aldol reactions are commonly accelerated at elevated pressure. Concerted cycloadditions, such as Diels-Alder reactions and ozonolysis, can exhibit particularly strong acceleration because multiple bonds are formed simultaneously in the transition state. By the same mechanistic reasoning, unimolecular fragmentation processes (e.g., eliminations) tend to be slowed at high pressure (Chen et al., 2017). Acid-base equilibria can also be pressure dependent. Dissociation equilibria often exhibit negative  $\Delta V$  because ion formation induces electrostriction, which can increase apparent acid and/or base strength under pressure (Kumar, 2005).

### 1.3.2 Heterogeneous Ozonolysis of Unsaturated Compounds

Ozone, together with hydroxyl radicals and nitrate radicals, is among the principal oxidants responsible for the atmospheric processing of VOCs in the lower atmosphere (Kroll and Seinfeld, 2008; Campbell et al., 2022). The reaction of ozone with alkenes proceeds via a 1,3-dipolar cycloaddition, initially forming a primary ozonide (POZ; see Figure 1.4) (Criegee, 1975). The POZ rapidly decomposes in an exothermic step to yield a carbonyl compound and a Criegee intermediate (CI\*). Owing to the large energy release upon POZ cleavage, the CI\* is initially formed in an excited state, which may undergo further decomposition, resulting in the formation of an alkyl radical and an OH radical. (Chhantyal-Pun et al., 2020). This pathway is commonly referred to as the hydroperoxide channel and can contribute, among other outcomes, to the formation of highly oxidized molecules via radical autoxidation initiated by  $O_2$  addition to the alkyl radical (Kroll and Seinfeld, 2008; Bianchi et al., 2019). Alternatively,

CI\* can be collisionally stabilized through energy transfer to surrounding molecules, yielding stabilized Criegee intermediates (SCI); this pathway is referred to as the SCI channel (Kroll and Seinfeld, 2008).

Both the hydroperoxide channel and the SCI channel are relevant for alkene ozonolysis in the gas phase. In heterogeneous ozonolysis, however, the hydroperoxide channel is often considered less important, likely because the higher number density in the condensed phase promotes rapid collisional stabilization of CI\* (Zhao et al., 2019). Nonetheless, autoxidation processes may still be relevant at the particle surface.

Once formed, SCIs can react through multiple pathways depending on the available reaction partners. Reaction with aldehydes and ketones yields secondary ozonides (SOZ) (Kroll and Seinfeld, 2008). Reaction with water produces  $\alpha$ -hydroxyalkyl hydroperoxides (HAHP) (Enami, 2021; Wang et al., 2023). HAHPs can subsequently decompose to aldehydes or ketones with elimination of hydrogen peroxide, or form carboxylic acids via water elimination if R is a hydrogen; carboxylic acids may also form directly from SCIs through isomerization (Zhao et al., 2019). Analogous to reaction with water, reaction of SCIs with alcohols yields  $\alpha$ -alkoxyalkyl hydroperoxides (AHP), whereas reaction with acids yields  $\alpha$ -acyloxyalkyl hydroperoxides (AAHP) (Enami, 2021; Wang et al., 2023).

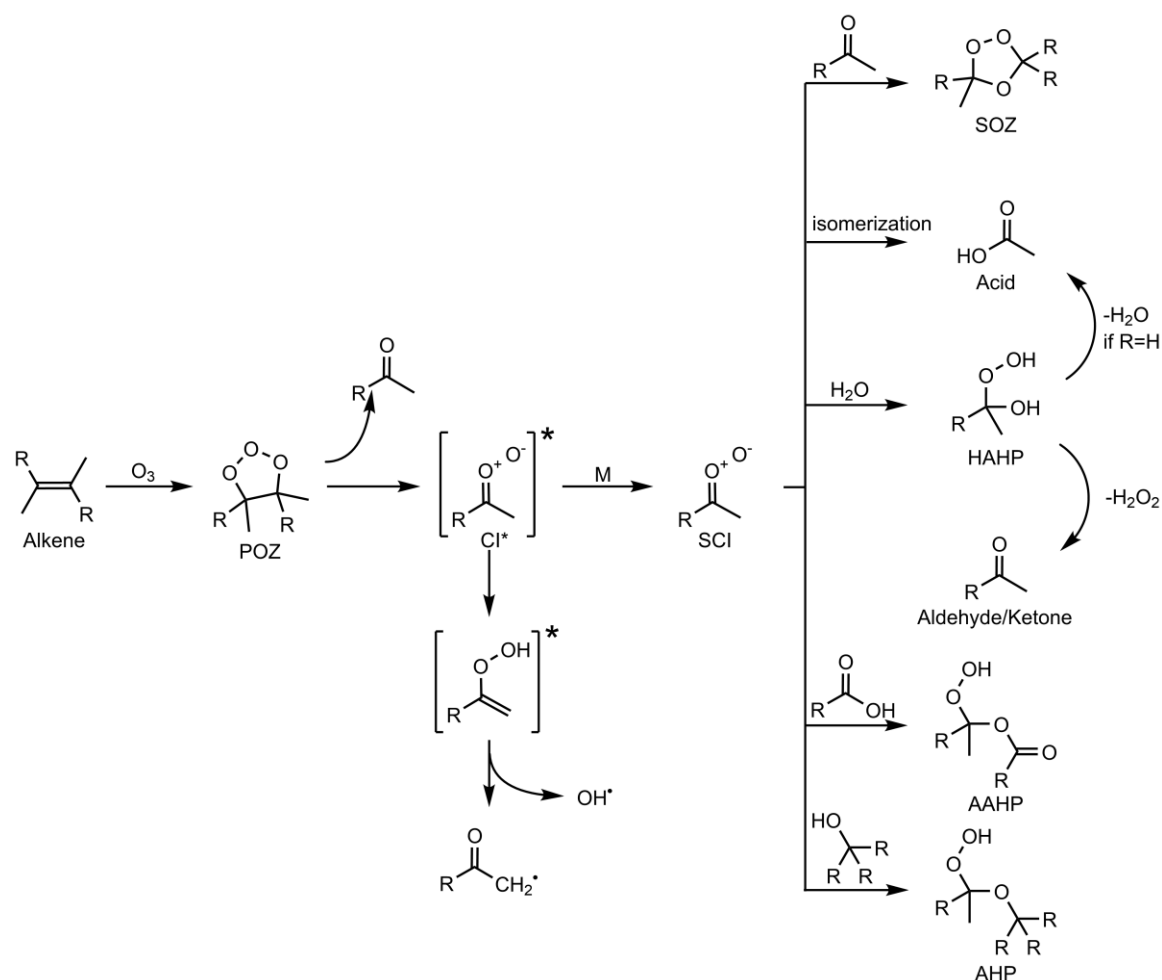


Figure 1.4: Schematic of alkene ozonolysis. Modified by Kroll and Seinfeld (2008).

Aerosol particles exhibit a wide range of physicochemical properties, several of which were deliberately controlled or investigated in the experiments conducted in this work. Accordingly, a set of specialized instruments was employed. A differential mobility analyzer (DMA) was used to select specific particle sizes from the polydisperse aerosol in order to probe size-resolved reaction behavior. Particle number concentrations were monitored with a condensation particle counter (CPC) to ensure comparable particle mass loadings across experiments. The size-selected particles were then thermally transferred to the gas phase using an evaporator, and the chemical composition of the particle-phase material was characterized by nitrate chemical ionization Orbitrap mass spectrometry ( $\text{NO}_3^-$ -CI-Orbitrap MS).

### 1.4.1 Particle Concentrations

Several approaches are available to quantify aerosol particle concentrations in an air mass. A simple and widely used method is filter-based sampling. There, an air stream is drawn through a filter, particles are collected, and the particulate mass is subsequently determined gravimetrically by weighing the filter. Dividing the collected mass by the sampled air volume yields the aerosol mass concentration (Kulkarni et al., 2011). However, this approach provides only poor time resolution and does not deliver information on particle number concentrations.

These limitations are addressed by instruments capable of counting individual particles in an aerosol stream. One such online technique is the optical particle counter (OPC). In an OPC, the aerosol is passed through a focused light beam. Each particle scatters light, and the scattered intensity is detected by a photodiode. The particle number concentration is obtained from the number of light pulses recorded per unit time (TSI Incorporated, 2019). OPCs are typically applied in the micrometer and submicrometer size range. As particle size decreases, light-scattering efficiency declines, and the lower detection limit is therefore commonly on the order of  $\sim 100$  nm diameter (Kulkarni et al., 2011).

Condensation particle counters (CPCs) also rely on optical detection by light scattering, but they extend counting capability into the lower nanometer regime by preceding detection with condensational growth. Specifically, the aerosol is exposed to a supersaturated vapor of a working fluid, which condenses onto the particles and grows them to optically detectable diameters of roughly 2-15  $\mu\text{m}$  (Kulkarni et al., 2011). Typical working fluids include water

and n-butanol. Supersaturation can be generated in different CPC designs via adiabatic expansion, thermal diffusion, or mixing of hot and cold streams (Kulkarni et al., 2011).

The instrument employed in this work was a water-based CPC (TSI Model 3789), which uses a thermal diffusion growth tube (see Figure 1.5). The growth tube comprises three sections: the conditioner, initiator, and moderator which are traversed by a porous, cylindrical wick saturated with water. The aerosol flow enters through the conditioner, where it is either cooled below ambient temperature (2 nm mode) or warmed above ambient temperature (7 nm mode) and brought to water saturation, thereby establishing a flow with well-defined temperature and humidity. The aerosol then passes into the heated initiator section. There, water evaporates from the wick and mixes with the cooler aerosol stream, producing supersaturation. Supersaturation arises because water vapor mixes into the aerosol stream more rapidly than the aerosol warms via thermal diffusion, owing to the higher mass diffusivity of water relative to the thermal diffusivity of air (TSI Incorporated, 2019). Under these conditions, water condenses onto the aerosol particles, leading to their growth. The magnitude of supersaturation is governed by the temperature difference between the conditioner and initiator; smaller particles require higher supersaturation to activate condensational growth due to the Kelvin effect (see 1.2.1). In the subsequent moderator section, the walls are cooled again, maintaining conditions favorable for continued growth while removing excess water by condensation to the walls, thereby reducing the risk of water deposition on the optical components of the detector (TSI Incorporated, 2019).

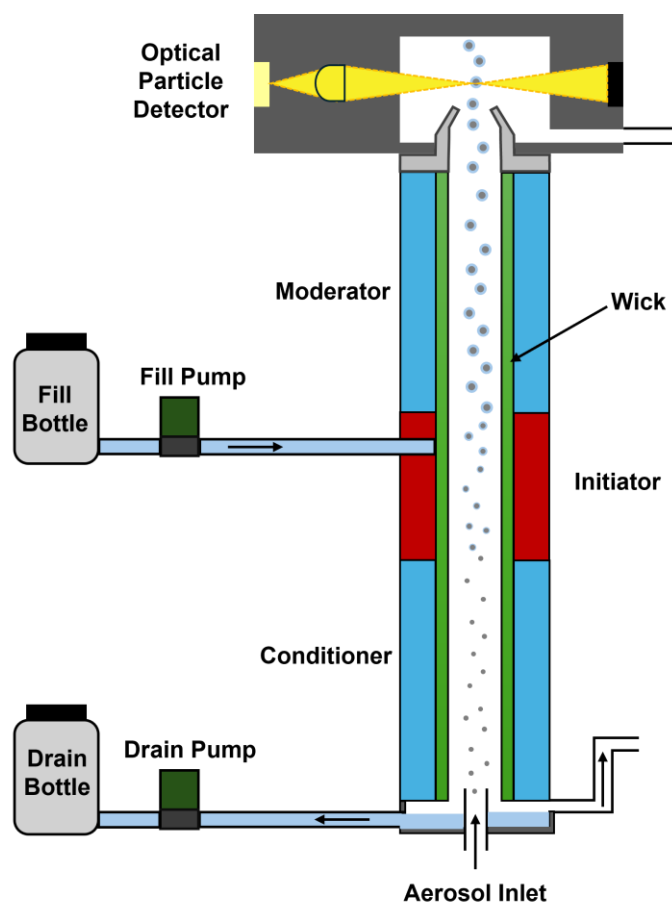


Figure 1.5: Schematic of the water-based condensation particle counter (TSI Model 3789). Modified after TSI Incorporated (2019).

To investigate aerosol particles in a size-resolved manner, specific size fractions must be isolated from the initially polydisperse aerosol. Two instruments that enable such size selection are the differential mobility analyzer (DMA) and the aerodynamic aerosol classifier (AAC). In a DMA, particles are classified according to their electrical mobility in an applied electric field, whereas in an AAC classification is based on mechanical mobility in a rotating (centrifugal) flow field, which are both particle-size dependent quantities (Kulkarni et al., 2011; Tavakoli and Olfert, 2013).

In this work, an electrostatic classifier (TSI Model 3082) equipped with a nano-DMA (TSI Model 3085A) was used. Prior to classification, particles are passed through a neutralizer, which in this setup was an X-ray source generating high concentrations of positive and negative ions. Because DMA-based size selection depends on particle charge and the charge distribution can vary with aerosol generation conditions, interaction with the bipolar ions establishes a well-defined charge equilibrium with known charging probabilities (TSI Incorporated, 2016; Wiedensohler, 1988). The charge-conditioned aerosol is then introduced into the nano-DMA. The operating principle is illustrated in Figure 1.6. The DMA consists of two concentric metal cylinders between which a laminar sheath flow is directed from top to bottom. The aerosol enters near the top through a narrow slit and is confined near the outer cylinder wall without significant mixing with the sheath flow. A voltage is applied to the inner cylinder, attracting charged particles toward the central electrode. Smaller particles have higher electrical mobility and therefore drift more rapidly toward the inner electrode, depositing higher up on the cylinder. Particles with a narrow range of electrical mobility are extracted through a small outlet slit near the bottom of the inner cylinder, yielding a monodisperse aerosol. The selected electrical mobility and thus the corresponding particle size is controlled by adjusting the voltage applied to the inner electrode (TSI Incorporated, 2016).

When coupled to a CPC downstream of the DMA, the system can be operated as a scanning mobility particle sizer (SMPS). In SMPS mode, the DMA voltage is ramped continuously, sequentially transmitting particles from different mobility (size) intervals. Combining the particle counts acquired over the scan yields the particle number size distribution of the aerosol (TSI Incorporated, 2016; Kulkarni et al., 2011).

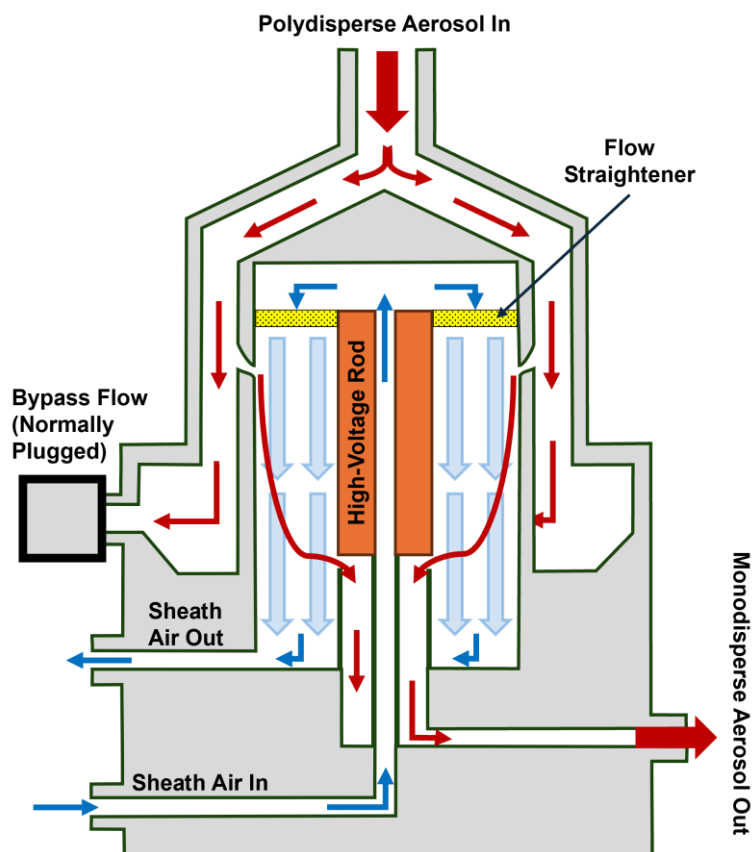


Figure 1.6: Schematic of the nano differential mobility analyzer (TSI Model 3085A). Modified after TSI Incorporated (2016).

### 1.4.3 Molecular Composition

Mass spectrometry has become an essential tool for elucidating the chemical composition of organic aerosol particles (Johnston and Kerecman, 2019; Li et al., 2023). In this technique, analytes are transferred to the gas phase, ionized, and subsequently separated and detected according to their mass-to-charge ratio ( $m/z$ ). In this thesis, aerosol particles were analyzed using an aerosol inlet coupled to a nitrate chemical ionization (CI) source interfaced with a Q Exactive Orbitrap mass spectrometer. The operating principles of this setup are described in the following sections.

### 1.4.3.1 Inlet System

Because organic aerosol particles exist in the condensed phase as solid or liquid, they must first be converted into a form suitable for ionization, which is most commonly the gas phase. Several approaches are available, which differ in whether particles are collected offline for subsequent analysis or characterized continuously in online measurements. For offline analysis, aerosol mass is typically collected on filters and extracted with organic solvents; the dissolved analytes are then analyzed by high performance liquid chromatography coupled to mass spectrometry (HPLC-MS), most commonly using atmospheric pressure chemical ionization (APCI) or electrospray ionization (ESI). Key advantages of this workflow are the ability to accumulate analyte mass over extended sampling times and the chromatographic separation of complex mixtures prior to mass spectrometric detection. These benefits come at the expense of time resolution and may involve losses or transformation of labile and/or reactive compounds during sampling and processing.

For online analysis, various strategies have been developed to transfer particle-phase material into the gas phase. Most of these rely on thermal energy input to volatilize the condensed-phase constituents. The aerosol mass spectrometer (AMS), one of the most widely used online instruments for aerosol characterization, employs a heated tungsten surface (~600 °C) onto which particles are impacted and evaporated (Johnston and Kerecman, 2019). However, direct heat transfer from highly conductive surfaces can promote thermal decomposition of labile organic compounds and thus induce fragmentation. Other inlet concepts aim for gentler heating via the surrounding carrier gas, for example by passing particles through a heated tube or exposing them to a stream of heated gas (Lopez-Hilfiker et al., 2014; Eichler et al., 2015; Zuth et al., 2018). Even with such approaches, thermal decomposition can still substantially affect the measured signal (Zhao et al., 2020; Yang et al., 2021). More recent inlet designs employ short, hot evaporators in combination with sheath flows, enabling rapid volatilization and efficient removal of excess thermal energy by the cooling gas, which can reduce the extent of thermal decomposition (Zhao et al., 2024; Gao et al., 2025).

### 1.4.3.2 Chemical Ionization

For mass spectrometric analysis, analytes must first be converted into gas-phase ions. A wide range of ionization methods exists, and the choice depends on the target compound classes and the information to be obtained. Chemical ionization mass spectrometry (CIMS) is generally considered a soft ionization technique because only limited excess energy is transferred to the analyte, thereby reducing fragmentation. Ion formation proceeds via ion-molecule reactions in which the charge is transferred from reagent ions that are generated from a reagent gas.

Figure 1.7 illustrates the configuration and operating principle of the CI-Orbitrap inlet used in this work (Riva et al., 2019a). The analyte flow is concentrically enveloped by a sheath gas, which minimizes analyte losses to surfaces. The sheath gas also contains the reagent gas, which generates reagent ions when irradiated by an X-ray source. Other CI inlets generate

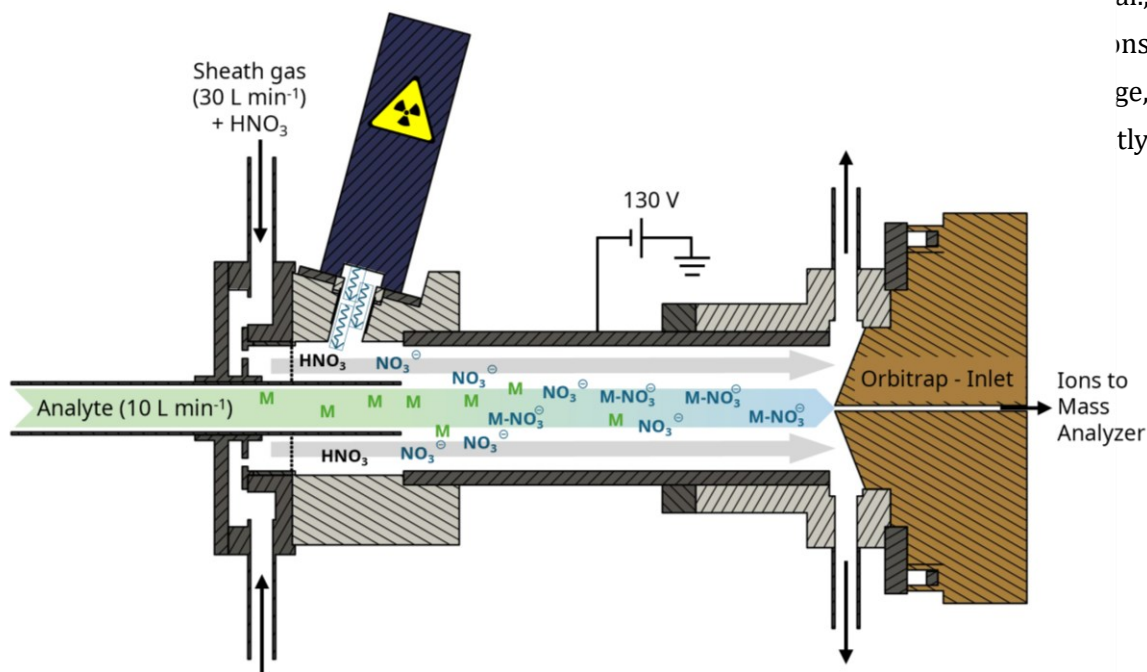
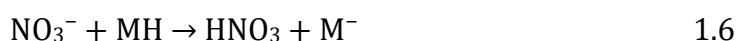


Figure 1.7: Schematic of the CI-Orbitrap inlet.

Ionization with  $\text{NO}_3^-$  proceeds primarily via adduct (cluster) formation with the neutral analyte (MH) (see Equation 1.5). These clusters are stabilized by intermolecular interactions such as dipole-dipole interactions and hydrogen bonding. Because nitrate can accept multiple hydrogen bonds via its three oxygen atoms, cluster formation is favored for molecules bearing several hydrogen-bond donating functional groups, such as alcohol and carboxylic acid moieties (Hyttinen et al., 2015). In addition to clustering, deprotonated analyte ions may form (see Equation 1.6), particularly when the analyte is more acidic than nitric acid and the resulting negative charge can be stabilized by intramolecular interactions (Wang et al., 2024).



NO<sub>3</sub> CIMS is highly sensitive and selective for highly oxygenated molecules (typically > 4-5 oxygen atoms), making it well suited for detecting low-volatility species that may contribute to NPF (Riva et al., 2019b; Bianchi et al., 2019). Conversely, less oxygenated compounds are often inefficiently ionized and may therefore be underrepresented (Tröstl et al., 2016). A variety of alternative reagent systems is available, including ammonia- and iodide-based CIMS, which exhibit different selectivities and can be selected according to the analytical target (Riva et al., 2019b; Li et al., 2024).

Because ionization depends on the ability of an analyte to form stabilizing interactions with the reagent ions, ionization efficiencies are strongly compound dependent and can differ by orders of magnitude. Consequently, relative signal intensities generally do not provide robust quantitative information on the abundance ratios of different analytes within a sample (Lopez-Hilfiker et al., 2016; Alage et al., 2024).

### 1.4.3.3 Orbitrap Mass Spectrometer

In addition to the diversity of ionization techniques, a wide range of mass analyzers and detection concepts is available for the analysis of gas-phase ions. While the ionization method largely defines which classes of analytes can be detected, the mass analyzer and detector determine the performance characteristics of the measurement (Zubarev and Makarov, 2013). One central metric is the mass resolving power  $R'$ , defined as the ratio of an ion mass  $m$  to the smallest mass difference  $\Delta m$  that can still be resolved from a neighboring peak (see Equation 1.7) (Murray et al., 2013).

$$R' = \frac{m}{\Delta m} \quad 1.7$$

Orbitrap analyzers belong to the class of ultrahigh-resolution mass analyzers ( $R' > 100,000$ ), and measurements are therefore commonly referred to as ultrahigh-resolution mass spectrometry (UHRMS) (Hawkes et al., 2016). Such resolving power can enable direct assignment of measured  $m/z$  values to elemental compositions. The Q Exactive Orbitrap used in this work provides a resolving power of  $R' = 140,000$  at  $m/z$  200 and a mass accuracy of < 2 ppm (Michalski et al., 2011).

The Orbitrap is an electrostatic ion trap in which ions are confined on stable orbital trajectories (Makarov, 2000). It comprises three electrodes: two outer, cup-shaped electrodes and a central spindle-shaped electrode (see Figure 1.8) (Makarov and Scigelova, 2010). The two outer electrodes are electrically insulated from each other by a thin insulator and are held at ground potential, whereas the central electrode is biased with a voltage of opposite polarity to the ions. This configuration generates a radial electric field that attracts ions toward the central electrode. Upon injection into the analyzer, ions are forced onto curved trajectories

around the central electrode. The orbit radius is governed by the balance between electrostatic attraction and the centrifugal force associated with the ions' kinetic energy (Scigelova and Makarov, 2006).

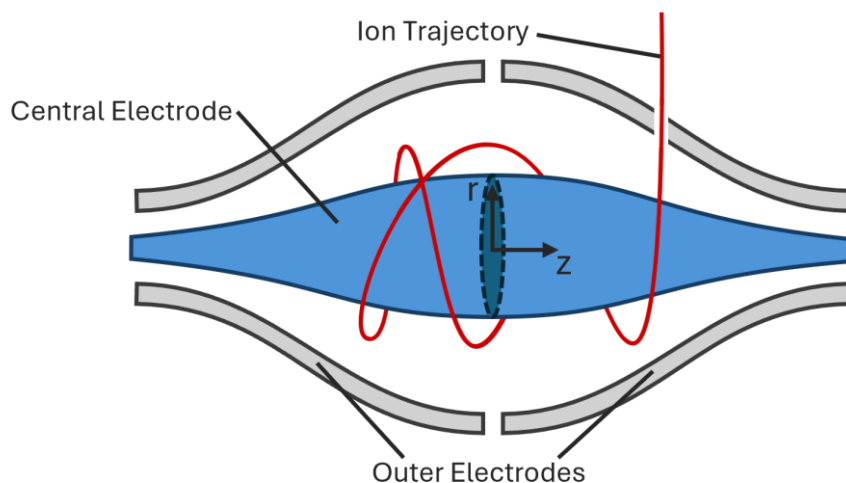


Figure 1.8: Schematic setup of the Orbitrap mass analyzer. Modified after Makarov and Scigelova (2010).

Because of the specific electrode geometry, the electrostatic field also includes an axial component that drives ions toward the widest region of the trap near its mid-plane. As ions are injected off-axis, they undergo harmonic oscillation along the  $z$ -axis. The angular frequency  $\omega$  of this axial motion depends on the square root of the reciprocal  $m/z$  and the field curvature parameter  $k$ , which is determined by electrode geometry and the applied voltages (see Equation 1.8) (Makarov, 2000).

$$\omega = \sqrt{\frac{z}{m} \cdot k} \quad 1.8$$

The frequency at which the ions oscillate along the axial axis can be determined because their motion induces an image current in the two outer electrodes. The temporal fluctuation in the current flow yields the oscillation frequencies of the various  $m/z$  values, that induced the current, via a Fourier transform. Because the axial oscillation frequency is independent of the ions' kinetic energy, very high mass resolving power can be achieved.

## 1.5 Thesis Objective and Outline

Atmospheric aerosol particles exert a strong influence on both Earth's climate and human health (see Chapter 1.1). A substantial fraction of atmospheric particulate mass consists of OA formed via NPF. To act as CCN, newly formed particles must grow to diameters of at least 30-100 nm (Riipinen et al., 2011). However, the small freshly nucleated particles are particularly susceptible to scavenging by pre-existing aerosol through coagulation. Consequently, rapid growth is required for these particles to survive and reach CCN-relevant sizes.

The molecular identity of the compounds driving this growth remains an active area of research. Growth may proceed via condensation of HOMs produced during gas-phase oxidation of VOCs. In addition, particle-phase reactions involving VOC oxidation products and SVOCs may generate lower-volatility species and thereby promote growth. In this size regime, aerosol particles constitute a distinctive reaction environment because high surface tension gives rise to size-dependent effects such as the Kelvin effect and elevated Laplace pressure (see Chapter 1.2). The latter may catalyze particle-phase chemistry that forms low-volatility products. In particular, bond-forming reactions such as cycloadditions and addition reactions, which underlie oligomer formation, are expected to be accelerated at higher pressure due to their negative activation volumes, whereas competing unimolecular decomposition pathways may be suppressed (see Chapter 1.3).

Accordingly, the aim of this thesis was to test whether selected reactions in nanometer-sized aerosol particles exhibit particle-size-dependent behavior, thereby providing insight into the growth of freshly nucleated particles. Because the detection of such small particles is challenging due to low mass loadings and substantial diffusional wall losses, chapter 2 first describes the development of an aerosol inlet comprising a particle evaporator and a gas-cooling unit. Coupled to a  $\text{NO}_3^-$ -CI-Orbitrap mass spectrometer, this setup enables the detection of particle-phase molecules in ultrafine aerosol particles. The subsequent chapters use the developed instrumentation to investigate model systems in which size-dependent reactivity is expected.

Chapter 3 examines the particle-size-dependent ozonolysis of 5-norbornene-2-endo,3-exo-dicarboxylic acid (NDA). As an endocyclic alkene bearing two carboxylic acid groups, NDA serves as a low-volatility proxy for cyclic monoterpenes, an important precursor class in SOA formation from VOC ozonolysis. Ozonolysis as a cycloaddition, together with multiple intra- and intermolecular follow-up reactions of the oxidation products, is expected to exhibit pressure sensitivity. The reaction mechanism and the effects of particle size and relative humidity on kinetics and product distributions are discussed.

Ascorbic acid (AA) is a particularly informative compound because, as a cyclic alkene, it can undergo ozonolysis via cycloaddition and can also be oxidized by ozone via electron-transfer chemistry. The latter pathway requires deprotonation of AA. Because dissociation equilibria can be pressure-dependent, particle-size-dependent reactivity may arise. Chapter 4 investigates the heterogeneous reaction of size-selected AA particles with ozone under different relative humidities.

In contrast to the heterogeneous systems of Chapters 3 and 4, Chapter 5 focuses on a purely particle-phase reaction. Boric acid forms stable borate complexes with alcohols, particularly with diols. Complex formation involves both bond formation and charge separation and therefore exhibits a strongly negative reaction volume. The particle-size dependence of this chemistry is investigated using tartaric-acid particles under different experimental conditions.

## 2 Design and Characterization of an Aerosol Inlet for a CI-Orbitrap Mass Spectrometer

**This chapter contains a first manuscript draft. After further coauthor exchange and optimization, it will be submitted to a peer-review journal as**

Douverne, M., XXX, X. and XXX, X.: Design and characterization of an aerosol inlet for a CI-Orbitrap mass spectrometer for organic aerosol studies

### **Contribution to this manuscript by Marcel Douverne**

As the first author of this work, I developed the aerosol inlet and optimized the CIMS measurement method and operating conditions for the inlet. I designed the inlet-characterization experiments, carried out all measurements, and performed the data analysis. I prepared the figures and wrote the manuscript. The manuscript was revised with input from all co-authors.

## 2.1 Introduction

Atmospheric aerosols exert a significant influence on the Earth's climate, both directly by absorbing and scattering radiation, and indirectly by impacting the planetary radiation budget. The indirect effect results from the particles acting as cloud condensation nuclei (CCN) (Pöschl, 2005; Seinfeld and Pandis, 2012; Curtius, 2006). The number of CCN controls the number and size of cloud droplets, and thus precipitation and cloud albedo (Lohmann and Feichter, 2005; Twomey, 1977). In order to act as CCN, particles must exceed a critical size, typically falling between 30 and 100 nm in diameter depending on supersaturation (Dusek et al., 2006; Pierce et al., 2011). A large proportion of atmospheric particulate matter (approximately 20–90%) is organic aerosol (Kanakidou et al., 2005). These particles form and grow through nucleation, followed by the condensation of semi-volatile and low-volatility organic compounds (Kroll and Seinfeld, 2008). However, freshly nucleated nanoparticles diffuse rapidly and are therefore highly susceptible to scavenging by coagulation with larger particles. Whether they can grow to CCN-active diameters depends on their condensational growth rate (Riipinen et al., 2011). The organic compounds and mechanisms that most strongly control this early growth remain uncertain.

In order to investigate the complex chemical composition and mechanisms of nanometer-scale particles in real time, sensitive online detection methods for organic aerosols are required. Mass spectrometry has become essential for determining the elemental composition of organic aerosol constituents (Li et al., 2023; Johnston and Kerecman, 2019). Detection at the molecular level requires the transfer of analytes from the particle phase to the gas phase, followed by ionization. In offline methods, this can be achieved by dissolving the collected particles and then evaporating or nebulizing the resulting solution. In online measurements, however, the transfer and ionization steps are more challenging, and several approaches have been developed in recent years to enable the online mass spectrometric analysis of organic aerosol particles (Vogel et al., 2013; Lopez-Hilfiker et al., 2014; Eichler et al., 2015).

Many instruments rely on thermal evaporation to transfer molecules from the particle phase to the gas phase. One approach uses modified atmospheric pressure chemical ionization (APCI) inlets, where particles are evaporated in a heated ceramic tube and then ionized by a corona discharge. However, because evaporator temperatures can exceed 200 °C, fragile organic compounds are prone to thermal decomposition (Vogel et al., 2013; Zuth et al., 2018). The Chemical Analysis of Aerosols Online (CHARON) inlet mitigates this issue by first removing gas-phase species with an activated-carbon denuder, followed by focusing particles using critical orifices and aerodynamic lenses into a thermal desorption unit that operates at reduced pressure. This reduces the temperature required for evaporation (Eichler et al., 2015). However, downstream ionization in a proton-transfer-reaction mass spectrometer

(PTR-MS) induces fragmentation, which introduces uncertainty in reported molecular abundances (Peng et al., 2023).

The Filter Inlet for Gases and Aerosols (FIGAERO), which is coupled to a high-resolution time-of-flight chemical ionization mass spectrometer (HR-ToF-CIMS), minimizes fragmentation during ionization via soft chemical ionization (Lopez-Hilfiker et al., 2014). This semi-online technique involves collecting particles on a filter for several minutes before desorbing them with a heated nitrogen stream. Controlled temperature ramps provide volatility-resolved information for different aerosol components (Thornton et al., 2020; Bannan et al., 2019). However, significant thermal decomposition can still occur during desorption, with some analytes being almost completely converted to decomposition products (Stark et al., 2017; Yang et al., 2021).

An alternative approach avoids thermal evaporation entirely. In extractive electrospray ionization (EESI), charged droplets from an electrospray extract particle-phase molecules upon collision. As the solvent evaporates, charge is transferred to the analyte molecules, which remain as gas-phase ions (Lopez-Hilfiker et al., 2019). However, this method has its own challenges, including greater sensitivity to gas-phase species than particle-phase species, ion suppression and significant background signals caused by low selectivity (Lopez-Hilfiker et al., 2019; Lee et al., 2022; Wüthrich et al., 2023).

This study presents a new aerosol inlet based on thermal evaporation for detecting compounds in nanometer-sized organic aerosol particles. The particles are evaporated at high temperatures (up to 400 °C) and a high flow rate (2 L/min) with a very short residence time (~0.3 s) to minimize thermal decomposition. When coupled with a nitrate chemical ionization Orbitrap mass spectrometer, the inlet allows for the real-time detection of highly oxidized organic molecules and the direct assignment of elemental formulas, which is made possible by the high resolving power of the Q Exactive Orbitrap ( $R = 140\,000$  at  $m/z\,200$ ) (Riva et al., 2019a). By varying the vaporizer temperature, we can obtain thermograms that reveal the volatility of the particle-phase compounds. By coupling the inlet to a scanning mobility particle sizer (SMPS), additional particle-phase information can be obtained. Here, we evaluate the inlet's performance with a series of test aerosols.

## 2.2 Materials and Methods

### 2.2.1 Setup

The aerosol inlet was designed to thermally evaporate aerosol particles with minimal decomposition and to ionize the resulting gas phase molecules using a CI-Orbitrap inlet (Riva et al., 2019a). In this way, the system enables not only the detection of gas phase molecules but also high-resolution online measurements of the particle phase using CIMS techniques. The inlet comprises two components: a particle evaporator that transfers aerosol particle constituents to the gas phase, and a gas cooling unit that dilutes and cools the hot gas stream before entering the CI inlet, thereby reducing turbulence in the CI-Orbitrap and improving adduct formation with the reagent gas.

#### 2.2.1.1 Particle Evaporator

The particle evaporator consists of a modified commercially available nozzle heater cartridge (HS Heizelemente). It consists of a 20 cm stainless steel tube with 8 mm inner diameter that is tightly wound on the outside with a resistive heating element. A NiCr Ni thermocouple (type K) is mounted on the surface to monitor the evaporator temperature. The tube is thermally insulated with mineral wool. The heater is controlled by a W 35/M temperature controller with a PID loop, allowing set points from 50 to 400 °C. The internal gas volume of the evaporator is 10 mL. The aerosol flow through the evaporator is set to 2 L min<sup>-1</sup>, yielding a residence time of about 0.3 s for the aerosol particles. At this short residence time, particles are unlikely to collide with the evaporator walls by diffusion or gravitational settling. Heat transfer to the particles is therefore expected to be dominated by the rapidly diffusing carrier gas and by infrared radiation emitted by the evaporator.

#### 2.2.1.2 Cooling Unit

This in-house fabricated component is installed between the particle evaporator and the CI-Orbitrap. The hot metal transfer line that carries the analyte gas is radially sheathed and cooled by 8 L min<sup>-1</sup> of purified air supplied by the cooling unit. Subsequently, the warmed air is routed coaxially around the analyte stream, thereby bringing the total gas flow to the 10 L min<sup>-1</sup> required by the CI-Orbitrap. The CI-Orbitrap inlet, with an inner diameter of 1.9 cm, connects directly to the cooling unit outlet, facilitating transfer into the ion source with minimal additional wall losses.

### 2.2.1.3 Instruments

Test aerosols used to characterize the aerosol inlet were generated with a Model 3076 Constant Output Atomizer (TSI Incorporated, Shoreview, MN). A syringe pump delivered various aqueous solutions to the atomizer, where they were nebulized with  $2 \text{ L min}^{-1}$  of clean, dry air. The resulting aerosol was dried with a silica gel denuder and size-selected with an Electrostatic Classifier Model 3082, which was equipped with an Advanced Aerosol Neutralizer Model 3088 and a Nano DMA (all from TSI Incorporated, Shoreview, MN). The DMA sheath flow was  $6 \text{ L min}^{-1}$ . The particle number concentration was monitored using a water-based condensation particle counter (CPC) model 3789 (TSI Incorporated, Shoreview, MN), operated in the 2 nm mode.

The particle size distribution and remaining particle concentration after passing through the aerosol inlet were determined using an SMPS comprising a butanol-based CPC (Model 5416) and an upstream L-DMA (Model 55U) (both Grimm Aerosol Technik, Ainring, Germany).

Gas-phase analytes transferred via the aerosol inlet were characterized using a CI-Orbitrap. This instrument consists of an atmospheric-pressure Eisele CI inlet adapted for high-resolution Orbitrap mass spectrometers (Riva et al., 2019a), coupled to a Q Exactive Orbitrap (Thermo Fisher Scientific) in this study.  $\text{HNO}_3$  was used as the reagent gas. Concentrated nitric acid (70 %, analytical grade, Fisher Scientific) was purged with a constant airflow of  $5 \text{ mL min}^{-1}$ ; the resulting  $\text{HNO}_3$  vapor was mixed with the sheath gas and ionized with a soft X-ray photoionizer (Model L9491, Hamamatsu). The sheath flow was  $30 \text{ L min}^{-1}$ , yielding a total flow of  $40 \text{ L min}^{-1}$ . The Orbitrap operating parameters are listed in Table 2.1. Data analysis was performed using Orbitool, a program developed for analyzing online Orbitrap data (Cai et al., 2021).

Table 2.1: Instrument parameters of the Q Exactive Orbitrap used for the nitrate-CIMS measurements.

Instrument parameters	
Mass resolution	140000
Microscans	10
AGC target	1e6
Maximum inject time	1000 ms
Capillary temperature	90 °C
S-Lens RF level	60

## 2.2.2 Experiments

### 2.2.2.1 Particle Transmission and Evaporation Efficiency

To determine the evaporator's particle transmission efficiency as a function of temperature and particle size, aerosol particles were generated from a 200 mg L<sup>-1</sup> aqueous sodium chloride solution (99.99%, Fisher Scientific). Particles with mobility diameters of 30, 50, 80, and 110 nm were size selected and then investigated at evaporator set points ranging from 20 to 350 °C. Particle number concentrations were measured upstream ( $N_{up}$ ) and downstream ( $N_{down}$ ) of the evaporation unit, and the transmission efficiency was calculated as the ratio of downstream to upstream number concentration (see Equation 2.1).

$$\text{transmission efficiency} = \frac{N_{down}}{N_{up}} \quad 2.1$$

To assess the evaporation efficiency, particles were generated from aqueous solutions of ammonium sulfate (200 mg L<sup>-1</sup>, >99.5%, Merck) and tricarballic acid (200 mg L<sup>-1</sup>, 98%, Alfa Aesar). The particle diameters of 30, 50, 80, and 110 nm were studied at evaporator set points ranging from 20 to 320 °C. The evaporated particle fraction was calculated based on the change in particle diameter measured upstream ( $d_{up}$ ) and downstream ( $d_{down}$ ) of the evaporator (see Equation 2.2).

$$\text{evaporated particle fraction} = 1 - \frac{d_{down}^3}{d_{up}^3} \quad 2.2$$

### 2.2.2.2 Concentration Dependence

To quantify the dependence of the CI-Orbitrap signal on the particle concentration of the evaporated aerosol, particles were generated from tricarballic acid solutions at concentrations of 0.4, 4, 40, and 400 mg L<sup>-1</sup>. Particle diameters of 30, 50, 80, and 110 nm were examined at an evaporator set point of 260 °C.

After drying and size selection, the particle number concentration was adjusted using a parallel branch comprising a valve and a HEPA filter. Particle number concentrations measured by the CPC were converted to mass concentrations by assuming spherical particles with density 1.2 g cm<sup>-3</sup> (Zuth et al., 2018). The conversion followed

$$\text{particle mass concentration} = N \cdot \frac{\pi}{6} \rho d_p^3 \quad 2.3$$

where  $N$  is the particle number concentration,  $\rho$  is the particle density, and  $d_p$  is the selected particle diameter.

Tricarballic acid was quantified using the CI-Orbitrap at  $m/z$  175.0243 and assigned to the elemental composition  $C_6H_7O_6^-$ . The absolute tricarballic-acid signal was corrected by the absolute reagent-gas signal ( $NO_3^-$ ) to compensate for intensity fluctuations (see Equation 2.4).

$$\text{relative analyte signal} = \frac{\text{absolute analyte signal}}{\text{reagent gas signal}} \quad 2.4$$

### 2.2.2.3 Thermal Decomposition in the Evaporator

To characterize the thermal decomposition of labile molecules in the evaporator, particles were generated from various aqueous solutions of 1,2,3,4-butanetetracarboxylic acid (40 mg L<sup>-1</sup>, 99%, Fluka), citric acid (180 mg L<sup>-1</sup>, 99%, Sigma-Aldrich), tartaric acid (180 mg L<sup>-1</sup>, 99%, Sigma-Aldrich), tricarballic acid (200 mg L<sup>-1</sup>, 98%, Alfa Aesar), and trimellitic acid (180 mg L<sup>-1</sup>, 98%, TCI). The dried particles were vaporized at 280 °C, and the potential thermal decomposition products were identified using the CI-Orbitrap.

### 2.2.2.4 Thermograms

To test the inlet's capability to record thermograms, which provide information on the volatility of the compounds contained in the aerosol particles, ozonolysis products of  $\alpha$ -pinene were generated. Three GC vials were filled with  $\alpha$ -pinene (>99%, Fluka), and a metal needle (0.8 mm i.d., 40 mm length) was inserted into each vial cap. The vials were placed in a temperature-controlled evaporator and the  $\alpha$ -pinene was evaporated at 40 °C.

The gas-phase  $\alpha$ -pinene was delivered at 0.5 L min<sup>-1</sup> to a 3.5 L flow tube where it was mixed with 2 L min<sup>-1</sup> of dry air and 0.1 L min<sup>-1</sup> of ozone. Ozone was produced with a modified generator (Dasibi 1008-RS). The resulting concentrations were 10 ppm of ozone and 8.6 ppm of alpha-pinene at 19% relative humidity. With a total flow of 2.6 L min<sup>-1</sup>, this yields a residence time of 1.35 min. The resulting aerosol was characterized by SMPS (sample flow: 0.6 L min<sup>-1</sup>) and evaporated in the aerosol inlet where it was then analyzed with the CI-Orbitrap (2 L min<sup>-1</sup>). The evaporator temperature was set to 350 °C, after which it was allowed to cool at a rate of 4±1 °C per minute.

## 2.3 Results and Discussion

### 2.3.1 Performance of the In-House Built Gas-Cooling Unit

Initially, the particle evaporator was connected directly to the CI-Orbitrap inlet. However, even at low evaporator temperatures (below 150 °C), we observed a significant decrease (over 70%) in both the reagent ion and analyte signals (Figure 2.2). One possible cause could be turbulence in the ionization region where the hot analyte gas meets the cold sheath air. Eisele-type inlets are known to be sensitive to non-laminar flow (Zhao et al., 2024). Another possibility is that the elevated temperature weakens the formation of adducts between the analytes and the nitrate reagent ions ( $\text{analyte}\cdot\text{NO}_3^-$ ) and within the reagent ions itself ( $\text{HNO}_3\cdot\text{NO}_3^-$  and  $(\text{HNO}_3)_2\cdot\text{NO}_3^-$ ). Similar behavior has been reported for bromide and iodide CIMS, albeit over smaller temperature ranges (20–40 °C) (Sanchez et al., 2016; Robinson et al., 2022). To address this issue, we installed a gas-cooling unit between the evaporator and the CI-Orbitrap (see Figure 2.1). Comparable units have been used in other particle evaporators to cool the analyte gas (Häkkinen et al., 2023; Zhao et al., 2024). The present unit cools the hot gas in two stages. First, 8 L min<sup>-1</sup> of clean air is flushed around the hot stainless steel transfer line carrying the analyte to cool it passively and bring the coolant temperature toward that of the analyte stream. The air is introduced radially through three ports to promote a laminar coolant flow. In the second stage, the coolant serves as a sheath flow guided radially around the hot analyte gas. This configuration reduces wall losses, cools the stream through mixing, and suppresses the re-nucleation of the cooled analyte through dilution. Since the coolant and analyte temperatures have largely equilibrated in the first stage, turbulence arising from large temperature contrasts at their interface should be reduced in the second stage.

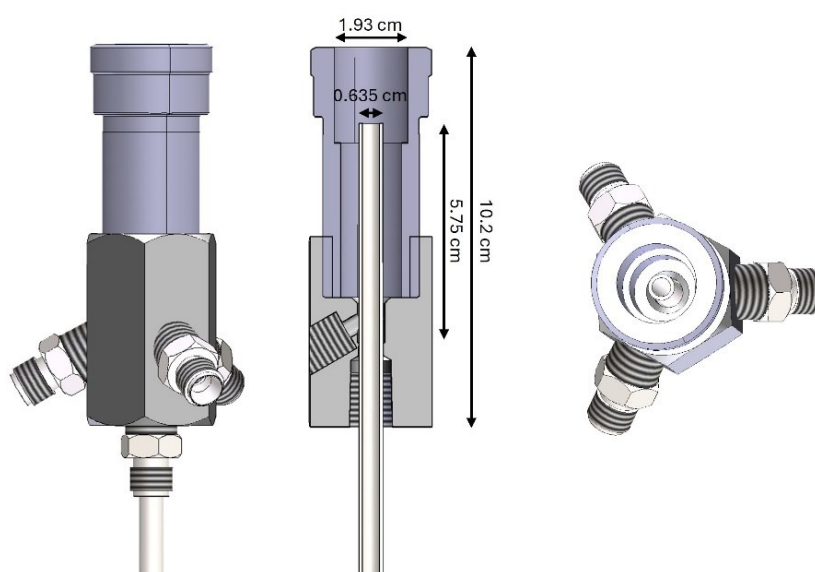


Figure 2.1: Technical drawing of the gas-cooling unit with key dimensions shown from multiple views: side elevation (left), longitudinal section (center), and front elevation (right).

Figure 2.2 shows the gas temperature measured downstream of both the particle evaporator and the gas cooling unit, plotted against the evaporator set point (heater temperature). Across the investigated range of 20 to 305 °C, the measured gas temperature is linearly proportional to the set point, reaching an average of  $80\pm 1\%$  of the set point (solid red). Over the same range, the cooling performance is also linear, with the unit removing  $90\pm 1\%$  of the temperature increase relative to ambient conditions (dashed red). Consequently, the reagent ion intensity remains above 60% of the value at room temperature, even at an evaporator set point of 320 °C, when using the cooling unit.

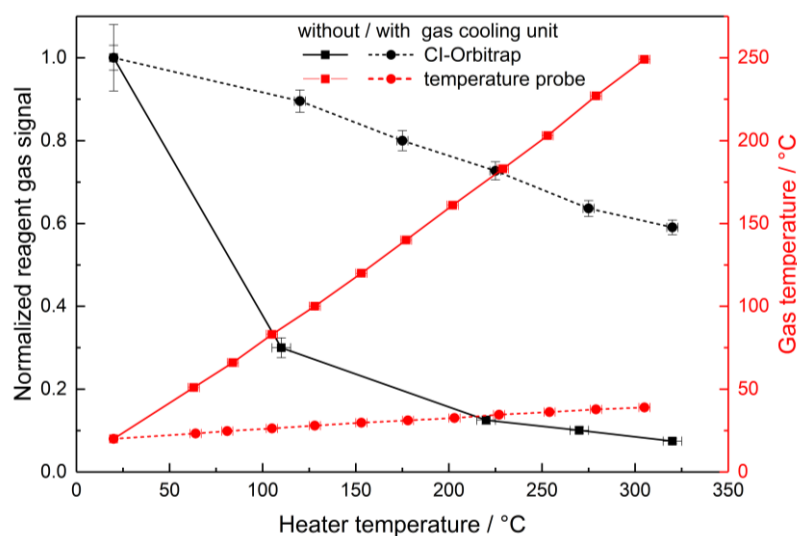


Figure 2.2 Normalized reagent-gas signal as a function of set evaporator temperature with (dashed black) and without (solid black) the gas-cooling unit installed. The resulting gas temperature measured downstream of the evaporator (solid red) and downstream of the gas-cooling unit (dashed red) is shown for comparison.

### 2.3.2 Particle Transmission

Gentle vaporization is required to transfer analyte molecules from the particulate to the gas phase without decomposition. Excessive energy transfer can rapidly induce fragmentation, especially in reactive and labile molecules. Therefore, it is critical that aerosol particles in the evaporator vaporize through heat transfer from the heated air within the evaporator and absorption of infrared radiation emitted by the hot heating element. Direct heat transfer at the heated steel tube is likely too intense and may catalyze additional decomposition reactions on the steel surface. This can lead to signal loss and the possible detection of degradation products.

Several processes can cause particle loss to the walls, including turbulent flow, diffusion, and sedimentation (Zhao et al., 2024). With Reynolds numbers of 350 (at 20 °C) and 100 (at 350 °C), the flow in the evaporator should be laminar, as flows in pipes or tubes become

turbulent at Reynolds numbers  $>2300$  (Schlichting, 2017). Therefore turbulence-driven losses in the evaporator should be minimal. Diffusive losses increase as particle size decreases and temperature increases. At  $350\text{ }^{\circ}\text{C}$ , a  $30\text{ nm}$  NaCl particle has a diffusion coefficient of  $1.42 \cdot 10^{-4}\text{ cm}^2\text{ s}^{-1}$  and a root mean square displacement of  $9.24 \cdot 10^{-3}\text{ cm}$  for a residence time of  $0.3\text{ s}$  in the evaporator (Hinds, 1999). Under idealized conditions, this would correspond to a 5% loss of particle mass. Sedimentation becomes more important for larger particles and at lower temperatures. For a  $110\text{ nm}$  NaCl particle at room temperature, this corresponds to a sedimentation distance of  $6.81 \cdot 10^{-5}\text{ cm}$  within the evaporator. According to these calculations, particle loss by sedimentation can be neglected for small particles, whereas diffusion cannot.

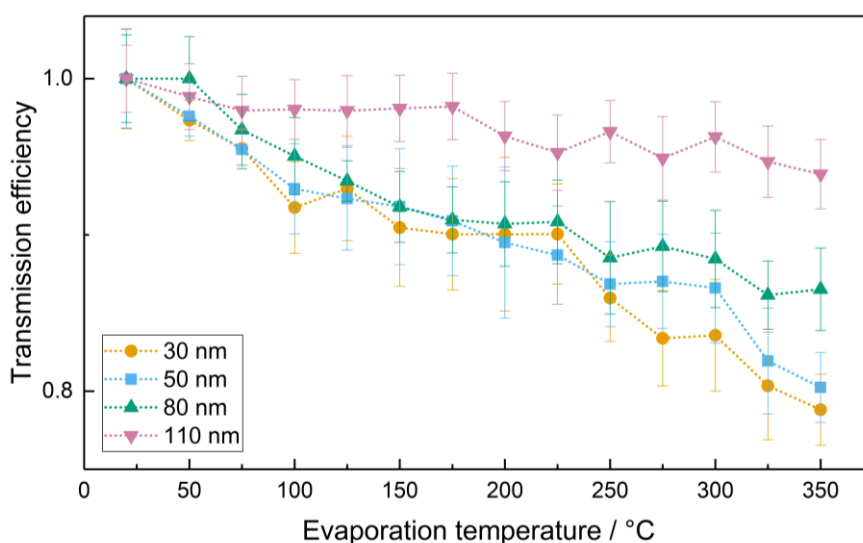


Figure 2.3: Transmission efficiency, defined as the ratio of NaCl particles passing through the vaporization unit measured via SMPS, as a function of the set heater temperature. Particle mobility diameters: 110 nm (pink), 80 nm (green), 50 nm (blue), and 30 nm (yellow).

With a boiling point above  $1450\text{ }^{\circ}\text{C}$ , sodium chloride is sufficiently nonvolatile that losses of pure sodium chloride particles in the evaporator should only occur through wall interactions. Test measurements of sodium chloride aerosol particles (Figure 2.3) yield results comparable to the theoretical estimates above. There is a clear temperature dependence, with particle losses increasing at higher temperatures. Smaller particles appear to be more strongly affected by temperature, with  $30\text{ nm}$  diameter particles losing  $\sim 20\%$  of particle concentration at  $350\text{ }^{\circ}\text{C}$ , while  $110\text{ nm}$  particle concentration only goes down by  $\sim 5\%$  compared to room temperature. These observations suggest that increased diffusivity at higher temperatures primarily drives particle losses. However, the measured losses are approximately three times greater than calculated. It cannot be ruled out that nonuniform heating of the carrier gas induces turbulence or recirculation within the evaporator, thereby contributing to additional particle losses.

### 2.3.3 Evaporation Efficiency

The concept of vaporizing aerosol particles is not new. Several thermodenuders have been introduced in recent years (Burtscher et al., 2001; Wehner et al., 2002; Huffman et al., 2008). These were often used to quantify the non-volatile fraction alongside SMPS instruments operated in series. These designs employed much longer tubes and lower gas flow rates since the priority was to ensure the complete evaporation of individual particle components. The aerosol inlet developed here enables the comprehensive analysis of particles in the nanometer range. Therefore, the evaporator is kept as short as possible to minimize diffusion losses of small particles. Consequently, the residence time in the evaporator is much shorter than in conventional systems, necessitating higher temperatures for vaporization. To obtain a complete picture of the aerosols investigated, it is essential that particles are fully transferred to the gas phase.

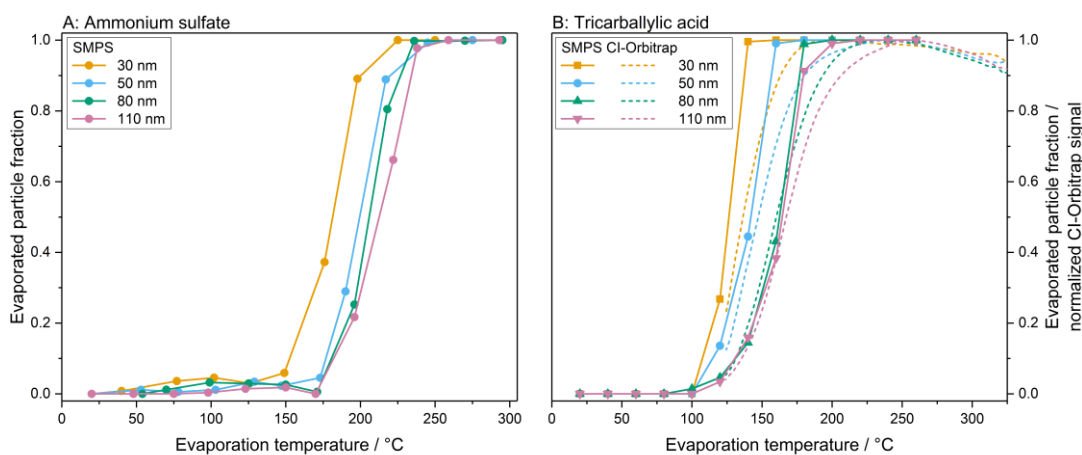


Figure 2.4: Evaporated fraction of ammonium sulfate particles (A) and tricarballic acid particles (B), calculated as the loss of aerosol volume concentration via SMPS, as function of the set heater temperature. In panel (B), the corresponding  $\text{NO}_3^-$ -CI-Orbitrap signals are shown as dashed lines. Particle mobility diameters: 110 nm (pink), 80 nm (green), 50 nm (blue), and 30 nm (yellow).

To verify that the evaporator can vaporize organic aerosols within this short residence time, test aerosols containing tricarballic acid and ammonium sulfate were generated. In terms of volatility, these two substances fall within the range of low-volatility organic compounds (LVOCs) and extremely low-volatility organic compounds (ELVOCs) (Bianchi et al., 2019). If the inlet can transfer these substances to the gas phase, then most of the species involved in the formation of atmospheric organic aerosols should also be suitable for analysis. The SMPS data indicates that smaller particles of both ammonium sulfate (Figure 2.4A) and tricarballic acid (Figure 2.4B) evaporate faster than larger ones. This behavior is also observed with other thermodenuders and is expected because it takes more time for heat to reach the core of larger particles. The 110 nm ammonium sulfate particles completely evaporate at 250 °C, which is consistent with the findings of Zhao et al. (2024).

Figure 2.4B also shows the CI-Orbitrap signal of tricarballylic acid as a function of temperature. The CI-Orbitrap and SMPS signals demonstrate consistent trends. However, the SMPS data suggest complete evaporation at lower temperatures, while the CIMS signal only reaches its maximum at higher temperatures. This discrepancy is likely due to particle losses in the SMPS with its lower flow rate ( $0.3 \text{ L min}^{-1}$  compared to  $10 \text{ L min}^{-1}$ ), particularly of small particles that have nearly fully evaporated. This leads to an underestimation at high evaporation fractions. In the MS data, the signal intensity decreases at higher temperatures, which is a known phenomenon. One possible cause is the loss of the gas-phase analyte to the evaporator walls coupled with subsequent thermal decomposition reactions (Zhao et al., 2024). This effect increases with higher temperatures because the particles transfer to the gas phase more quickly. Conversely, adduct formation with  $\text{HNO}_3$  may be disrupted by the higher energy supplied to the molecule (see Figure 2.2) (Sanchez et al., 2016; Robinson et al., 2022).

### 2.3.4 Particle-Size Dependent Sensitivity

Increases in particle mass concentration produced a proportional increase of the CI Orbitrap signal (see Figure 2.5). Rapid fluctuations in particle number concentration recorded by the CPC were mirrored by the CI Orbitrap in real time, which indicates that the detected ions originate from analyte transferred directly from the particle phase into the gas phase by the vaporizer. If the dominant contribution arose from desorption or re-evaporation on the vaporizer surface or the downstream metal tubing, a broader response and lower temporal fidelity would be expected.

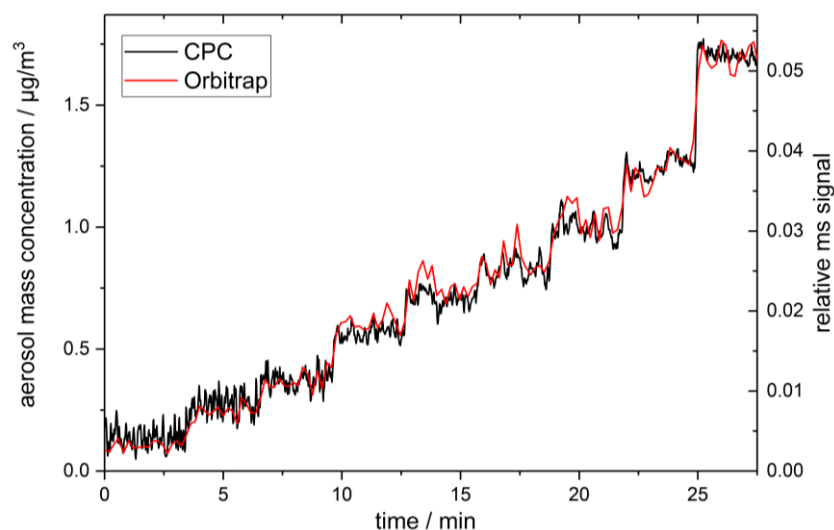


Figure 2.5: Time series of the derived aerosol mass concentration (from CPC measurements) for generated tricarballylic acid aerosol with a particle mobility diameter of 110 nm (black), and the corresponding CI-Orbitrap signal after particle vaporization, corrected by the reagent-gas signal (red).

Across all investigated particle diameters, the relationship between particle mass concentration and CI Orbitrap signal was linear from approximately  $10 \text{ ng m}^{-3}$  to  $1 \text{ } \mu\text{g m}^{-3}$  (Figure 2.6A). The fitted calibration lines yielded coefficients of determination  $R^2 > 0.99$  (Table 2.2). This dynamic range suggests that measurements of particle-phase organic molecules at atmospherically relevant levels in the low  $\text{ng m}^{-3}$  regime are feasible (Zhang et al., 2010; Gómez-González et al., 2012). Sensitivity increased with particle diameter. The calibration slope for 30 nm particles was 84 % of the slope for 110 nm particles. This difference is comparable to the independently measured differences in particle transmission through the vaporizer (see Figure 2.3). The observed size trend is consistent with higher diffusivities of smaller particles and the resulting enhanced wall losses in the vaporizer and transfer lines.

The absolute mass accuracy depends on the assumed particle density and on the validity of the spherical particle approximation. Within these constraints, the CI Orbitrap coupled to the aerosol particle vaporizer provides linear and time-resolved quantification of tricarballic acid over nearly two orders of magnitude in mass concentration, with sensitivity sufficient for ambient applications.

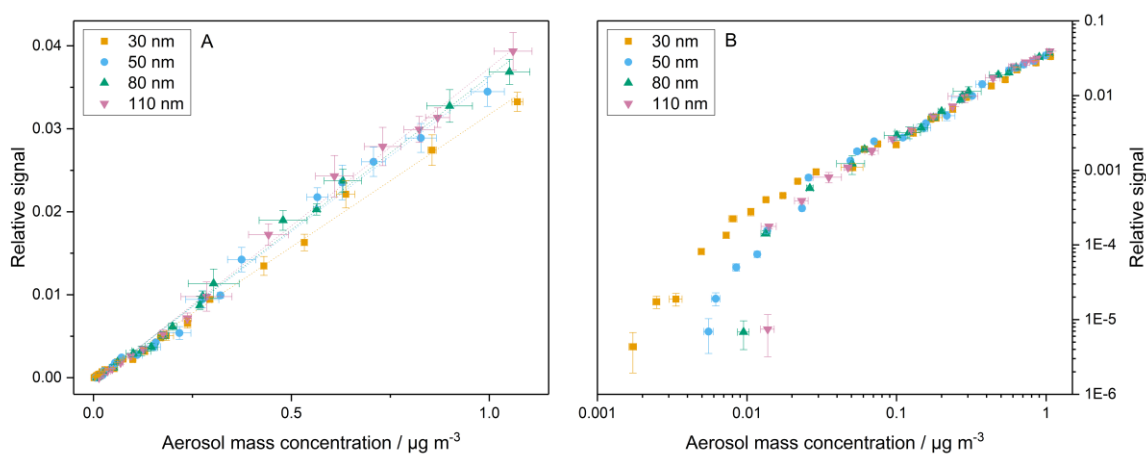


Figure 2.6: Linear correlation between aerosol mass concentration (derived from CPC measurements) for generated monodisperse tricarballic acid aerosol and the CI Orbitrap signal after particle vaporization, for particle mobility diameters of 110 nm (pink), 80 nm (green), 50 nm (blue), and 30 nm (orange). Data are shown with linearly scaled axes (A) and with both axes on logarithmic scales (B).

Table 2.2: Fitted parameters of the linear regressions between aerosol mass concentration and the resulting CI Orbitrap signal for the investigated particle diameters.

Particle diameter (nm)	Slope ( $\text{m}^3 \mu\text{g}^{-1}$ )	Intercept	R <sup>2</sup>
30	$0.03197 \pm 0.00041$	$-0.00023 \pm 0.00014$	0.996
50	$0.03636 \pm 0.00068$	$-0.00056 \pm 0.00026$	0.993
80	$0.03694 \pm 0.00064$	$-0.00062 \pm 0.00027$	0.995
110	$0.03805 \pm 0.00056$	$-0.00074 \pm 0.00027$	0.996

### 2.3.5 Decomposition

Thermal decomposition is a known challenge for many thermodesorber-type techniques (Stark et al., 2017; Zhao et al., 2020). Prolonged or intense heating promotes fragmentation of thermally labile compounds. The vaporizer developed here addresses this by limiting analyte residence time at elevated temperature and by removing excess heat with a cooling sheath gas downstream of the heated zone.

To evaluate thermal artifacts, we nebulized a set of multifunctional carboxylic acids and used the CI Orbitrap after vaporization to monitor for characteristic decomposition products. We used nitrate as the reagent ion, which provides high sensitivity toward organic acids. Carboxylic acids are a stringent test because they readily fragment upon heating. The most common pathway is dehydration; additional channels include decarboxylation and combined losses of multiple water and carbon dioxide molecules (Yang et al., 2021). At a set temperature of 280 °C, the parent ion accounted for more than 93% of the measured signal for all tested acids (Table 2.3). Thus, while thermal decomposition is detectable, it contributes only a minor fraction of the total signal under our standard conditions. For context, Yang et al. (2021) reported substantially larger decomposition in a FIGAERO system, with parent-ion fractions of about 2% for 1,2,3,4-butanetetracarboxylic acid, 45% for citric acid, and 40% for tricarballic acid, the balance arising from dehydration and decarboxylation products. An inlet design by Gao et al. (2025) achieved even lower decomposition for citric acid (< 0.2%) by employing a second preheated sheath gas that envelopes the analyte before it encounters the hot surface, thereby reducing surface-mediated reactions. These comparisons indicate that the present vaporizer substantially suppresses thermal artifacts, though shielding the analyte from hot surfaces can reduce them further.

Table 2.3: Organic acids tested for thermal decomposition as aerosol particles vaporized in the evaporator at 280 °C. The table lists the percentage contributions of the parent compounds and the detected decomposition products.

Substance	Molecular formula	Parental compound	Dehydration product	Other thermal fragmentation products
1,2,3,4-Butanetetracarboxylic acid	$C_8H_{10}O_8$	$95.03 \pm 0.43\%$	$3.93 \pm 0.50\%$	$1.04 \pm 0.15\%$ (- 2 H <sub>2</sub> O)
Citric acid	$C_6H_8O_7$	$99.37 \pm 0.22\%$	$0.54 \pm 0.20\%$	$0.09 \pm 0.03\%$ (- H <sub>2</sub> O, -CO <sub>2</sub> )
Tartaric acid	$C_4H_6O_6$	$98.39 \pm 1.05\%$	$1.44 \pm 0.92\%$	$0.17 \pm 0.13\%$ (- 2 H <sub>2</sub> O)
Tricarballic acid	$C_6H_8O_6$	$97.64 \pm 0.45\%$	$2.36 \pm 0.45\%$	-
Trimellitic acid	$C_9H_6O_6$	$93.29 \pm 1.24\%$	$3.13 \pm 0.67\%$	$3.57 \pm 0.66\%$ (- CO <sub>2</sub> )

For tricarballic acid, the temperature stability over a temperature range, from 120 °C to 350 °C, was also analyzed. Across the investigated temperature range there was no systematic increase in the decomposition fraction (Figure 2.7). The dehydration product ( $C_6H_6O_5$ ) tracked the parent signal ( $C_6H_8O_6$ ) proportionally over temperature, consistent with a nearly constant branching ratio in our configuration. The relative abundance of decomposition products did also not depend on particle size. The dehydration product appeared at lower set temperatures for 30 nm particles (Figure 2.7A) than for 110 nm particles (Figure 2.7B), which we attribute to faster evaporation and shorter thermal equilibration times of smaller particles rather than to enhanced fragmentation at a given temperature.

Sensitivity of the CI Orbitrap generally increases with the number of functional groups. Because thermal fragmentation removes small neutral molecules such as water and carbon dioxide, it reduces the number of functional groups in the remaining ionizable product spectrum. The instrument could therefore be less sensitive to many decomposition products than to the intact parent acids. A residual underestimation of the true extent of decomposition is expected. The parent-dominant signals and the size- and temperature-independent decomposition fractions nevertheless indicate that the current design maintains chemical stability to a degree suitable for quantitative work on particle-phase organics.

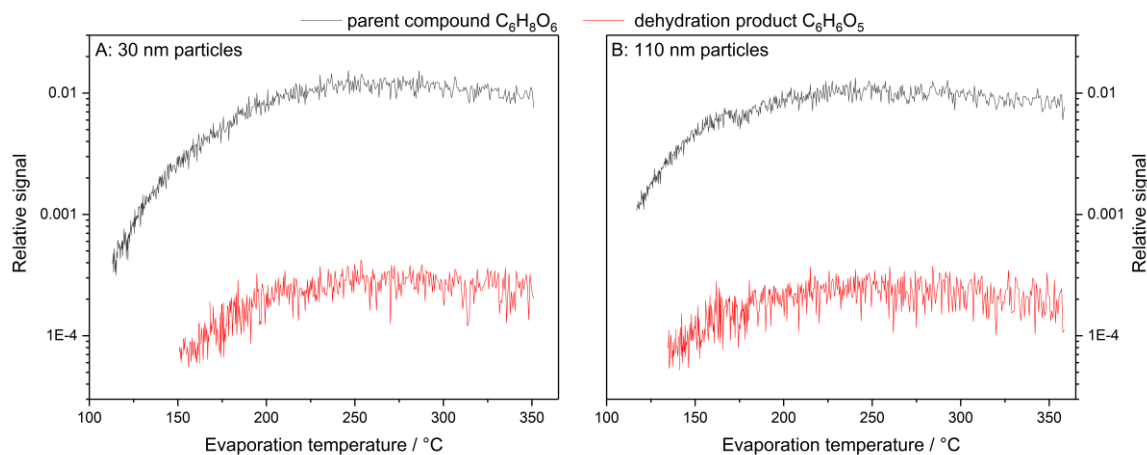


Figure 2.7: CI-Orbitrap signals of vaporized tricarballic acid particles as a function of the set evaporator temperature. The parent compound ( $C_6H_8O_6$ ) is shown in black; the dehydration product ( $C_6H_6O_5$ ) is shown in red. Panel (A) shows the data for 30 nm particles; panel (B) shows the data for 110 nm particles.

### 2.3.6 Thermograms from $\alpha$ -pinene Ozonolysis

We evaluated the information content of thermograms using  $\alpha$ -pinene ozonolysis, a major global source of monoterpene SOA that produces a chemically diverse product spectrum (Messina et al., 2016). In the flow-tube experiment the highly oxidized products nucleated. The median particle diameter was  $55 \pm 5$  nm and the particle mass concentration was approximately  $73 \mu\text{g m}^{-3}$ . The CI-Orbitrap detected 216 distinct compositions. High mass resolution enabled direct assignment of elemental formulas to the observed  $m/z$  signals. Products were detected either as deprotonated ions or as  $\text{HNO}_3$ -adducts; all species were analyzed as neutral, non-adduct formulas for classification and counting.

Because products span a wide oxidation range, both vaporization and ionization depend strongly on temperature. Figure 2.8A and Figure 2.8B show the fractional signal by temperature after grouping species by carbon number and by oxygen number, respectively. For both categorizations a decrease in volatility with increasing carbon or oxygen count is expected, with the oxygen effect typically stronger because those add functional groups which increase polarity and reduce vapor pressure via dipolar interactions (Donahue et al., 2011). Between 75 °C and  $\sim 225$  °C the data follow this expectation. In Figure 2.8A, monomers ( $\leq C_{10}$ ) dominate up to  $\sim 125$  °C. At higher temperatures dimers ( $> C_{10}$ ) also evaporate in the gas phase and their fraction increases steadily. Above  $\sim 225$  °C the  $C_{20}$  dimer fraction declines while  $C_{17}$  dimers increase. This is counterintuitive and could be an indication of thermal decomposition of the  $C_{20}$  dimers. Because oxygen content strongly governs volatility, one might suspect that the  $C_{17}$  dimers contain either more oxygen atoms or oxygen in more polar

functional groups than the  $C_{20}$  dimers. The first explanation is inconsistent with the assigned elemental formulas: both classes exhibit similar oxygen numbers. The observed difference therefore likely arises from functional group composition rather than total oxygen content. Consistent patterns have been reported for  $\alpha$ -pinene ozonolysis:  $C_{20}$  dimers dominated the gas phase, whereas  $C_{17}$  dimers dominated the particle phase (Zhao et al., 2023).

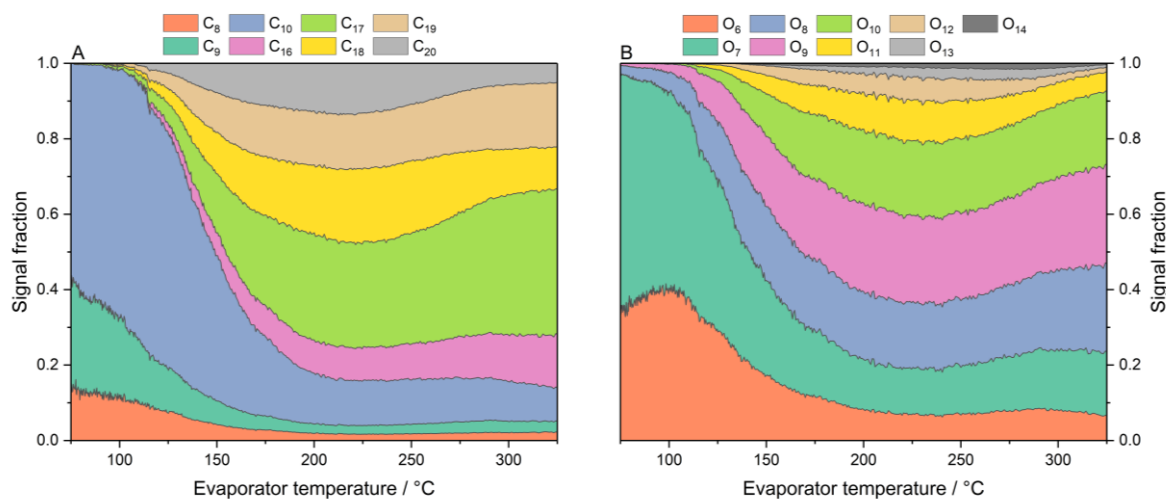


Figure 2.8: Relative contributions of signals from vaporized particles generated from  $\alpha$ -pinene ozonolysis, grouped by the number of carbon atoms per molecule (A) and by the number of oxygen atoms per molecule (B), as a function of the set evaporator temperature.

In Figure 2.8B, the fraction of more highly oxygenated products increases with temperature, as expected, until  $\sim 275$  °C. This follows the expected trend, as more oxygen atoms decrease the volatility as explained above. At even higher temperatures the most oxygen-rich classes ( $\geq O_{11}$ ) decline, likely due to thermal loss of labile functionalities, plausibly peroxy-containing motifs (Claflin and Ziemann, 2019).

Figure 2.9 summarizes thermograms for two series, the monomers  $C_{10}H_{14}O_x$  and the dimers  $C_{20}H_{32}O_x$ . In both series, higher-oxygen members desorb at higher temperatures, consistent with lower volatility. For dimers (Figure 2.9B), however, signals of the most oxidized members decrease more strongly at elevated temperature than those of less oxidized members, consistent with thermal fragmentation that removes oxygen (e.g.,  $H_2O$ ,  $CO_2$ ), yielding lower oxygen products.

Monomers (Figure 2.9A) show a different feature: species with low oxygen content ( $C_{10}H_{14}O_{8-10}$ ) exhibit multiple maxima or inflection points in their thermograms. This behavior suggests contributions from distinct constitutional isomers with different volatilities, which is plausible given the many  $\alpha$ -pinene ozonolysis pathways. In this sense, the thermogram provides an additional dimension for distinguishing product isomers beyond elemental formula.

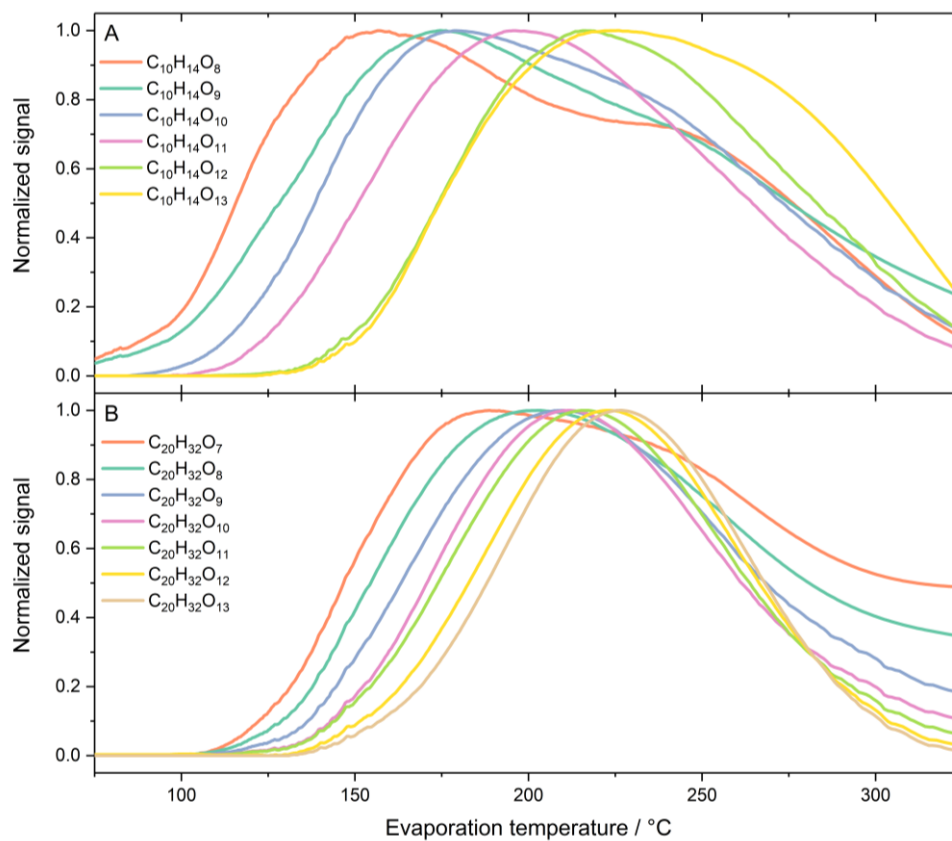


Figure 2.9: Normalized CI-Orbitrap signal profiles from vaporized aerosol generated by  $\alpha$ -pinene ozonolysis for C<sub>10</sub>H<sub>14</sub>O<sub>x</sub> monomers (A) and C<sub>20</sub>H<sub>32</sub>O<sub>x</sub> dimers (B) as a function of the set evaporator temperature.

## 2.4 Conclusion

We present and characterize a fast thermal evaporation aerosol inlet that transfers nanometer-scale organic particles to the gas phase for real-time molecular analysis with a nitrate chemical ionization Orbitrap. The design combines a short stainless-steel evaporator operated up to 400 °C at 2 L min<sup>-1</sup> with a residence time of ~0.3 s and a two-stage gas cooling unit that dilutes and cools the analyte stream before ionization. The cooling unit maintains reagent-ion stability and minimizes turbulence.

Transmission tests with sodium chloride indicate wall losses that increase with temperature and are stronger for smaller particles, consistent with diffusion-driven losses under laminar flow. Evaporation tests with ammonium sulfate and tricarballic acid show complete transfer of low- and extremely low-volatility molecules to the gas phase within the short residence time. Coupling to a CI-Orbitrap enables linear quantification of tricarballic acid over ~10 ng m<sup>-3</sup> to 1 µg m<sup>-3</sup> with R<sup>2</sup> > 0.99 for all studied diameters. Sensitivity increases with particle size; the calibration slope for 30 nm particles is 84 % of that for 110 nm, consistent with size-dependent diffusion losses. Real-time CPC-MS agreement and high temporal fidelity indicate that the measured ions originate from direct particle-to-gas transfer rather than delayed desorption from hot surfaces.

Thermal decomposition was assessed with multifunctional carboxylic acids. At 280 °C the parent ion contributes >93 % of signal for all compounds, indicating minor fragmentation under standard conditions. Compared with FIGAERO literature, decomposition is strongly reduced, though designs that fully shield analyte from hot surfaces can suppress it further.

Finally, α-pinene ozonolysis products illustrate the value of thermograms. A median particle diameter of 55±5 nm and a mass concentration of ~73 µg m<sup>-3</sup> yielded 216 assigned formulas. Composition-resolved thermograms display expected volatility trends with carbon and oxygen number. Highly oxygenated dimers decline above ~225–275 °C, consistent with thermal loss of labile functionalities, while monomer series show multiple maxima suggestive of isomeric contributions. Overall, the inlet provides rapid, composition-resolved access to particle-phase organics with low thermal artefacts and a dynamic range and sensitivity suitable for ambient applications.



### 3 Size-Dependent Ozonolysis of Norbornene-Dicarboxylic-Acid-Aerosol Particles

**This chapter contains a paper that has been published as:**

Douverne, M. and Hoffmann, T.: When Size Matters: Size-Selective Chemistry in the Heterogeneous Processing of Organic Aerosols, *ACS ES&T Air*, 2, 2491–2503, <https://doi.org/10.1021/acsestair.5c00189>, 2025. This publication is licensed under CC-BY 4.0.

**Contribution to this manuscript by Marcel Douverne**

As the first author of this work, I designed and performed all experiments. I analyzed and interpreted the data, prepared the figures, and wrote the majority of the manuscript. The Introduction was written in collaboration with Thorsten Hoffmann. The manuscript was reviewed and edited by Thorsten Hoffmann.

### 3.1 Abstract

New particle formation and growth in the atmosphere critically influence cloud properties and climate, as well as human health through the presence of ultrafine particles. While the early stages of particle nucleation are increasingly understood, the mechanisms driving the subsequent growth of nanoparticles, particularly the role of organic compounds, remain unclear. This study investigates the heterogeneous ozonolysis of 5-norbornene-2-endo,3-exo-dicarboxylic acid (NDA) in size-selected aerosol particles (30–110 nm) under varying relative humidity and ozone conditions. NDA serves as a model compound representative of unsaturated monoterpene derivatives with low volatility and high particle-phase partitioning. Using real-time mass spectrometry, we explore how particle size influences both reactivity and product distribution. Our results reveal pronounced particle-size and humidity dependencies: smaller particles favor dimerization and oligomer formation, likely due to increased Laplace pressure, whereas larger particles promote hydrolysis and decomposition reactions. The findings suggest that nanometer-sized particles provide a distinct chemical microenvironment that alters the course of multiphase reactions, thereby affecting particle aging, volatility, and growth potential. These results underscore the importance of considering particle-size-dependent chemistry in models of atmospheric aerosol formation and evolution.

### 3.2 Introduction

The formation of new particles in the atmosphere is the source of about half of cloud condensation nuclei (CCN) and thus influences the properties of clouds and the Earth's energy balance (Andreae, 2013; Bianchi et al., 2016; Williamson et al., 2019; Curtius et al., 2024). Ultra-fine particles in the atmosphere (<100 nm) also pose a health risk because they can penetrate deep into the respiratory tract (Chen et al., 2025). Although new insights into the chemical compounds involved in the initial stages of particle formation have been obtained in recent years (Ehn et al., 2014; Kirkby et al., 2016), there are still considerable gaps in our knowledge regarding the growth processes of nanoparticles (Hong et al., 2024; Stolzenburg et al., 2025; Li et al., 2022). An open question is which substances drive the further growth of particles in the nanometer range after the formation of the first molecular clusters. Although it is generally accepted that organics make the greatest contribution during this growth phase, it is not known which compounds and through which mechanism the organic substances actually contribute. Since sufficiently low volatility is a necessary prerequisite, potential candidate molecules must either be highly oxidized multifunctional products (so-called HOMs) or have higher molecular weights formed by accretion reactions of ubiquitous smaller molecular units (oligomerization) (Dam et al., 2023; Berndt et al., 2025; Zhao et al., 2023; Shen

et al., 2022; Bianchi et al., 2019). Today, the nucleation process is mainly discussed on the basis of the first pathway, the formation of low-volatile substances from oxidation reactions in the gas phase with additional functional groups and their phase transition through condensation (Stolzenburg et al., 2018). However, evidence also suggests that accretion reactions, in which SOA components combine to form higher-molecular-weight products, occur in the particle phase. This provides a pathway for the formation of extremely low-volatility compounds (Kenseth et al., 2023; Kenseth et al., 2020; Kenseth et al., 2018). If particle-phase chemistry is size-dependent (i.e. more favourable in smaller particles), this process could be particularly important, as it may critically affect the balance between survival and loss of freshly formed particles. Such reactions could enhance particle growth and help counteract the tendency of small particles to be lost through Brownian coagulation. Size-dependent particle-phase chemistry may even proceed more rapidly than gas-phase pathways that generate low-volatility compounds (Pierce et al., 2011).

An obvious difference in the properties of aerosol particles that is strongly dependent on particle size is the surface-to-volume ratio. In particular for heterogeneous reactions, when one of the reaction partners from the gas phase comes into contact with reaction partners in the particle phase, as is the case in the heterogeneous ozonolysis of particle-bound olefins carried out here, smaller particles with a correspondingly larger surface area result in an increased conversion at the same mass concentration. However, it is more interesting to ask whether there are other size-dependent differences besides the purely geometric ratio of surface area to volume, especially those that can influence product formation itself (i.e., resulting in different products in particles of different sizes). In connection with aqueous aerosols, special properties of the air-water interface have been discussed recently. For example, molecular dynamics simulations suggest that although the pH value in aqueous aerosol particles is uniform on average (i.e., not size-dependent), the hydronium and hydroxide ions within a particle exhibit significant concentration gradients which extend from the outer molecular layers to the interior of the particles, with the interface being enriched with hydronium cations and depleted with hydroxide anions (La Puente and Laage, 2023). In small aqueous aerosol particles in particular, this leads to different conditions prevailing inside the particles than in the surface layers. In fact, there have been a number of recent studies in this field of research dealing with nano- and microdroplets, which focus on the question of whether chemical reactions proceed differently here than in a homogeneous phase (Martins-Costa and Ruiz-Lopez, 2023; Lacour et al., 2025). In particular, the massive influence on a number of redox reactions has attracted considerable attention and is currently being discussed from various perspectives (Mehrgardi et al., 2022; Eatoo and Mishra, 2024; Angelaki et al., 2024).

In addition to the current discussions on size- or curvature-dependent reactivity of aqueous aerosols, there are undoubtedly other particle size-dependent phenomena that may be directly related to chemical reactions in the particle phase, such as the viscosity of aerosol particles, which can have a direct influence on the course of reactions, particularly in heterogeneous chemical processes (Cheng et al., 2015). Another strongly size-dependent phenomenon is the rise in internal pressure, known as Laplace pressure, as particle diameter decreases (van Eldik, 2008). This pressure difference between the particle interior and exterior arises from the interplay of surface tension and curvature, increasing significantly with smaller radii (Riva et al., 2021; Petters, 2022; Dubois et al., 2024). Since bond-forming chemical reactions (e.g. oligomerization) are favored at higher pressures, such reactions gain importance in the smallest particles.

Real-time studies of the chemical composition of nanometer particles are challenging (Li et al., 2023; Thomas et al., 2025). For this work, we use a self-built particle evaporator coupled to a CI-Orbitrap mass spectrometer with upstream particle size selection. As a chemical system, we investigate the heterogeneous ozonolysis of 5-norbornene-2-endo,3-exo-dicarboxylic acid (NDA) in aerosol particles of different sizes. NDA combines the high ring strain of a bicyclic monoterpene system, similar to  $\alpha$ -pinene (Kugel and Ault, 2015), with two additional polar carboxylic acid groups, resulting in a lower vapor pressure and enhanced particle-phase partitioning. Due to its structural characteristics, NDA serves as a proxy for unsaturated monoterpene derivatives, which are known to contribute to secondary organic aerosol (SOA) formation. Although previous studies have shown that oxidized unsaturated monoterpene derivatives (e.g., limononic acid) in the condensed phase undergo further oxidation and thereby influence aerosol formation during atmospheric aging (Witkowski et al., 2018; Witkowski et al., 2019), indicating that the reactions investigated here are also relevant to atmospheric aerosol formation, NDA was primarily chosen for this study because it serves as a suitable model compound. Specifically, NDA enables the generation of a stable aerosol population within the targeted size range (30–110 nm) and facilitates real-time investigation of the particle phase using mass spectrometry. Special emphasis is placed on how particle size influences not only the overall reactivity but also the chemical composition and evolution of the reaction products. By systematically varying particle sizes and environmental conditions (relative humidity and O<sub>3</sub> concentrations), we provide mechanistic insights into particle-size-dependent chemistry, contributing to a better understanding of the molecular-level processes that govern the aging of organic aerosols in the atmosphere. The purpose of this publication is to present experimental results that seek to answer the question of whether very small organic aerosol particles provide a unique chemical environment in the nanometer range that can influence the course of chemical reactions.

## 3.3 Materials and Methods

### 3.3.1 Flow Tube Experiments

For particle generation, a solution was prepared using a 9:1 (v/v) mixture of deionized water (18.2 M $\Omega$  cm) and isopropanol (>98%, Fisher Chemical) containing 540 mg L<sup>-1</sup> 5-norbornene-2-endo,3-exo-dicarboxylic acid (NDA) (97%, Sigma-Aldrich) and 60 mg L<sup>-1</sup> tricarballylic acid (TA) (98%, Alfa Aesar) as internal standard. This solution was then nebulized using a Model 3076 Constant Output Atomizer (TSI Incorporated, Shoreview, MN) with purified air (2 L min<sup>-1</sup>) at a flow rate of 350  $\mu$ L min<sup>-1</sup> supplied by a syringe pump. The experimental setup is illustrated in Figure 3.1. The experiments were conducted at three different relative humidity (RH) conditions. These were adjusted by passing the aerosol either through no silica denuder (85 $\pm$ 3%), one silica denuder (50 $\pm$ 3%), or two silica denuders (35 $\pm$ 4%) after nebulization. Under these conditions, the resulting particle-size distributions peak at around 40 and 50 nm, with most particles falling within the 20–120 nm range (Appendix Figure 8.1). The polydisperse aerosol was subsequently size-selected using an Electrostatic Classifier Model 3082 with an Advanced Aerosol Neutralizer Model 3088 and a Nano-DMA (TSI Incorporated). Particles with diameters of 30, 50, 80, and 110 nm were investigated. The particle concentration was controlled via a valve and an inline HEPA filter. Based on the TA signal from the mass spectrometer, the volume concentration in the flow tubes was maintained nearly constant across particle sizes. The resulting particle concentration was measured using a water-based Condensation Particle Counter (CPC) Model 3789 (TSI Incorporated) operating in 2 nm mode, with an aerosol sample flow of 0.1 L min<sup>-1</sup>. The remaining monodisperse aerosol flow (1.9 L min<sup>-1</sup>) was mixed with 0.1 L min<sup>-1</sup> ozone-containing air. Ozone was generated using a modified ozone generator (Dasibi 1008-RS) and subsequently diluted to the desired concentrations. To investigate the reaction system at different reaction times, the reaction mixture was analyzed either immediately after mixing or after passing through four different flow tubes of varying volumes under dark conditions. The dimensions of the flow tubes and the corresponding reaction times are provided in Table 3.1. Table 3.2 summarizes the experimental conditions for each experiment.

Because at a given classifier voltage not only singly charged particles but also larger, multiply charged particles can pass the DMA, there is a risk that the measured signal is dominated by the latter due to their greater volume. To assess this effect, we performed tandem-DMA measurements using a butanol-based condensation particle counter (CPC, Model 5416) downstream of a long DMA (L-DMA, Model 55-U; both Grimm Aerosol Technik). (Mamakos, 2016) These measurements indicate that doubly and triply charged particles contribute only marginally (Appendix Figure 8.2). The cumulative particle-volume distributions show that, for all investigated setpoint diameters, the majority of the signal arises from particles within the target size range (Appendix Figure 8.3).

Table 3.1: Length and volume of the utilized flow tubes and the corresponding reaction time with a flowrate of 2 L min<sup>-1</sup>.

Length (cm)	Volume (mL)	Reaction time (s)
-	-	1.3 ± 0.5
45	264 ± 5	9.3 ± 0.7
67	610 ± 5	19.6 ± 0.7
82	1334 ± 5	41.3 ± 0.7
120	3514 ± 5	106.8 ± 0.7

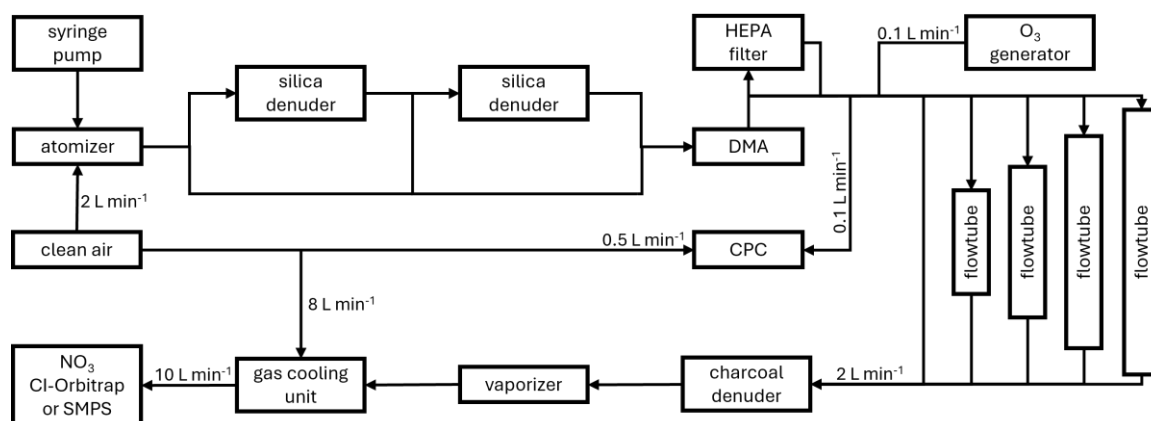


Figure 3.1: Schematic of the experimental setup. The SMPS was used as the detection system only in experiments dedicated to determining particle evaporation efficiency. In the experiments listed in Table 3.2, the CI-Orbitrap served as the detection system.

### 3.3.2 Particle Evaporation

After the flow tubes the aerosol was first passed through an activated carbon denuder to remove the gas-phase components. The aerosol particles were then evaporated in a commercially available nozzle heater cartridge (HS Heizelemente) at 285 °C. This cartridge consists of a 20 cm long stainless steel tube with an inner diameter of 8 mm, tightly wrapped with a resistive heating element. A NiCrNi thermocouple is mounted on the surface to monitor the evaporator temperature, and the tube is thermally insulated with mineral wool. The nozzle heater cartridge is controlled by a W-35/M temperature controller with a PID control loop, allowing precise temperature adjustments in the range of 50–400 °C. At the applied flow rate of 2 L min<sup>-1</sup>, the residence time of the particles in the evaporator is 0.3 s. The completeness of evaporation was assessed in a separate experiment using a butanol-based Condensation Particle Counter (CPC) Model 5416 with a preceding L-DMA Model 55-U (both Grimm Aerosol Technik). For this purpose, the evaporator temperature was varied between

25 °C and 325 °C, and the resulting particle-size distributions were measured. It has been shown that thermal decomposition reactions (primarily dehydration and decarboxylation) in other thermal aerosol evaporators can lead to measurement artifacts (Guo et al., 2024; Yang et al., 2021). In our inlet, the short residence time and the use of a cooling-gas unit reduce such effects. To test this, several organic polyacids were nebulized at identical conditions and evaporated at 285 °C and the fractions of decomposition products determined (Appendix Table 8.2). For all acids investigated, the fraction of dehydration products was <4%, substantially lower than for other thermal aerosol evaporators (Yang et al., 2021). The influence of thermal decomposition is therefore expected to be minor under our conditions.

### 3.3.3 CI-Orbitrap Measurements

The ion source of the CI-Orbitrap used in this study is an Eisele type CI inlet modified for a high-resolution Orbitrap mass spectrometer (Riva et al., 2019a; Riva et al., 2020a). The mass spectrometer used is a high-resolution Q Exactive Orbitrap and HNO<sub>3</sub> was used as reagent gas. Initially, the particle evaporator was directly connected to the CI-Orbitrap. However, even at low evaporator temperatures below 100 °C, a significant decrease in both reagent gas and analyte signal was observed. A possible explanation for this could be the formation of turbulence within the ionization source, as Eisele-type inlets are known to be highly sensitive to flow changes (Zhao et al., 2024). To address this issue, a gas cooling unit was developed and placed between the evaporator and the CI-Orbitrap (see Figure 2.1). This unit cools the hot gas in two stages. First, 8 L min<sup>-1</sup> of clean air is flushed around the hot stainless steel tubing coming out of the evaporator, passively cooling it and adjusting the temperature of the cooling gas to that of the analyte gas stream. Subsequently, this cooling gas serves as a sheath gas, reducing wall losses, further cooling the gas stream through mixing, and minimizing the re-nucleation of the cooling analyte by dilution. Implementation of the gas cooling unit reduced the loss of reagent ion signal at 320 °C from over 90% to less than 40% (see Figure 2.2). Data analysis was performed using Orbitool, a program specifically developed for the analysis of online Orbitrap data (Cai et al., 2021).

Table 3.2: Experimental conditions for the different experiments. In each experiment, particles with diameters of 30, 50, 80, and 110 nm were examined at the reaction times listed in Table 3.1.

Experiment	[O <sub>3</sub> ] (ppm)	RH (%)	Particle volume concentration ( $\mu\text{m}^3 \cdot \text{cm}^{-3}$ )	TA signal <sup>a</sup> ( $\cdot 10^{-2}$ )
1	10	32-35	$2.7 \pm 0.3$	$1.38 \pm 0.08$
2	1	32-35	$2.9 \pm 0.1$	$1.26 \pm 0.03$
3	0.1	35-37	$2.5 \pm 0.2$	$1.24 \pm 0.07$
4	10	49-51	$3.1 \pm 0.2$	$1.22 \pm 0.05$
5	1	48-51	$3.4 \pm 0.3$	$1.17 \pm 0.04$
6	0.1	50-53	$3.3 \pm 0.3$	$1.22 \pm 0.08$
7	10	83-86	$6.9 \pm 0.4$	$2.18 \pm 0.08$
8	1	83-87	$6.4 \pm 0.7$	$1.92 \pm 0.08$
9	0.1	83-87	$6.5 \pm 0.5$	$2.07 \pm 0.07$

<sup>a</sup>normalized to the reagent-ion signal.

## 3.4 Results and Discussion

### 3.4.1 Characterization of Reaction Products

Typical for the ozonolysis of unsaturated compounds, the reaction of NDA with ozone produces a wide range of products. Figure 3.2 shows a typical mass spectrum in negative ion mode recorded in this study using the CI-Orbitrap. Due to the high resolution of the Orbitrap, the elemental composition of the detected  $m/z$  can be directly assigned. The products are detected either as  $\text{NO}_3^-$  adducts or as deprotonated ions. For simplicity, the products are referred to as neutral species throughout this study. The signals of nitrate adducts and deprotonated species with the same elemental composition are summed, where applicable, and considered as a single products.

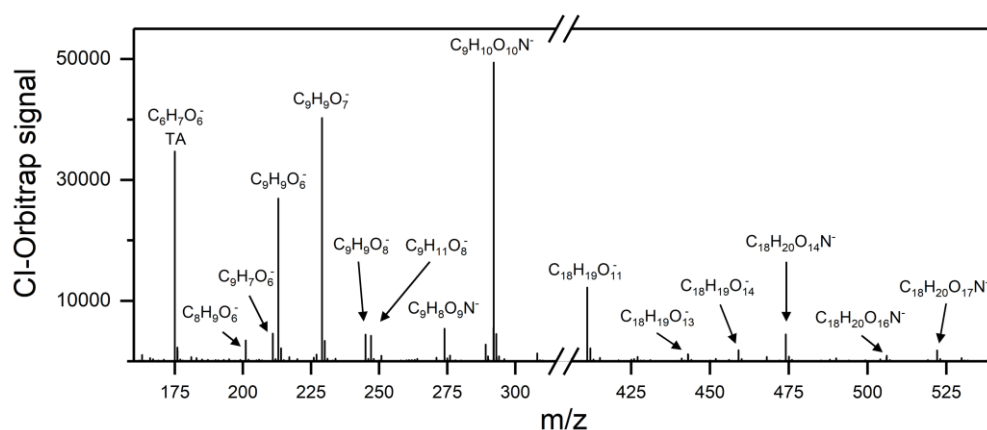


Figure 3.2: CI-Orbitrap mass spectra for the ozonolysis of NDA using nitrate as reagent gas. Molecular formulas of the most intense signals are indicated. For comparisons at the product level, we sum the intensities of the nitrate adducts and deprotonated ions that have the same elemental composition and then refer to the corresponding neutral species throughout. For example, the two dominant peaks ( $\text{C}_9\text{H}_{10}\text{O}_{10}\text{N}^-$  (nitrate adduct);  $\text{C}_9\text{H}_9\text{O}_7^-$  (deprotonated ion)) both originate from the same neutral species,  $\text{C}_9\text{H}_{10}\text{O}_7$ .

Similar to other unsaturated compounds, the reaction of NDA with ozone is expected to follow the Criegee mechanism (Figure 3.3) (Criegee, 1975; Testero et al., 2007). We therefore attempt to derive the structures corresponding to the detected molecular formulas based on established reaction pathways of comparable unsaturated hydrocarbons. The neutral losses observed in the MS/MS measurements for the various reaction products further support the proposed structural assignments (Appendix Figure 8.4 and Figure 8.5). The stabilized Criegee intermediate (SCI) formed in this process can undergo various reaction pathways, leading to the formation of a diverse set of product molecules. The two most intense product signals correspond to the elemental compositions  $\text{C}_9\text{H}_{10}\text{O}_6$  and  $\text{C}_9\text{H}_{10}\text{O}_7$ , with the latter typically accounting for 50% of the signal attributed to NDA-ozonolysis products. Since NDA has the molecular formula  $\text{C}_9\text{H}_{10}\text{O}_4$ , these products formally represent molecules in which two or

three oxygen atoms have been added to the NDA structure. The molecular formula  $C_9H_{10}O_7$  probably corresponds to multiple structural isomers, including a secondary ozonide (SOZ) (I) or an  $\alpha$ -acyloxyalkyl hydroperoxide (AAHP) (II) formed via an intramolecular reaction with one of NDA's carboxylic acid groups (Testero et al., 2007; Zhao et al., 2019; Wang et al., 2023). However, it could also represent a tricarboxylic acid (III), formed through isomerization of the SCI. The reaction of SCIs with water leads to the formation of  $\alpha$ -hydroxyalkyl hydroperoxides (HAHP) which would in our case correspond to the molecular formula  $C_9H_{12}O_8$  (IV) (Wang et al., 2023; Enami, 2021; Witkowski et al., 2018). HAHPs decompose by elimination of  $H_2O$  or  $H_2O_2$  (Leviss et al., 2016; Riva et al., 2016). The latter would lead to the formation of the dialdehyde  $C_9H_{10}O_6$  (V). Alternatively, HAHPs can isomerize to yield a cyclic peroxyhemiacetal (VI) (Qiu et al., 2022; Qiu et al., 2020). In addition to these unimolecular products, signals from bimolecular reactions forming several first generation dimers are also observed. AAHPs can also form through the reaction of the SCI with carboxylic acid groups of other molecules. This would lead to the formation of  $C_{15}H_{18}O_{13}$  (VII) from the reaction with the internal standard TA and  $C_{18}H_{20}O_{11}$  (VIII) from the reaction with NDA. Similarly, an  $\alpha$ -alkoxyalkyl hydroperoxide  $C_{12}H_{18}O_{18}$  (IX) is produced via the reaction of the hydroxy group of isopropanol, which is added to the nebulized solution to increase particle number concentration, with the SCI.

In addition to these first-generation products, a series of  $m/z$  signals observed in the mass spectrum are likely to originate from subsequent reactions. The possible formation pathways of these compounds are depicted in Figure 3.4.  $C_{18}H_{20}O_{13}$  and  $C_{18}H_{20}O_{14}$  are probably aged dimers formed through the reaction of the unreacted double bond of the bimolecular AAHP  $C_{18}H_{20}O_{11}$  (VIII) with ozone, initially generating a new SCI (Wang et al., 2023). Similar to the monomeric SCI, this dimeric SCI can react to form an aldehyde (XII), a carboxylic acid (XIII), or an AAHP (XIV). However, alternative formation pathways for these highly oxidized dimers are also conceivable, such as the formation of a SOZ (X, XI) via the reaction of a monomeric SCI with carbonyl functionalities of  $C_9H_{10}O_6$  or  $C_9H_{10}O_7$  (Zhao et al., 2019).

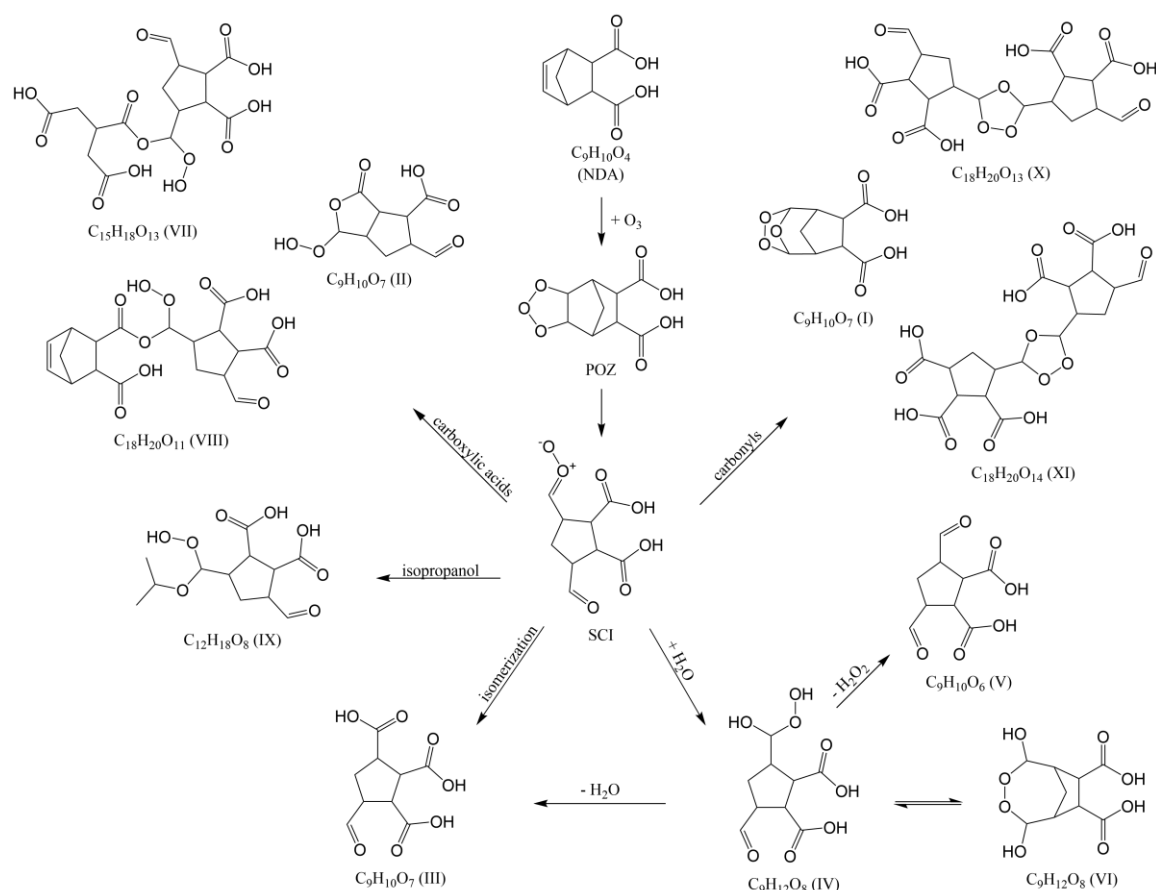


Figure 3.3: Proposed reaction pathways for the ozonolysis of NDA and the subsequent reactions of the SCI to form first generation oxidation products. All molecular formulas in this figure were observed in the mass spectra; structures are assigned based on established mechanisms.

Another group of detected products has additional oxygen atoms in the molecule, including the molecular formulas  $C_9H_{10}O_8$ ,  $C_9H_{12}O_9$ , and  $C_{18}H_{20}O_{15}$ . In the gas phase, autoxidation is the primary mechanism leading to highly oxygenated organic molecules (HOMs). This process involves isomerization of the SCI to a vinyl hydroperoxide, followed by the loss of an OH radical. The resulting carbon-centered radical can undergo oxygen addition to form a peroxy radical, which can further isomerize and incorporate additional oxygen atoms (Rissanen et al., 2014). The formation of  $C_9H_{10}O_8$  could proceed via this mechanism at the particle surface. Since this reaction pathway leads to the formation of OH radicals, we would expect to detect reaction products resulting from radical chemistry. In particular, products from the reaction of TA with OH radicals should be readily identifiable (Zhao et al., 2019). However, no such reaction products from the interaction of TA with OH radicals were observed. The MS/MS spectrum of  $C_9H_{10}O_8$  shows the neutral loss of  $H_2O_2$  (Appendix Figure 8.5), suggesting that it could be a hydroperoxide resulting from the reaction with oxygen. Another potential pathway for the formation of highly oxidized aged products involves reactions with hydrogen peroxide

or hydroperoxide species formed during ozonolysis.  $\text{H}_2\text{O}_2$  is known to oxidize carboxylic acids to peroxy acids (Greenspan, 1946).  $\text{C}_9\text{H}_{10}\text{O}_8$  may therefore represent a corresponding peroxy acid (XVII) formed via the reaction of  $\text{C}_9\text{H}_{10}\text{O}_7$  (III) with  $\text{H}_2\text{O}_2$ . Additionally, both  $\text{H}_2\text{O}_2$  and hydroperoxide compounds can react with aldehydes via a Baeyer-Villiger oxidation. This reaction has been suggested to play a role in SOA particle-phase chemistry and may contribute to the aging of oxidation products within particles (Pagonis and Ziemann, 2018; Pospisilova et al., 2020).  $\text{H}_2\text{O}_2$  is released through the reaction of the SCI with water and should therefore be present in the particle phase along with various hydroperoxide species. Zhao et al. (2019) demonstrated through comparison with a reference standard that 4-cyclohexene-1,2-dicarboxylic acid undergoes oxidation to the corresponding tetraacid in a heterogeneous ozonolysis reaction, with peroxide-mediated oxidation being the most likely pathway. Although the formation of carboxylic acids from aldehydes is often emphasized as the principal outcome of Baeyer-Villiger chemistry, the product distribution is shown to depend strongly on the oxidant, the solvent, and the substrate structure (Lehtinen et al., 2000, 2001; Snowden et al., 2004). Baeyer-Villiger oxidations of terpenoid aldehydes have been reported to produce formate ester in yields of 80-90% (Barrero et al., 1999). Marteau et al. (2013) and Lehtinen et al. (2000) demonstrated that substitution at the  $\alpha$ -carbon significantly increases the likelihood of formate ester formation, with bulkier substituents enhancing this effect. It is therefore plausible that the ozonolysis product  $\text{C}_9\text{H}_{10}\text{O}_8$  could also correspond to the tetraacid (XV) and the formate ester (XVI). This being the case would further suggest that a portion of the  $\text{C}_9\text{H}_{10}\text{O}_7$  signal probably also results from the Baeyer-Villiger oxidation of one of the aldehyde groups of  $\text{C}_9\text{H}_{10}\text{O}_6$  (V).

Another group of signals in the mass spectrum exhibits a loss of carbon in their molecular formula. The most prominent representatives are  $\text{C}_8\text{H}_{10}\text{O}_6$  and  $\text{C}_8\text{H}_{10}\text{O}_7$ . We propose that these compounds could be formed through the hydrolysis of the formate esters (XVI) generated via the Baeyer-Villiger reaction (Pospisilova et al., 2020). This pathway would lead to the formation of alcohols (XVIII) and formic acid. Formate esters exhibit high carbonyl reactivity due to the absence of an alkyl group, making them highly susceptible to a nucleophilic attack by  $\text{H}_2\text{O}$  or other nucleophiles. Therefore, rapid hydrolysis of these esters in the aqueous particle phase would not be unlikely.

The final group of detected products is characterized by a reduced amount of hydrogen in their molecular formula. This could be explained by the elimination of molecular hydrogen or water from the molecule. The main product in this category is  $\text{C}_9\text{H}_7\text{O}_6$ , which could be an anhydride. Since the precursor molecule, NDA, already contains two carboxyl groups, anhydride formation could, in principle, occur prior to ozonolysis. However, due to the steric hindrance of the bicyclic structure and the fact that the two carboxyl groups are positioned in endo and exo conformations, this scenario appears unlikely. It is therefore more plausible that a carboxyl group formed during the ozonolysis process contributes to the formation. Several

potential reaction pathways could lead to the formation of such an anhydride. Durham et al. (1958) demonstrated that hydroperoxides can react with aldehydes to form peroxyhemiacetals, which may decompose with the elimination of either molecular hydrogen or water. It has already been proposed that this type of reaction could also occur in aerosol particles (Pagonis and Ziemann, 2018; Claflin et al., 2018). In our system, such a transformation could proceed via an intramolecular pathway, resulting in the formation of a cyclic peroxyhemiacetal (XIX). These cyclic intermediates are believed to decompose more rapidly than their acyclic counterparts (Bakker-Arkema and Ziemann, 2020). The decomposition of a cyclic peroxyhemiacetal could, depending on the elimination step, yield either an anhydride and an aldehyde (XXI) if H<sub>2</sub>O is eliminated, or an anhydride and a carboxylic acid (XX) if molecular hydrogen is eliminated. A bimolecular variant of this reaction, involving a hydroperoxide and a carbonyl compound forming an acyclic peroxyhemiacetal, is also conceivable, although it is likely to proceed more slowly, as mentioned above. An alternative formation mechanism could involve the direct decomposition of an AAHP into an anhydride and water (Zhao et al., 2018). This reaction likely occurs in the gas-phase ozonolysis of ethene in the presence of formic acid (Neeb et al., 1996). However, this pathway appears to be negligible in the decomposition of AAHPs derived from the ozonolysis of  $\alpha$ -pinene SCI with pinonic acid or adipic acid in aqueous phase systems (Zhao et al., 2018). Another proposed pathway leading to a dehydrated product involves an aldol condensation followed by dehydration (Zhao et al., 2019). In this mechanism, a CH-acidic carbon would act as a nucleophile and attack an aldehyde, forming a  $\beta$ -hydroxy carbonyl intermediate, which subsequently eliminates water to form an  $\alpha,\beta$ -unsaturated carbonyl compound. However, in the reaction system studied here, such a mechanism is highly unlikely. All potentially nucleophilic carbon centers are part of the cyclopentane ring structure of NDA, and any bond formation would necessarily lead to the generation of a sterically hindered bicyclic structure. Furthermore, the resulting ring system would correspond to a cyclopropane or cyclobutane structure, both of which are energetically disfavored due to pronounced ring strain and significant steric hindrance.

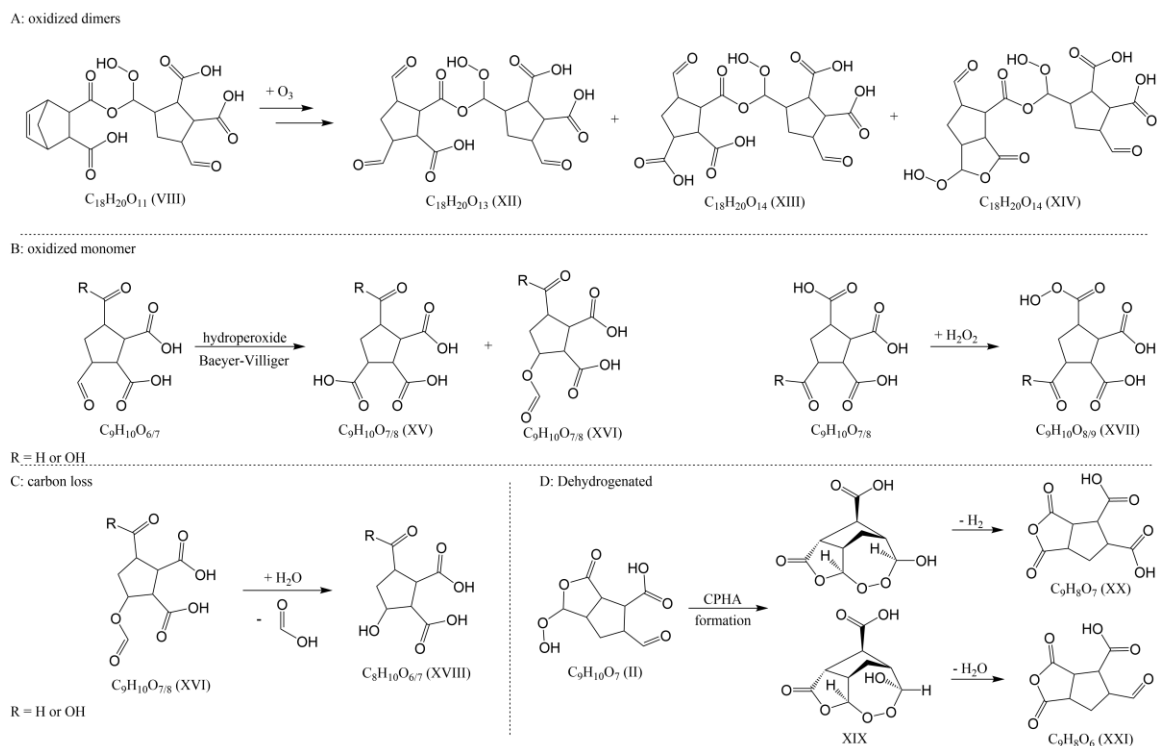


Figure 3.4: Proposed particle-phase reactions that lead to A: oxidized dimers, B: oxidized monomers, C: carbon loss products and D: dehydrogenated products. All molecular formulas in this figure were observed in the mass spectra; structures are assigned based on established mechanisms.

### 3.4.2 Particle Evaporation Efficiency

Due to the varying surface-to-volume ratios, the investigated particles do not evaporate at the same rate in the vaporizer. The larger the particle volume, the higher the temperature required for complete evaporation within the same residence time in the vaporizer. As shown in Figure 3.5A, at a very short reaction time of 1.3 s, the intensity maxima of the sum of all particle-derived ions follows this expected trend. As the reaction progresses, the volatility of the particles decreases because the resulting ozonolysis products have significantly lower vapor pressures than the precursor compound NDA. Notably, the maximum evaporation temperature for 30 nm particles shifts significantly towards higher temperatures, making them comparable in volatility to 110 nm particles. To ensure complete gas-phase transfer of all particles, the particle-size distribution of the residual particles after the vaporizer was determined at different temperatures using an SMPS, and the fraction of evaporated particle volume was calculated. Figure 3.5B presents this data alongside the corresponding CI-Orbitrap thermogram. The highest ozone concentration used in this study (10 ppm) and the longest reaction time (106.8 s) in the flow tube at 50% RH were selected for these measurements to ensure representativeness across all experiments. The data show that all examined aerosol particle sizes are completely evaporated at temperatures above 275 °C.

Unlike the CI-Orbitrap signal, the particles evaporate in the expected order from 30 nm to 110 nm particle diameter. However, the differences in the temperature curves are small. The SMPS measurements indicate that the particles already appear to shrink at lower temperatures than expected from the CI-Orbitrap signal. This is likely due to the evaporation of H<sub>2</sub>O from the particle phase, which is not detected by the CI-Orbitrap. Overall, the particle evaporation profile closely follows the trend of the thermogram at temperatures above 200 °C, indicating that the transition of the particle-phase molecules into the gas phase is proportional to the increase in signal intensity. We therefore assume that no significant signal loss occurs due to particle evaporation. Therefore, a vaporizer temperature of 285 °C was chosen for the ozonolysis experiments to ensure complete evaporation while maintaining maximum signal intensity.

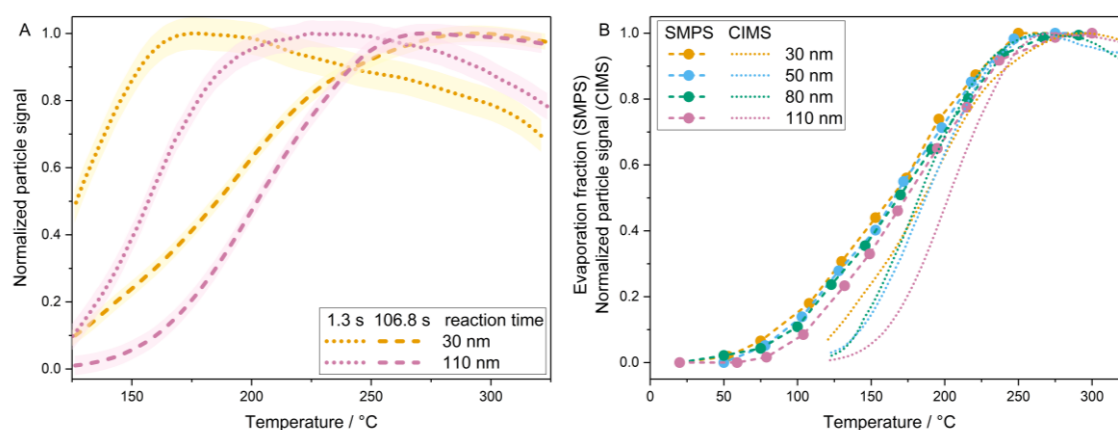


Figure 3.5: Adjacent-averaged thermograms of 30 nm (yellow) and 110 nm (pink) particles recorded with the CI-Orbitrap after 1.3 s (dotted lines) and 106.8 s (dashed lines) of ozonolysis time at 50% RH and 10 ppm O<sub>3</sub> concentration. The semi-transparent, broader band plotted behind the thermograms denotes  $\pm 1$  standard deviation (A). Comparison of adjacent-averaged thermograms recorded with the CI-Orbitrap (dotted lines) and the evaporation fraction calculated from SMPS data (dashed lines) each after 106.8 s reaction time for the respective particle sizes at 50% RH and 10 ppm O<sub>3</sub> concentration for particles of 30, 50, 80 and 110 nm in diameter (B).

We were not able to ionize the precursor NDA using nitrate reagent ions, which is likely due to steric hindrance of the polycyclic structure and the oppositely oriented endo and exo carboxyl groups. As a result, the reaction progress with ozone cannot be directly monitored. To ensure a constant aerosol mass in the flow tubes during the experiments, to maintain a consistent ratio with ozone and to enable comparison of absolute signal intensities, TA was used as an internal standard. TA was nebulized together with NDA at a fixed mass ratio; consequently, the TA signal and the signals of the NDA ozonolysis products are subject to the same fluctuations in particle concentration and in the ionization process. Accordingly, the normalization commonly used in CIMS was performed with respect to the TA signal rather

than the reagent-ion signal. The relative signals shown are therefore calculated as the quotient of the respective product signal divided by the signal of the internal standard. The mass traces of the ozonolysis products exhibit the same temporal evolution in signal intensity as the TA signal (Appendix Figure 8.6). Thus, the internal standard not only facilitates the correction for signal fluctuations but also enables the differentiation between true signals originating from the reaction system and potential background signals not associated with particle-phase molecules. To verify that TA and the NDA ozonolysis products remained in the particle phase, we also operated the system without the activated-carbon denuder and without the particle evaporator. No gas-phase molecules were detected, indicating that gas-phase partitioning is not significant under the used conditions. It should be noted however, since TA is a triacid, it can also react with Criegee intermediates formed during ozonolysis reactions, leading to the formation of a TA-AAHP (Figure 3.3). Although this reaction is observed, it does not lead to a noticeable reduction in the internal standard signal. With a measured maximum contribution of only 1.5% of the total product signal, TA-AAHP is not a significant reaction product. Nevertheless, we have decided to take it into account so that the sum of the internal standard signal and TA-AAHP is used for correction.

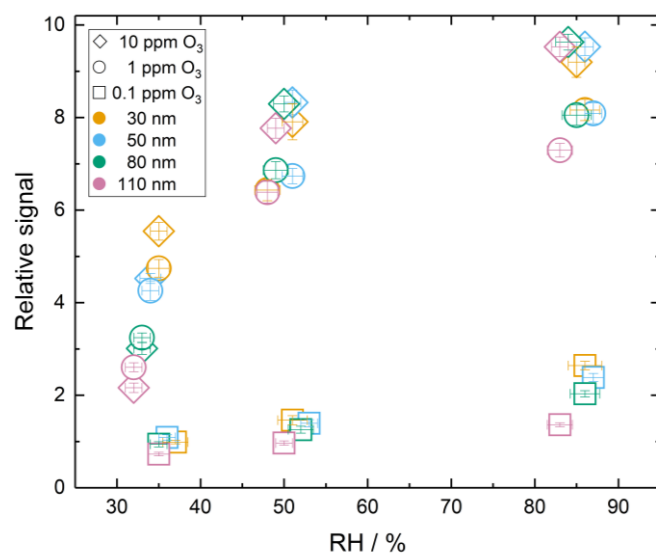


Figure 3.6: Sum of product signals of the heterogeneous ozonolysis of NDA as a function of RH at a reaction time of 106.8 s, for particles with diameters of 30, 50, 80 and 110 nm and ozone concentrations of 0.1, 1 and 10 ppm. The molecular formulas included in the sum are listed in Appendix Table 8.3.

### 3.4.3 Humidity Dependence of the Reaction Rate

To monitor the progress of the reaction, we examine the total signal, defined as the sum of the detected and normalized ozonolysis product signals. The molecular formulas included in this sum are listed in Appendix Table 8.3. Figure 3.6 shows the TA-normalized total signal after 106.8 s of reaction, plotted as a function of relative humidity for three ozone concentrations and four particle sizes. A clear dependence on RH is observed, with higher humidity leading to higher product signals. Both NDA and TA, as di- and triacids, respectively, are hygroscopic. It therefore suggests that the results can be attributed to the water content and thus the changing phase state of the organic particles. The phase transition from an amorphous solid state under dry conditions to a semi-solid state and finally to a liquid state has a major influence on the diffusion coefficients of the reaction partners. At high RH, ozone uptake is driven by reactions throughout the particle volume; at low RH, it is limited to reactions near the particle surface and kinetically limited by slow diffusion and replenishment of unreacted organic molecules (Berkemeier et al., 2016). Beyond RH, a dependence on particle size is also evident, particularly under dry conditions at ozone concentrations of 1 ppm and 10 ppm. At the highest ozone concentration, the total signal for 30 nm particles is nearly three times higher than that for 110 nm particles. In general, it can be expected that smaller particles react more rapidly with ozone due to their larger surface-to-volume ratio. However, an additional effect seems to influence the observed kinetics, as illustrated in Figure 3.7A. This figure illustrates the evolution of the total signal at 35% RH and 10 ppm ozone. After a rapid initial product formation within the first 10 s, the rate of product accumulation slows significantly for the remainder of the reaction period, independent of particle size. One possible explanation for this could be the formation of a crust on the outer particle surface due to lower diffusion rates in dry particles. This crust could hinder the further diffusion of ozone into the particle core and thus effectively limit the reaction to an outer shell region. Such a mechanism would also account for the greater extent of precursor conversion in smaller particles. For instance, if a 4 nm thick crust were to form, approximately 60% of the volume of a 30 nm particle would be affected, whereas only 20% of a 110 nm particle would react. This crusting effect appears to be less pronounced at lower ozone concentrations. At 0.1 ppm  $O_3$ , the relative total signal across all particle sizes is almost identical, and at 1 ppm  $O_3$ , the differences are significantly smaller.

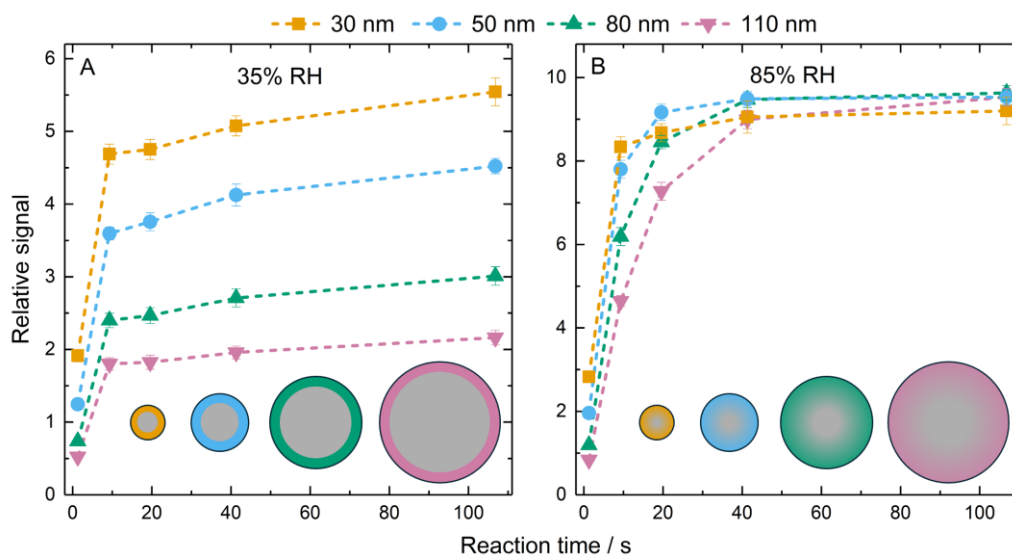


Figure 3.7: Evolution of the relative total signal of ozonolysis products over the reaction time at 35% RH (A) and 85% RH (B) at 10 ppm  $O_3$  for particles with diameters of 30, 50, 80 and 110 nm. The molecular formulas included in the total signal are listed in Appendix Table 8.3. The schematic particle illustrations represent the hypothesized formation of a surface crust under dry conditions and unimpeded diffusion under humid conditions.

The situation at a relative humidity of 85% is quite different, as can be seen in Figure 3.7B. Here, particles with a size of 30 nm react the fastest, which was to be expected due to their highest surface-to-volume ratio. However, after a reaction time of 106.8 s, all particle sizes show approximately the same overall signal in the CI Orbitrap. Since the overall signal does not change significantly between the second longest and longest reaction times, with the exception of the 110 nm particles, this suggests that the starting material NDA has already reacted completely with  $O_3$  at this point. This indicates that the higher water content in the particle causes faster diffusion into the interior of the particle and no crust forms.

### 3.4.4 Particle-Size-Dependent Chemistry

Although all particle sizes show similar total signals at 85% RH, there are still significant deviations in the product distribution of the resulting ozonolysis products. This is illustrated by a few exemplary products in Figure 3.8. Time profiles of all the signals corresponding to the major NDA ozonolysis-derived molecular formulas are shown in Appendix Figure 8.7 to Figure 8.15. The carbon loss product with the formula  $C_8H_{10}O_6$  (XVIII) forms significantly faster and in larger quantities in larger particles. In contrast, the water addition product  $C_9H_{12}O_8$  forms more abundantly in smaller particles. The first-generation dimer  $C_{18}H_{20}O_{11}$  (VIII), on the other hand, shows an unusual trend. The signal of this compound

increases sharply at short reaction times, but then drops almost as quickly. The time required to reach the maximum signal intensity increases with particle size. In the 30 nm particles, the formation and subsequent decomposition of this dimer are so rapid that the signal already drops even at the shortest reaction time observed. The most likely products formed from this decay are further oxidized aged dimers through reaction with an additional ozone molecule, as well as NDA and  $C_9H_{10}O_7$  (II) as decomposition products, or NDA and  $C_9H_{12}O_8$  (IV) through hydrolysis (Zhao et al., 2018). The signal evolution of the aged dimer  $C_{18}H_{20}O_{14}$  exhibits the most pronounced particle-size-dependent differences among the compounds shown. The relative signal intensity for 30 nm particles is almost eight times higher than for particles with a diameter of 110 nm. While the particle-size dependency for carbon loss and hydrated products shows an approximately linear trend, the effect for the dimer becomes more pronounced with decreasing particle size. In summary, it can be concluded that smaller particles favor the formation of higher molecular weight products, while decomposition reactions proceed more slowly. This could be due to the higher internal pressure in smaller particles caused by the Laplace pressure (Petters, 2022). In general, bond-forming reactions, i.e., reactions in which the product side has more bonds than the reactant side, have negative activation volumes. This is due to shorter atomic distances in covalent-bonded molecules compared to Van der Waals interactions, a property that is also exploited in high-pressure synthesis (van Eldik, 2008). If smaller particles have higher internal pressure due to Laplace pressure, this would explain the significantly higher proportion of compounds with higher molecular weight. Another explanation could be the influence of the pH in the particles, although the data here is somewhat contradictory. Studies have shown that smaller aerosol particles are more acidic and have a higher pH gradient between the surface and the bulk (Craig et al., 2018; Gong et al., 2023). Other studies suggest that the degradation of HAHPs is favored by lower pH values, while the degradation of bimolecular AAHPs occurs more rapidly at higher pH values (Qiu et al., 2020; Zhao et al., 2018). The latter could explain the lower proportion of bimolecular AAHPs in the larger particles, as these should be less acidic than the smaller particles. However, this is not consistent with the results found here, which show that more hydrated product is present in the smaller particles. This would have to be the opposite if the decomposition of HAHPs occurs faster under acidic conditions. In conclusion, our results provide direct evidence for particle-size-dependent chemistry in the studied heterogeneous reactions. The mechanistic origins of these size dependencies, however, are not yet fully resolved, and further studies specifically designed to address these questions are warranted.

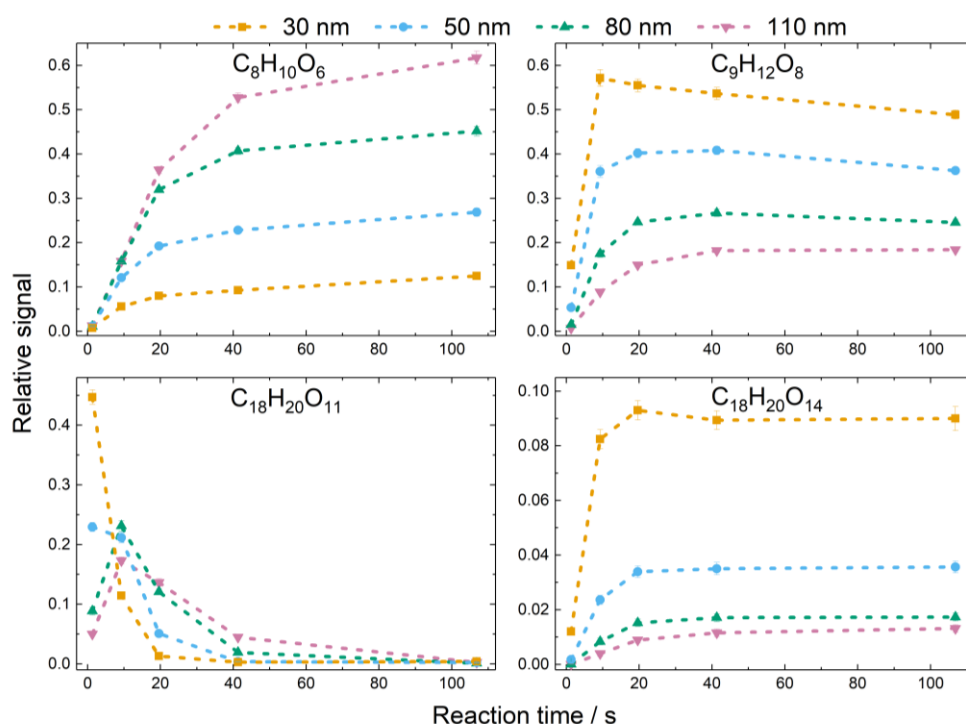


Figure 3.8: Temporal evolution of selected ozonolysis product signal intensities exhibiting pronounced particle-size-dependent differences (10 ppm  $O_3$ , 85% RH).

### 3.4.5 Influence of Relative Humidity on the Product Distribution

The particle-size-dependent differences observed at 85% RH are also found at the other investigated humidities (Figure 3.9). This figure presents the distribution of the various product groups for 30 nm and 110 nm particles after 106.8 seconds of reaction time across three RH conditions at 10 ppm ozone. As previously noted in Figure 3.8, the most pronounced differences in product signals between particle sizes occur between those with the largest diameter disparity. This trend is consistent across all examined RH levels and ozone concentrations. Consequently, only the data for 30 nm and 110 nm particles is displayed, with signals for 50 nm and 80 nm particles falling intermediate to these values.

The proportion of hydrated products, with the main product being  $C_9H_{12}O_8$ , is consistently higher in the 30 nm particles. Across all particle sizes, the proportion decreases with drier reaction conditions, which is expected since we assume these are reaction products involving  $H_2O$ . Therefore, the size-dependent differences could also stem from varying water content within the particles depending on the particle diameter. However, this is contradicted by the measured signal of the first-generation product  $C_9H_{10}O_6$  (V). Previous studies have demonstrated that the proportion of this ozonolysis product increases with higher humidity levels (Zhao et al., 2019; Heine et al., 2017), which is anticipated since its formation in the particle phase likely involves water. This influence is also evident in our results, as the

proportion is much higher at 85% RH than under drier conditions. However, there is no clear size dependence for  $C_9H_{10}O_6$ . Therefore, a varying water content in the particles is unlikely to explain the observed differences.

The dehydrogenated products show the opposite dependence on RH as the hydrated products. As depicted in Figure 3.4, these products likely form either through the elimination of  $H_2$  or  $H_2O$  from the AAHP  $C_9H_{10}O_7$  (II) via the formation of a cyclic peroxyhemiacetal (XIX). Therefore, if water is eliminated during the reaction, it is reasonable to expect higher product formation under dry conditions. Moreover, the decomposition pathway likely involves the formation of anhydrides, which are expected to rapidly hydrolyze back to their corresponding acids under humid conditions. Interestingly, the proportion of these decomposition products, similar to the carbon loss products, is higher in larger particles. As with the hydrated products, the formation of the cyclic intermediate appears to play a crucial role. The effect of particle size is less pronounced here compared to other products, possibly because the decomposition reaction likely proceeds through the formation of the cyclic peroxyhemiacetal, which we suspect is preferentially formed in smaller particles (Laplace pressure). Thus, two opposing particle-size-dependent effects may be at play: the formation of the cyclic peroxyhemiacetal, favored in smaller particles, and its decomposition, favored in larger particles.

The particle-size dependency of the carbon loss product  $C_8H_{10}O_6$  (XVIII) at 85% RH was previously shown in Figure 3.8. This dependency of higher amounts in larger particles is also observed for the entire carbon loss product group across all investigated RH levels. However, these products exhibit a particular dependency on RH, being most abundant under moderate conditions of 50% RH. We hypothesize that these products are alcohols resulting from the hydrolysis of esters formed during the Baeyer-Villiger oxidation. Typically, ester hydrolysis should be more favorable under humid conditions, whereas Baeyer-Villiger oxidation is anticipated to be more intensive under dry conditions (Pospisilova et al., 2020). Therefore, the moderate humidity range could be the ideal condition where enough esters are formed, but there is also sufficient water in the particle phase to enable rapid hydrolysis. This hypothesis is further supported by the observation that the aged monomer group in Figure 3.9 also exhibits the highest proportions at 35% and 50% RH. The proposed products of the Baeyer-Villiger oxidation, the tetraacid (XV) and the formic acid ester (XVI), both with the molecular formula  $C_9H_{10}O_8$ , constitute the largest fraction of this aged monomer group. Furthermore, this group exhibits the inverse particle-size dependence, with higher fractions of aged monomers observed in smaller particles. Preferential hydrolysis of the esters within this group in the 110 nm particles could explain the observed differences.

A clear particle-size dependence is also evident for the bimolecular reaction products (green product groups in Figure 3.9) across all investigated RHs. This effect is most pronounced for the highly oxidized aged dimer group, whose contribution in 30 nm particles is consistently

at least three times greater than in 110 nm particles. One possible cause for the high fraction of bimolecular reaction products could again be the effect of increased internal pressure within smaller particles, favoring dimer formation. An increased formation of first-generation dimers would consequently lead to higher levels of aged dimers.

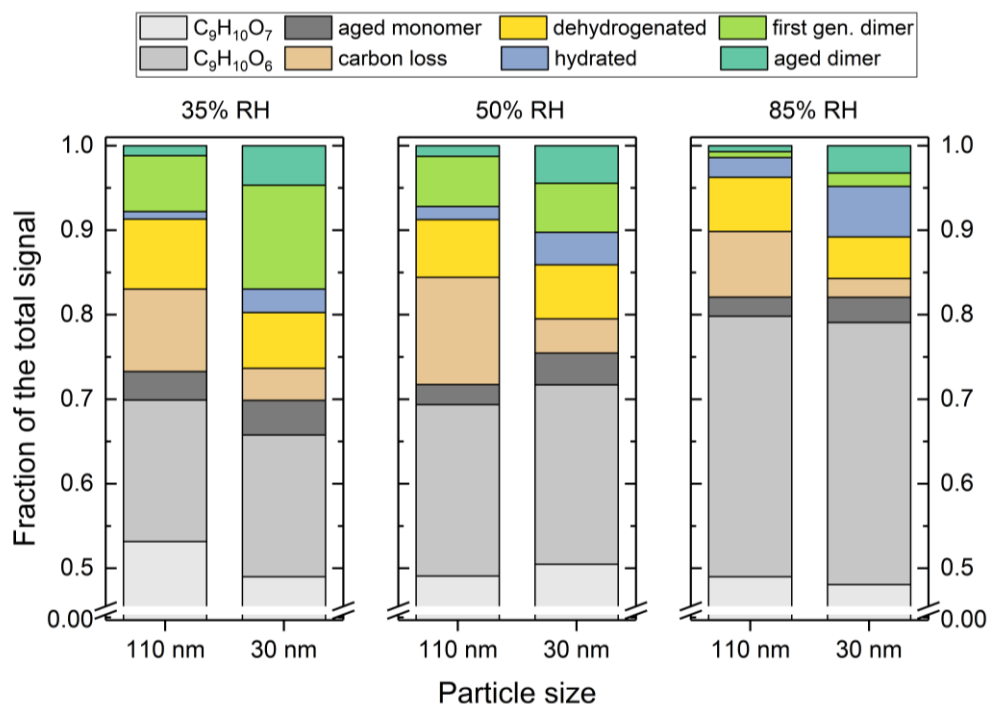


Figure 3.9: Product distribution of the total signal from the heterogeneous ozonolysis of NDA after 106.8 s at 10 ppm  $O_3$  for particles with diameters of 30 nm and 110 nm and relative humidities of 35%, 50% and 85%. The molecular formulas included in the total signal, and their assignments to the different product classes, are listed in Appendix Table 8.3.

### 3.5 Conclusion

The heterogeneous ozonolysis of NDA leads to a complex series of reaction products that depend heavily on relative humidity, particle size, and reaction time. The tentatively assigned first-generation products include a dialdehyde, a tricarboxylic acid, and a monomolecular and a bimolecular  $\alpha$ -hydroxyalkyl hydroperoxide, which appear to undergo further oxidation, decomposition, and hydrolysis reactions. Particle-phase aging mechanisms such as Baeyer-Villiger oxidation, hydroperoxide-driven oxidation, and decomposition of AAHPs could play a crucial role in the formation of the final product distribution. Our results show that relative humidity strongly influences the proposed reaction pathways. Higher relative humidity promotes hydrolysis reactions, leading to an increased formation of hydrated species and a lower dimer fraction. Lower relative humidity, on the other hand, favors the formation of anhydrides and slows down decomposition reactions. The observed strong particle-size dependence of several product groups motivates the hypothesis that Laplace pressure could play a role in influencing chemical reactivity. In smaller particles, dimerization is enhanced, leading to a higher proportion of oligomeric species. This trend could be caused by the increased internal pressure in these particles, which is known to favor bond-forming reactions, as these often have negative activation volumes. Conversely, larger particles exhibit higher proportions of decomposition products, especially those formed by hydrolysis and leading to carbon loss products, as well as dehydrated products due to the loss of  $H_2$  or  $H_2O$ .

Overall, our results highlight the importance of particle size and humidity for the chemical processing of organic aerosol particles. The interaction of these factors influences not only the volatility and chemical composition of the particles, but also their potential to form highly oxidized and low-volatile products, an observation that may be particularly relevant for understanding the early growth phase of aerosol particles in the nanometer range—and thus their survival probability. The results underscore the need for further studies that explicitly consider particle-size effects and multiphase processes in order to better understand the role of organic substances in atmospheric new particle formation.

#### ACKNOWLEDGMENTS

The study was supported through the German Research Foundation (DFG) Reinhart Koselleck-Project HO 1748/19-1 and the Max Planck Graduate Center Mainz.



## 4 Size-Dependent Ozonolysis of Ascorbic Acid Aerosol Particles

### 4.1 Introduction

Chemical reactions in nanometer-sized particles proceed differently from reactions in the gas phase and often also differently from reactions in macroscopic liquids or solids. This divergence stems from microphysical effects, whose significance rises as particle size decreases. For instance, the increase in surface-to-volume ratios enhances the apparent rate coefficients of heterogeneous reactions in smaller particles. This is because gas-phase reactants encounter a larger fraction of particle-bound reaction partners more rapidly (Zeng et al., 2025). Additionally, surface curvature increases as particle diameter decreases. The resulting change in intermolecular interaction has been shown to shift the chemical potential of molecules at the interface, thereby increasing their reactivity (Murzin, 2009; Fu et al., 2014).

Research indicates that smaller aerosol particles have higher viscosities and tend to remain in a liquid mixed phase, while larger particles are more prone to phase separation (Virtanen et al., 2011; Cheng et al., 2015; Tumminello et al., 2024). These trends may originate from elevated Laplace pressure within small particles, resulting from high curvature and the associated surface tension (Riva et al., 2021; Petters, 2022; Dubois et al., 2024). Increased internal pressure favors reactions with negative reaction and activation volumes, thereby accelerating and shifting the equilibrium to the products in bond-forming reactions (e.g., oligomerization) and slowing unimolecular decay reactions. Such pressure-related effects were previously observed in Chapter 3 for the ozonolysis of NDA.

In the model system investigated here, the reaction of ascorbic acid (AA) with ozone, the reactant AA is directly detectable by  $\text{NO}_3\text{-CI-Orbitrap}$ . This enables comparison of relative product signals across particle sizes not only as a function of reaction time but also as a function of the extent of the reaction, because reactant-normalized product yields can be tracked continuously. As a result, product distributions can be evaluated with reduced confounding from particle-size-dependent kinetics, like the faster ozone uptake in smaller particles, because of their higher surface area.

The course of AA ozonolysis is pH-dependent, with increased ozonolysis at low pH and more general oxidation at high pH (Enami et al., 2008; Chang et al., 2021). A further size-dependent factor identified in micro- and nanodroplets is the modification of pH and its spatial distribution within particles. For  $(\text{NH}_4)_2\text{SO}_4\text{-H}_2\text{SO}_4$  particles, the bulk pH level declines with

decreasing particle diameter (Craig et al., 2018). Furthermore, microdroplets have been shown to sustain a radial pH gradient, with lower pH at the surface and higher pH in the core (Wei et al., 2018; Hua et al., 2015). Additionally, the magnitude of this gradient increases as particle radius decreases (Gong et al., 2023).

Taken together, Laplace-pressure-induced changes in thermodynamics and kinetics, and size-dependent pH fields motivate the central hypothesis of this chapter: if these microphysical effects operate in the AA–ozone system, the reaction progress and product distributions should display a clear dependence on particle size.

## 4.2 Materials and Methods

### 4.2.1 Aerosol Generation

Refer to Figure 3.1 for a schematic of the experimental setup. A solution consisting of a 9:1 (v/v) mixture of deionized water (18.2 M $\Omega$  cm) and isopropanol (>98%, Fisher Chemical) containing 360 mg L<sup>-1</sup> ascorbic acid (AA, analytical reagent grade, Fisher Chemical) and 40 mg L<sup>-1</sup> 1,2,3,4- butanetetracarboxylic acid (BTA, >99 %, Fluka) was atomized with a Model 3076 Constant Output Atomizer (TSI Incorporated, Shoreview, MN). The solution was supplied to the atomizer at 250  $\mu$ L min<sup>-1</sup> using a syringe pump, and atomization was performed with purified air at 2 L min<sup>-1</sup>.

To achieve dry conditions (~30% RH), the aerosol was directed directly through two silica denuders following atomization. For experiments conducted under humid conditions, no drying was applied, and an RH of approximately ~80% was obtained. Under both RH conditions, the polydisperse aerosol was size-selected with an Electrostatic Classifier (Model 3082) equipped with an Advanced Aerosol Neutralizer (Model 3088) and a nano differential mobility analyzer (nano-DMA; all TSI Incorporated). Four mobility diameters were investigated: 30, 50, 80, and 110 nm. The sheath flows of the classifier were 10, 10, 8, and 6 L min<sup>-1</sup>, respectively. Lower sheath flows were required for 80 and 110 nm particles because these diameters are not separable in the nano-DMA at higher sheath flows.

The concentration of particles was adjusted by using a HEPA filter in parallel with a bypass valve. The fraction of filtered aerosol was varied via the valve. The resulting particle number concentration was then measured using a water-based Condensation Particle Counter (CPC, Model 3789, TSI Incorporated) operated in the 2 nm mode. Of the CPC's 0.6 L min<sup>-1</sup> flow, 0.1 L min<sup>-1</sup> was sampled from the aerosol stream, and the remaining 0.5 L min<sup>-1</sup> was supplied as purified air.

## 4.2.2 Flow Tube Experiments

The generated aerosol ( $1.9 \text{ L min}^{-1}$ ) was mixed with ozone-containing air ( $0.1 \text{ L min}^{-1}$ ). Ozone was produced using a modified ozone monitor (Dasibi 1008-RS) and subsequently diluted to the target concentration. The ozone levels achieved were determined using separate measurements. These measurements were taken with a Dual Beam Ozone Monitor (Model 205, 2B Technologies). The reaction mixture was then either analyzed directly or routed, under darkened conditions, through four flow tubes of different volumes (see Table 3.1). The dimensions of the flow tubes were based on the methods outlined by Huang et al. (2017), with the objective of enhancing the efficiency of particle-gas mixing and reducing wall losses. For each particle size, data were collected over a period of seven minutes at each but the highest residence time. Here, the collection of data occurred over a period of 10 minutes, as a longer equilibration time was deemed necessary.

## 4.2.3 Aerosol Measurement

Following the reaction in the flow tubes, the aerosol was passed through an activated-carbon denuder to remove gas-phase species. Then, it was introduced to the aerosol inlet (described in Chapter 2) for thermal evaporation. The evaporator temperature was set at  $285 \text{ }^\circ\text{C}$ , and the cooling-gas flow was maintained at  $8 \text{ L min}^{-1}$ . The analytes were detected using a  $\text{NO}_3\text{-CI-Orbitrap}$  (Riva et al., 2019a). Instrument parameters are listed in Table 2.1. The analyzed  $m/z$  range was between 120 and 600. While this approach does not detect the  $\text{NO}_3^-$  reagent ion, the enhanced sensitivity resulting from the higher analyte ion fraction in the C-trap of the Orbitrap is consistent with subsequent studies (Yuan et al., 2025). Signal variability can still be characterized using the  $\text{HN}_2\text{O}_6^-$  reagent ion signal. In the present experiments, correction with a reagent ion was not required because BTA served as an internal standard. The BTA signal was adjusted using the HEPA-filter bypass valve so that the same signal intensity was obtained for all investigated particle sizes. This ensured that mass concentrations remained similar and the ratio to ozone was comparable.

## 4.2.4 Data Evaluation

Mass traces were extracted using Orbitool, a software developed for the analysis of online Orbitrap data (Cai et al., 2021). To compensate for temporal fluctuations in particle concentration within a given size class, as well as for overall concentration differences across sizes, analyte mass traces were normalized to the BTA internal-standard mass trace to yield comparable relative signals.

## 4.3 Results and Discussion

### 4.3.1 Kinetics of the Heterogeneous Reaction

Across all experiments, the variation in relative humidity is below 5% and internal-standard signal variation between different particle diameters is below 10% (see Table 4.1). The investigated particles should therefore exhibit similar water contents, and the detected ions should display similar sensitivities in the Orbitrap (Riva et al., 2020b). The particle-volume concentration decreases from large to small diameters. Particle number concentration is measured directly downstream of the size selection. Smaller particles experience stronger wall losses in the flow tubes and the evaporator due to their higher diffusivity (see Chapter 2). This necessitates higher initial number concentrations to achieve comparable signal intensities in the CI-Orbitrap.

Table 4.1: Experimental conditions for the reaction of aqueous ascorbic acid aerosol particles with ozone. In each experiment, particles with diameters of 30, 50, 80, and 110 nm were examined at the residence times listed in Table 3.1. BTA was used as internal standard in the nebulized solution.

Experiment	[O <sub>3</sub> ] (ppm)	Particle diameter	RH (%)	Particle-volume concentration (μm <sup>3</sup> · cm <sup>-3</sup> )	BTA signal
1	1	110	26-28	0.58 ± 0.09	0.27 ± 0.02
		80	29	0.79 ± 0.08	0.30 ± 0.03
		50	30	0.98 ± 0.08	0.27 ± 0.01
		30	31	1.17 ± 0.07	0.29 ± 0.01
2	1	110	75-77	1.07 ± 0.12	0.41 ± 0.02
		80	77	1.22 ± 0.11	0.40 ± 0.01
		50	76-77	1.55 ± 0.15	0.40 ± 0.01
		30	77	2.10 ± 0.10	0.41 ± 0.02
3	10	110	80-81	1.29 ± 0.22	0.54 ± 0.02
		80	79-80	1.30 ± 0.19	0.53 ± 0.02
		50	77-79	1.62 ± 0.17	0.57 ± 0.03
		30	77	1.79 ± 0.16	0.58 ± 0.03

In the following figures, in addition to the data points at residence times determined by the different flow-tube volumes, a value at an effective reaction time of 0 s is shown. The “0 s” point corresponds to the signal after 1.3 s residence time at 0 ppm O<sub>3</sub>, because no particle-phase reaction is expected in the absence of ozone. To confirm this, signals after 106.8 s residence time without ozone were also examined. No significant changes in the detected ions were observed at different residence times in the absence of ozone, supporting the assumption that the observed reactant decay and product formation arise solely from reaction with ozone (see Appendix Figure 8.16).

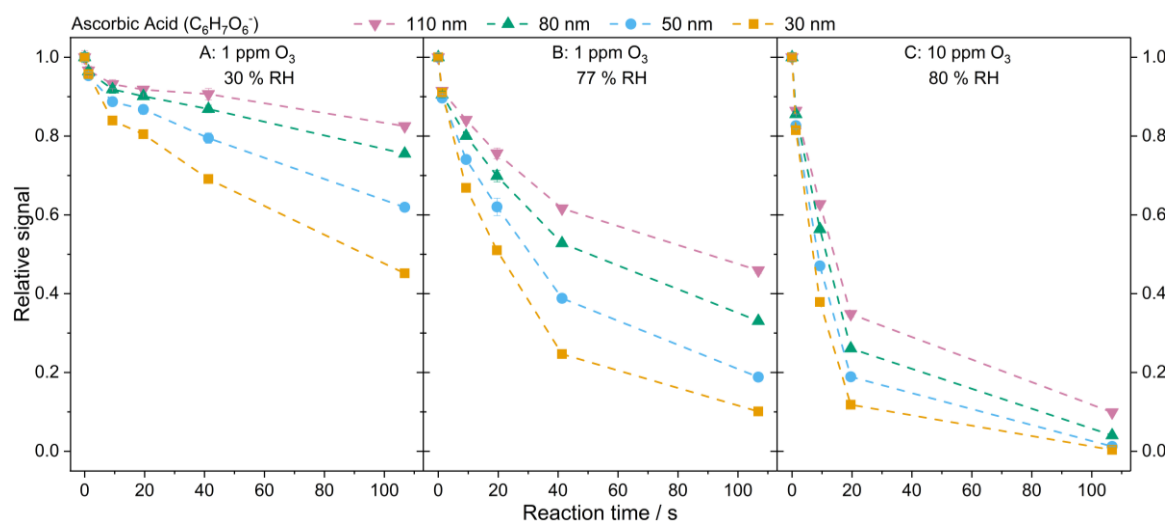


Figure 4.1: Normalized decay of the AA signal during the reaction with ozone as a function of residence time at 1 ppm O<sub>3</sub> and 30% RH (A), 1 ppm O<sub>3</sub> and 77% RH (B) and 10 ppm O<sub>3</sub> and 80% RH (C). Particle mobility diameters were: 110 nm (pink), 80 nm (green), 50 nm (blue) and 30 nm (yellow).

Figure 4.1 shows the decay of ascorbic acid (AA) as a function of reaction time for the different particle diameters at the investigated relative humidities and ozone concentrations. For this, the relative, normalized intensity of  $m/z$  175.025 (C<sub>6</sub>H<sub>7</sub>O<sub>6</sub><sup>-</sup>) after passage through the flow tubes is plotted. A dependence on ozone concentration is observed, as expected. At 1 ppm O<sub>3</sub>, only ~50% of ascorbic acid is consumed after 20 s (Figure 4.1B), whereas at 10 ppm O<sub>3</sub> the AA signal is already reduced to ~10% of its initial intensity (Figure 4.1C), indicating near-complete decay. However, the decay rate is governed by more than ozone concentration alone; particle size also plays a significant role. The decrease in the AA signal proceeds more slowly for larger particle diameters. Given that this is a heterogeneous reaction in which ozone must first diffuse from the gas phase into the particle, it is expected that ozone will react more rapidly with the smaller 30 nm particles due to their larger surface-to-volume ratio.

Additionally, a strong correlation with relative humidity is evident. The reaction at high RH progresses at a significantly faster rate than at 30% RH. This finding aligns with the significant impact of RH on the phase state of aerosol particles containing hygroscopic solutes (Zhao et al., 2019). It has been determined that both the self-diffusion of particle-phase molecules and the diffusion of ozone within the particle are strongly affected. According to the calculations by Berkemeier et al. (2016), the self-diffusion coefficient of shikimic acid increased from  $10^{-18} \text{ cm}^2 \text{ s}^{-1}$  at <30 % RH to  $10^{-7} \text{ cm}^2 \text{ s}^{-1}$  at >90 % RH. The study also revealed an increase in the diffusion coefficient of ozone, from  $10^{-12} \text{ cm}^2 \text{ s}^{-1}$  to  $10^{-6} \text{ cm}^2 \text{ s}^{-1}$ . It is highly probable that the particle properties in the present system are influenced by RH in a similar manner, which would account for the observed kinetic differences between dry and humid particles.

Under humid conditions, AA exhibits a clear exponential decay, consistent with an apparent bimolecular reaction. Conversely, the decay at low RH follows a nearly linear trend. In dry conditions, diffusion is likely the rate-limiting step due to the inhibition of ozone transport within the particle.

### 4.3.2 Reaction Mechanism

AA (vitamin C) functions as a radical scavenger and antioxidant in physiological systems and in food chemistry because its electron-rich endiol structure reacts efficiently with reactive oxygen species. The reactive species in this oxidation is not neutral AA, but its deprotonated form, ascorbate ( $A^-$ ) (see Figure 4.2).  $A^-$  reacts with oxidants via a sequence of single-electron-transfer steps and proton loss to form dehydroascorbic acid (DHA) (Njus et al., 2020). In an aqueous solution, DHA is in equilibrium with a hydrated bicyclic hemiacetal form (aqDHA). Njus et al. (2020) also proposed that aqDHA can form directly via disproportionation of two monodehydroascorbate radicals. This is due to the reaction of the ascorbate radical anion with another radical being thermodynamically favored over reaction with a closed-shell oxidant. This disproportionation is thought to proceed via a dimeric intermediate with a molecular formula of  $C_{12}H_{14}O_{12}$ .

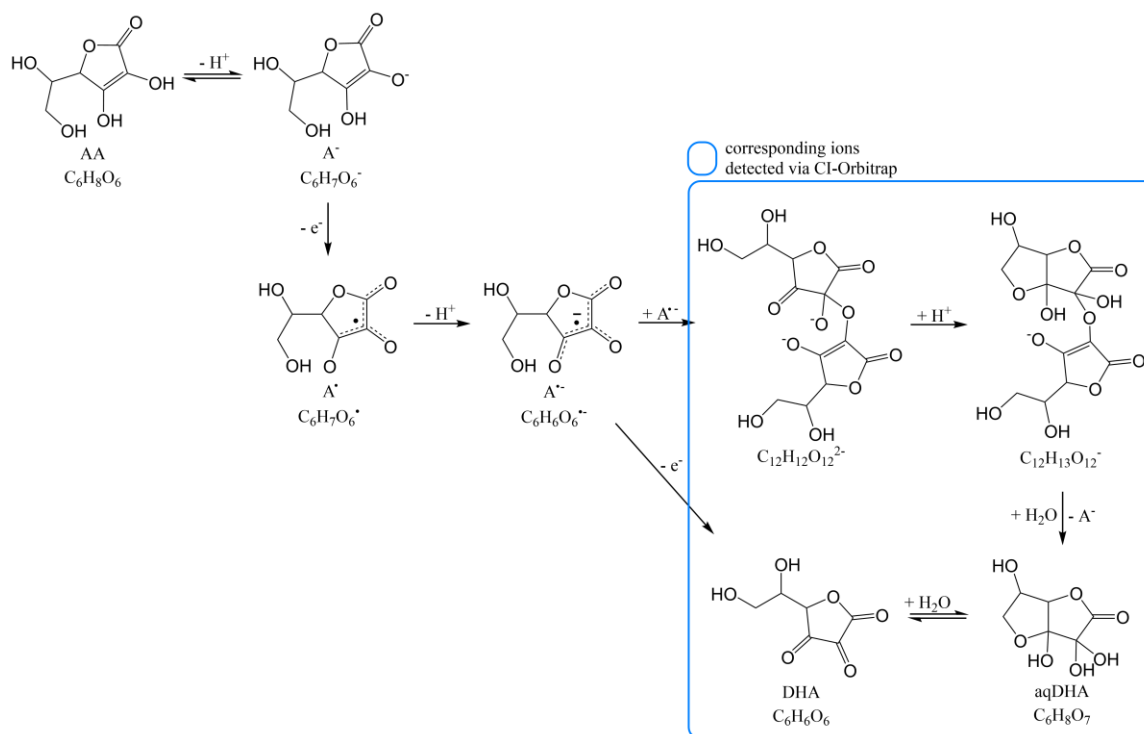


Figure 4.2: Reaction scheme of the oxidative pathway of AA reacting with ozone. The lower pathway corresponds to the standard mechanism reported in the literature, while the upper pathway proceeds via the dimer proposed by Njus et al. (2020).

When ozone is used as oxidant, a second pathway becomes possible. This pathway is formed by the 1,3-dipolar cycloaddition of ozone to the double bond of the endiol motif in AA. As for the ozonolysis of other unsaturated organic compounds, this reaction is expected to follow the Criegee mechanism (Criegee, 1975; Enami et al., 2008). To date, only a limited number of ozonolysis products of AA have been identified. As illustrated in Figure 4.3, an initial primary ozonide (POZ) forms, which then yields a short-lived stabilized Criegee intermediate (SCI). According to Enami et al. (2008), the SCI either decomposes to threonic acid ( $C_4H_8O_5$ , THR) or rearranges to a secondary ozonide (SOZ). In the current literature, there have been no reports of additional ozonolysis products. This is not surprising, since many plausible SCI reaction channels for AA would produce unstable species. In the present experiments, no ions consistent with the composition  $C_6H_8O_9$  that could be attributed to the POZ or SOZ were detected. Enami et al. (2008) observed the ion assigned to the SOZ only for AA particles produced by electrospray and subsequently exposed to ozone in the transfer region of the mass spectrometer (reaction time in millisecond scale). For atomized particles, in which ascorbic-acid-containing and ozone-containing aqueous solutions were combined shortly before the electrospray (4 s), no SOZ signal was observed. These highly oxidized species are likely to be so unstable that they rapidly decompose into more stable products, such as THR.

The thermal energy in the evaporator used in this study will likely further accelerate their decomposition.

Additionally, previously unreported ions consistent with AA ozonolysis products were observed. The species with elemental composition  $C_6H_8O_8$  may be a diacid formed by stabilization of the SCI by  $H_2O$  followed by loss of  $H_2O_2$  (Zhao et al., 2019). MS/MS measurements of this compound (see Appendix Figure 8.20) show fragmentation to THR, indicating that it is very likely an intermediate in the SCI decay. This finding is consistent with the nearly identical temporal evolution of  $C_6H_8O_8$  and THR (see Figure 4.6 and Appendix Figure 8.19). In addition to intermolecular stabilization of the SCI by  $H_2O$ , intramolecular stabilization by one of the hydroxyl groups of the AA backbone is also a possibility. This could account for the detected species with composition  $C_6H_6O_7$ .

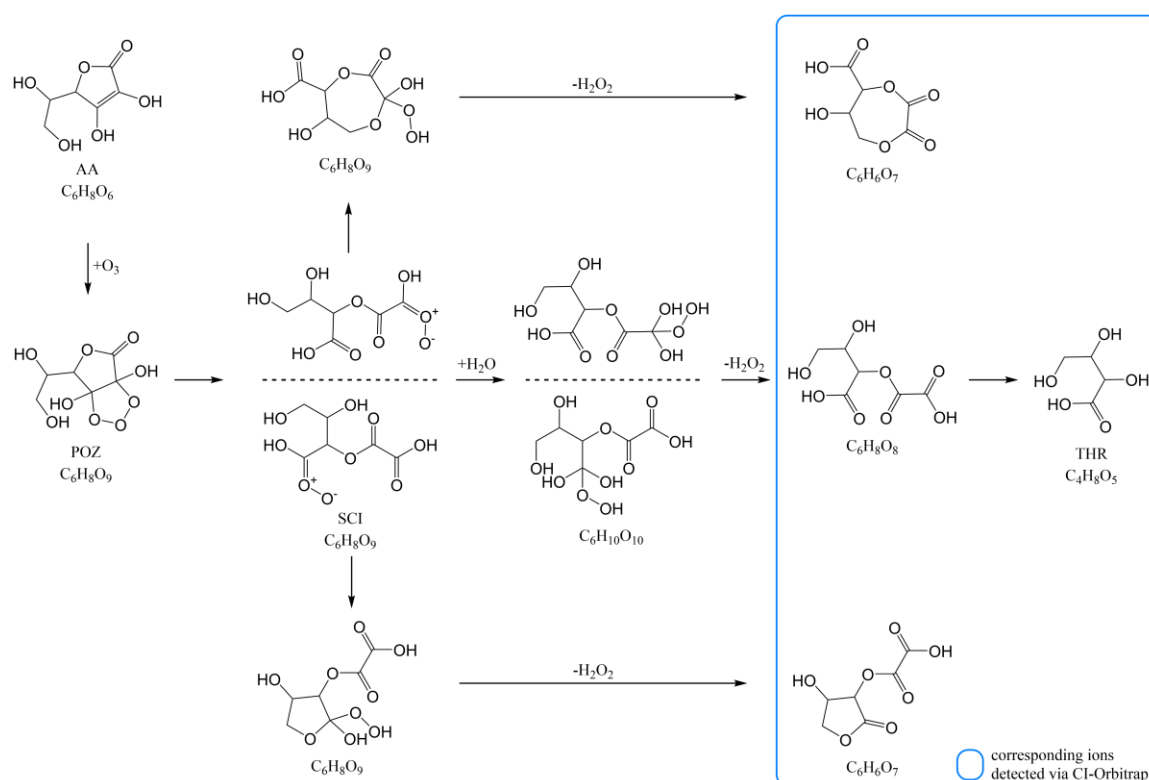


Figure 4.3: Proposed reaction scheme for the ozonolysis pathway of AA reacting with ozone and the subsequent reactions of the SCI to form first generation oxidation products. The structures shown are based on established mechanisms.

### 4.3.3 Equilibrium between DHA and Cyclic aqDHA

Thermodynamically, the equilibrium between DHA and aqDHA lies on the side of the hydrated cyclic aqDHA (Parsons and Fry, 2012; Dewhirst and Fry, 2018). It is therefore anticipated that DHA will convert to aqDHA over time. Figure 4.4 shows the fraction of DHA relative to the sum of DHA and aqDHA as a function of the fraction of reacted AA (see Equation 4.1).

$$1 - \frac{[\text{AA}]}{[\text{AA}]_0} \quad 4.1$$

By expressing the x-axis as reaction progress rather than residence time in the following figures, the analysis becomes independent of surface-area dependent ozone diffusion, since signals are compared at equal extents of reaction.

A consistently faster conversion of DHA into aqDHA is observed in smaller particles. The formation of aqDHA is a bimolecular reaction with  $\text{H}_2\text{O}$ . As already found in chapter 3, this type of reaction appears to be accelerated in smaller particles. This can be explained by the higher internal particle pressure and the associated increase in collision frequency between molecules.

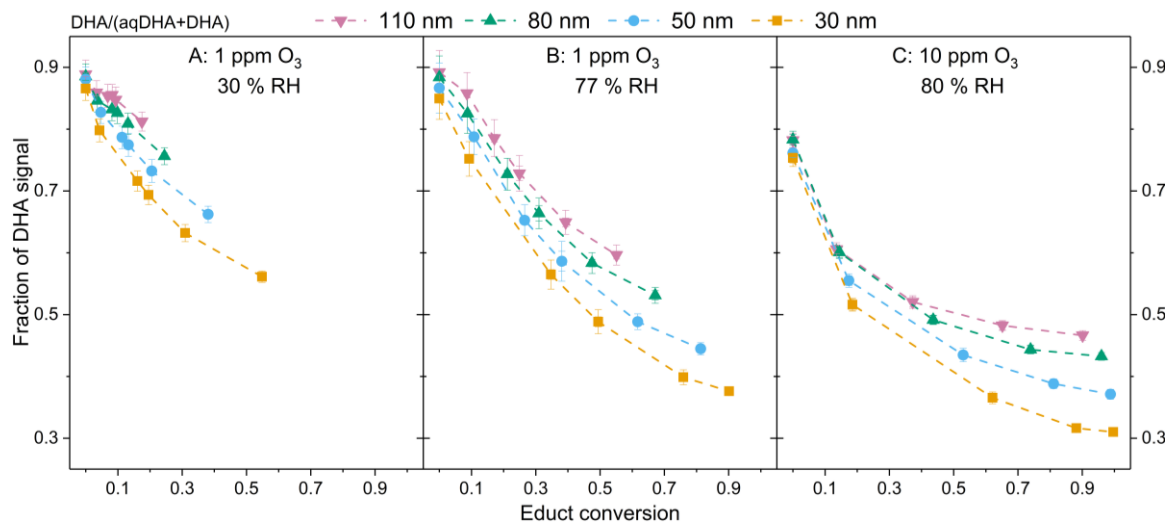


Figure 4.4: Evolution of the DHA fraction relative to the sum of DHA and aqDHA signals as a function of AA consumption at 1 ppm O<sub>3</sub> and 30% RH (A), 1 ppm O<sub>3</sub> and 77% RH (B) and 10 ppm O<sub>3</sub> and 80% RH (C). Particle mobility diameters were: 110 nm (pink), 80 nm (green), 50 nm (blue) and 30 nm (yellow).

As expected, at 30% RH, the DHA-to-aqDHA conversion is slower, because the water content of the particles is supposed to be lower. It is noteworthy that ozone concentration also appears to influence the approach to equilibrium. At a concentration of 10 ppm of ozone, the formation of aqDHA is more advanced at the same level of reactant conversion. According to Njus et al. (2020) the process of forming aqDHA may also occur directly from the

disproportionation of two ascorbate radical anions, thereby bypassing DHA as an intermediate step (Figure 4.2). The rate of this reaction depends on the concentration of the radical anion, which will be higher at elevated ozone concentrations due to the faster consumption of AA, which could explain the further dependence on the ozone concentration.

The  $m/z$  of the dimer that should form during this disproportionation reaction was observed in the experiments (see Figure 4.5). Under humid conditions, this signal displays a clear particle-size dependence, with higher dimer signals in smaller particles. This process could therefore also contribute to the faster establishment of the DHA:aqDHA equilibrium in the smaller particles. At high levels of reactant conversion the dimer signal experiences a decrease, likely due to the absence of new dimer formation and the predominance of its decay to the disproportionation products AA and aqDHA (Figure 4.2). The dimer signal intensity is higher at 1 ppm ozone than at 10 ppm under humid conditions, indicating that the dimer decay is also accelerated at higher ozone concentrations, which is in line with the faster aqDHA production at high ozone levels.

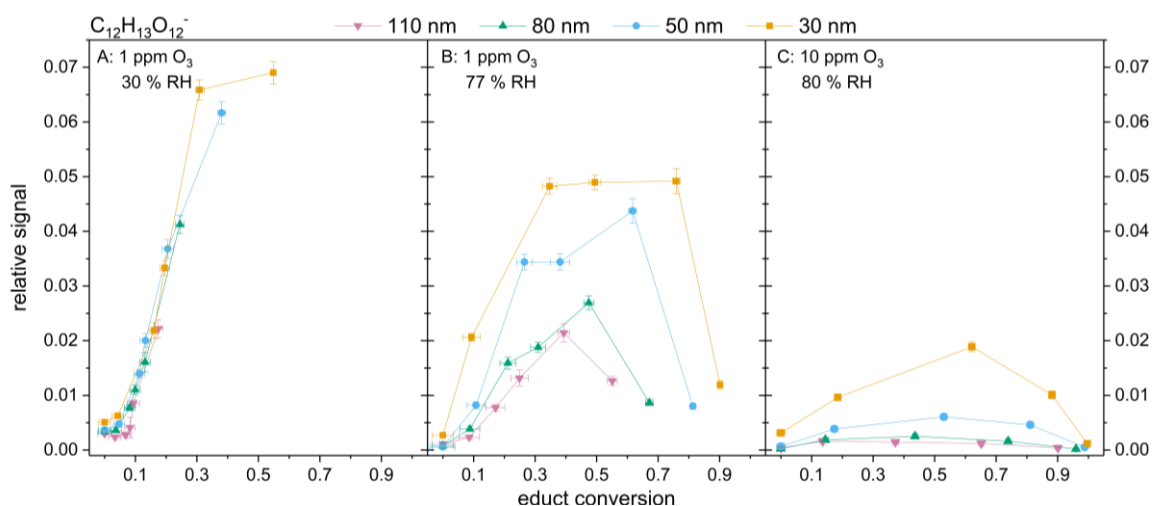


Figure 4.5: Evolution of the signal of the intermediate dimer ( $C_{12}H_{14}O_{12}$ ) proposed by Njus et al. during the oxidation of AA particles, shown as a function of AA consumption at 1 ppm  $O_3$  and 30% RH (A), 1 ppm  $O_3$  and 77% RH (B) and 10 ppm  $O_3$  and 80% RH (C). Particle mobility diameters were: 110 nm (pink), 80 nm (green), 50 nm (blue) and 30 nm (yellow).

Under dry conditions, there is neither a noticeable size dependence nor a reduction in the dimer signal. The absence of a particle-size effect may be attributed to restricted diffusion in dry particles, which hinders an increase in effective collision frequency despite the presumed higher internal pressure in smaller particles. The dimer signal exhibits a higher magnitude at low RH compared to high RH levels. This is likely related to the absence of a detectable decay at higher conversions; water is required for dimer degradation, and its concentration should be lower in the drier particles, thereby slowing decomposition.

#### 4.3.4 Size-Dependent Reaction Pathways

The ozonolysis products demonstrate a comparable reliance on RH as the dimer in Figure 4.5. In dry conditions, the formation of  $C_6H_6O_7$  and  $C_6H_8O_8$  is essentially independent of particle size, whereas under humid conditions higher product signals are observed for smaller particles (see Figure 4.6 and Figure 4.7). In contrast to the oxidation, the magnitude of this effect appears to correlate with ozone concentration, as the size-dependent differences are more pronounced at 10 ppm ozone. However, this does not necessarily imply a direct dependence on RH and ozone concentration alone. At low levels of reactant conversion, the signal evolution is largely size-independent. The observed size dependence may therefore arise because the corresponding reaction channels proceed faster, or are less hindered, at high reactant conversion in small particles than in large ones.

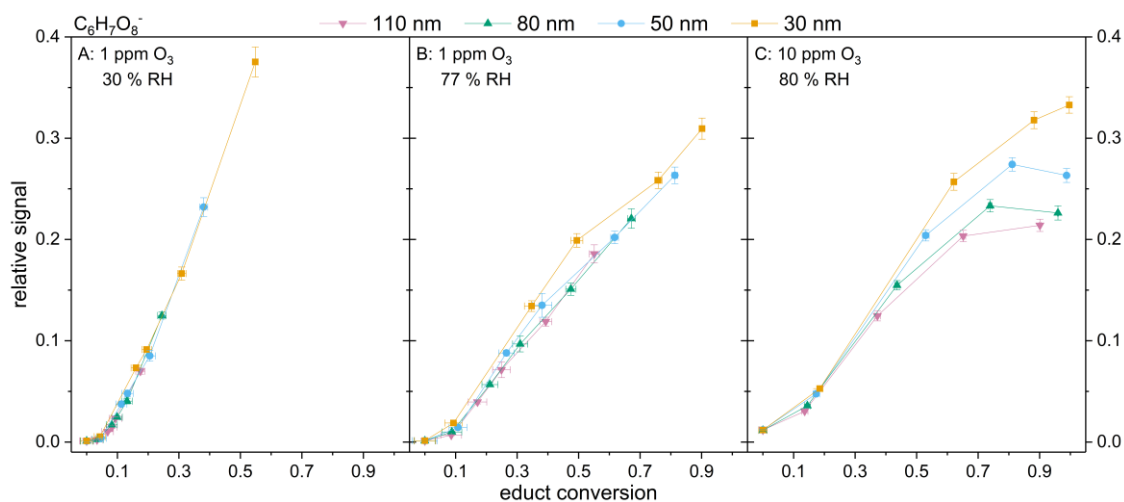


Figure 4.6: Evolution of the relative signal of the product with elemental composition  $C_6H_8O_8$  formed in the reaction of AA particles with ozone as a function of educt conversion at 1 ppm  $O_3$  and 30% RH (A), 1 ppm  $O_3$  and 77% RH (B) and 10 ppm  $O_3$  and 80% RH (C). Particle mobility diameters were: 110 nm (pink), 80 nm (green), 50 nm (blue) and 30 nm (yellow).

In dry conditions, more ozonolysis products are formed at the same reactant conversion compared to under humid conditions. This can be rationalized by considering that the reactive species in the oxidation pathway is the deprotonated ascorbate anion ( $A^-$ ). This species is less efficiently formed at lower water content due to reduced dissociation. In humid conditions, the ozonolysis products in small particles exhibit higher concentrations at the same overall conversion, suggesting that the relative contribution of ozonolysis compared to oxidation should be higher in small particles than in large ones. This conclusion cannot be further supported by the behavior of the oxidation products, because DHA and aqDHA display opposite particle-size dependences (see Appendix Figure 8.21). Furthermore, ionization efficiencies in chemical ionization mass spectrometry can vary significantly, making it challenging to make reliable statements about the impact of particle size on the yield of total

oxidation products (Lopez-Hilfiker et al., 2016; Gao et al., 2025). In contrast, all ozonolysis products are enhanced in smaller particles, so the conclusion that ozonolysis is favored in small particles is robust. By implication, oxidation is likely comparatively suppressed in smaller particles.

Analogous to the difference in ozonolysis-product formation between low and high RH, the observed size-dependent differences may also be linked to a particle-size-dependent degree of dissociation. Previous studies have shown that both effective acid and base strength of aerosol components increase as particle diameter decreases (Wei et al., 2018). Additionally, the pH difference between the particle surface and core increases with decreasing particle size, with the surface being more acidic than the core (Gong et al., 2023). As demonstrated by Enami et al. (2008), the fraction of ozonolysis products of the AA-ozone reaction increases at higher pH, where a larger fraction of ascorbic acid is present in the undissociated form.

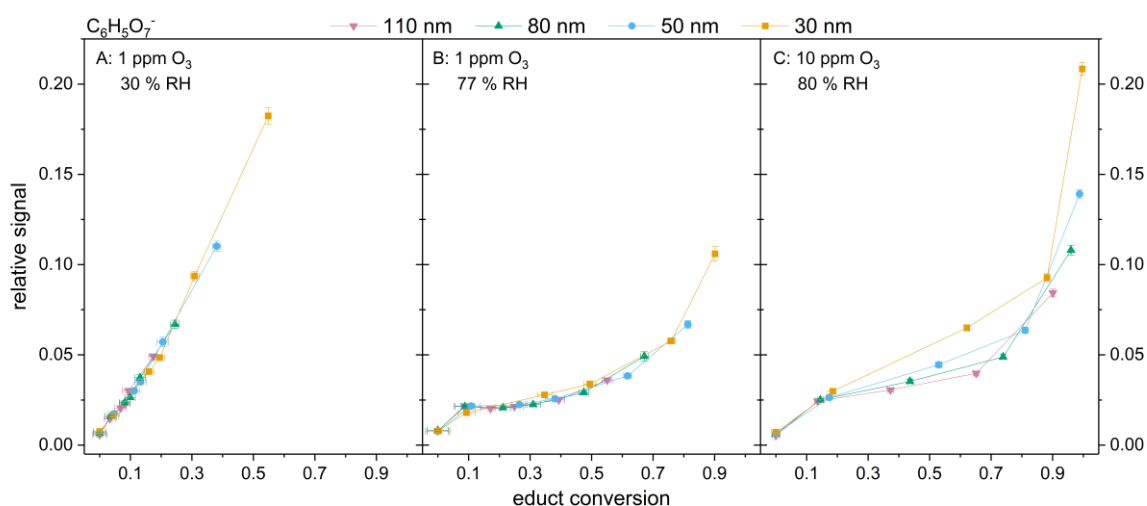


Figure 4.7: Evolution of the relative signals of the product with elemental composition  $C_6H_6O_7$  formed in the reaction of AA particles with ozone, as a function of educt conversion at 1 ppm  $O_3$  and 30% RH (A), 1 ppm  $O_3$  and 77% RH (B) and 10 ppm  $O_3$  and 80% RH (C). Particle mobility diameters were: 110 nm (pink), 80 nm (green), 50 nm (blue) and 30 nm (yellow).

Although  $C_6H_6O_7$  and  $C_6H_8O_8$  exhibit the same particle-size dependence, their temporal profiles differ substantially. The formation rate of  $C_6H_6O_7$  increases at high reactant conversion, while the formation rate of  $C_6H_8O_8$  decreases at later stages of the reaction. One plausible explanation for this phenomenon is that  $C_6H_8O_8$  forms via an intermolecular reaction with water, while  $C_6H_6O_7$  is produced by an intramolecular reaction. The shift in their relative importance at later reaction stages could indicate evolving particle properties. An increase in viscosity would favor intramolecular over intermolecular reactions, which could explain the relative enhancement of  $C_6H_6O_7$ . Such viscosity increases are frequently observed in secondary organic aerosol undergoing progressive oxidation and ozonolysis (Virtanen et al., 2010).

### 4.3.5 Size-Dependent Dimer Formation

In addition to the dimer formed in the disproportionation of the ascorbate radical anion, further dimers were identified as intermediates or products (see Figure 4.8). The species with compositions  $C_{12}H_{12}O_{12}$  and  $C_{12}H_{14}O_{14}$  are also formed in higher relative amounts in smaller particles. In contrast to the other reaction products, these dimers exhibit a pronounced size dependence even under dry conditions. It appears that both species are reaction intermediates because their signals decrease again at high reactant conversion and long reaction times. As outlined in chapter 3, these compounds may undergo fragmentation back to monomeric units or undergo further reactions to form more highly oxidized, less volatile compounds. At least partial formation of such more highly oxidized dimers is indicated by the behavior of  $C_{12}H_{14}O_{16}$ , a fourth dimer, which is observed only at 10 ppm ozone (Appendix Figure 8.22). This dimer, which has the highest oxygen amount among the detected dimers, shows no signal decay and a slower formation rate, which could be consistent with production from the less oxidized dimers.

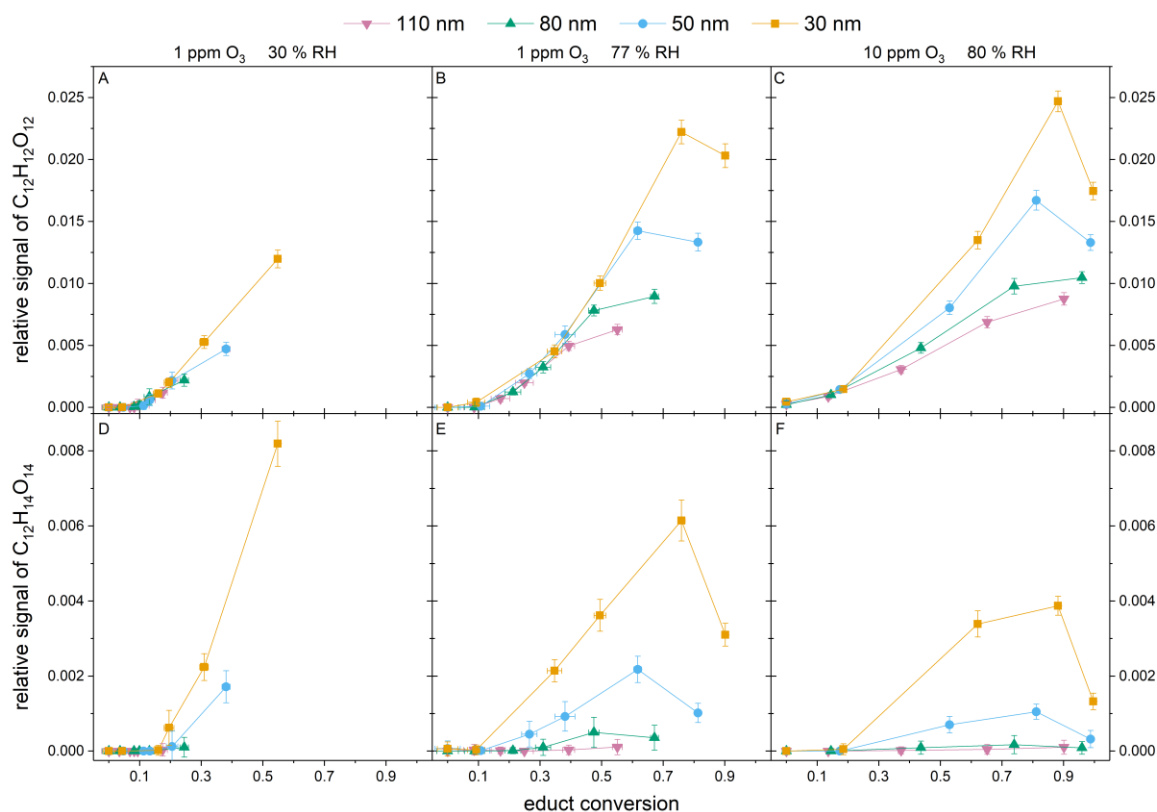


Figure 4.8: Evolution of the relative signals of the dimers  $C_{12}H_{12}O_{12}$  (A,B and C) and  $C_{12}H_{14}O_{14}$  (D,E and F) detected in the reaction of AA particles with ozone, as a function of educt conversion at 1 ppm  $O_3$  and 30% RH (A and D), 1 ppm  $O_3$  and 77% RH (B and E) and 10 ppm  $O_3$  and 80% RH (C and F). Particle mobility diameters were: 110 nm (pink), 80 nm (green), 50 nm (blue) and 30 nm (yellow).

## 4.4 Conclusion

In this study, the reaction of ascorbic acid with ozone was used to investigate particle-size-dependent effects on the reaction progress. In this context, two previously unreported ozonolysis products were observed for the first time. In addition, the dimer proposed by Njus et al. (2020), which provides a pathway for direct formation of aqDHA from ascorbate radical anions in the oxidation sequence, was detected.

As anticipated, the heterogeneous reaction exhibited accelerated rates in smaller particles, as expected from their higher surface-to-volume ratio. Additionally, clear size-dependent differences in product distributions were observed. Particles with diameters of 30 nm, 50 nm, 80 nm, and 110 nm consistently exhibited higher aqDHA fractions in the DHA/aqDHA equilibrium of the oxidation pathway in smaller particles. On the one hand, the bimolecular reaction with water leading to aqDHA may proceed more rapidly in smaller particles because of their higher Laplace pressure. On the other hand, direct formation of aqDHA from the ascorbate radical anion via the dimer may be favored for the same reason. This dimer likewise shows higher intensities in smaller particles.

The relative contributions of oxidation and ozonolysis products also appear to depend on particle size, but only under humid conditions; no particle-size effects were observed under dry conditions, probably because of hindered dissociation of AA. One plausible explanation for this phenomenon is the particle-size dependency of the pH value, which consequently leads to size-dependent dissociation of ascorbic acid within the aqueous particles. Further experimentation, including systematic adjustments to the pH level through controlled addition of acids and bases to the precursor solution, could provide more insights into this effect. Furthermore, extending these measurements to other pH-dependent reaction systems that can be realized in nanometer-sized particles would allow us to determine whether the observed behavior represents a more general phenomenon.

# 5 Size-Dependent Borate Cluster Formation in Tartrate Aerosol Particles

## 5.1 Introduction

Nanoparticles and microdroplets provide unique reaction environments. There, numerous transformations proceed faster than in bulk solutions, and some occur that are otherwise inaccessible in bulk (Petters, 2022; Ruiz-López and Martins-Costa, 2022). For instance, metal-organic frameworks crystallize in under one hour at room temperature when the solution is atomized into microdroplets, whereas bulk synthesis typically requires elevated temperatures and longer reaction times (Song et al., 2025). Accelerations of up to five orders of magnitude compared to the bulk have also been reported for certain carbonyl reactions (Yan et al., 2016; Zhang et al., 2021).

The origins of these rate enhancements remain under active investigation. Several microphysical effects present in small particles may contribute. One straightforward explanation is enrichment of reactants within particles relative to the bulk solution (Chen and Williams, 2023; Wilson et al., 2020). This is due to the fact that the solvent evaporates into the gas phase due to the much higher surface area of the particles. Another is the curvature-induced changes in intermolecular interactions that shift the chemical potential at the particle interface and thereby increase reactivity (Fu et al., 2014; Murzin, 2009). A further consequence of high curvature is the elevated Laplace pressure arising from surface tension (Riva et al., 2021; Petters, 2022; Dubois et al., 2024), which is expected to accelerate reactions with negative reaction volumes and/or negative activation volumes (van Eldik et al., 1989).

Aerosol particles may also have functioned as prebiotic “floating reactors” in the nascent atmosphere by concentrating relevant molecules and catalyzing intra-particle and heterogeneous reactions (Trainer, 2013; Sebree et al., 2018; Ruiz-Bermejo et al., 2007). In the classic Miller-Urey experiment, which sought to simulate the primitive atmosphere, subsequent studies demonstrated that substantially fewer organic products form when the apparatus is constructed from PTFE rather than borosilicate glass (MILLER, 1953; Criado-Reyes et al., 2021). Leached silicon, boron, or alkali metals from glass may therefore have contributed to catalysis of organic chemistry under early atmospheric conditions.

Boron leaching is relevant to modern laboratory chemistry as well, because experiments are commonly conducted in borosilicate glassware. Adducts of analytes with boric acid leached from solvent glass bottles have been observed by LC-ESI-MS (Nagasathiya et al., 2014). The boron adducts coelute with the free analytes, suggesting that adduct formation occurs in the electrospray-generated microdroplets. Boric acid has been observed to form highly stable

complexes with  $\alpha$ -hydroxy acids and with diols/polyols, resulting in the formation of borate esters (Maseda et al., 2021; Qin et al., 2023). These reactions have particularly negative reaction volumes, reflecting both an increase in the total number of bonds and charge separation during ester formation (van Eldik et al., 1989). The resulting borate esters are typically several orders of magnitude more acidic than boric acid itself (Springsteen and Wang, 2002), implying that such species could serve as proton donors for acid-catalyzed reactions within nanometer-sized particles.

One factor often overlooked in nanoparticle and microdroplet chemistry is the explicit dependence on particle size. As the radius of the particles decreases, the surface curvature increases, thereby amplifying curvature-driven effects such as Laplace pressure. Consequently, pressure-sensitive reactions, such as the formation of borate esters from boric acid with tartaric acid, are expected to demonstrate a quantifiable dependence on particle size under conditions where Laplace pressure exerts its anticipated effect.

## 5.2 Materials and Methods

In this study, the generation and probing of size-selected, monodisperse tartaric acid aerosol particles with nanometer-scale diameters for the formation of boric acid/tartaric acid complexes following different reaction times was conducted using online nitrate chemical ionization Orbitrap mass spectrometry. The experimental setup is illustrated schematically in Figure 3.1.

### 5.2.1 Aerosol Generation

The precursor solution contained 360 mg L<sup>-1</sup> tartaric acid (99%, Sigma-Aldrich) and 40 mg L<sup>-1</sup> tricarballic acid (TA, 98%, Alfa Aesar) as an internal standard dissolved in a 9:1 (v/v) mixture of deionized water (18.2 M $\Omega$  cm) and isopropanol (> 98%, Fisher Chemical). The solution was delivered at a rate of 250  $\mu$ L min<sup>-1</sup> by a syringe pump to a Model 3076 Constant Output Atomizer (TSI Incorporated, Shoreview, MN), which atomized it with purified air at a rate of 2 L min<sup>-1</sup>.

For experiments conducted under dry conditions, the resulting aerosol was passed through two silica denuders, yielding approximately 30% relative humidity (RH). For experiments conducted under humid conditions, no drying was applied, and an RH of approximately 81% was obtained. The polydisperse aerosol was then size-selected with an Electrostatic Classifier (Model 3082) equipped with an Advanced Aerosol Neutralizer (Model 3088) and a nano differential mobility analyzer (nano-DMA; all TSI Incorporated). Four mobility diameters were selected: 30, 50, 80, and 110 nm. The sheath flows were 10, 10, 8, and 6 L min<sup>-1</sup>,

respectively. Lower sheath flows were required for 80 and 110 nm particles because these diameters are not separable in the nano-DMA at higher sheath flows.

The concentration of the monodisperse aerosol was adjusted by splitting the flow through two parallel PTFE lines, one containing a HEPA filter that removed all particles. The split ratio was modulated by a valve situated within the bypass line. The measurement of the resulting particle number concentration was conducted using a water-based Condensation Particle Counter (CPC, Model 3789, TSI Incorporated) operated in the 2 nm mode. For the purposes of this measurement, 0.1 L min<sup>-1</sup> of aerosol was diluted with 0.5 L min<sup>-1</sup> of purified air, the latter of which was used to match the CPC flow of 0.6 L min<sup>-1</sup>.

### 5.2.2 Flow Tube Experiments

The remaining aerosol stream (1.9 L min<sup>-1</sup>) was mixed with 0.1 L min<sup>-1</sup> purified air and either analyzed immediately or routed through one of four flow tubes. The flow-tube dimensions followed Huang et al. (2017) to promote efficient particle-gas mixing and to minimize wall losses. The volumes of the tubes and the corresponding residence times are listed in Table 3.1. The experiments were conducted under dark conditions. For each particle size, data were collected over a period of seven minutes at each but the highest residence time. Here, the collection of data occurred over a period of 10 minutes, as a longer equilibration time was deemed necessary.

### 5.2.3 Aerosol Measurement

Subsequent to exiting the reaction volume, the aerosol passed through an activated-carbon denuder to remove gas-phase species and was then directed to the aerosol inlet for thermal desorption (see Chapter 2.2.1 for a detailed description). The vaporizer temperature was set at 285 °C, and the cooling-gas flow was 8 L min<sup>-1</sup>. Vaporized analytes were detected with a Q Exactive Orbitrap mass spectrometer (Thermo Fisher Scientific) which was equipped with a nitrate chemical ionization source (NO<sub>3</sub><sup>-</sup>-CI-Orbitrap). The instrument settings are listed in Table 2.1. The analyzed mass range was from  $m/z$  120–600. Although this excludes direct detection of the NO<sub>3</sub><sup>-</sup> reagent ion, the reduced reagent-ion fraction in the C-trap increased sensitivity for product ions, consistent with the findings reported by Yuan et al. (2025). The signal stability could be monitored via the reagent-ion signal at  $m/z$  124.984 (HN<sub>2</sub>O<sub>6</sub><sup>-</sup>). In this study, reagent-ion correction was not necessary because TA functioned as an internal standard within the aerosol particles. The HEPA-bypass flow was adjusted to achieve comparable internal-standard signal intensities across particle sizes, thereby ensuring similar mass concentrations in the flow tubes.

## 5.2.4 Data Evaluation

Mass traces were extracted using Orbitool, a software designed for the analysis of online Orbitrap data (Cai et al., 2021). Product signals were identified based on their correlated temporal behavior relative to the internal standard. Compounds containing boron were additionally recognized by the characteristic boron isotopic pattern:  $^{10}\text{B} : ^{11}\text{B} = 19.9 : 80.1$  (see Appendix Figure 8.21). In order to compensate for temporal fluctuations in particle concentration and to enable comparison across particle sizes, analyte signals at each time point were normalized to the TA internal-standard signal to yield relative intensities (see Equation 5.1).

$$\text{relative signal} = \frac{\text{analyte signal}}{\text{TA signal}} \quad 5.1$$

## 5.3 Results and Discussion

### 5.3.1 Particle-Size-Dependent Complexation

Boric acid forms multinuclear complexes with diols and  $\alpha$ -hydroxy acids, including tartaric acid. The formation of these borate-tartrate complexes proceeds via a nucleophilic attack of a tartaric acid alcohol oxygen at the electron-deficient boron center of boric acid. This is followed by water elimination and coordination of the acid oxygen to boron to yield a five-membered ring (see Figure 5.1). This equilibrium is established rapidly; therefore, the tartaric acid solution is expected to have been at equilibrium with dissolved boric acid prior to atomization (Roy et al., 1957).

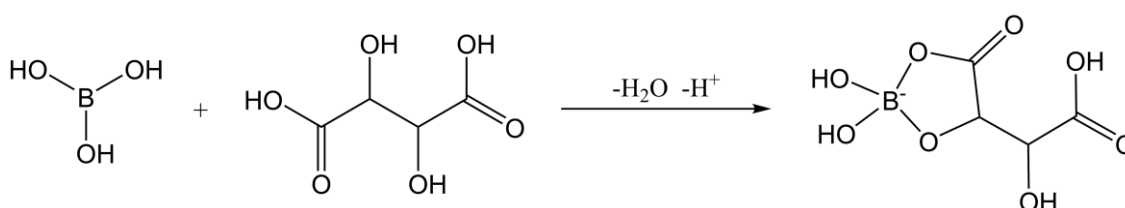


Figure 5.1: Reaction scheme for the formation of negatively charged borate-tartrate ester complexes. The pathway proceeds via nucleophilic attack of a tartaric-acid hydroxyl oxygen at the electron-deficient boron center, followed by elimination of water and coordination of a carboxylate oxygen to boron, yielding a tetrahedral complex.

As shown in Figure 5.2, the signals attributed to borate-tartrate complexes in the generated aerosol at 81% RH increase with residence time in the flow tubes. The transfer from bulk solution to aerosol evidently shifts the balance between free boric acid/tartaric acid and the complexed forms towards complexation. The rate of complex formation increases with decreasing particle radius. The shift of the equilibrium towards the complexed species is most pronounced for the smallest particles, with up to approximately threefold higher signals in 30 nm particles compared to 110 nm particles. The system thus displays a clear particle-size dependence of the complexation equilibrium.

Complexes can be stabilized at elevated pressure when the reaction exhibits a negative activation volume. The formation of tetrahedral borate esters has a particularly negative activation volume because conversion from trigonal boric acid entails both bond formation and charge separation (van Eldik et al., 1989). This trigonal-to-tetrahedral transition is accompanied by a substantial decrease in  $pK_a$  as borate esters are typically several orders of magnitude more acidic than boric acid (Springsteen and Wang, 2002). An increase in internal particle pressure with decreasing diameter, arising from Laplace pressure, could therefore account both for the enhancement of borate-tartrate signals relative to bulk and for the observed particle-size trends.

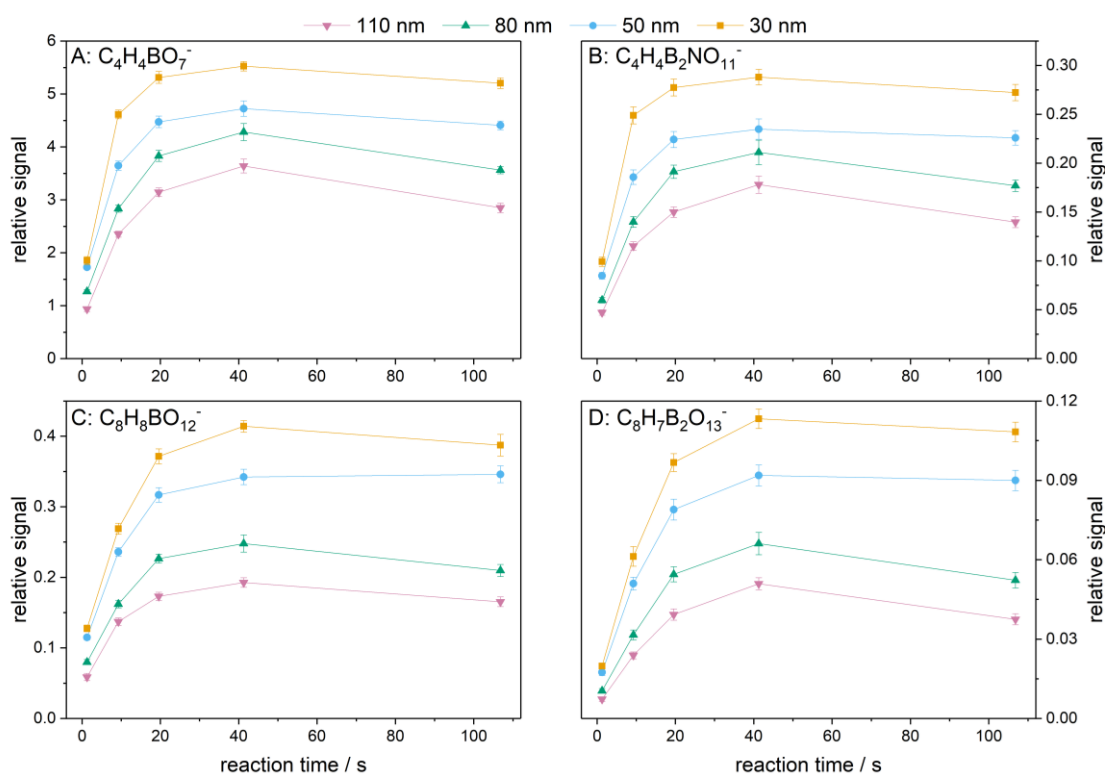


Figure 5.2: Mean relative signals of borate-tartrate ester complexes formed in aerosol particles as a function of residence time at 81% RH:  $C_4H_4BO_7^-$  (A),  $C_4H_4B_2NO_{11}^-$  (B),  $C_8H_8BO_{12}^-$  (C) and  $C_8H_7B_2O_{13}^-$  (D). Particle mobility diameters were: 110 nm (pink), 80 nm (green), 50 nm (blue) and 30 nm (yellow).

### 5.3.2 Particle-Size Dependent Stoichiometry Distribution

The complexes that are detected can be distinguished by their stoichiometries (Jiang et al., 2024), which consist of 1 or 2 boric acid units and 1 or 2 tartaric acid units (see Figure 5.3). While larger assemblies have been documented by Jiang et al. (2024), they were not observed in this particular study. Inspection of the temporal profiles indicates that higher-order complexes, with more boric acid and tartaric acid molecules, appear to form from the 1:1 complex (Figure 5.2A), since it exhibits the fastest signal growth and reaches equilibrium first. The incorporation of an additional boron unit appears to be a more rapid process in comparison to the incorporation of an additional tartaric acid unit. This observation can be attributed to the fact that the 1:2 and 2:2 complexes (Figure 5.2B+D) exhibit a growth rate that is less rapid in comparison to the 2:1 complex (Figure 5.2C).

Interestingly, the stoichiometries seem to demonstrate varying degrees of sensitivity to variations in particle size. Table 5.1 lists the signal ratios of the complexes detected between 30 nm particles and the larger particle sizes. The differences between the particle sizes increase with the number of constituent molecules, and the number of tartaric acid units appears to exert a larger influence than the number of boric-acid units. This behavior is consistent with a pressure effect: as complex size increases, more borate-ester bonds (each with negative reaction volume) are formed, yielding a more negative overall reaction volume and, consequently, a stronger dependence on pressure. Consequently, complex stabilities should exhibit heightened pressure sensitivity in conjunction with increasing stoichiometric size.

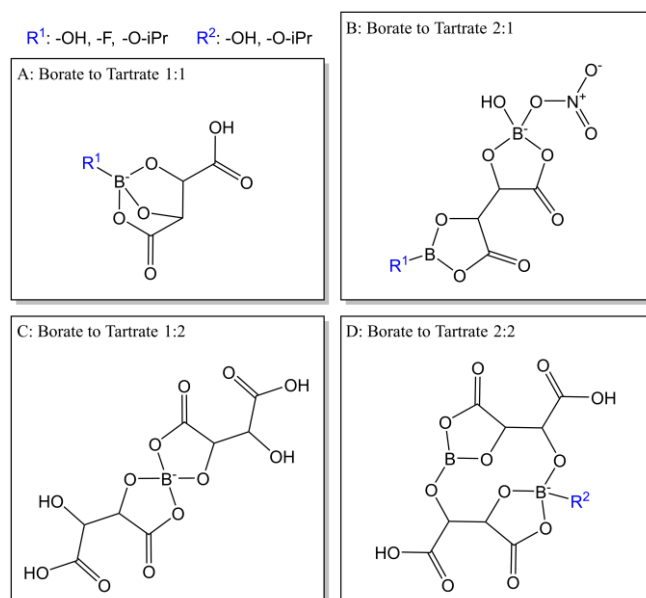


Figure 5.3: Proposed chemical structures of the detected borate–tartrate ester complexes, classified by stoichiometry (boric acid : tartaric acid): 1:1 (A), 2:1 (B), 1:2 (C), and 2:2 (D). Depending on stoichiometry, complexes may bear hydroxyl, fluoride, or isopropoxy substituents.

Table 5.1: Ratios of the relative signals of borate–tartrate ester complexes detected in 30 nm particles to those in 50, 80, and 110 nm particles after a residence time of 106.8 s at 81% RH. Complexes are grouped by stoichiometry.

Sum formula	stoichiometry (Borate : Tartrate)	Signal ratio (30 nm : 50 nm)	Signal ratio (30 nm : 80 nm)	Signal ratio (30 nm : 110 nm)
$C_4H_4BO_7^-$	1 : 1	$1.18 \pm 0.03$	$1.46 \pm 0.04$	$1.83 \pm 0.07$
$C_4H_3BFO_6^-$	1 : 1	$1.21 \pm 0.05$	$1.45 \pm 0.06$	$1.74 \pm 0.08$
$C_7H_{10}BO_7^-$	1 : 1	$1.18 \pm 0.04$	$1.55 \pm 0.05$	$1.92 \pm 0.09$
$C_4H_4B_2NO_{11}^-$	2 : 1	$1.21 \pm 0.05$	$1.54 \pm 0.07$	$1.95 \pm 0.10$
$C_4H_3B_2FNO_{10}^-$	2 : 1	$1.23 \pm 0.09$	$1.49 \pm 0.12$	$1.79 \pm 0.16$
$C_7H_{10}B_2NO_{11}^-$	2 : 1	$1.19 \pm 0.10$	$1.57 \pm 0.12$	$1.86 \pm 0.17$
$C_8H_8BO_{12}^-$	1 : 2	$1.12 \pm 0.06$	$1.85 \pm 0.11$	$2.34 \pm 0.14$
$C_8H_7B_2O_{13}^-$	2 : 2	$1.20 \pm 0.07$	$2.07 \pm 0.14$	$2.89 \pm 0.19$
$C_{11}H_{13}B_2O_{13}^-$	2 : 2	$1.20 \pm 0.14$	$2.14 \pm 0.25$	$2.86 \pm 0.4$

### 5.3.3 Source Attribution

In addition to borate-tartrate complexes with hydroxyl substituents at boron, complexes bearing fluoride and isopropoxy substituents were detected. Their temporal evolution and size dependence mirror those of the corresponding hydroxy-substituted complexes, but with lower overall intensity (see Appendix Figure 8.24 and Figure 8.25). The isopropoxy groups likely originate from the atomized solution, which involved the addition of isopropanol to facilitate aerosol generation. The source of fluoride is less clear given the use of Milli-Q water and LC-MS-grade solvents. Because boric acid was not added explicitly to atomized solution, its origin is also in question. Boron leaches from borosilicate glass and can form boric acid in solution (Nagasathiya et al., 2014; Green et al., 1976; Zhao et al., 2014). As both the isopropanol and the water was stored in borosilicate bottles, this could be the source of boric acid.

To test the influence of the isopropanol used for the atomization, an aerosol was also generated from a solution that did not contain isopropanol, and the complex signals with and without isopropanol were compared (see Figure 5.4). Signals were normalized to the corresponding complex signal in the experiment with isopropanol. As anticipated, signals of isopropoxy-substituted complexes decreased strongly. The residual detection likely reflects memory effects resulting from incomplete purging of the system prior to the measurement, leaving traces of volatile isopropanol on flow-tube surfaces and within the classifier. Notably,

the fluoride-containing complexes also decreased, though less strongly, suggesting that at least a portion of the fluoride contribution may be associated with the usage of isopropanol.

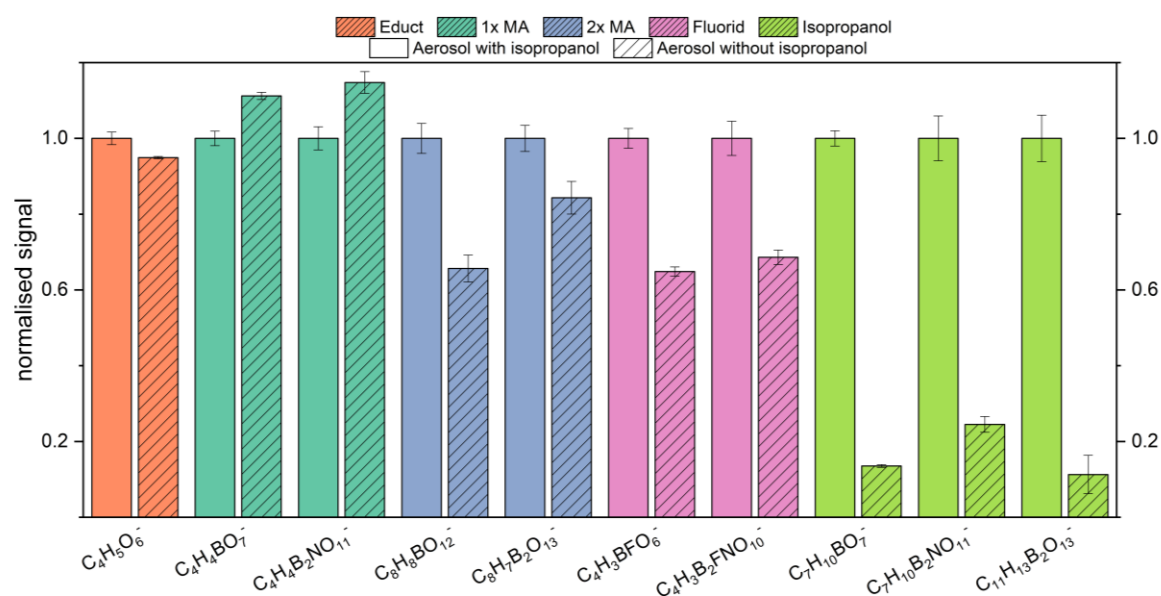


Figure 5.4: Signals of the detected borate–tartrate ester complexes with (unfilled bars) and without (hatched bars) isopropanol in the atomizer solution after a residence time of 106.8 s at 81% RH, normalized to the signal of each complex measured with isopropanol. Bars are color-grouped as follows: reactant (orange), complexes with one tartaric-acid unit (dark green), complexes with two tartaric-acid units (blue), fluoride-containing complexes (pink), and isopropoxy-substituted complexes (light green).

With regard to boron content, no single trend emerged. The signals of complexes containing one tartaric acid unit increased in intensity in the absence of isopropanol, whereas signals of complexes with two tartaric acid units decreased. This is unexpected, as in isopropanol–water mixtures, the  $pK_a$  is higher than in pure water, favoring neutral, trigonal species. Under such conditions 1:1 and 2:1 complexes are expected to be more stable than 1:2 and 2:2 complexes (Fan et al., 1998; Springsteen and Wang, 2002). Overall, the borate fraction does not seem to decrease in the absence of isopropanol.

Boric acid is comparatively difficult to remove by the ion-exchange resins commonly used in Milli-Q systems because of its high  $pK_a$ , which renders it largely uncharged. Consequently, boron breakthrough can occur before a detectable change in water resistivity, indicating exhausted exchange media (Dydo et al., 2012; Dimitrakopoulos et al., 2012). The possibility of boron entering the system through Milli-Q water remains a viable hypothesis. Additional tests are required to unambiguously identify the boron source.

### 5.3.4 Dry Conditions

Under dry conditions, the formation of borate-tartrate complexes seems to be much slower (see Figure 5.5). Unlike in the humid case, equilibrium is not reached. This likely reflects restricted diffusion within dry particles. Even so, here the formation rate also increases as particle diameter decreases. Several studies have reported size-dependent phase behavior in nanoparticles. Bounce behavior measurements in an electrical low-pressure impactor indicated that secondary organic aerosol (SOA) particles at approximately 30 nm and below behave more like viscous liquids, whereas larger particles behave more like solids (Virtanen et al., 2010). Atmospheric SOA particles with diameters < 20 nm are also expected to be liquid at room temperature (Cheng et al., 2015). Such size-dependent phase behavior could explain the observed size dependence of reaction rates in the dry particles. In the event that the smaller particles possess a lower viscosity, diffusion and, consequently, complex formation would be accelerated.

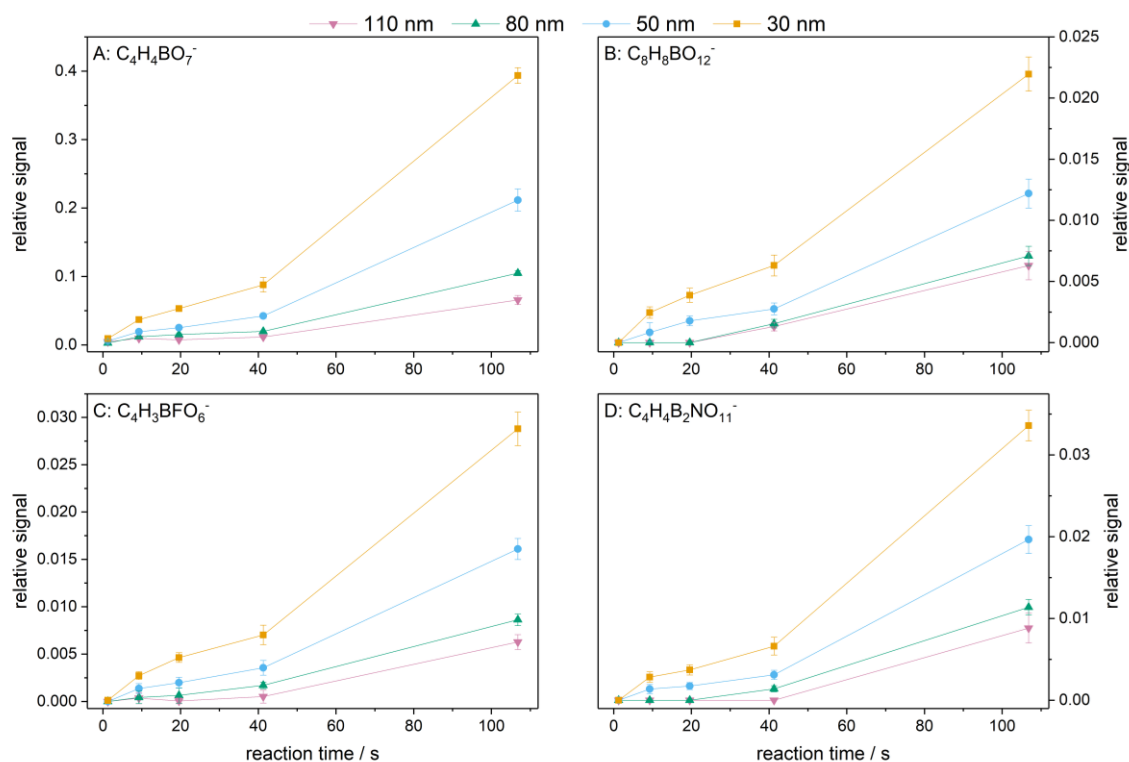


Figure 5.5: Mean relative signals of borate-tartrate ester complexes formed in aerosol particles as a function of residence time at 30% RH:  $C_4H_4BO_7^-$  (A),  $C_8H_8BO_{12}^-$  (B),  $C_4H_3BFO_6^-$  (C) and  $C_4H_4B_2NO_{11}^-$  (D). Particle mobility diameters were: 110 nm (pink), 80 nm (green), 50 nm (blue) and 30 nm (yellow).

Changes in RH seem to affect not only the rate but also the product ratios. As illustrated in Figure 5.6, under dry conditions the relative fraction of complexes bearing fluoride or isopropoxy substituents decreases across all complex types, with an even stronger decrease for the isopropoxy-substituted species. This is surprising because the silica denuders should primarily reduce water content. With the exception of the 1:2 complex  $C_8H_8BO_{12}^-$ , the green-labeled species in Figure 5.6 all possess a hydroxyl substituent. One might therefore have expected their relative abundance to decrease. Interestingly, only  $C_8H_8BO_{12}^-$  shows this behavior.

With a diffusion rate of  $2.3 \cdot 10^{-9} \text{ m}^2 \text{ s}^{-1}$ , water has approximately twice the diffusion rate of fluoride ions and almost four times that of isopropanol, with diffusion rates of  $1.48 \cdot 10^{-9} \text{ m}^2 \text{ s}^{-1}$  and  $0.6 \cdot 10^{-9} \text{ m}^2 \text{ s}^{-1}$  respectively (Holz et al., 2000; Haynes et al., 2016; Zhang and Scherer, 2017). Since the diffusion of large molecules like boric acid and tartaric acid should be strongly limited under dry conditions, the faster diffusion of the smaller substituents could drive the complex formation in this system. This could lead to an increased fraction of hydroxy-substituted complexes in the dry regime, a finding that is qualitatively consistent with the observed trend.

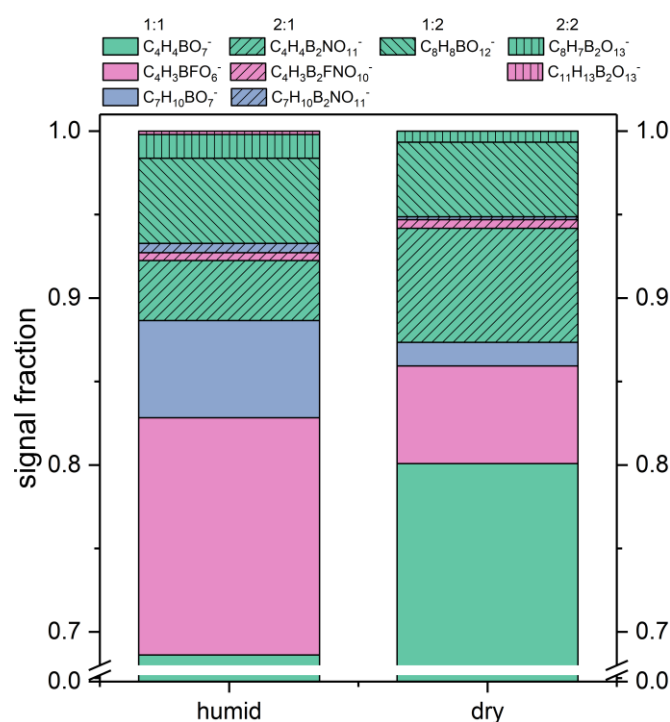


Figure 5.6: Fractional contributions of borate-tartrate ester complexes to the total product signal after a residence time of 106.8 s under humid (81% RH, left) and dry (30% RH, right) conditions. Complexes are grouped by stoichiometry via hatching pattern and by substituents via color.

### 5.3.5 Discrepancy in the Educt Signal

The evolution of the tartaric acid reactant signal (Figure 5.7) differs from the consistent behavior observed for the borate-tartrate products. In dry conditions, the tartaric acid signal remains approximately constant. However, under humid conditions, a particle-size-dependent decrease is observed, with the strongest decrease occurring for 110 nm particles and diminishing with decreasing particle size.

Given that product signals are generally higher in the smaller (30 nm) particles, this is a somewhat surprising observation. A process other than complex formation, undetected by  $\text{NO}_3^-$ -CIMS, may reduce the tartaric acid signal under humid conditions. If this process is sufficiently large in absolute magnitude, it could mask the expected stronger depletion in smaller particles. Although the signal intensities of the various borate-tartrate esters can exceed the observed decrease in tartaric acid (see Figure 5.2 and Figure 5.7), it has been demonstrated that the ionization efficiencies of chemical ionization vary strongly among analytes, sometimes by 1 or 2 orders of magnitude (Lopez-Hilfiker et al., 2016; Alage et al., 2024). Consequently, the actual fraction of complexed tartaric acids may be considerably smaller than suggested by relative intensities.

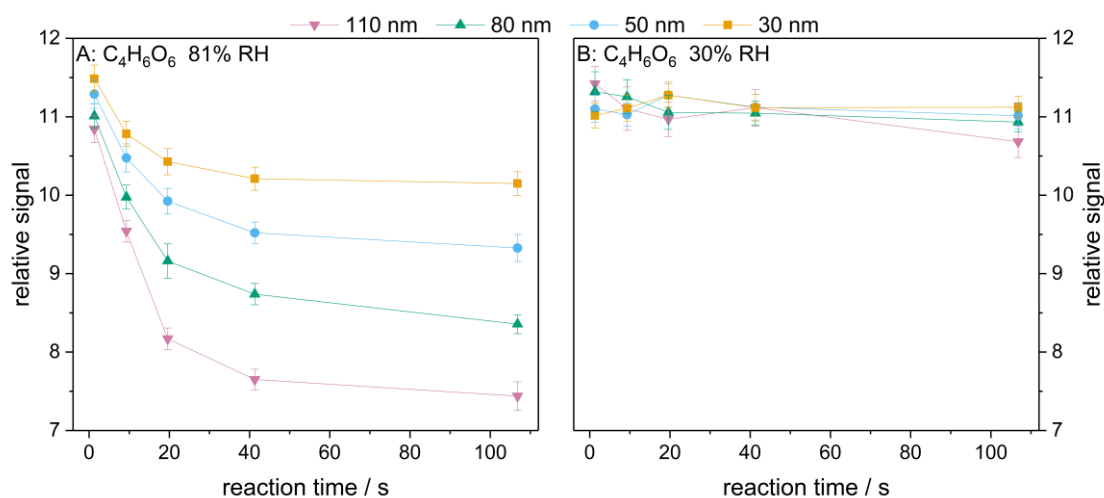


Figure 5.7: Mean relative signal of tartaric acid as a function of residence time at 81% RH (A) and 30% RH (B). Particle mobility diameters were: 110 nm (pink), 80 nm (green), 50 nm (blue) and 30 nm (yellow).

Evaporation of tartaric acid from the particles during transport through the flow tubes is a plausible contributor to the observed signal loss. With an estimated vapor pressure of  $1.98 \cdot 10^{-8}$  atm at 293 K (modeled estimate by EVAPORATION), tartaric acid is a semi-volatile compound (Compernelle et al., 2011; Bianchi et al., 2019). Consequently gas-particle partitioning is expected. In a pure tartaric acid system it can be assumed that the proportion of evaporated tartaric acid is elevated in the smaller particles due to the Kelvin effect. However, borate-tartrate complexes likely have much lower vapor pressures than pure tartaric acid due to their higher molecular masses (Dommen et al., 2006; Vesterinen et al., 2007). Lower-volatility constituents have been demonstrated to enhance particle-phase partitioning of semi-volatile species and reduce overall particle volatility (Pankow, 1994; Hallquist et al., 2009). Thus, the higher fraction of borate complexes in smaller particles might impede the evaporation of tartaric acid within these particles.

In dry particles, the process of SVOC evaporation is found to be strongly suppressed by reduced diffusivity (Bastelberger et al., 2017; Ingram et al., 2021). Furthermore, at low RH, phase separation into an dry amorphous organic-rich shell and an aqueous core can occur, which would further restrict the evaporation of organic components (Davies et al., 2013; Choczynski et al., 2024). This could explain why no significant decrease in the tartaric acid signal is observed at 30% RH (Figure 5.7B).

## 5.4 Conclusion

The present study examined the influence of Laplace pressure on the formation of borate-ester complexes from boric acid and tartaric acid in ultrafine aerosol particles. The generation of particles with diameters of 30, 50, 80, and 110 nm was conducted, and the temporal evolution of product signals was meticulously monitored. A notable increase in complex signals was observed following the transition from a bulk solution to a particulate state. This observation signifies a shift in the complexation equilibrium.

The equilibrium shift displays a clear particle-size dependence. In the case of smaller particles, complexes were formed at a faster rate and reached higher absolute signal levels. This behavior is consistent with the expectation that the internal particle pressure increases as the particle diameter decreases, since borate-ester formation is strongly pressure sensitive. The size effect was evident under both humid and dry conditions, although formation rates were substantially slower at low RH than at high RH.

The detected borate-tartrate complexes could be grouped by stoichiometry in terms of the numbers of boric-acid and tartaric-acid units. Different product groups showed different magnitudes of size dependence. The greater the number of constituent molecules in a complex, the stronger its size dependence. Within each stoichiometric group, the sign and trend of the size effect were found to be uniform.

The source of boric acid could not be unambiguously identified. Additional experiments with deliberately added boric acid or boric acid derivatives would help to further constrain the reaction system. A second open question is the inverse size dependence of the tartaric-acid signal relative to the borate esters. Under humid conditions, the tartaric acid signal exhibits a stronger decrease for larger particles. One plausible explanation is that the higher complex fraction in smaller particles lowers overall particle volatility, thereby impeding the evaporation of the semi-volatile tartaric acid. Tandem-DMA experiments could help determine whether particle diameters evolve during reaction in a manner consistent with this interpretation.



## 6 Conclusion and Outlook

The objective of this dissertation was to determine whether, and to what extent, chemical reactions in nanometer-sized aerosol particles depend on particle size, and to develop an experimental approach capable of probing such effects at the molecular level. To this end, an online workflow was established that combines generation and differential-mobility size selection of monodisperse aerosols in the 30-110 nm regime with controlled residence times in flow tubes under defined relative humidity, and molecular detection by  $\text{NO}_3$ -CI-Orbitrap mass spectrometry coupled to a custom-built aerosol inlet. The inlet combines rapid thermal evaporation with a downstream gas-cooling unit to enable efficient transfer of volatilized analytes into the ion source while reducing additional wall losses and limiting thermal decomposition relative to less controlled evaporation concepts. Instrument performance and sensitivity were evaluated using model aerosols and dedicated transmission and vaporization experiments, providing the analytical basis for the subsequent reaction studies. Across the investigated model systems, the data shows that, in this ultrafine regime, particle size can influence not only the apparent rate or extent of chemical transformation but also the distribution of detectable intermediates and products.

All three systems exhibited faster apparent conversion in smaller particles. For the heterogeneous reactions of 5-norbornene-2-endo,3-exo-dicarboxylic acid (NDA) and ascorbic acid (AA) with ozone, this tendency is broadly consistent with expectations based on the higher surface-to-volume ratio of smaller particles, which can accelerate oxidant uptake and interfacial processes. At the same time, the observations do not exclude additional size-dependent contributions beyond this geometric effect. Because ozonolysis proceeds via cycloaddition chemistry, the results are also consistent with the possibility that curvature-related pressure (i.e., Laplace pressure) contributes to the observed size dependence under certain conditions. Importantly, the purely condensed-phase formation of borate–tartrate complexes indicates that particle-size-dependent effects can also influence reaction progress when increased surface area does not directly facilitate uptake of a gas-phase reactant. In an atmospheric context, this observation could help explain why freshly nucleated particles can grow so rapidly.

A recurring finding across the studied systems is that particle size affects more than the overall speed of signal decay or growth. Instead, the data indicates that particle size can alter the balance between competing pathways, resulting in measurable shifts in the observed product distribution. This is important because the climate relevance of aerosol processing is often mediated through the formation of low-volatility material and compositional changes, not solely through total conversion. Across the investigated conditions, smaller particles tended to exhibit larger relative contributions of higher-molecular-weight products among

---

the detected species. The most pronounced differences were observed for dimer signals formed during ozonolysis. Under selected conditions, the relative contribution of dimers to the total detected signal was more than fourfold higher in 30 nm NDA particles than in 110 nm particles. Comparable trends were also observed for dimer signals in the ozonolysis of AA particles. In addition to oligomeric products, more highly oxygenated follow-up products from ozonolysis were detected with higher relative contributions in smaller particles. Such trends are consistent with the expectation that bond-forming chemistry is favored under elevated pressure. The borate–tartrate system provides a particularly clear example of a stoichiometry-dependent size effect. The larger the detected complex and thus the greater the number of newly formed bonds, the higher is the signal in 30 nm particles relative to 110 nm particles. Conversely, the reduced signals of fragmentation products in the NDA ozonolysis are consistent with diminished formation of pathways that would be expected to be disfavored under elevated pressure. Taken together, these patterns support the concept that the nanometer regime should not be treated as a simple scaled-down analogue of bulk-phase chemistry.

The experiments further show that relative humidity is a key control parameter for size-dependent behavior; likely because humidity affects viscosity, diffusivity, and potentially microstructural properties such as phase separation or the formation of diffusion-limiting surface layers. In addition, water content influences particle surface tension and thus the magnitude of curvature-related pressure. The humidity dependence was most evident in the AA–ozone system, where size-dependent differences in the reaction pathways were observed under humid conditions, while no pronounced size dependence was detected under dry conditions. Humidity also affected the NDA–ozone system, influencing both product distributions and absolute signal intensities. Under dry conditions, the data is consistent with rapid formation of a diffusion-limiting surface layer that reduces transport, which could contribute to the observed shifts toward dimers and the higher conversion in smaller particles. Across systems, dry conditions generally reduced overall transformation rates, consistent with restricted diffusion. Overall, the combined dependence on humidity and particle size underscores that size and phase state must be considered jointly, because they can modulate each other's impact on chemistry.

Taken together, this dissertation provides two main contributions. First, it establishes an experimentally practical framework for time-resolved, molecular-level analysis of nanometer aerosols under controlled residence time and humidity. Second, it demonstrates across heterogeneous ozonolysis, redox-active multipathway chemistry, and condensed-phase complexation that particle diameter can measurably influence reaction progress and the detectable distribution of products in the 30–110 nm regime. These findings support the broader concept that curvature-related effects may contribute to the chemical evolution of

freshly formed ultrafine particles and thereby influence the formation of low-volatility material relevant to particle growth.

The results motivate follow-up work aimed at identifying which physicochemical effects dominate under which conditions and at assessing how general the observed size dependencies are across reaction classes. The most informative next steps are those that discriminate between competing mechanistic explanations rather than merely extending the number of investigated systems.

One approach would be to target surface tension explicitly by co-nebulizing surface-active compounds during particle generation. If surface tension is reduced in a controlled manner, the magnitude of Laplace pressure should decrease, and a corresponding reduction in the strength of the size dependence would be expected if curvature-related pressure is a major driver. At the same time, surface-active species can also modify interfacial composition and phase state, so such experiments would benefit from careful control experiments to separate these effects. In parallel, targeted addition of plasticizing compounds could be used to test whether the pronounced differences between dry and humid conditions arise primarily from diffusion limitations in viscous particles. Finally, for pH-sensitive multipathway chemistry such as the AA–ozone system, deliberate manipulation of particle acidity could help determine whether the observed size dependence is consistent with size-dependent dissociation equilibria or whether other size-related effects dominate.

For the borate–tartrate system, it would be valuable to add boric acid intentionally to the nebulized solution to quantify the magnitude of background boron and to assess how sensitively complex signals respond to changes in precursor concentration. In addition, studying other borate esters and additional diols could help determine whether the observed size dependence generalizes across a broader reaction class or whether it is specific to the particular borate–tartrate system investigated here.

This work employed nitrate chemical ionization because it is robust, highly selective and sensitive for highly oxygenated compounds, which made it well suited for developing and evaluating the new inlet. However, the limitations of this selectivity were also evident. Key species such as the NDA reactant and boric acid were not detected, and additional ozonolysis products with low oxygen content may have escaped detection. It would therefore be valuable to explore whether the developed aerosol inlet can be made compatible with alternative reagent ions that provide sensitivity to less oxygenated species. Broadening the accessible chemical spectrum would improve coverage of complex systems such as ozonolysis and could enable studies of additional reaction types whose reactants and products are poorly detected by nitrate CI.

---

## 7 References

- Adamson, A. W. and Gast, A. P.: Physical chemistry of surfaces, 6. ed., A Wiley-Interscience publication, Wiley, New York, 784 pp., 1997.
- Alage, S., Michoud, V., Harb, S., Picquet-Varrault, B., Cirtog, M., Kumar, A., Rissanen, M., and Cantrell, C.: A nitrate ion chemical-ionization atmospheric-pressure-interface time-of-flight mass spectrometer (NO<sub>3</sub>-ToFCIMS) sensitivity study, *Atmospheric Measurement Techniques*, 17, 4709–4724, <https://doi.org/10.5194/amt-17-4709-2024>, 2024.
- Albrecht, B. A.: Aerosols, cloud microphysics, and fractional cloudiness, *Science (New York, N.Y.)*, 245, 1227–1230, <https://doi.org/10.1126/science.245.4923.1227>, 1989.
- Alemán, J. V., Chadwick, A. V., He, J., Hess, M., Horie, K., Jones, R. G., Kratochvíl, P., Meisel, I., Mita, I., Moad, G., Penczek, S., and Stepto, R. F. T.: Definitions of terms relating to the structure and processing of sols, gels, networks, and inorganic-organic hybrid materials (IUPAC Recommendations 2007), *Pure and Applied Chemistry*, 79, 1801–1829, <https://doi.org/10.1351/pac200779101801>, 2007.
- Almeida, J., Schobesberger, S., Kürten, A., Ortega, I. K., Kupiainen-Määttä, O., Praplan, A. P., Adamov, A., Amorim, A., Bianchi, F., Breitenlechner, M., David, A., Dommen, J., Donahue, N. M., Downard, A., Dunne, E., Duplissy, J., Ehrhart, S., Flagan, R. C., Franchin, A., Guida, R., Hakala, J., Hansel, A., Heinritzi, M., Henschel, H., Jokinen, T., Junninen, H., Kajos, M., Kangasluoma, J., Keskinen, H., Kupc, A., Kurtén, T., Kvashin, A. N., Laaksonen, A., Lehtipalo, K., Leiminger, M., Leppä, J., Loukonen, V., Makhmutov, V., Mathot, S., McGrath, M. J., Nieminen, T., Olenius, T., Onnela, A., Petäjä, T., Riccobono, F., Riipinen, I., Rissanen, M., Rondo, L., Ruuskanen, T., Santos, F. D., Sarnela, N., Schallhart, S., Schnitzhofer, R., Seinfeld, J. H., Simon, M., Sipilä, M., Stozhkov, Y., Stratmann, F., Tomé, A., Tröstl, J., Tsagkogeorgas, G., Vaattovaara, P., Viisanen, Y., Virtanen, A., Vrtala, A., Wagner, P. E., Weingartner, E., Wex, H., Williamson, C., Wimmer, D., Ye, P., Yli-Juuti, T., Carslaw, K. S., Kulmala, M., Curtius, J., Baltensperger, U., Worsnop, D. R., Vehkamäki, H., and Kirkby, J.: Molecular understanding of sulphuric acid-amine particle nucleation in the atmosphere, *Nature*, 502, 359–363, <https://doi.org/10.1038/nature12663>, available at: <https://www.nature.com/articles/nature12663>, 2013.
- Andreae, M. O.: The Aerosol Nucleation Puzzle, *Science*, 339, 911–912, <https://doi.org/10.1126/science.1233798>, 2013.
- Angelaki, M., d'Erceville, J., Donaldson, D. J., and George, C.: pH Affects the Spontaneous Formation of H<sub>2</sub>O<sub>2</sub> at the Air-Water Interfaces, *Journal of the American Chemical Society*, 146, 25889–25893, <https://doi.org/10.1021/jacs.4c07356>, 2024.
- Augusti, R., Chen, H., Eberlin, L. S., Nefliu, M., and Cooks, R. G.: Atmospheric pressure Eberlin transacetalization reactions in the heterogeneous liquid/gas phase, *International Journal of Mass Spectrometry*, 253, 281–287, <https://doi.org/10.1016/j.ijms.2006.05.005>, 2006.
- Bakker-Arkema, J. G. and Ziemann, P. J.: Measurements of Kinetics and Equilibria for the Condensed Phase Reactions of Hydroperoxides with Carbonyls to Form Peroxyhemiacetals, *ACS Earth and Space Chemistry*, 4, 467–475, <https://doi.org/10.1021/acsearthspacechem.0c00008>, 2020.
- Bannan, T. J., Le Breton, M., Priestley, M., Worrall, S. D., Bacak, A., Marsden, N. A., Mehra, A., Hammes, J., Hallquist, M., Alfarra, M. R., Krieger, U. K., Reid, J. P., Jayne, J., Robinson, W., McFiggans, G., Coe, H., Percival, C. J., and Topping, D.: A method for extracting calibrated volatility information from the FIGAERO-HR-ToF-CIMS and its

- experimental application, *Atmospheric Measurement Techniques*, 12, 1429–1439, <https://doi.org/10.5194/amt-12-1429-2019>, 2019.
- Barrero, A. F., Alvarez-Manzaneda, E. J., Alvarez-Manzaneda, R., Chahboun, R., Meneses, R., and Aparicio B., M.: Ring A Functionalization of Terpenoids by the Unusual Baeyer-Villiger Rearrangement of Aliphatic Aldehydes, *Synlett*, 1999, 713–716, <https://doi.org/10.1055/s-1999-2722>, 1999.
- Bastelberger, S., Krieger, U. K., Luo, B., and Peter, T.: Diffusivity measurements of volatile organics in levitated viscous aerosol particles, *Atmos. Chem. Phys.*, 17, 8453–8471, <https://doi.org/10.5194/acp-17-8453-2017>, 2017.
- Bellouin, N., Quaas, J., Gryspeerdt, E., Kinne, S., Stier, P., Watson-Parris, D., Boucher, O., Carslaw, K. S., Christensen, M., Daniau, A.-L., Dufresne, J.-L., Feingold, G., Fiedler, S., Forster, P., Gettelman, A., Haywood, J. M., Lohmann, U., Malavelle, F., Mauritsen, T., McCoy, D. T., Myhre, G., Mülmenstädt, J., Neubauer, D., Possner, A., Rugenstein, M., Sato, Y., Schulz, M., Schwartz, S. E., Sourdeval, O., Storelvmo, T., Toll, V., Winker, D., and Stevens, B.: Bounding Global Aerosol Radiative Forcing of Climate Change, *Reviews of geophysics* (Washington, D.C. 1985), 58, e2019RG000660, <https://doi.org/10.1029/2019RG000660>, available at: <https://agupubs.onlinelibrary.wiley.com/doi/full/10.1029/2019RG000660>, 2020.
- Benito-López, F., Egberink, R. J., Reinhoudt, D. N., and Verboom, W.: High pressure in organic chemistry on the way to miniaturization, *Tetrahedron*, 64, 10023–10040, <https://doi.org/10.1016/j.tet.2008.07.108>, 2008.
- Berkemeier, T., Steimer, S. S., Krieger, U. K., Peter, T., Pöschl, U., Ammann, M., and Shiraiwa, M.: Ozone uptake on glassy, semi-solid and liquid organic matter and the role of reactive oxygen intermediates in atmospheric aerosol chemistry, *Physical Chemistry Chemical Physics PCCP*, 18, 12662–12674, <https://doi.org/10.1039/c6cp00634e>, 2016.
- Berndt, T., Hoffmann, E. H., Tilgner, A., and Herrmann, H.: Highly oxidized products from the atmospheric reaction of hydroxyl radicals with isoprene, *Nature Communications*, 16, 2068, <https://doi.org/10.1038/s41467-025-57336-1>, 2025.
- Bianchi, F., Trostl, J., Junninen, H., Frege, C., Henne, S., Hoyle, C. R., Molteni, U., Herrmann, E., Adamov, A., Bukowiecki, N., Chen, X., Duplissy, J., Gysel, M., Hutterli, M., Kangasluoma, J., Kontkanen, J., Kuerten, A., Manninen, H. E., Muench, S., Perakyla, O., Petaja, T., Rondo, L., Williamson, C., Weingartner, E., Curtius, J., Worsnop, D. R., Kulmala, M., Dommen, J., and Baltensperger, U.: New particle formation in the free troposphere: A question of chemistry and timing, *Science*, 352, 1109–1112, <https://doi.org/10.1126/science.aad5456>, 2016.
- Bianchi, F., Kurtén, T., Riva, M., Mohr, C., Rissanen, M. P., Roldin, P., Berndt, T., Crouse, J. D., Wennberg, P. O., Mentel, T. F., Wildt, J., Junninen, H., Jokinen, T., Kulmala, M., Worsnop, D. R., Thornton, J. A., Donahue, N., Kjaergaard, H. G., and Ehn, M.: Highly Oxygenated Organic Molecules (HOM) from Gas-Phase Autoxidation Involving Peroxy Radicals: A Key Contributor to Atmospheric Aerosol, *Chemical Reviews*, 119, 3472–3509, <https://doi.org/10.1021/acs.chemrev.8b00395>, 2019.
- Breslow, R.: Hydrophobic effects on simple organic reactions in water, *Acc. Chem. Res.*, 24, 159–164, <https://doi.org/10.1021/ar00006a001>, 1991.
- Burtscher, H., Baltensperger, U., Bukowiecki, N., Cohn, P., Hüglin, C., Mohr, M., Matter, U., Nyeki, S., Schmatloch, V., Streit, N., and Weingartner, E.: Separation of volatile and non-volatile aerosol fractions by thermodesorption: instrumental development and applications, *Journal of Aerosol Science*, 32, 427–442, [https://doi.org/10.1016/S0021-8502\(00\)00089-6](https://doi.org/10.1016/S0021-8502(00)00089-6), 2001.

- Cai, R., Li, Y., Clément, Y., Li, D., Dubois, C., Fabre, M., Besson, L., Perrier, S., George, C., Ehn, M., Huang, C., Yi, P., Ma, Y., and Riva, M.: Orbitool: a software tool for analyzing online Orbitrap mass spectrometry data, *Atmospheric Measurement Techniques*, 14, 2377–2387, <https://doi.org/10.5194/amt-14-2377-2021>, 2021.
- Campbell, S. J., Wolfer, K., Gallimore, P. J., Giorio, C., Häussinger, D., Boillat, M.-A., and Kalberer, M.: Characterization and Quantification of Particle-Bound Criegee Intermediates in Secondary Organic Aerosol, *Environmental Science & Technology*, 56, 12945–12954, <https://doi.org/10.1021/acs.est.2c04101>, available at: <https://pmc.ncbi.nlm.nih.gov/articles/PMC9494744/>, 2022.
- Chan, K. Y., Zhuang, C., Vuong, V. G., Qian, N., Gao, X., and Min, W.: Electric fields at hydrophobic water interfaces: spectroscopic evidence, physical origin, and implications on reactivity, *Chemical Society reviews*, 55, 336–357, <https://doi.org/10.1039/d5cs00778j>, 2026.
- Chandrasekhar, J., Smith, S. F., and Jorgensen, W. L.: SN2 reaction profiles in the gas phase and aqueous solution, *J. Am. Chem. Soc.*, 106, 3049–3050, <https://doi.org/10.1021/ja00322a059>, 1984.
- Chang, Y.-P., Wu, S.-J., Lin, M.-S., Chiang, C.-Y., and Huang, G. G.: Ionic-strength and pH dependent reactivities of ascorbic acid toward ozone in aqueous micro-droplets studied using aerosol optical tweezers, *Physical Chemistry Chemical Physics PCCP*, 23, 10108–10117, <https://doi.org/10.1039/d0cp06493a>, 2021.
- Chen, B., Hoffmann, R., and Cammi, R.: The Effect of Pressure on Organic Reactions in Fluids—a New Theoretical Perspective, *Angewandte Chemie (International ed. in English)*, 56, 11126–11142, <https://doi.org/10.1002/anie.201705427>, 2017.
- Chen, C. J. and Williams, E. R.: The role of analyte concentration in accelerated reaction rates in evaporating droplets, *Chem. Sci.*, 14, 4704–4713, <https://doi.org/10.1039/d3sc00259d>, 2023.
- Chen, L., Yousaf, M., Xu, J., Ma, X., Zhou, X., Li, G., Symonds, J., Chen, R., Tang, S., Salehi, F., Njue, J. C. W., and Lelieveld, J.: Ultrafine particles deposition in human respiratory tract: Experimental measurement and modeling, *Ecotoxicology and Environmental Safety*, 295, <https://doi.org/10.1016/j.ecoenv.2025.118123>, 2025.
- Cheng, Y., Su, H., Koop, T., Mikhailov, E., and Poeschl, U.: Size dependence of phase transitions in aerosol nanoparticles, *Nature Communications*, 6, <https://doi.org/10.1038/ncomms6923>, 2015.
- Chhantyal-Pun, R., Khan, M. A. H., Taatjes, C. A., Percival, C. J., Orr-Ewing, A. J., and Shallcross, D. E.: Criegee intermediates: production, detection and reactivity, *International Reviews in Physical Chemistry*, 39, 385–424, <https://doi.org/10.1080/0144235X.2020.1792104>, 2020.
- Choczynski, J. M., Shokoor, B., Salazar, J., Zuend, A., and Davies, J. F.: Probing the evaporation dynamics of semi-volatile organic compounds to reveal the thermodynamics of liquid-liquid phase separated aerosol, *Chem. Sci.*, 15, 2963–2974, <https://doi.org/10.1039/d3sc05164a>, 2024.
- Clafin, M. S. and Ziemann, P. J.: Thermal desorption behavior of hemiacetal, acetal, ether, and ester oligomers, *Aerosol Science and Technology*, 53, 473–484, <https://doi.org/10.1080/02786826.2019.1576853>, 2019.
- Clafin, M. S., Krechmer, J. E., Hu, W., Jimenez, J. L., and Ziemann, P. J.: Functional Group Composition of Secondary Organic Aerosol Formed from Ozonolysis of  $\alpha$ -Pinene Under High VOC and Autoxidation Conditions, *ACS Earth and Space Chemistry*, 2, 1196–1210, <https://doi.org/10.1021/acsearthspacechem.8b00117>, 2018.
- Compernelle, S., Ceulemans, K., and Müller, J.-F.: EVAPORATION: a new vapour pressure estimation method for organic molecules including non-additivity and intramolecular interactions, *Atmos. Chem. Phys.*, 11, 9431–9450, <https://doi.org/10.5194/acp-11-9431-2011>, 2011.

- Craig, R. L., Peterson, P. K., Nandy, L., Lei, Z., Hossain, M. A., Camarena, S., Dodson, R. A., Cook, R. D., Dutcher, C. S., and Ault, A. P.: Direct Determination of Aerosol pH: Size-Resolved Measurements of Submicrometer and Supermicrometer Aqueous Particles, *Analytical Chemistry*, 90, 11232–11239, <https://doi.org/10.1021/acs.analchem.8b00586>, 2018.
- Criado-Reyes, J., Bizzarri, B. M., García-Ruiz, J. M., Saladino, R., and Di Mauro, E.: The role of borosilicate glass in Miller-Urey experiment, *Scientific reports*, 11, 21009, <https://doi.org/10.1038/s41598-021-00235-4>, 2021.
- Criegee, R.: Mechanism of Ozonolysis, *Angewandte Chemie International Edition in English*, 14, 745–752, <https://doi.org/10.1002/anie.197507451>, 1975.
- Curtius, J., Weigel, R., Vössing, H.-J., Wernli, H., Werner, A., Volk, C.-M., Konopka, P., Krebsbach, M., Schiller, C., Roiger, A., Schlager, H., Dreiling, V., and Borrmann, S.: Observations of meteoric material and implications for aerosol nucleation in the winter Arctic lower stratosphere derived from in situ particle measurements, *Atmos. Chem. Phys.*, 5, 3053–3069, <https://doi.org/10.5194/acp-5-3053-2005>, 2005.
- Curtius, J.: Nucleation of atmospheric aerosol particles, *Comptes Rendus. Physique*, 7, 1027–1045, <https://doi.org/10.1016/j.crhy.2006.10.018>, 2006.
- Curtius, J., Heinritzi, M., Beck, L. J., Poehlker, M. L., Tripathi, N., Krumm, B. E., Holzbeck, P., Nussbaumer, C. M., Pardo, L. H., Klimach, T., Barmounis, K., Andersen, S. T., Bardakov, R., Bohn, B., Cecchini, M. A., Chaboureau, J.-P., Dauhut, T., Dienhart, D., Doerich, R., Edtbauer, A., Giez, A., Hartmann, A., Holanda, B. A., Joppe, P., Kaiser, K., Keber, T., Klebach, H., Krueger, O. O., Kuerten, A., Mallaun, C., Marno, D., Martinez, M., Monteiro, C., Nelson, C., Ort, L., Raj, S. S., Richter, S., Ringsdorf, A., Rocha, F., Simon, M., Sreekumar, S., Tsokankunku, A., Unfer, G. R., Valenti, I. D., Wang, N., Zahn, A., Zauner-Wieczorek, M., Albrecht, R. I., Andreae, M. O., Artaxo, P., Crowley, J. N., Fischer, H., Harder, H., Herdies, D. L., Machado, L. A. T., Poehlker, C., Poeschl, U., Possner, A., Pozzer, A., Schneider, J., Williams, J., and Lelieveld, J.: Isoprene nitrates drive new particle formation in Amazon's upper troposphere, *Nature*, 636, <https://doi.org/10.1038/s41586-024-08192-4>, 2024.
- Dam, M., Thomas, A. E., and Smith, J. N.: Formation of Highly Oxidized Organic Compounds and Secondary Organic Aerosol from  $\alpha$ -Thujene Ozonolysis, *The Journal of Physical Chemistry A*, 127, 6989–6998, <https://doi.org/10.1021/acs.jpca.3c02584>, 2023.
- Davies, J. F., Miles, R. E. H., Haddrell, A. E., and Reid, J. P.: Influence of organic films on the evaporation and condensation of water in aerosol, *Proceedings of the National Academy of Sciences of the United States of America*, 110, 8807–8812, <https://doi.org/10.1073/pnas.1305277110>, 2013.
- Dewhirst, R. A. and Fry, S. C.: The oxidation of dehydroascorbic acid and 2,3-diketogulonate by distinct reactive oxygen species, *The Biochemical journal*, 475, 3451–3470, <https://doi.org/10.1042/BCJ20180688>, 2018.
- Dimitrakopoulos, T., Feuillas, E., Darbouret, D., and Mabic, S.: MilliQ-Electrodeionization-technology-and-application: The R&D Notebook 10 A publication of the Lab Water Division of Merck Millipore, RD010EN00, 12 pp., 2012.
- Dommen, J., Metzger, A., Duplissy, J., Kalberer, M., Alfarra, M. R., Gascho, A., Weingartner, E., Prevot, A. S. H., Verheggen, B., and Baltensperger, U.: Laboratory observation of oligomers in the aerosol from isoprene/NO<sub>x</sub> photooxidation, *Geophysical Research Letters*, 33, <https://doi.org/10.1029/2006GL026523>, 2006.
- Donahue, N. M., Epstein, S. A., Pandis, S. N., and Robinson, A. L.: A two-dimensional volatility basis set: 1. organic-aerosol mixing thermodynamics, *Atmos. Chem. Phys.*, 11, 3303–3318, <https://doi.org/10.5194/acp-11-3303-2011>, 2011.

- Donaldson, D. J. and Valsaraj, K. T.: Adsorption and reaction of trace gas-phase organic compounds on atmospheric water film surfaces: a critical review, *Environmental Science & Technology*, 44, 865–873, <https://doi.org/10.1021/es902720s>, 2010.
- Dubois, C., Perrier, S., George, C., and Riva, M.: The High Pressure Inside Aerosol Particles Enhances Photochemical Reactions of Biomass Burning Compounds, *ACS Earth and Space Chemistry*, 8, 1062–1071, <https://doi.org/10.1021/acsearthspacechem.4c00011>, 2024.
- Durham, L. J., Wurster, C. F., and Mosher, H. S.: Peroxides. VIII. The Mechanism for the Thermal Decomposition of n-Butyl Hydroperoxide and n-Butyl 1-Hydroxybutyl Peroxide 1, *Journal of the American Chemical Society*, 80, 332–337, <https://doi.org/10.1021/ja01535a020>, 1958.
- Dusek, U., Frank, G. P., Hildebrandt, L., Curtius, J., Schneider, J., Walter, S., Chand, D., Drewnick, F., Hings, S., Jung, D., Borrmann, S., and Andreae, M. O.: Size matters more than chemistry for cloud-nucleating ability of aerosol particles, *Science (New York, N.Y.)*, 312, 1375–1378, <https://doi.org/10.1126/science.1125261>, 2006.
- Dydo, P., Nemš, I., and Turek, M.: Boron removal and its concentration by reverse osmosis in the presence of polyol compounds, *Separation and Purification Technology*, 89, 171–180, <https://doi.org/10.1016/j.seppur.2012.01.018>, 2012.
- Eatoo, M. A. and Mishra, H.: Busting the myth of spontaneous formation of H<sub>2</sub>O<sub>2</sub> at the air-water interface: Contributions of the liquid-solid interface and dissolved oxygen exposed, *Chemical Science*, 15, <https://doi.org/10.1039/d3sc06534k>, 2024.
- Ehn, M., Thornton, J. A., Kleist, E., Sipilä, M., Junninen, H., Pullinen, I., Springer, M., Rubach, F., Tillmann, R., Lee, B., Lopez-Hilfiker, F., Andres, S., Acir, I.-H., Rissanen, M., Jokinen, T., Schobesberger, S., Kangasluoma, J., Kontkanen, J., Nieminen, T., Kurtén, T., Nielsen, L. B., Jørgensen, S., Kjaergaard, H. G., Canagaratna, M., Maso, M. D., Berndt, T., Petäjä, T., Wahner, A., Kerminen, V.-M., Kulmala, M., Worsnop, D. R., Wildt, J., and Mentel, T. F.: A large source of low-volatility secondary organic aerosol, *Nature*, 506, 476–479, <https://doi.org/10.1038/nature13032>, 2014.
- Eichler, P., Müller, M., D'Anna, B., and Wisthaler, A.: A novel inlet system for online chemical analysis of semi-volatile submicron particulate matter, *Atmospheric Measurement Techniques*, 8, 1353–1360, <https://doi.org/10.5194/amt-8-1353-2015>, 2015.
- El Haber, M., Gérard, V., Kleinheins, J., Ferronato, C., and Nozière, B.: Measuring the Surface Tension of Atmospheric Particles and Relevant Mixtures to Better Understand Key Atmospheric Processes, *Chemical Reviews*, 124, 10924–10963, <https://doi.org/10.1021/acs.chemrev.4c00173>, 2024.
- Elliott, J. A. W.: Surface thermodynamics at the nanoscale, *The Journal of Chemical Physics*, 154, 190901, <https://doi.org/10.1063/5.0049031>, 2021.
- Enami, S.: Fates of Organic Hydroperoxides in Atmospheric Condensed Phases, *The Journal of Physical Chemistry A*, 125, 4513–4523, <https://doi.org/10.1021/acs.jpca.1c01513>, 2021.
- Enami, S., Hoffmann, M. R., and Colussi, A. J.: Acidity enhances the formation of a persistent ozonide at aqueous ascorbate/ozone gas interfaces, *Proceedings of the National Academy of Sciences of the United States of America*, 105, 7365–7369, <https://doi.org/10.1073/pnas.0710791105>, 2008.
- Fan, J., Wang, J., and Ye, C.: Acid-base dissociation constants of 2,2'-bipyridyl in mixed protic solvents, *Talanta*, 46, 1285–1292, [https://doi.org/10.1016/s0039-9140\(97\)00395-0](https://doi.org/10.1016/s0039-9140(97)00395-0), 1998.
- Fu, Q.-S., Xue, Y.-Q., Cui, Z.-X., and Wang, M.-F.: Study on the Size-Dependent Oxidation Reaction Kinetics of Nanosized Zinc Sulfide, *Journal of Nanomaterials*, 2014, <https://doi.org/10.1155/2014/856489>, 2014.

## References

---

- Gao, L., Zgheib, I., Stergiou, E., Carstens, C., Sari Doré, F., Dupanloup, M., Bourgain, F., Perrier, S., and Riva, M.: Characterization of the Newly Designed Wall-Free Particle Evaporator (WALL-E) for Online Measurements of Atmospheric Particles, 32 pp., 2025.
- Gennes, P.-G. de, Brochard-Wyart, F., and Quéré, D.: Capillarity and wetting phenomena: Drops, bubbles, pearls, waves, [Nachdr.], Springer, New York, NY, 291 pp., 2009.
- George, C., Ammann, M., D'Anna, B., Donaldson, D. J., and Nizkorodov, S. A.: Heterogeneous photochemistry in the atmosphere, *Chemical Reviews*, 115, 4218–4258, <https://doi.org/10.1021/cr500648z>, 2015.
- George, I. J. and Abbatt, J. P. D.: Heterogeneous oxidation of atmospheric aerosol particles by gas-phase radicals, *Nature chemistry*, 2, 713–722, <https://doi.org/10.1038/nchem.806>, 2010.
- Girod, M., Moyano, E., Campbell, D. I., and Cooks, R. G.: Accelerated bimolecular reactions in microdroplets studied by desorption electrospray ionization mass spectrometry, *Chem. Sci.*, 2, 501–510, <https://doi.org/10.1039/C0SC00416B>, 2011.
- Gómez-González, Y., Wang, W., Vermeylen, R., Chi, X., Neiryneck, J., Janssens, I. A., Maenhaut, W., and Claeys, M.: Chemical characterisation of atmospheric aerosols during a 2007 summer field campaign at Brasschaat, Belgium: sources and source processes of biogenic secondary organic aerosol, *Atmos. Chem. Phys.*, 12, 125–138, <https://doi.org/10.5194/acp-12-125-2012>, 2012.
- Gong, K., Ao, J., Li, K., Le Liu, Liu, Y., Xu, G., Wang, T., Cheng, H., Wang, Z., Zhang, X., Wei, H., George, C., Mellouki, A., Herrmann, H., Wang, L., Chen, J., Ji, M., Zhang, L., and Francisco, J. S.: Imaging of pH distribution inside individual microdroplet by stimulated Raman microscopy, *Proceedings of the National Academy of Sciences of the United States of America*, 120, e2219588120, <https://doi.org/10.1073/pnas.2219588120>, 2023.
- Green, G. H., Blincoe, C., and Weeth, H. J.: Boron contamination from borosilicate glass, *Journal of agricultural and food chemistry*, 24, 1245–1246, <https://doi.org/10.1021/jf60208a016>, 1976.
- Greenspan, F. P.: The Convenient Preparation of Per-acids, *Journal of the American Chemical Society*, 68, 907, <https://doi.org/10.1021/ja01209a502>, 1946.
- Guo, Q., Hu, W., Hu, M., Wang, Y., Guo, S., Wu, Z., Zheng, J., and Zeng, L.: Bulk Quantification and Molecular Characterization of Thermal Decomposition from the Thermal Desorption of Organic Aerosol, *ACS ES&T Air*, 1, 628–636, <https://doi.org/10.1021/acsestair.4c00001>, 2024.
- Häkkinen, E., Zhao, J., Graeffe, F., Fauré, N., Krechmer, J. E., Worsnop, D., Timonen, H., Ehn, M., and Kangasluoma, J.: Online measurement of highly oxygenated compounds from organic aerosol, *Atmospheric Measurement Techniques*, 16, 1705–1721, <https://doi.org/10.5194/amt-16-1705-2023>, 2023.
- Hallquist, M., Wenger, J. C., Baltensperger, U., Rudich, Y., Simpson, D., Claeys, M., Dommen, J., Donahue, N. M., George, C., Goldstein, A. H., Hamilton, J. F., Herrmann, H., Hoffmann, T., Iinuma, Y., Jang, M., Jenkin, M. E., Jimenez, J. L., Kiendler-Scharr, A., Maenhaut, W., McFiggans, G., Mentel, T. F., Monod, A., Prévôt, A. S. H., Seinfeld, J. H., Surratt, J. D., Szmigielski, R., and Wildt, J.: The formation, properties and impact of secondary organic aerosol: current and emerging issues, *Atmospheric Chemistry and Physics*, 9, 5155–5236, <https://doi.org/10.5194/acp-9-5155-2009>, 2009.
- Hawkes, J. A., Dittmar, T., Patriarca, C., Tranvik, L., and Bergquist, J.: Evaluation of the Orbitrap Mass Spectrometer for the Molecular Fingerprinting Analysis of Natural Dissolved Organic Matter, *Analytical Chemistry*, 88, 7698–7704, <https://doi.org/10.1021/acs.analchem.6b01624>, 2016.
- Haynes, W. M., Lide, D. R., and Bruno, T. J.: *CRC Handbook of Chemistry and Physics*, CRC Press, 2016.

- Heine, N., Houle, F. A., and Wilson, K. R.: Connecting the Elementary Reaction Pathways of Criegee Intermediates to the Chemical Erosion of Squalene Interfaces during Ozonolysis, *Environmental Science & Technology*, 51, 13740–13748, <https://doi.org/10.1021/acs.est.7b04197>, 2017.
- Hinds, W. C.: *Aerosol Technology: Properties, Behavior, and Measurement of Airborne Particles*, Second Edition, Wiley-Interscience, s.l., 483 pp., 1999.
- Holz, M., Heil, S. R., and Sacco, A.: Temperature-dependent self-diffusion coefficients of water and six selected molecular liquids for calibration in accurate 1H NMR PFG measurements, *Phys. Chem. Chem. Phys.*, 2, 4740–4742, <https://doi.org/10.1039/b005319h>, 2000.
- Hong, J., Ma, J., Ma, N., Shi, J., Xu, W., Zhang, G., Zhu, S., Zhang, S., Tang, M., Pan, X., Xie, L., Li, G., Kuhn, U., Yan, C., Qi, X., Zha, Q., Nie, W., Tao, J., He, Y., Zhou, Y., Sun, Y., Xu, H., Liu, L., Cai, R., Zhou, G., Kuang, Y., Yuan, B., Wang, Q., Petaejae, T., Kerminen, V.-M., Kulmala, M., Cheng, Y., and Su, H.: Low Hygroscopicity of Newly Formed Particles on the North China Plain and Its Implications for Nanoparticle Growth, *Geophysical Research Letters*, 51, <https://doi.org/10.1029/2023GL107516>, 2024.
- Hritz, A. D., Raymond, T. M., and Dutcher, D. D.: A method for the direct measurement of surface tension of collected atmospherically relevant aerosol particles using atomic force microscopy, *Atmos. Chem. Phys.*, 16, 9761–9769, <https://doi.org/10.5194/acp-16-9761-2016>, 2016.
- Hua, W., Verreault, D., and Allen, H. C.: Relative Order of Sulfuric Acid, Bisulfate, Hydronium, and Cations at the Air-Water Interface, *Journal of the American Chemical Society*, 137, 13920–13926, <https://doi.org/10.1021/jacs.5b08636>, 2015.
- Huang, Y., Coggon, M. M., Zhao, R., Lignell, H., Bauer, M. U., Flagan, R. C., and Seinfeld, J. H.: The Caltech Photooxidation Flow Tube reactor: design, fluid dynamics and characterization, *Atmospheric Measurement Techniques*, 10, 839–867, <https://doi.org/10.5194/amt-10-839-2017>, 2017.
- Huffman, J. A., Ziemann, P. J., Jayne, J. T., Worsnop, D. R., and Jimenez, J. L.: Development and Characterization of a Fast-Stepping/Scanning Thermodenuder for Chemically-Resolved Aerosol Volatility Measurements, *Aerosol Science and Technology*, 42, 395–407, <https://doi.org/10.1080/02786820802104981>, 2008.
- Hyttinen, N., Kupiainen-Määttä, O., Rissanen, M. P., Muuronen, M., Ehn, M., and Kurtén, T.: Modeling the Charging of Highly Oxidized Cyclohexene Ozonolysis Products Using Nitrate-Based Chemical Ionization, *The journal of physical chemistry. A*, 119, 6339–6345, <https://doi.org/10.1021/acs.jpca.5b01818>, 2015.
- Ingram, S., Rovelli, G., Song, Y.-C., Topping, D., Dutcher, C. S., Liu, S., Nandy, L., Shiraiwa, M., and Reid, J. P.: Accurate Prediction of Organic Aerosol Evaporation Using Kinetic Multilayer Modeling and the Stokes-Einstein Equation, *The Journal of Physical Chemistry A*, 125, 3444–3456, <https://doi.org/10.1021/acs.jpca.1c00986>, 2021.
- Ismael Cotte-Rodríguez, Hao Chen, and R. Graham Cooks: Rapid trace detection of triacetone triperoxide (TATP) by complexation reactions during desorption electrospray ionization, *Chemical Communications*, 0, 953–955, <https://doi.org/10.1039/B515122H>, available at: <https://pubs.rsc.org/en/content/articlehtml/2006/cc/b515122h>, 2006.
- Jiang, Z., Zhang, Z., Xia, B., Xiong, S., Yang, L., and Li, Z.: Mechanism of boric acid extraction by trioctylamine and tartaric acid, *Separation and Purification Technology*, 331, 125597, <https://doi.org/10.1016/j.seppur.2023.125597>, 2024.
- Johnston, M. V. and Kerecman, D. E.: Molecular Characterization of Atmospheric Organic Aerosol by Mass Spectrometry, *Annual review of analytical chemistry (Palo Alto, Calif.)*, 12, 247–274, <https://doi.org/10.1146/annurev-anchem-061516-045135>, 2019.

- Jokinen, T., Sipilä, M., Junninen, H., Ehn, M., Lönn, G., Hakala, J., Petäjä, T., Mauldin, R. L., Kulmala, M., and Worsnop, D. R.: Atmospheric sulphuric acid and neutral cluster measurements using CI-API-TOF, *Atmospheric Chemistry and Physics*, 12, 4117–4125, <https://doi.org/10.5194/acp-12-4117-2012>, 2012.
- Jung, Y. and Marcus, R. A.: On the nature of organic catalysis "on water", *Journal of the American Chemical Society*, 129, 5492–5502, <https://doi.org/10.1021/ja068120f>, 2007.
- Kanakidou, M., Seinfeld, J. H., Pandis, S. N., Barnes, I., Dentener, F. J., Facchini, M. C., van Dingenen, R., Ervens, B., Nenes, A., Nielsen, C. J., Swietlicki, E., Putaud, J. P., Balkanski, Y., Fuzzi, S., Horth, J., Moortgat, G. K., Winterhalter, R., Myhre, C. E. L., Tsigaridis, K., Vignati, E., Stephanou, E. G., and Wilson, J.: Organic aerosol and global climate modelling: a review, *Atmospheric Chemistry and Physics*, 5, 1053–1123, <https://doi.org/10.5194/acp-5-1053-2005>, 2005.
- Kenseth, C. M., Hafeman, N. J., Rezgui, S. P., Chen, J., Huang, Y., Dalleska, N. F., Kjaergaard, H. G., Stoltz, B. M., Seinfeld, J. H., and Wennberg, P. O.: Particle-phase accretion forms dimer esters in pinene secondary organic aerosol, *Science (New York, N.Y.)*, 382, 787–792, <https://doi.org/10.1126/science.adi0857>, 2023.
- Kenseth, C. M., Hafeman, N. J., Huang, Y., Dalleska, N. F., Stoltz, B. M., and Seinfeld, J. H.: Synthesis of Carboxylic Acid and Dimer Ester Surrogates to Constrain the Abundance and Distribution of Molecular Products in  $\alpha$ -Pinene and  $\beta$ -Pinene Secondary Organic Aerosol, *Environmental Science & Technology*, 54, 12829–12839, <https://doi.org/10.1021/acs.est.0c01566>, 2020.
- Kenseth, C. M., Huang, Y., Zhao, R., Dalleska, N. F., Hethcox, C., Stoltz, B. M., and Seinfeld, J. H.: Synergistic O<sub>3</sub> + OH oxidation pathway to extremely low-volatility dimers revealed in  $\beta$ -pinene secondary organic aerosol, *Proceedings of the National Academy of Sciences of the United States of America*, 115, 8301–8306, <https://doi.org/10.1073/pnas.1804671115>, 2018.
- Kirkby, J., Duplissy, J., Sengupta, K., Frege, C., Gordon, H., Williamson, C., Heinritzi, M., Simon, M., Yan, C., Almeida, J., Troestl, J., Nieminen, T., Ortega, I. K., Wagner, R., Adamov, A., Amorim, A., Bernhammer, A.-K., Bianchi, F., Breitenlechner, M., Brilke, S., Chen, X., Craven, J., Dias, A., Ehrhart, S., Flagan, R. C., Franchin, A., Fuchs, C., Guida, R., Hakala, J., Hoyle, C. R., Jokinen, T., Junninen, H., Kangasluoma, J., Kim, J., Krapf, M., Kuerten, A., Laaksonen, A., Lehtipalo, K., Makhmutov, V., Mathot, S., Molteni, U., Onnela, A., Peraekylae, O., Piel, F., Petaja, T., Praplan, A. P., Pringle, K., Rap, A., Richards, N. A. D., Riipinen, I., Rissanen, M. P., Rondo, L., Sarnela, N., Schobesberger, S., Scott, C. E., Seinfeld, J. H., Sipilä, M., Steiner, G., Stozhkov, Y., Stratmann, F., Tome, A., Virtanen, A., Vogel, A. L., Wagner, A. C., Wagner, P. E., Weingartner, E., Wimmer, D., Winkler, P. M., Ye, P., Zhang, X., Hansel, A., Dommen, J., Donahue, N. M., Worsnop, D. R., Baltensperger, U., Kulmala, M., Carslaw, K. S., and Curtius, J.: Ion-induced nucleation of pure biogenic particles, *Nature*, 533, 521–+, <https://doi.org/10.1038/nature17953>, 2016.
- Klärner, F.-G. and Wurche, F.: The Effect of Pressure on Organic Reactions, *J. prakt. Chem.*, 342, 609–636, [https://doi.org/10.1002/1521-3897\(200009\)342:7<609:AID-PRAC609>3.0.CO;2-Z](https://doi.org/10.1002/1521-3897(200009)342:7<609:AID-PRAC609>3.0.CO;2-Z), 2000.
- Kroll, J. H. and Seinfeld, J. H.: Chemistry of secondary organic aerosol: Formation and evolution of low-volatility organics in the atmosphere, *Atmospheric Environment*, 42, 3593–3624, <https://doi.org/10.1016/j.atmosenv.2008.01.003>, 2008.
- Kugel, R. W. and Ault, B. S.: Infrared matrix isolation and theoretical studies of reactions of ozone with bicyclic alkenes:  $\alpha$ -pinene, norbornene, and norbornadiene, *The Journal of Physical Chemistry A*, 119, 312–322, <https://doi.org/10.1021/jp510883k>, 2015.
- Kulkarni, P., Baron, P. A., and Willeke, K.: *Aerosol Measurement*, Wiley, 2011.
- Kulmala, M., Kontkanen, J., Junninen, H., Lehtipalo, K., Manninen, H. E., Nieminen, T., Petäjä, T., Sipilä, M., Schobesberger, S., Rantala, P., Franchin, A., Jokinen, T., Järvinen, E., Äijälä, M., Kangasluoma, J., Hakala, J., Aalto,

- P. P., Paasonen, P., Mikkilä, J., Vanhanen, J., Aalto, J., Hakola, H., Makkonen, U., Ruuskanen, T., Mauldin, R. L., Duplissy, J., Vehkamäki, H., Bäck, J., Kortelainen, A., Riipinen, I., Kurtén, T., Johnston, M. V., Smith, J. N., Ehn, M., Mentel, T. F., Lehtinen, K. E. J., Laaksonen, A., Kerminen, V.-M., and Worsnop, D. R.: Direct observations of atmospheric aerosol nucleation, *Science (New York, N.Y.)*, 339, 943–946, <https://doi.org/10.1126/science.1227385>, 2013.
- Kumar, A.: Pressure dependence of the dissociation of acetic, benzoic, mandelic and succinic acids at 298.15K, *Thermochimica Acta*, 439, 154–157, <https://doi.org/10.1016/j.tca.2005.06.045>, available at: <https://www.sciencedirect.com/science/article/pii/S0040603105004557>, 2005.
- Kürten, A., Rondo, L., Ehrhart, S., and Curtius, J.: Performance of a corona ion source for measurement of sulfuric acid by chemical ionization mass spectrometry, *Atmospheric Measurement Techniques*, 4, 437–443, <https://doi.org/10.5194/amt-4-437-2011>, 2011.
- Kwon, H.-S., Ryu, M. H., and Carlsten, C.: Ultrafine particles: unique physicochemical properties relevant to health and disease, *Experimental & molecular medicine*, 52, 318–328, <https://doi.org/10.1038/s12276-020-0405-1>, available at: <https://www.nature.com/articles/s12276-020-0405-1>, 2020.
- La Puente, M. de and Laage, D.: How the Acidity of Water Droplets and Films Is Controlled by the Air-Water Interface, *Journal of the American Chemical Society*, 145, 25186–25194, <https://doi.org/10.1021/jacs.3c07506>, 2023.
- Lacour, R. A., Heindel, J. P., Zhao, R., and Head-Gordon, T.: The Role of Interfaces and Charge for Chemical Reactivity in Microdroplets, *Journal of the American Chemical Society*, 147, 6299–6317, <https://doi.org/10.1021/jacs.4c15493>, 2025.
- Lee, C. P., Surdu, M., Bell, D. M., Dommen, J., Xiao, M., Zhou, X., Baccharini, A., Giannoukos, S., Wehrle, G., Schneider, P. A., Prevot, A. S. H., Slowik, J. G., Lamkaddam, H., Wang, D., Baltensperger, U., and El Haddad, I.: High-frequency gaseous and particulate chemical characterization using extractive electrospray ionization mass spectrometry (Dual-Phase-EESI-TOF), *Atmospheric Measurement Techniques*, 15, 3747–3760, <https://doi.org/10.5194/amt-15-3747-2022>, 2022.
- Lehtinen, C., Nevalainen, V., and Brunow, G.: Experimental and computational studies on solvent effects in reactions of peracid–aldehyde adducts, *Tetrahedron*, 57, 4741–4751, [https://doi.org/10.1016/S0040-4020\(01\)00397-0](https://doi.org/10.1016/S0040-4020(01)00397-0), 2001.
- Lehtinen, C., Nevalainen, V., and Brunow, G.: Experimental and Computational Studies on Substituent Effects in Reactions of Peracid–Aldehyde Adducts, *Tetrahedron*, 56, 9375–9382, [https://doi.org/10.1016/S0040-4020\(00\)00908-X](https://doi.org/10.1016/S0040-4020(00)00908-X), 2000.
- Leviss, D. H., van Ry, D. A., and Hinrichs, R. Z.: Multiphase Ozonolysis of Aqueous  $\alpha$ -Terpineol, *Environmental Science & Technology*, 50, 11698–11705, <https://doi.org/10.1021/acs.est.6b03612>, 2016.
- Li, D., Wang, D., Caudillo, L., Scholz, W., Wang, M., Tomaz, S., Marie, G., Surdu, M., Eccli, E., Gong, X., Gonzalez-Carracedo, L., Granzin, M., Pfeifer, J., Rörup, B., Schulze, B., Rantala, P., Perrier, S., Hansel, A., Curtius, J., Kirkby, J., Donahue, N. M., George, C., El-Haddad, I., and Riva, M.: Ammonium Cl-Orbitrap: a tool for characterizing the reactivity of oxygenated organic molecules, *Atmos. Meas. Tech.*, 17, 5413–5428, <https://doi.org/10.5194/amt-17-5413-2024>, 2024.
- Li, X., Cai, R., Hao, J., Smith, J. N., and Jiang, J.: Online detection of airborne nanoparticle composition with mass spectrometry: Recent advances, challenges, and opportunities, *Trac-Trends in Analytical Chemistry*, 166, <https://doi.org/10.1016/j.trac.2023.117195>, 2023.

- Li, X., Li, Y., Cai, R., Yan, C., Qiao, X., Guo, Y., Deng, C., Yin, R., Chen, Y., Li, Y., Yao, L., Sarnela, N., Zhang, Y., Petäjä, T., Bianchi, F., Liu, Y., Kulmala, M., Hao, J., Smith, J. N., and Jiang, J.: Insufficient Condensable Organic Vapors Lead to Slow Growth of New Particles in an Urban Environment, *Environmental Science & Technology*, 56, 9936–9946, <https://doi.org/10.1021/acs.est.2c01566>, 2022.
- Lohmann, U. and Feichter, J.: Global indirect aerosol effects: a review, *Atmos. Chem. Phys.*, 5, 715–737, <https://doi.org/10.5194/acp-5-715-2005>, 2005.
- Lopez-Hilfiker, F. D., Mohr, C., Ehn, M., Rubach, F., Kleist, E., Wildt, J., Mentel, T. F., Lutz, A., Hallquist, M., Worsnop, D., and Thornton, J. A.: A novel method for online analysis of gas and particle composition: description and evaluation of a Filter Inlet for Gases and AEROsols (FIGAERO), *Atmospheric Measurement Techniques*, 7, 983–1001, <https://doi.org/10.5194/amt-7-983-2014>, 2014.
- Lopez-Hilfiker, F. D., Pospisilova, V., Huang, W., Kalberer, M., Mohr, C., Stefenelli, G., Thornton, J. A., Baltensperger, U., Prevot, A. S. H., and Slowik, J. G.: An extractive electrospray ionization time-of-flight mass spectrometer (EESI-TOF) for online measurement of atmospheric aerosol particles, *Atmospheric Measurement Techniques*, 12, 4867–4886, <https://doi.org/10.5194/amt-12-4867-2019>, 2019.
- Lopez-Hilfiker, F. D., Iyer, S., Mohr, C., Lee, B. H., D'Ambro, E. L., Kurtén, T., and Thornton, J. A.: Constraining the sensitivity of iodide adduct chemical ionization mass spectrometry to multifunctional organic molecules using the collision limit and thermodynamic stability of iodide ion adducts, *Atmospheric Measurement Techniques*, 9, 1505–1512, <https://doi.org/10.5194/amt-9-1505-2016>, 2016.
- Lu, H. M. and Jiang, Q.: Size-dependent surface tension and Tolman's length of droplets, *Langmuir the ACS journal of surfaces and colloids*, 21, 779–781, <https://doi.org/10.1021/la0489817>, 2005.
- Makarov, A.: Electrostatic axially harmonic orbital trapping: a high-performance technique of mass analysis, *Analytical Chemistry*, 72, 1156–1162, <https://doi.org/10.1021/ac991131p>, 2000.
- Makarov, A. and Scigelova, M.: Coupling liquid chromatography to Orbitrap mass spectrometry, *Journal of chromatography. A*, 1217, 3938–3945, <https://doi.org/10.1016/j.chroma.2010.02.022>, 2010.
- Mamakos, A.: Methodology to quantify the ratio of multiple-to single-charged fractions acquired in aerosol neutralizers, *Aerosol Science and Technology*, 50, 363–372, <https://doi.org/10.1080/02786826.2016.1153034>, 2016.
- Marteau, C., Ruyffelaere, F., Aubry, J.-M., Penverne, C., Favier, D., and Nardello-Rataj, V.: Oxidative degradation of fragrant aldehydes. Autoxidation by molecular oxygen, *Tetrahedron*, 69, 2268–2275, <https://doi.org/10.1016/j.tet.2013.01.034>, 2013.
- Martins-Costa, M. T. C. and Ruiz-Lopez, M. F.: Electrostatics and Chemical Reactivity at the Air-Water Interface, *Journal of the American Chemical Society*, <https://doi.org/10.1021/jacs.2c12089>, 2023.
- Maseda, M., Miyazaki, Y., and Takamuku, T.: Thermodynamics for complex formation of boric acid and borate with hydroxy acids and diols, *Journal of Molecular Liquids*, 341, 117343, <https://doi.org/10.1016/j.molliq.2021.117343>, 2021.
- McNeill, V. F.: Atmospheric Aerosols: Clouds, Chemistry, and Climate, *Annual review of chemical and biomolecular engineering*, 8, 427–444, <https://doi.org/10.1146/annurev-chembioeng-060816-101538>, 2017.
- Mehrgardi, M. A., Mofidfar, M., and Zare, R. N.: Sprayed Water Microdroplets Are Able to Generate Hydrogen Peroxide Spontaneously, *Journal of the American Chemical Society*, 144, 7606–7609, <https://doi.org/10.1021/jacs.2c02890>, 2022.

- Messina, P., Lathière, J., Sindelarova, K., Vuichard, N., Granier, C., Ghattas, J., Cozic, A., and Hauglustaine, D. A.: Global biogenic volatile organic compound emissions in the ORCHIDEE and MEGAN models and sensitivity to key parameters, *Atmos. Chem. Phys.*, 16, 14169–14202, <https://doi.org/10.5194/acp-16-14169-2016>, 2016.
- Michalski, A., Damoc, E., Hauschild, J.-P., Lange, O., Wiegand, A., Makarov, A., Nagaraj, N., Cox, J., Mann, M., and Horning, S.: Mass spectrometry-based proteomics using Q Exactive, a high-performance benchtop quadrupole Orbitrap mass spectrometer, *Molecular & cellular proteomics MCP*, 10, M111.011015, <https://doi.org/10.1074/mcp.M111.011015>, 2011.
- MILLER, S. L.: A production of amino acids under possible primitive earth conditions, *Science*, 117, 528–529, <https://doi.org/10.1126/science.117.3046.528>, 1953.
- Mugele, F. and Heikenfeld, J.: *Electrowetting*, Wiley, 2018.
- Murray, K. K., Boyd, R. K., Eberlin, M. N., Langley, G. J., Li, L., and Naito, Y.: Definitions of terms relating to mass spectrometry (IUPAC Recommendations 2013), *Pure and Applied Chemistry*, 85, 1515–1609, <https://doi.org/10.1351/PAC-REC-06-04-06>, 2013.
- Murzin, D. Y.: Thermodynamic analysis of nanoparticle size effect on catalytic kinetics, *Chemical Engineering Science*, 64, 1046–1052, <https://doi.org/10.1016/j.ces.2008.10.066>, 2009.
- Nagasathiyar, K., Brinda, C., Parani, M., and Vairamani, M.: Artifacts from methanol stored in borosilicate glass bottles during electrospray ionization mass spectrometric analysis, *Rapid communications in mass spectrometry RCM*, 28, 2227–2230, <https://doi.org/10.1002/rcm.7009>, 2014.
- Narayan, S., Muldoon, J., Finn, M. G., Fokin, V. V., Kolb, H. C., and Sharpless, K. B.: “On Water”: Unique Reactivity of Organic Compounds in Aqueous Suspension, *Angewandte Chemie*, 117, 3339–3343, <https://doi.org/10.1002/ange.200462883>, 2005.
- Narendra, N., Chen, X., Wang, J., Charles, J., Cooks, R. G., and Kubis, T.: Quantum Mechanical Modeling of Reaction Rate Acceleration in Microdroplets, *The journal of physical chemistry. A*, 124, 4984–4989, <https://doi.org/10.1021/acs.jpca.0c03225>, 2020.
- Neeb, P., Horie, O., and Moortgat, G. K.: Gas-phase ozonolysis of ethene in the presence of hydroxylic compounds, *International Journal of Chemical Kinetics*, 28, 721–730, [https://doi.org/10.1002/\(SICI\)1097-4601\(1996\)28:10<721:AID-KIN2>3.0.CO;2-P](https://doi.org/10.1002/(SICI)1097-4601(1996)28:10<721:AID-KIN2>3.0.CO;2-P), 1996.
- Njus, D., Kelley, P. M., Tu, Y.-J., and Schlegel, H. B.: Ascorbic acid: The chemistry underlying its antioxidant properties, *Free radical biology & medicine*, 159, 37–43, <https://doi.org/10.1016/j.freeradbiomed.2020.07.013>, 2020.
- O'Dowd, C. D., Hämeri, K., Mäkelä, J., Väkeva, M., Aalto, P., Leeuw, G. de, Kunz, G. J., Becker, E., Hansson, H.-C., Allen, A. G., Harrison, R. M., Berresheim, H., Kleefeld, C., Geever, M., Jennings, S. G., and Kulmala, M.: Coastal new particle formation: Environmental conditions and aerosol physicochemical characteristics during nucleation bursts, *J. Geophys. Res.*, 107, <https://doi.org/10.1029/2000JD000206>, 2002.
- Olmstead, W. N. and Brauman, J. I.: Gas-phase nucleophilic displacement reactions, *J. Am. Chem. Soc.*, 99, 4219–4228, <https://doi.org/10.1021/ja00455a002>, 1977.
- Pagonis, D. and Ziemann, P. J.: Chemistry of hydroperoxycarbonyls in secondary organic aerosol, *Aerosol Science and Technology*, 52, 1178–1193, <https://doi.org/10.1080/02786826.2018.1511046>, 2018.
- Pankow, J. F.: An absorption model of gas/particle partitioning of organic compounds in the atmosphere, *Atmospheric Environment*, 28, 185–188, [https://doi.org/10.1016/1352-2310\(94\)90093-0](https://doi.org/10.1016/1352-2310(94)90093-0), 1994.

- Parsons, H. T. and Fry, S. C.: Oxidation of dehydroascorbic acid and 2,3-diketogulonate under plant apoplastic conditions, *Phytochemistry*, 75, 41–49, <https://doi.org/10.1016/j.phytochem.2011.12.005>, 2012.
- Peng, Y., Wang, H., Gao, Y., Jing, S., Zhu, S., Huang, D., Hao, P., Lou, S., Cheng, T., Huang, C., and Zhang, X.: Real-time measurement of phase partitioning of organic compounds using a proton-transfer-reaction time-of-flight mass spectrometer coupled to a CHARON inlet, *Atmospheric Measurement Techniques*, 16, 15–28, <https://doi.org/10.5194/amt-16-15-2023>, 2023.
- Petters, S. S.: Constraints on the Role of Laplace Pressure in Multiphase Reactions and Viscosity of Organic Aerosols, *Geophysical Research Letters*, 49, <https://doi.org/10.1029/2022GL098959>, 2022.
- Pierce, J. R., Riipinen, I., Kulmala, M., Ehn, M., Petäjä, T., Junninen, H., Worsnop, D. R., and Donahue, N. M.: Quantification of the volatility of secondary organic compounds in ultrafine particles during nucleation events, *Atmospheric Chemistry and Physics*, 11, 9019–9036, <https://doi.org/10.5194/acp-11-9019-2011>, 2011.
- Pöschl, U.: Atmospheric aerosols: composition, transformation, climate and health effects, *Angewandte Chemie (International ed. in English)*, 44, 7520–7540, <https://doi.org/10.1002/anie.200501122>, 2005.
- Pospisilova, V., Lopez-Hilfiker, F. D., Bell, D. M., El Haddad, I., Mohr, C., Huang, W., Heikkinen, L., Xiao, M., Dommen, J., Prevot, A. S. H., Baltensperger, U., and Slowik, J. G.: On the fate of oxygenated organic molecules in atmospheric aerosol particles, *Science Advances*, 6, eaax8922, <https://doi.org/10.1126/sciadv.aax8922>, 2020.
- Qin, R., Chen, H., Wen, R., Li, G., and Meng, Z.: Effect of Boric Acid on the Ionization Equilibrium of  $\alpha$ -Hydroxy Carboxylic Acids and the Study of Its Applications, *Molecules (Basel, Switzerland)*, 28, <https://doi.org/10.3390/molecules28124723>, 2023.
- Qiu, J., Fujita, M., Tonokura, K., and Enami, S.: Stability of Terpenoid-Derived Secondary Ozonides in Aqueous Organic Media, *The Journal of Physical Chemistry A*, 126, 5386–5397, <https://doi.org/10.1021/acs.jpca.2c04077>, 2022.
- Qiu, J., Tonokura, K., and Enami, S.: Proton-Catalyzed Decomposition of  $\alpha$ -Hydroxyalkyl-Hydroperoxides in Water, *Environmental Science & Technology*, 54, 10561–10569, <https://doi.org/10.1021/acs.est.0c03438>, 2020.
- Qiu, L., Wei, Z., Nie, H., and Cooks, R. G.: Reaction Acceleration Promoted by Partial Solvation at the Gas/Solution Interface, *ChemPlusChem*, 86, 1362–1365, <https://doi.org/10.1002/cplu.202100373>, 2021.
- Riener, N., Ault, A. P., West, M., Craig, R. L., and Curtis, J. H.: Aerosol Mixing State: Measurements, Modeling, and Impacts, *Reviews of Geophysics*, 57, 187–249, <https://doi.org/10.1029/2018RG000615>, 2019.
- Riipinen, I., Pierce, J. R., Yli-Juuti, T., Nieminen, T., Häkkinen, S., Ehn, M., Junninen, H., Lehtipalo, K., Petäjä, T., Slowik, J., Chang, R., Shantz, N. C., Abbatt, J., Leitch, W. R., Kerminen, V.-M., Worsnop, D. R., Pandis, S. N., Donahue, N. M., and Kulmala, M.: Organic condensation: a vital link connecting aerosol formation to cloud condensation nuclei (CCN) concentrations, *Atmos. Chem. Phys.*, 11, 3865–3878, <https://doi.org/10.5194/acp-11-3865-2011>, 2011.
- Rissanen, M. P., Kurtén, T., Sipilä, M., Thornton, J. A., Kangasluoma, J., Sarnela, N., Junninen, H., Jørgensen, S., Schallhart, S., Kajos, M. K., Taipale, R., Springer, M., Mentel, T. F., Ruuskanen, T., Petäjä, T., Worsnop, D. R., Kjaergaard, H. G., and Ehn, M.: The formation of highly oxidized multifunctional products in the ozonolysis of cyclohexene, *Journal of the American Chemical Society*, 136, 15596–15606, <https://doi.org/10.1021/ja507146s>, 2014.

- Riva, M., Brüggemann, M., Li, D., Perrier, S., George, C., Herrmann, H., and Berndt, T.: Capability of CI-Orbitrap for Gas-Phase Analysis in Atmospheric Chemistry: A Comparison with the CI-API-TOF Technique, *Analytical Chemistry*, 92, 8142–8150, <https://doi.org/10.1021/acs.analchem.0c00111>, 2020a.
- Riva, M., Brüggemann, M., Li, D., Perrier, S., George, C., Herrmann, H., and Berndt, T.: Capability of CI-Orbitrap for Gas-Phase Analysis in Atmospheric Chemistry: A Comparison with the CI-API-TOF Technique, *Analytical Chemistry*, 92, 8142–8150, <https://doi.org/10.1021/acs.analchem.0c00111>, 2020b.
- Riva, M., Ehn, M., Li, D., Tomaz, S., Bourgain, F., Perrier, S., and George, C.: CI-Orbitrap: An Analytical Instrument To Study Atmospheric Reactive Organic Species, *Analytical Chemistry*, 91, 9419–9423, <https://doi.org/10.1021/acs.analchem.9b02093>, 2019a.
- Riva, M., Sun, J., McNeill, V. F., Ragon, C., Perrier, S., Rudich, Y., Nizkorodov, S. A., Chen, J., Caupin, F., Hoffmann, T., and George, C.: High Pressure Inside Nanometer-Sized Particles Influences the Rate and Products of Chemical Reactions, *Environmental Science & Technology*, <https://doi.org/10.1021/acs.est.0c07386>, 2021.
- Riva, M., Rantala, P., Krechmer, J. E., Peräkylä, O., Zhang, Y., Heikkinen, L., Garmash, O., Yan, C., Kulmala, M., Worsnop, D., and Ehn, M.: Evaluating the performance of five different chemical ionization techniques for detecting gaseous oxygenated organic species, *Atmospheric Measurement Techniques*, 12, 2403–2421, <https://doi.org/10.5194/amt-12-2403-2019>, 2019b.
- Riva, M., Healy, R. M., Tomaz, S., Flaud, P.-M., Perraudin, E., Wenger, J. C., and Villenave, E.: Gas and particulate phase products from the ozonolysis of acenaphthylene, *Atmospheric Environment*, 142, 104–113, <https://doi.org/10.1016/j.atmosenv.2016.07.012>, 2016.
- Robinson, M. A., Neuman, J. A., Huey, L. G., Roberts, J. M., Brown, S. S., and Veres, P. R.: Temperature-dependent sensitivity of iodide chemical ionization mass spectrometers, *Atmospheric Measurement Techniques*, 15, 4295–4305, <https://doi.org/10.5194/amt-15-4295-2022>, 2022.
- Roy, G. L., Laferriere, A. L., and Edwards, J. O.: A comparative study of polyol complexes of arsenite, borate, and tellurate ions, *Journal of Inorganic and Nuclear Chemistry*, 4, 106–114, [https://doi.org/10.1016/0022-1902\(57\)80092-X](https://doi.org/10.1016/0022-1902(57)80092-X), 1957.
- Ruiz-Bermejo, M., Menor-Salván, C., Osuna-Esteban, S., and Veintemillas-Verdaguer, S.: Prebiotic microreactors: a synthesis of purines and dihydroxy compounds in aqueous aerosol, *Origins of life and evolution of the biosphere the journal of the International Society for the Study of the Origin of Life*, 37, 123–142, <https://doi.org/10.1007/s11084-006-9026-5>, 2007.
- Ruiz-López, M. F. and Martins-Costa, M. T. C.: Disentangling reaction rate acceleration in microdroplets, *Physical Chemistry Chemical Physics PCCP*, 24, 29700–29704, <https://doi.org/10.1039/d2cp04998h>, 2022.
- Sanchez, J., Tanner, D. J., Chen, D., Huey, L. G., and Ng, N. L.: A new technique for the direct detection of HO<sub>2</sub> radicals using bromide chemical ionization mass spectrometry (Br-CIMS): initial characterization, *Atmospheric Measurement Techniques*, 9, 3851–3861, <https://doi.org/10.5194/amt-9-3851-2016>, 2016.
- Schlichting, H.: *Boundary-Layer Theory*, 9th ed. 2017, Springer eBook Collection Engineering, Springer, Berlin, Heidelberg, 805 pp., 2017.
- Scigelova, M. and Makarov, A.: Orbitrap mass analyzer--overview and applications in proteomics, *Proteomics*, 6 Suppl 2, 16–21, <https://doi.org/10.1002/pmic.200600528>, 2006.
- Sebree, J. A., C. Roach, M., Shipley, E. R., He, C., and Hörst, S. M.: Detection of Prebiotic Molecules in Plasma and Photochemical Aerosol Analogs Using GC/MS/MS Techniques, *ApJ*, 865, 133, <https://doi.org/10.3847/1538-4357/aadba1>, 2018.

- Seinfeld, J. H. and Pandis, S. N.: Atmospheric Chemistry and Physics From Air Pollution to Climate Change John H. Seinfeld ; Spyros N. Pandis, 2., Auflage, John Wiley & Sons, New York, NY, Online-Ressource, 2012.
- Seinfeld, J. H. and Pandis, S. N. (Eds.): Atmospheric chemistry and physics: From air pollution to climate change, 2. ed., Wiley, Hoboken, NJ, 1203 pp., 2006.
- Shen, H., Vereecken, L., Kang, S., Pullinen, I., Fuchs, H., Zhao, D., and Mentel, T. F.: Unexpected significance of a minor reaction pathway in daytime formation of biogenic highly oxygenated organic compounds, *Science Advances*, 8, eabp8702, <https://doi.org/10.1126/sciadv.abp8702>, 2022.
- Shrivastava, M., Cappa, C. D., Fan, J., Goldstein, A. H., Guenther, A. B., Jimenez, J. L., Kuang, C., Laskin, A., Martin, S. T., Ng, N. L., Petaja, T., Pierce, J. R., Rasch, P. J., Roldin, P., Seinfeld, J. H., Shilling, J., Smith, J. N., Thornton, J. A., Volkamer, R., Wang, J., Worsnop, D. R., Zaveri, R. A., Zelenyuk, A., and Zhang, Q.: Recent advances in understanding secondary organic aerosol: Implications for global climate forcing, *Reviews of Geophysics*, 55, 509–559, <https://doi.org/10.1002/2016RG000540>, 2017.
- Snowden, M., Bermudez, A., Kelly, D. R., and Radkiewicz-Poutsma, J. L.: The preference for anti over Gauche migration in the Baeyer-Villiger reaction, *The Journal of organic chemistry*, 69, 7148–7156, <https://doi.org/10.1021/jo0491307>, 2004.
- Song, X., Jallow, J., Basheer, C., Bakdash, R. S., Alaliwi, A., Alzamil, A. A., and Zare, R. N.: Microdroplet-Driven Synthesis of a Metal-Organic Framework Catalyst, *Angewandte Chemie International Edition in English*, 64, e202515006, <https://doi.org/10.1002/anie.202515006>, 2025.
- Springsteen, G. and Wang, B.: A detailed examination of boronic acid–diol complexation, *Tetrahedron*, 58, 5291–5300, [https://doi.org/10.1016/S0040-4020\(02\)00489-1](https://doi.org/10.1016/S0040-4020(02)00489-1), 2002.
- Stark, H., Yatavelli, R. L. N., Thompson, S. L., Kang, H., Krechmer, J. E., Kimmel, J. R., Palm, B. B., Hu, W., Hayes, P. L., Day, D. A., Campuzano-Jost, P., Canagaratna, M. R., Jayne, J. T., Worsnop, D. R., and Jimenez, J. L.: Impact of Thermal Decomposition on Thermal Desorption Instruments: Advantage of Thermogram Analysis for Quantifying Volatility Distributions of Organic Species, *Environmental Science & Technology*, 51, 8491–8500, <https://doi.org/10.1021/acs.est.7b00160>, 2017.
- Stier, P., Feichter, J., Kinne, S., Kloster, S., Vignati, E., Wilson, J., Ganzeveld, L., Tegen, I., Werner, M., Balkanski, Y., Schulz, M., Boucher, O., Minikin, A., and Petzold, A.: The aerosol-climate model ECHAM5-HAM, *Atmos. Chem. Phys.*, 5, 1125–1156, <https://doi.org/10.5194/acp-5-1125-2005>, available at: <https://acp.copernicus.org/articles/5/1125/2005/>, 2005.
- Stolzenburg, D., Sarnela, N., Bianchi, F., Cai, J., Cai, R., Cheng, Y., Dada, L., Donahue, N. M., Grothe, H., Holm, S., Kerminen, V.-M., Lehtipalo, K., Petäjä, T., Sulo, J., Winkler, P. M., Yan, C., Kangasluoma, J., and Kulmala, M.: Incomplete mass closure in atmospheric nanoparticle growth, *Npj Climate and Atmospheric Science*, 8, <https://doi.org/10.1038/s41612-025-00893-5>, 2025.
- Stolzenburg, D., Cai, R., Blichner, S. M., Kontkanen, J., Zhou, P., Makkonen, R., Kerminen, V.-M., Kulmala, M., Riipinen, I., and Kangasluoma, J.: Atmospheric nanoparticle growth, *Rev. Mod. Phys.*, 95, <https://doi.org/10.1103/RevModPhys.95.045002>, 2023.
- Stolzenburg, D., Fischer, L., Vogel, A. L., Heinritzi, M., Schervish, M., Simon, M., Wagner, A. C., Dada, L., Ahonen, L. R., Amorim, A., Baccharini, A., Bauer, P. S., Baumgartner, B., Bergen, A., Bianchi, F., Breitenlechner, M., Brilke, S., Buenrostro Mazon, S., Chen, D., Dias, A., Draper, D. C., Duplissy, J., El Haddad, I., Finkenzeller, H., Frege, C., Fuchs, C., Garmash, O., Gordon, H., He, X., Helm, J., Hofbauer, V., Hoyle, C. R., Kim, C., Kirkby, J., Kontkanen, J., Kürten, A., Lampilahti, J., Lawler, M., Lehtipalo, K., Leiminger, M., Mai, H., Mathot, S., Mentler, B., Molteni, U., Nie, W., Nieminen, T., Nowak, J. B., Ojdanic, A., Onnela, A., Passananti, M., Petäjä, T., Quéléver, L. L. J., Rissanen, M. P., Sarnela, N., Schallhart, S., Tauber, C., Tomé, A., Wagner, R., Wang, M., Weitz, L., Wimmer, D., Xiao, M., Yan,

- C., Ye, P., Zha, Q., Baltensperger, U., Curtius, J., Dommen, J., Flagan, R. C., Kulmala, M., Smith, J. N., Worsnop, D. R., Hansel, A., Donahue, N. M., and Winkler, P. M.: Rapid growth of organic aerosol nanoparticles over a wide tropospheric temperature range, *Proceedings of the National Academy of Sciences of the United States of America*, 115, 9122–9127, <https://doi.org/10.1073/pnas.1807604115>, 2018.
- Szopa, S., V. Naik, B. Adhikary, P. Artaxo, T. Berntsen, W.D. Collins, S. Fuzzi, L. Gallardo, A. Kiendler-Scharr, Z. Klimont, H. Liao, N. Unger, and P. Zanis: 2021: Short-lived Climate Forcers In: *Climate Change 2021 – The Physical Science Basis: Working Group I Contribution to the Sixth Assessment Report of the Intergovernmental Panel on Climate Change.*, 817–922, <https://doi.org/10.1017/9781009157896.008>, 2023.
- Tavakoli, F. and Olfert, J. S.: An Instrument for the Classification of Aerosols by Particle Relaxation Time: Theoretical Models of the Aerodynamic Aerosol Classifier, *Aerosol Science and Technology*, 47, 916–926, <https://doi.org/10.1080/02786826.2013.802761>, 2013.
- Testero, S. A., Mangione, M. I., Poeylout-Palena, A. A., Sierra, M. G., and Spanevello, R. A.: Unsymmetrical ozonolysis of carbohydrate derived norbornene systems, *Tetrahedron*, 63, 11410–11420, <https://doi.org/10.1016/j.tet.2007.08.070>, 2007.
- Thomas, A. E., Glicker, H. S., Guenther, A. B., Seco, R., Bustillos, O. V., Tota, J., Souza, R. A. F., and Smith, J. N.: Seasonal investigation of ultrafine-particle organic composition in an eastern Amazonian rainforest, *Atmospheric Chemistry and Physics*, 25, 959–977, <https://doi.org/10.5194/acp-25-959-2025>, 2025.
- Thornton, J. A., Mohr, C., Schobesberger, S., D'Ambro, E. L., Lee, B. H., and Lopez-Hilfiker, F. D.: Evaluating Organic Aerosol Sources and Evolution with a Combined Molecular Composition and Volatility Framework Using the Filter Inlet for Gases and Aerosols (FIGAERO), *Accounts of chemical research*, 53, 1415–1426, <https://doi.org/10.1021/acs.accounts.0c00259>, 2020.
- Tolman, R. C.: The Effect of Droplet Size on Surface Tension, *The Journal of Chemical Physics*, 17, 333–337, <https://doi.org/10.1063/1.1747247>, available at: <https://pubs.aip.org/aip/jcp/article/17/3/333/200986/The-Effect-of-Droplet-Size-on-Surface-Tension>, 1949.
- Tomasi, C.: *Atmospheric aerosols: Life cycles and effects on air quality and climate*, Wiley series in atmospheric physics and remote sensing, Wiley-VCH Verlag GmbH & Co. KGaA, Weinheim, 680 pp., 2017.
- Trainer, M. G.: Atmospheric Prebiotic Chemistry and Organic Hazes, *Current organic chemistry*, 17, 1710–1723, <https://doi.org/10.2174/13852728113179990078>, 2013.
- Tröstl, J., Chuang, W. K., Gordon, H., Heinritzi, M., Yan, C., Molteni, U., Ahlm, L., Frege, C., Bianchi, F., Wagner, R., Simon, M., Lehtipalo, K., Williamson, C., Craven, J. S., Duplissy, J., Adamov, A., Almeida, J., Bernhammer, A.-K., Breitenlechner, M., Brilke, S., Dias, A., Ehrhart, S., Flagan, R. C., Franchin, A., Fuchs, C., Guida, R., Gysel, M., Hansel, A., Hoyle, C. R., Jokinen, T., Junninen, H., Kangasluoma, J., Keskinen, H., Kim, J., Krapf, M., Kürten, A., Laaksonen, A., Lawler, M., Leiminger, M., Mathot, S., Möhler, O., Nieminen, T., Onnela, A., Petäjä, T., Piel, F. M., Miettinen, P., Rissanen, M. P., Rondo, L., Sarnela, N., Schobesberger, S., Sengupta, K., Sipilä, M., Smith, J. N., Steiner, G., Tomé, A., Virtanen, A., Wagner, A. C., Weingartner, E., Wimmer, D., Winkler, P. M., Ye, P., Carslaw, K. S., Curtius, J., Dommen, J., Kirkby, J., Kulmala, M., Riipinen, I., Worsnop, D. R., Donahue, N. M., and Baltensperger, U.: The role of low-volatility organic compounds in initial particle growth in the atmosphere, *Nature*, 533, 527–531, <https://doi.org/10.1038/nature18271>, available at: <https://www.nature.com/articles/nature18271>, 2016.
- TSI Incorporated: *Water-based Condensation Particle Counter Model 3789 Operation Manual*, TSI Incorporated, Shoreview, MN, USA, 53 pp., 2019.

- TSI Incorporated: Model 3082 Electrostatic Classifier and Model 3938 Scanning Mobility Particle Sizer Spectrometer Operation and Service Manual, TSI Incorporated, Shoreview, MN, USA, 225 pp., 2016.
- Tumminello, P. R., Niles, R., Valdez, V., Madawala, C. K., Gamage, D. K., Kimble, K. A., Leibensperger, R. J., Huang, C., Kaluarachchi, C., Dinasquet, J., Malfatti, F., Lee, C., Deane, G. B., Stokes, M. D., Stone, E., Tivanski, A., Prather, K. A., Boor, B. E., and Slade, J. H.: Size-Dependent Nascent Sea Spray Aerosol Bounce Fractions and Estimated Viscosity: The Role of Divalent Cation Enrichment, Surface Tension, and the Kelvin Effect, *Environ. Sci. Technol.*, 58, 19666–19678, <https://doi.org/10.1021/acs.est.4c04312>, 2024.
- Twomey, S.: The Influence of Pollution on the Shortwave Albedo of Clouds, *J. Atmos. Sci.*, 34, 1149–1152, [https://doi.org/10.1175/1520-0469\(1977\)034<1149:TlOPOT>2.0.CO;2](https://doi.org/10.1175/1520-0469(1977)034<1149:TlOPOT>2.0.CO;2), 1977.
- van Eldik, R., Asano, T., and Le Noble, W. J.: Activation and reaction volumes in solution. 2, *Chem. Rev.*, 89, 549–688, <https://doi.org/10.1021/cr00093a005>, 1989.
- van Eldik, R.: *High Pressure Chemistry: Synthetic, Mechanistic, and Supercritical Applications*, John Wiley & Sons Incorporated, Hoboken, 476 pp., 2008.
- Vesterinen, M., Lehtinen, K., Kulmala, M., and Laaksonen, A.: Effect of particle phase oligomer formation on aerosol growth, *Atmospheric Environment*, 41, 1768–1776, <https://doi.org/10.1016/j.atmosenv.2006.10.024>, 2007.
- Virtanen, A., Kannosto, J., Kuuluvainen, H., Arffman, A., Joutsensaari, J., Saukko, E., Hao, L., Yli-Pirilä, P., Tiitta, P., Holopainen, J. K., Keskinen, J., Worsnop, D. R., Smith, J. N., and Laaksonen, A.: Bounce behavior of freshly nucleated biogenic secondary organic aerosol particles, *Atmos. Chem. Phys.*, 11, 8759–8766, <https://doi.org/10.5194/acp-11-8759-2011>, 2011.
- Virtanen, A., Joutsensaari, J., Koop, T., Kannosto, J., Yli-Pirilä, P., Leskinen, J., Mäkelä, J. M., Holopainen, J. K., Pöschl, U., Kulmala, M., Worsnop, D. R., and Laaksonen, A.: An amorphous solid state of biogenic secondary organic aerosol particles, *Nature*, 467, 824–827, <https://doi.org/10.1038/nature09455>, 2010.
- Vogel, A. L., Äijälä, M., Brüggemann, M., Ehn, M., Junninen, H., Petäjä, T., Worsnop, D. R., Kulmala, M., Williams, J., and Hoffmann, T.: Online atmospheric pressure chemical ionization ion trap mass spectrometry (APCI-IT-MS<sup>n</sup>) for measuring organic acids in concentrated bulk aerosol – a laboratory and field study, *Atmospheric Measurement Techniques*, 6, 431–443, <https://doi.org/10.5194/amt-6-431-2013>, 2013.
- Wang, H., Baker, Y., Shen, H., Wu, R., Kang, S., Zhao, D., Wahner, A., Zorn, S. R., and Mentel, T. F.: Decomposition of Clusters of Oxygenated Compounds with NO<sub>3</sub>– by Applying Voltage Scanning to Chemical Ionization Mass Spectrometry in Steady-State Experiments, *Environ. Sci. Technol. Lett.*, 11, 694–700, <https://doi.org/10.1021/acs.estlett.4c00276>, 2024.
- Wang, S., Zhao, Y., Chan, A. W. H., Yao, M., Chen, Z., and Abbatt, J. P. D.: Organic Peroxides in Aerosol: Key Reactive Intermediates for Multiphase Processes in the Atmosphere, *Chemical Reviews*, <https://doi.org/10.1021/acs.chemrev.2c00430>, 2023.
- Wehner, B., Philippin, S., and Wiedensohler, A.: Design and calibration of a thermodenuder with an improved heating unit to measure the size-dependent volatile fraction of aerosol particles, *Journal of Aerosol Science*, 33, 1087–1093, [https://doi.org/10.1016/S0021-8502\(02\)00056-3](https://doi.org/10.1016/S0021-8502(02)00056-3), 2002.
- Wei, H., Vejerano, E. P., Leng, W., Huang, Q., Willner, M. R., Marr, L. C., and Vikesland, P. J.: Aerosol microdroplets exhibit a stable pH gradient, *Proceedings of the National Academy of Sciences of the United States of America*, 115, 7272–7277, <https://doi.org/10.1073/pnas.1720488115>, 2018.

- Wei, Z., Li, Y., Cooks, R. G., and Yan, X.: Accelerated Reaction Kinetics in Microdroplets: Overview and Recent Developments, *Annual review of physical chemistry*, 71, 31–51, <https://doi.org/10.1146/annurev-physchem-121319-110654>, 2020.
- Whitby, K. T.: The physical characteristics of sulfur aerosols, *Atmospheric Environment* (1967), 12, 135–159, [https://doi.org/10.1016/0004-6981\(78\)90196-8](https://doi.org/10.1016/0004-6981(78)90196-8), 1978.
- Wiedensohler, A.: An approximation of the bipolar charge distribution for particles in the submicron size range, *Journal of Aerosol Science*, 19, 387–389, [https://doi.org/10.1016/0021-8502\(88\)90278-9](https://doi.org/10.1016/0021-8502(88)90278-9), 1988.
- Williamson, C. J., Kupc, A., Axisa, D., Bilsback, K. R., Bui, T., Campuzano-Jost, P., Dollner, M., Froyd, K. D., Hodshire, A. L., Jimenez, J. L., Kodros, J. K., Luo, G., Murphy, D. M., Nault, B. A., Ray, E. A., Weinzierl, B., Wilson, J. C., Yu, F., Yu, P., Pierce, J. R., and Brock, C. A.: A large source of cloud condensation nuclei from new particle formation in the tropics, *Nature*, 574, 399–+, <https://doi.org/10.1038/s41586-019-1638-9>, 2019.
- Wilson, K. R., Prophet, A. M., Rovelli, G., Willis, M. D., Rapf, R. J., and Jacobs, M. I.: A kinetic description of how interfaces accelerate reactions in micro-compartments, *Chem. Sci.*, 11, 8533–8545, <https://doi.org/10.1039/d0sc03189e>, 2020.
- Witkowski, B., Al-Sharafi, M., and Gierczak, T.: Ozonolysis of  $\beta$ -Caryophyllonic and Limononic Acids in the Aqueous Phase: Kinetics, Product Yield, and Mechanism, *Environmental Science & Technology*, 53, 8823–8832, <https://doi.org/10.1021/acs.est.9b02471>, 2019.
- Witkowski, B., Jurdana, S., and Gierczak, T.: Limononic Acid Oxidation by Hydroxyl Radicals and Ozone in the Aqueous Phase, *Environmental Science & Technology*, 52, 3402–3411, <https://doi.org/10.1021/acs.est.7b04867>, 2018.
- Wüthrich, C., Giannoukos, S., and Zenobi, R.: Elucidating the Role of Ion Suppression in Secondary Electrospray Ionization, *Journal of the American Society for Mass Spectrometry*, 34, 2498–2507, <https://doi.org/10.1021/jasms.3c00219>, 2023.
- Xiong, H., Lee, J. K., Zare, R. N., and Min, W.: Strong Concentration Enhancement of Molecules at the Interface of Aqueous Microdroplets, *The journal of physical chemistry. B*, 124, 9938–9944, <https://doi.org/10.1021/acs.jpcc.0c07718>, 2020.
- Xue, Y.-Q., Yang, X.-C., Cui, Z.-X., and Lai, W.-P.: The effect of microdroplet size on the surface tension and Tolman length, *The journal of physical chemistry. B*, 115, 109–112, <https://doi.org/10.1021/jp1084313>, 2011.
- Yan, X., Bain, R. M., and Cooks, R. G.: Organic Reactions in Microdroplets: Reaction Acceleration Revealed by Mass Spectrometry, *Angewandte Chemie International Edition in English*, 55, 12960–12972, <https://doi.org/10.1002/anie.201602270>, 2016.
- Yang, L. H., Takeuchi, M., Chen, Y., and Ng, N. L.: Characterization of thermal decomposition of oxygenated organic compounds in FIGAERO-CIMS, *Aerosol Science and Technology*, 55, 1321–1342, <https://doi.org/10.1080/02786826.2021.1945529>, 2021.
- Yuan, Y., Cai, R., Li, X., Li, Y., Li, D., He, K., Ehn, M., and Jiang, J.: Improving the sensitivity of on-line chemical ionization orbitrap mass spectrometry for detecting low-concentration atmospheric organic vapors, *Aerosol Science and Technology*, 1–11, <https://doi.org/10.1080/02786826.2025.2544793>, 2025.
- Zeng, G., Fu, D., Holladay, S., Langlois, D., Kelley, J., Kish, J. D., and Liu, Y.: Kinetics of Heterogeneous Reaction of Ozone with Oleic Acid and Its Dependence on Droplet Size, Relative Humidity, and Ozone Concentration, *Atmosphere*, 16, 433, <https://doi.org/10.3390/atmos16040433>, 2025.

- Zhang, Y. Y., Müller, L., Winterhalter, R., Moortgat, G. K., Hoffmann, T., and Pöschl, U.: Seasonal cycle and temperature dependence of pinene oxidation products, dicarboxylic acids and nitrophenols in fine and coarse air particulate matter, *Atmos. Chem. Phys.*, 10, 7859–7873, <https://doi.org/10.5194/acp-10-7859-2010>, 2010.
- Zhang, Y., Apsokardu, M. J., Kerecman, D. E., Achtenhagen, M., and Johnston, M. V.: Reaction Kinetics of Organic Aerosol Studied by Droplet Assisted Ionization: Enhanced Reactivity in Droplets Relative to Bulk Solution, *Journal of the American Society for Mass Spectrometry*, 32, 46–54, <https://doi.org/10.1021/jasms.0c00057>, 2021.
- Zhang, Z. and Scherer, G. W.: Supercritical drying of cementitious materials, *Cement and Concrete Research*, 99, 137–154, <https://doi.org/10.1016/j.cemconres.2017.05.005>, 2017.
- Zhao, J., Mickwitz, V., Luo, Y., Häkkinen, E., Graeffe, F., Zhang, J., Timonen, H., Canagaratna, M., Krechmer, J. E., Zhang, Q., Kulmala, M., Kangasluoma, J., Worsnop, D., and Ehn, M.: Characterization of the Vaporization Inlet for Aerosols (VIA) for online measurements of particulate highly oxygenated organic molecules (HOMs), *Atmospheric Measurement Techniques*, 17, 1527–1543, <https://doi.org/10.5194/amt-17-1527-2024>, 2024.
- Zhao, J., Häkkinen, E., Graeffe, F., Krechmer, J. E., Canagaratna, M. R., Worsnop, D. R., Kangasluoma, J., and Ehn, M.: A combined gas- and particle-phase analysis of highly oxygenated organic molecules (HOMs) from  $\alpha$ -pinene ozonolysis, *Atmospheric Chemistry and Physics*, 23, 3707–3730, <https://doi.org/10.5194/acp-23-3707-2023>, 2023.
- Zhao, J., Lavalley, V., Mangiagalli, P., Wright, J. M., and Bankston, T. E.: Glass delamination: a comparison of the inner surface performance of vials and pre-filled syringes, *AAPS PharmSciTech*, 15, 1398–1409, <https://doi.org/10.1208/s12249-014-0167-y>, 2014.
- Zhao, R., Kenseth, C. M., Huang, Y., Dalleska, N. F., Kuang, X. M., Chen, J., Paulson, S. E., and Seinfeld, J. H.: Rapid Aqueous-Phase Hydrolysis of Ester Hydroperoxides Arising from Criegee Intermediates and Organic Acids, *The Journal of Physical Chemistry A*, 122, 5190–5201, <https://doi.org/10.1021/acs.jpca.8b02195>, 2018.
- Zhao, Z., Yang, X., Lee, J., Tolentino, R., Mayorga, R., Zhang, W., and Zhang, H.: Diverse Reactions in Highly Functionalized Organic Aerosols during Thermal Desorption, *ACS Earth and Space Chemistry*, 4, 283–296, <https://doi.org/10.1021/acsearthspacechem.9b00312>, 2020.
- Zhao, Z., Xu, Q., Yang, X., and Zhang, H.: Heterogeneous Ozonolysis of Endocyclic Unsaturated Organic Aerosol Proxies: Implications for Criegee Intermediate Dynamics and Later-Generation Reactions, *ACS Earth and Space Chemistry*, 3, 344–356, <https://doi.org/10.1021/acsearthspacechem.8b00177>, 2019.
- Zubarev, R. A. and Makarov, A.: Orbitrap mass spectrometry, *Analytical Chemistry*, 85, 5288–5296, <https://doi.org/10.1021/ac4001223>, 2013.
- Zuth, C., Vogel, A. L., Ockenfeld, S., Huesmann, R., and Hoffmann, T.: Ultrahigh-Resolution Mass Spectrometry in Real Time: Atmospheric Pressure Chemical Ionization Orbitrap Mass Spectrometry of Atmospheric Organic Aerosol, *Analytical Chemistry*, 90, 8816–8823, <https://doi.org/10.1021/acs.analchem.8b00671>, 2018.

## 8 Appendix

### 8.1 Use of AI tools

Table 8.1: List of AI tools which were used throughout this work.

AI tool	Used for	Why	When
ChatGPT - gpt-4o/5o	Improvement of written language	Better readability	Throughout the entire work
DeepL Write	Improvement of written language	Better readability	Throughout the entire work

### 8.2 Supplementary Materials Chapter 3

Table 8.2: Relative contributions of the parent compound, dehydration products, and other thermal decomposition products for aerosol particles generated from various organic polyacids, measured using our custom-built aerosol inlet coupled to a CI-Orbitrap mass spectrometer. Particles with diameters of 30, 50, 80, and 110 nm were analyzed; no size dependence was observed. The evaporator temperature was 285 °C.

Substance	Molecular formula	Parental compound	Dehydration product	Other thermal fragmentation products
1,2,3,4-Butanetetracarboxylic acid	$C_8H_{10}O_8$	$95.03 \pm 0.43\%$	$3.93 \pm 0.50\%$	$1.04 \pm 0.15\%$ (- 2 H <sub>2</sub> O)
Citric acid	$C_6H_8O_7$	$99.37 \pm 0.22\%$	$0.54 \pm 0.20\%$	$0.09 \pm 0.03\%$ (- H <sub>2</sub> O, -CO <sub>2</sub> )
Tartaric acid	$C_4H_6O_6$	$98.39 \pm 1.05\%$	$1.44 \pm 0.92\%$	$0.17 \pm 0.13\%$ (- 2 H <sub>2</sub> O)
Tricarballic acid	$C_6H_8O_6$	$97.64 \pm 0.45\%$	$2.36 \pm 0.45\%$	-
Trimellitic acid	$C_9H_6O_6$	$93.29 \pm 1.24\%$	$3.13 \pm 0.67\%$	$3.57 \pm 0.66\%$ (- CO <sub>2</sub> )

Table 8.3: List of all molecular formulas whose signals were assigned to NDA ozonolysis products and included in the total ozonolysis-product signal, together with their classification into the proposed product groups.

Molecular formula	Product group
$C_9H_{10}O_7$	$C_9H_{10}O_7$
$C_9H_{10}O_6$	$C_9H_{10}O_6$
$C_9H_{10}O_8$	aged monomer
$C_9H_{10}O_9$	aged monomer
$C_8H_{10}O_6$	carbon loss
$C_8H_{10}O_7$	carbon loss
$C_9H_8O_6$	dehydrogenated
$C_9H_8O_7$	dehydrogenated
$C_9H_{12}O_8$	hydrated
$C_9H_{12}O_9$	hydrated
$C_{12}H_{18}O_8$	first gen. dimer
$C_{15}H_{18}O_{13}$	first gen. dimer
$C_{18}H_{20}O_{11}$	first gen. dimer
$C_{18}H_{18}O_{12}$	aged dimer
$C_{18}H_{18}O_{13}$	aged dimer
$C_{18}H_{20}O_{12}$	aged dimer
$C_{18}H_{20}O_{13}$	aged dimer
$C_{18}H_{20}O_{14}$	aged dimer
$C_{18}H_{20}O_{15}$	aged dimer

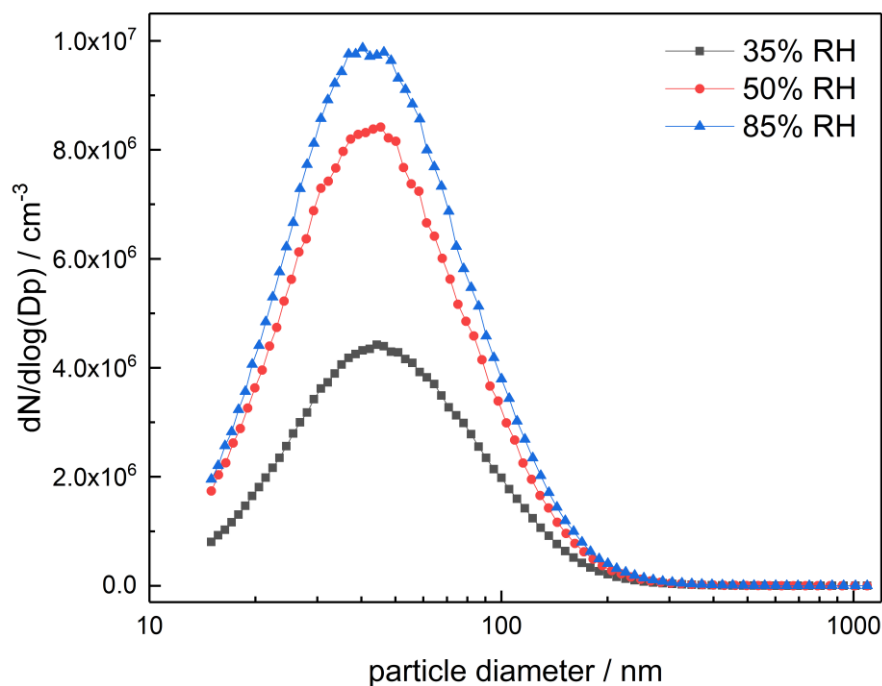


Figure 8.1: Particle number size distributions of NDA aerosol prior to size selection at 35%, 50%, and 85% relative humidity (RH).

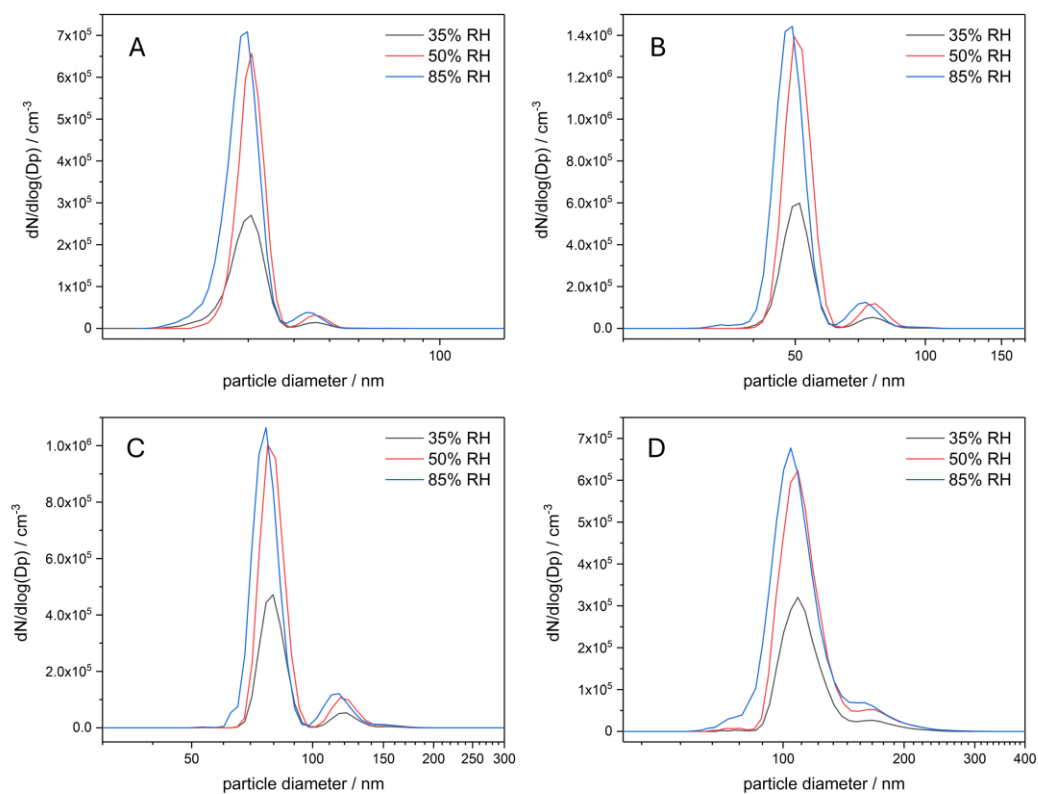


Figure 8.2: Particle number size distributions of size-selected NDA aerosol measured with a second SMPS in a tandem configuration. Shown are nominal mobility-diameter setpoints of 30 nm (A), 50 nm (B), 80 nm (C), and 110 nm (D) at 35%, 50%, and 85% relative humidity (RH).

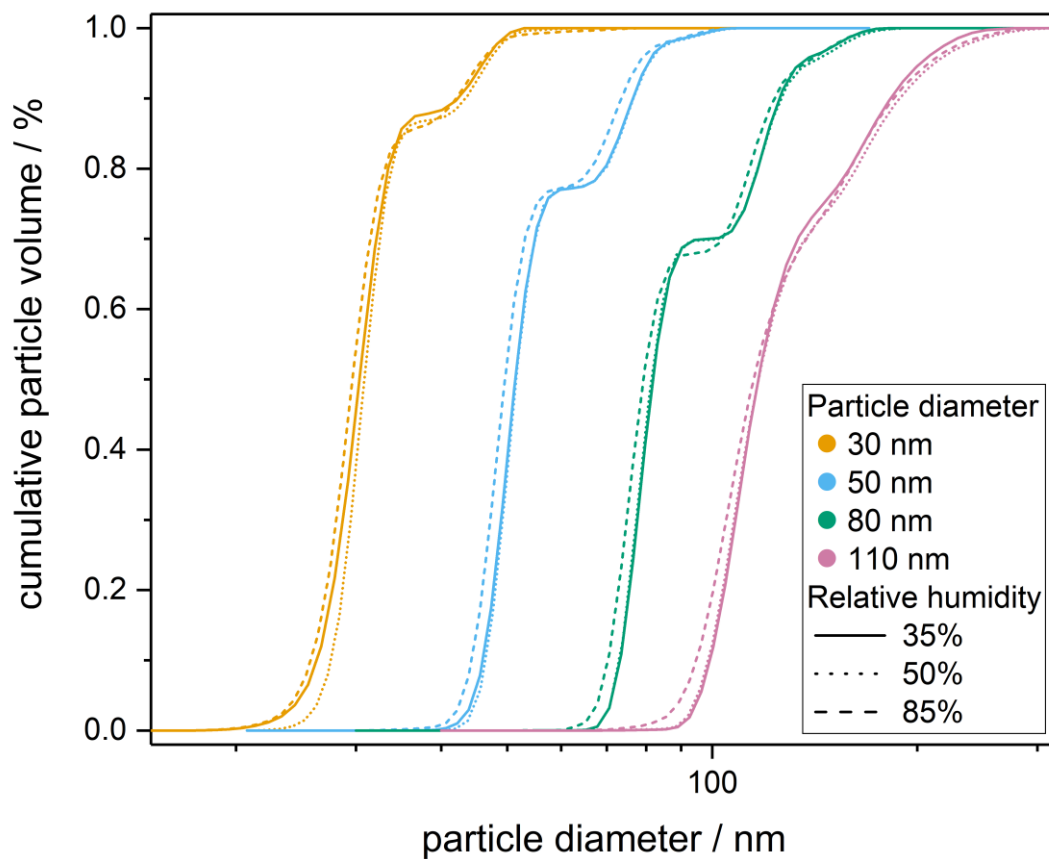


Figure 8.3: Cumulative volume-weighted particle size distributions of size-selected NDA aerosol measured with a second SMPS in a tandem configuration. Shown are nominal mobility-diameter setpoints of 30, 50, 80, and 110 nm at 35%, 50%, and 85% relative humidity (RH).

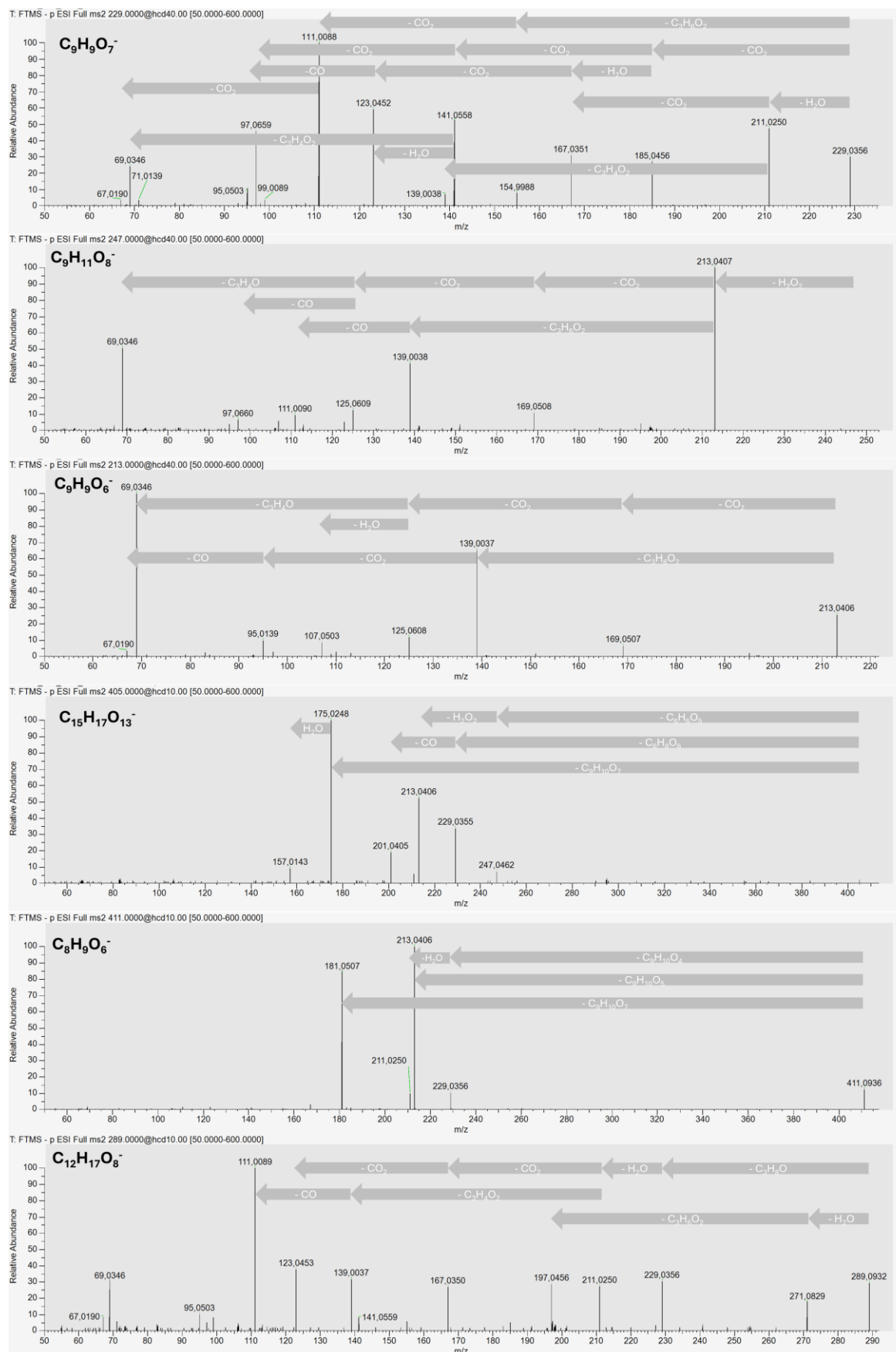


Figure 8.4: MS/MS spectra for selected m/z values assigned to major NDA ozonolysis products.

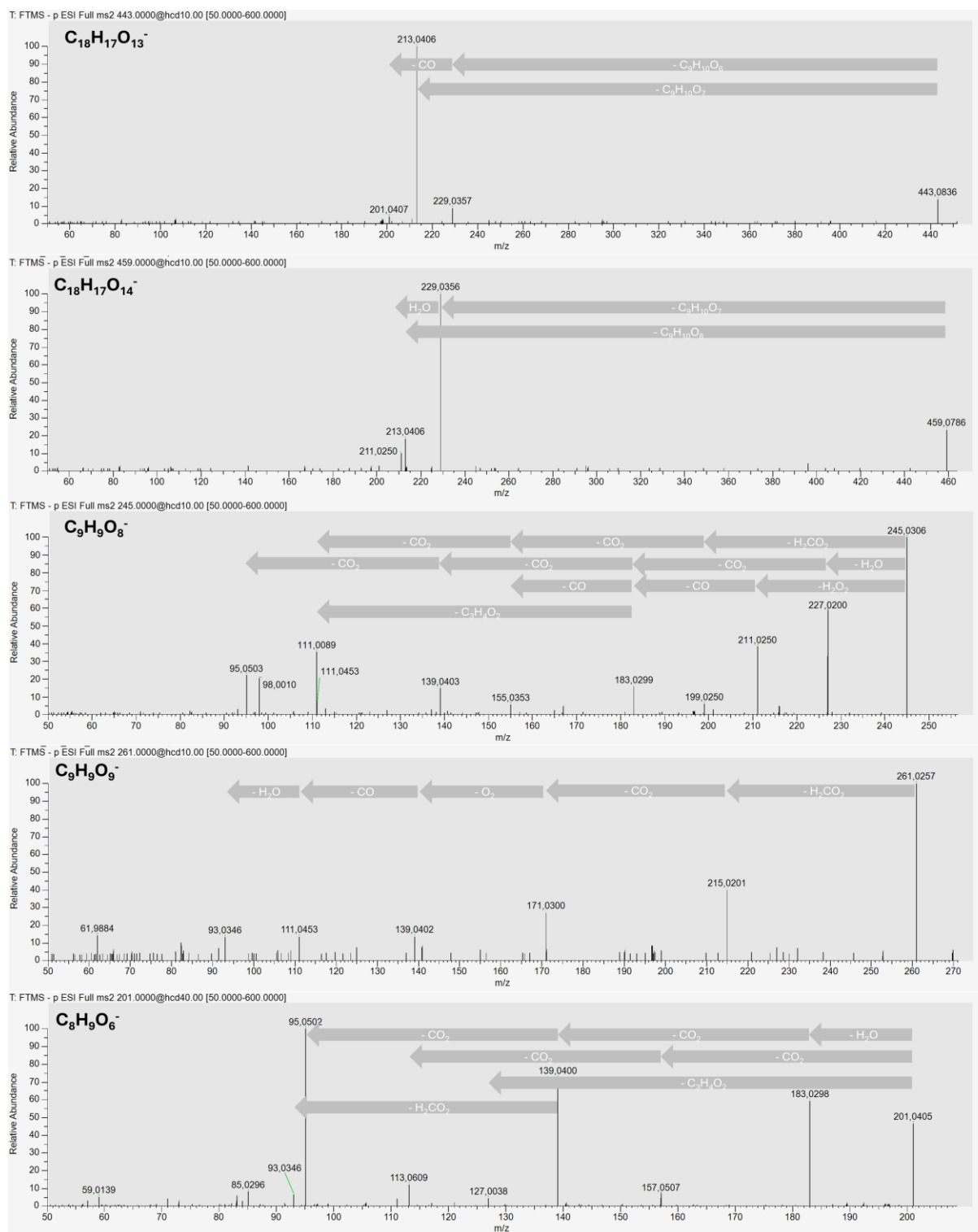


Figure 8.5: MS/MS spectra for selected m/z values assigned to major NDA ozonolysis products.

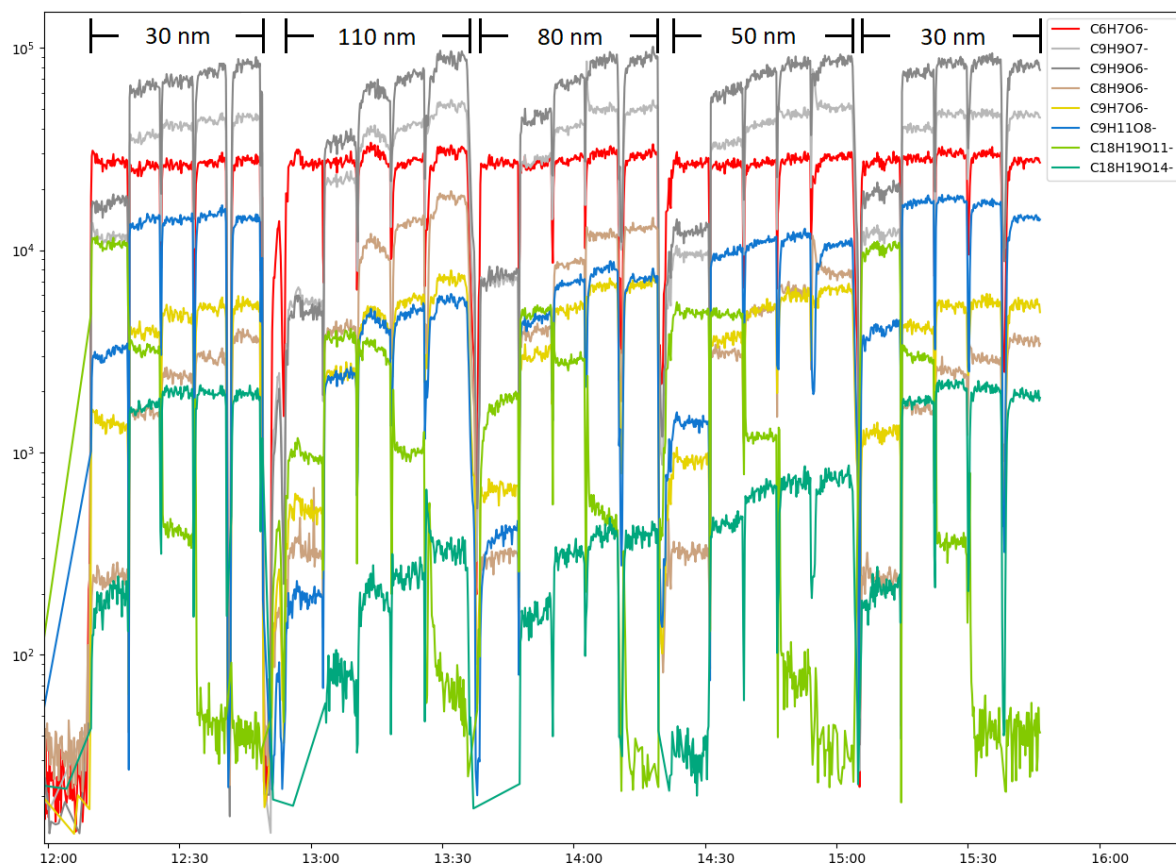


Figure 8.6: Mass traces of selected NDA ozonolysis products during experiment 7 (10 ppm O<sub>3</sub> and 83-86% RH).

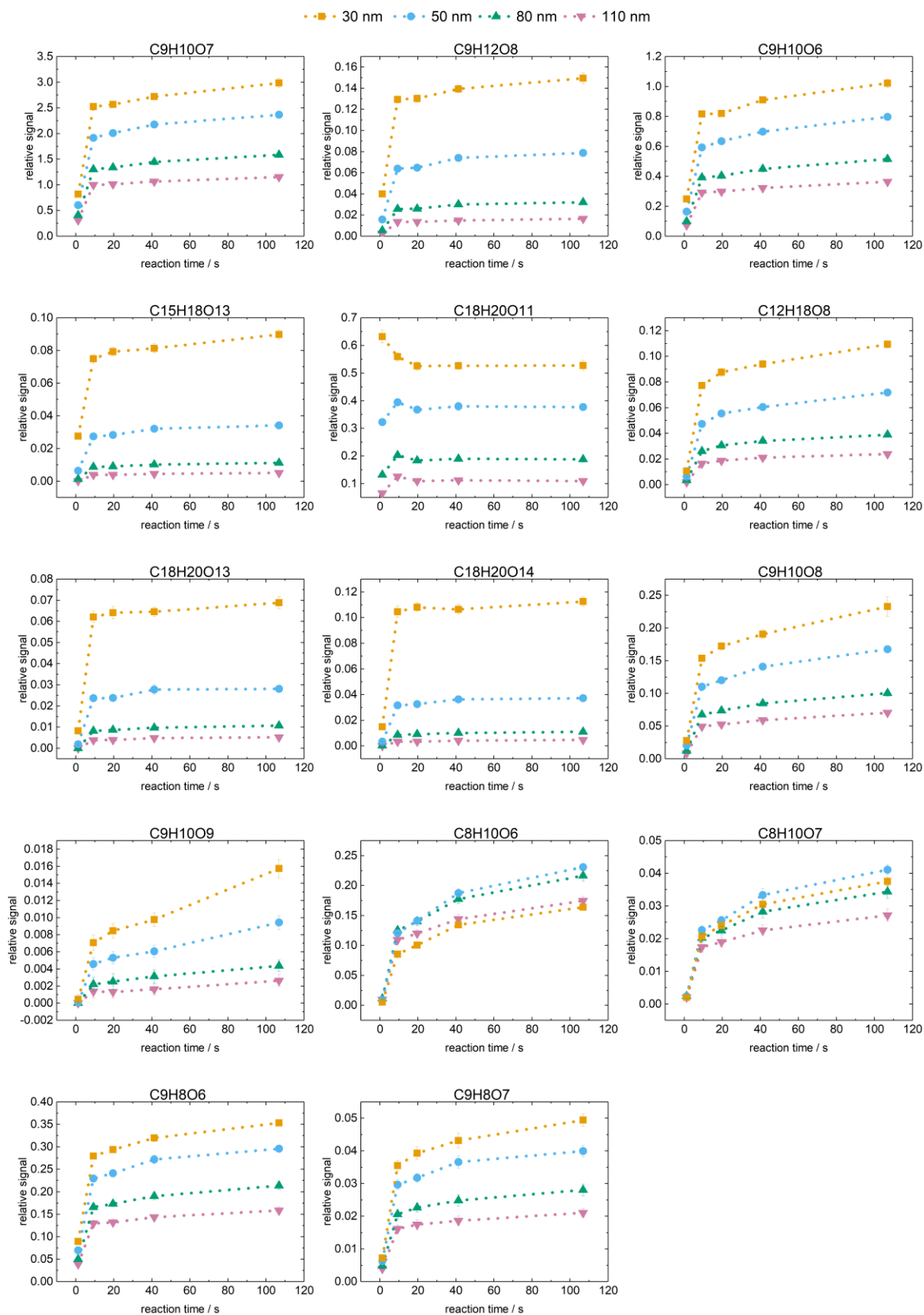


Figure 8.7: Temporal evolution of the relative intensities of the major signals assigned to NDA ozonolysis products for particles with mobility diameters of 30, 50, 80, and 110 nm at 10 ppm O<sub>3</sub> and 35% relative humidity (RH).

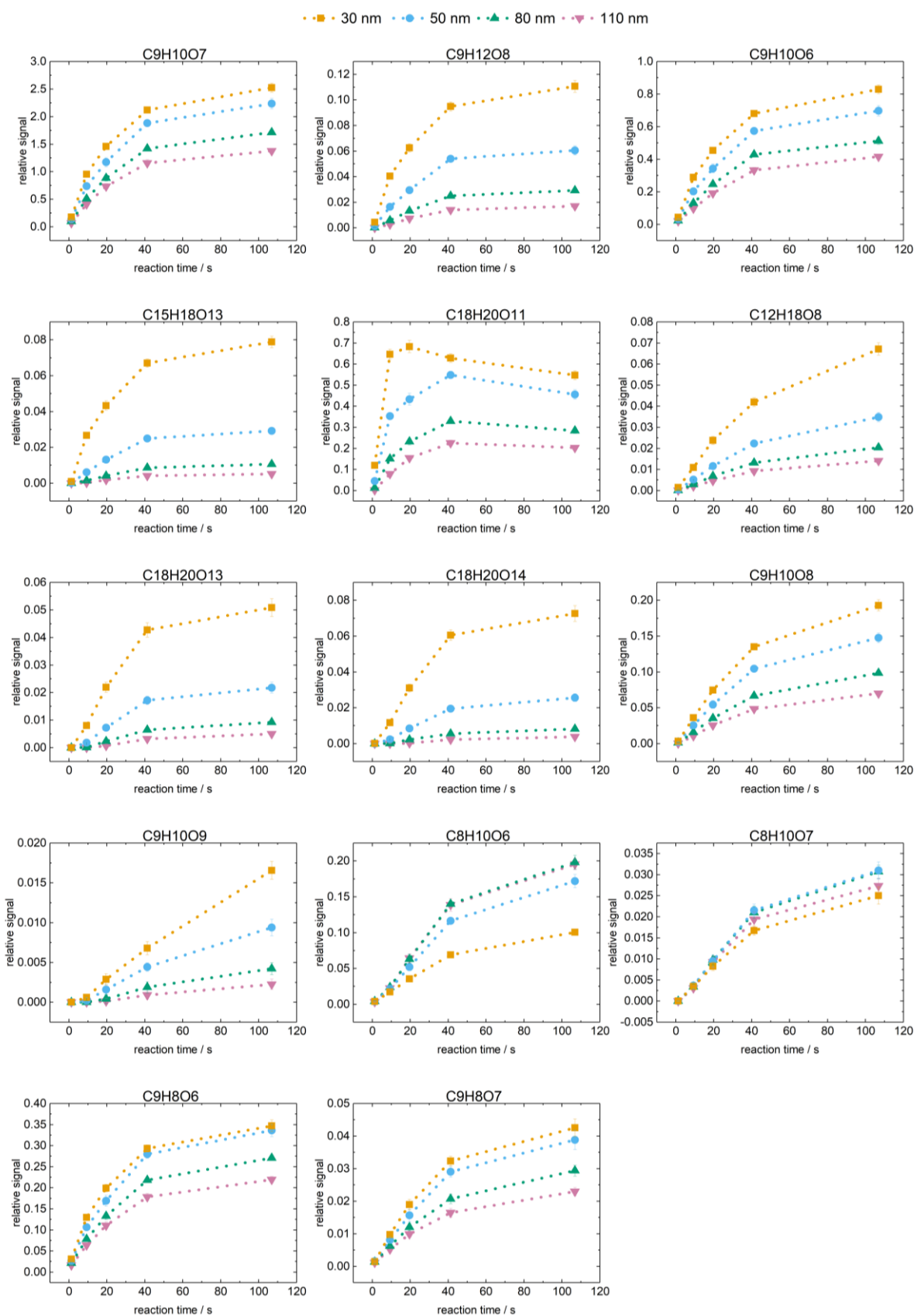


Figure 8.8: Temporal evolution of the relative intensities of the major signals assigned to NDA ozonolysis products for particles with mobility diameters of 30, 50, 80, and 110 nm at 1 ppm  $O_3$  and 35% relative humidity (RH).

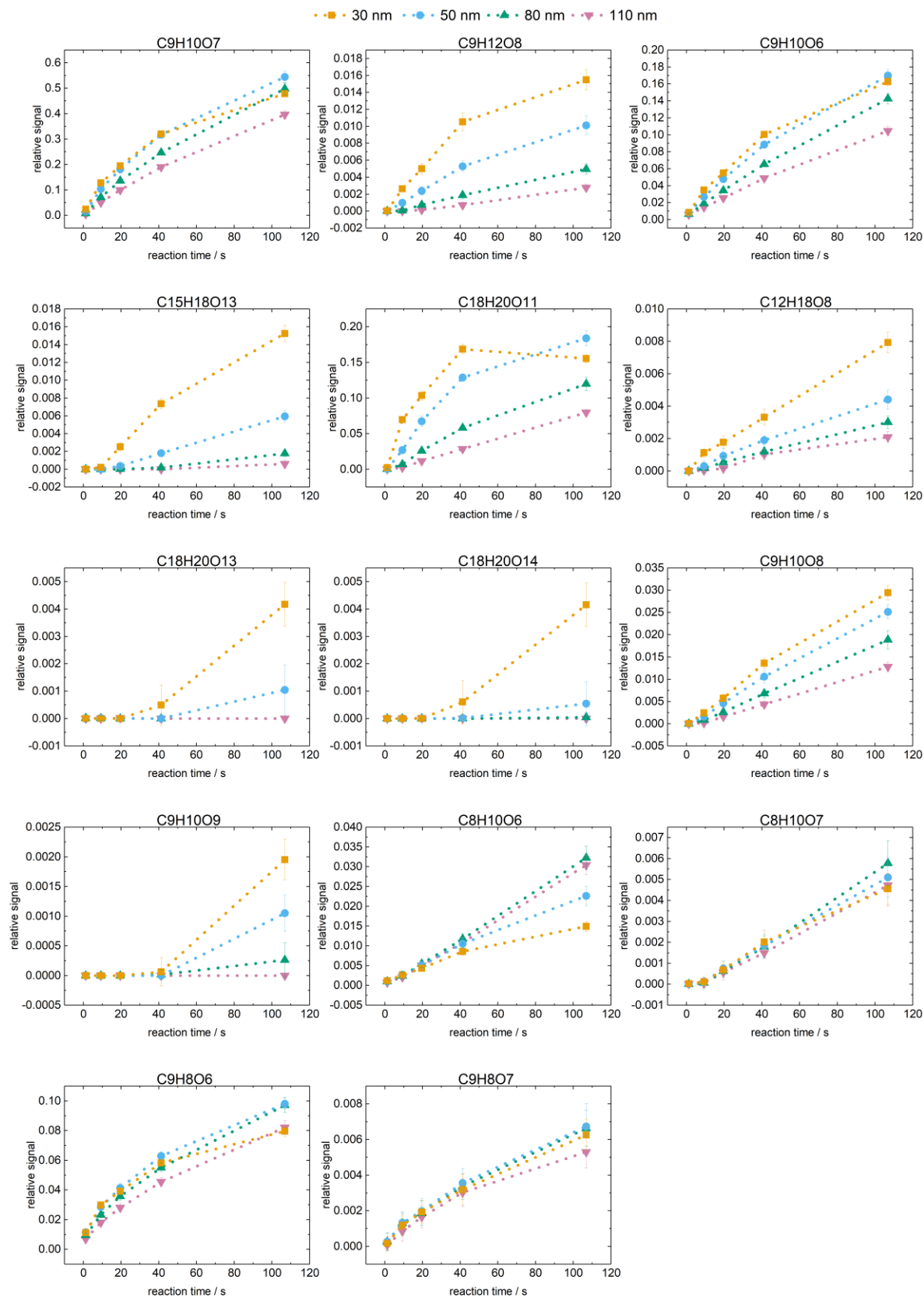


Figure 8.9: Temporal evolution of the relative intensities of the major signals assigned to NDA ozonolysis products for particles with mobility diameters of 30, 50, 80, and 110 nm at 0.1 ppm  $O_3$  and 35% relative humidity (RH).

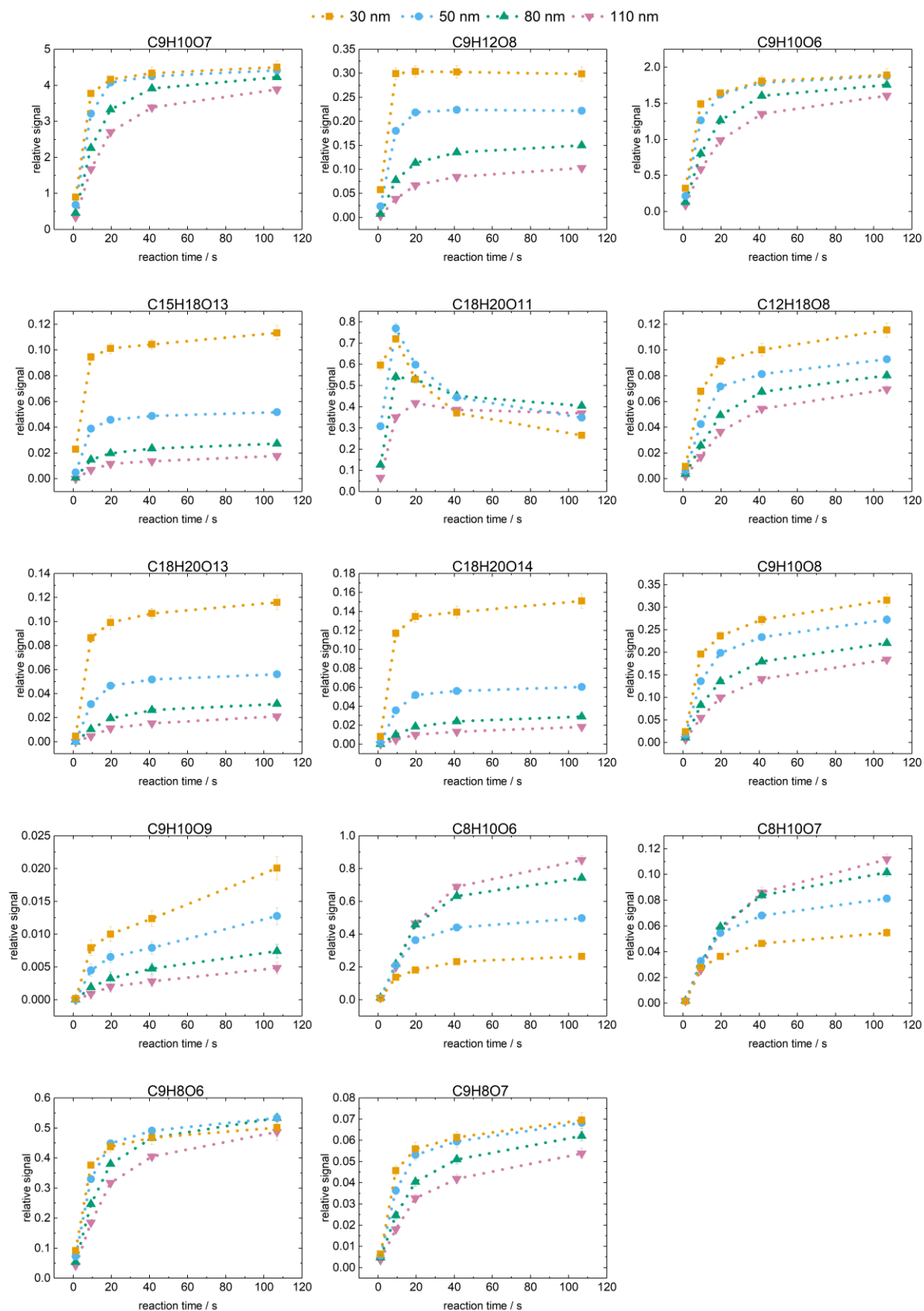


Figure 8.10: Temporal evolution of the relative intensities of the major signals assigned to NDA ozonolysis products for particles with mobility diameters of 30, 50, 80, and 110 nm at 10 ppm  $O_3$  and 50% relative humidity (RH).

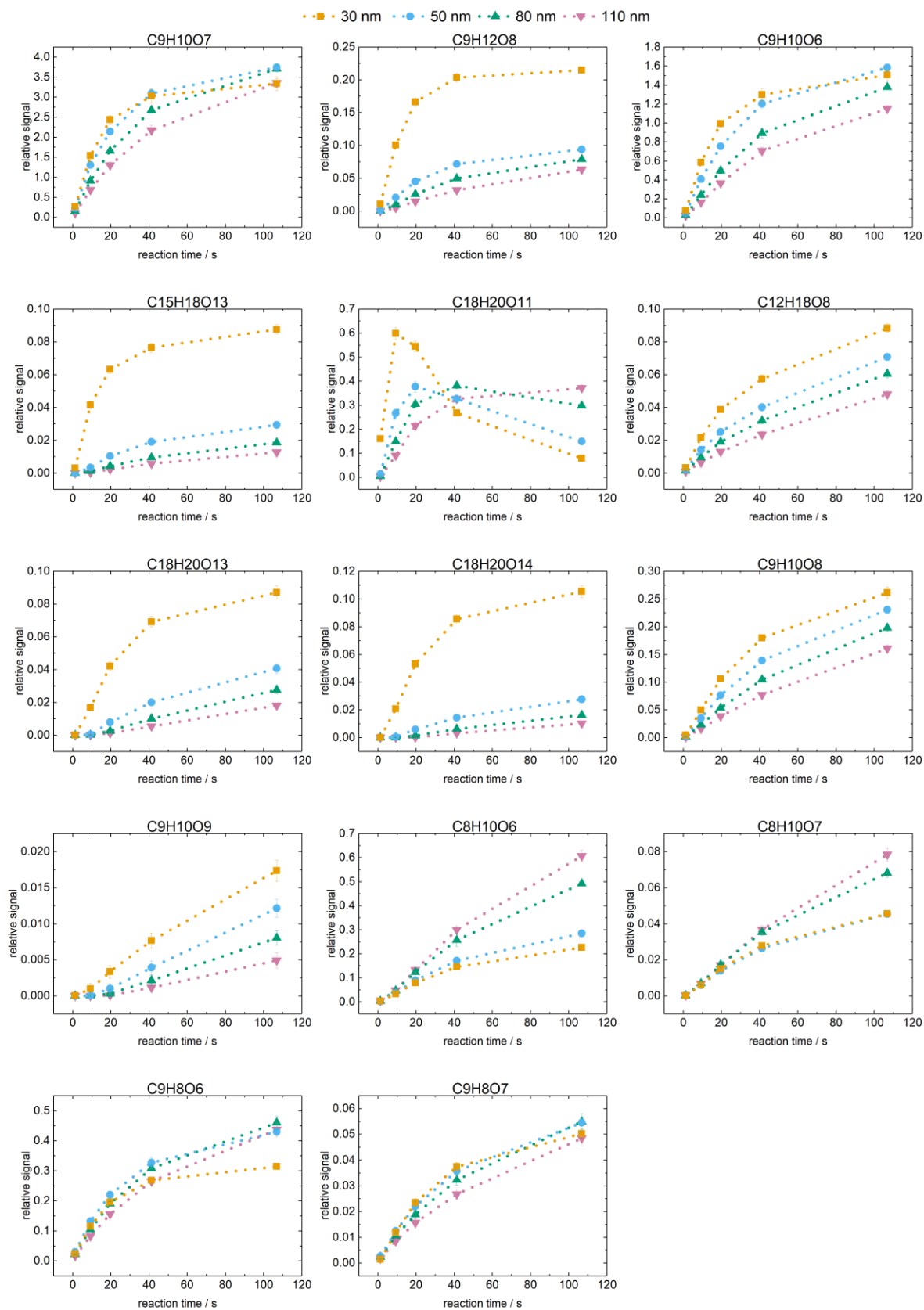


Figure 8.11: Temporal evolution of the relative intensities of the major signals assigned to NDA ozonolysis products for particles with mobility diameters of 30, 50, 80, and 110 nm at 1 ppm  $O_3$  and 50% relative humidity (RH).

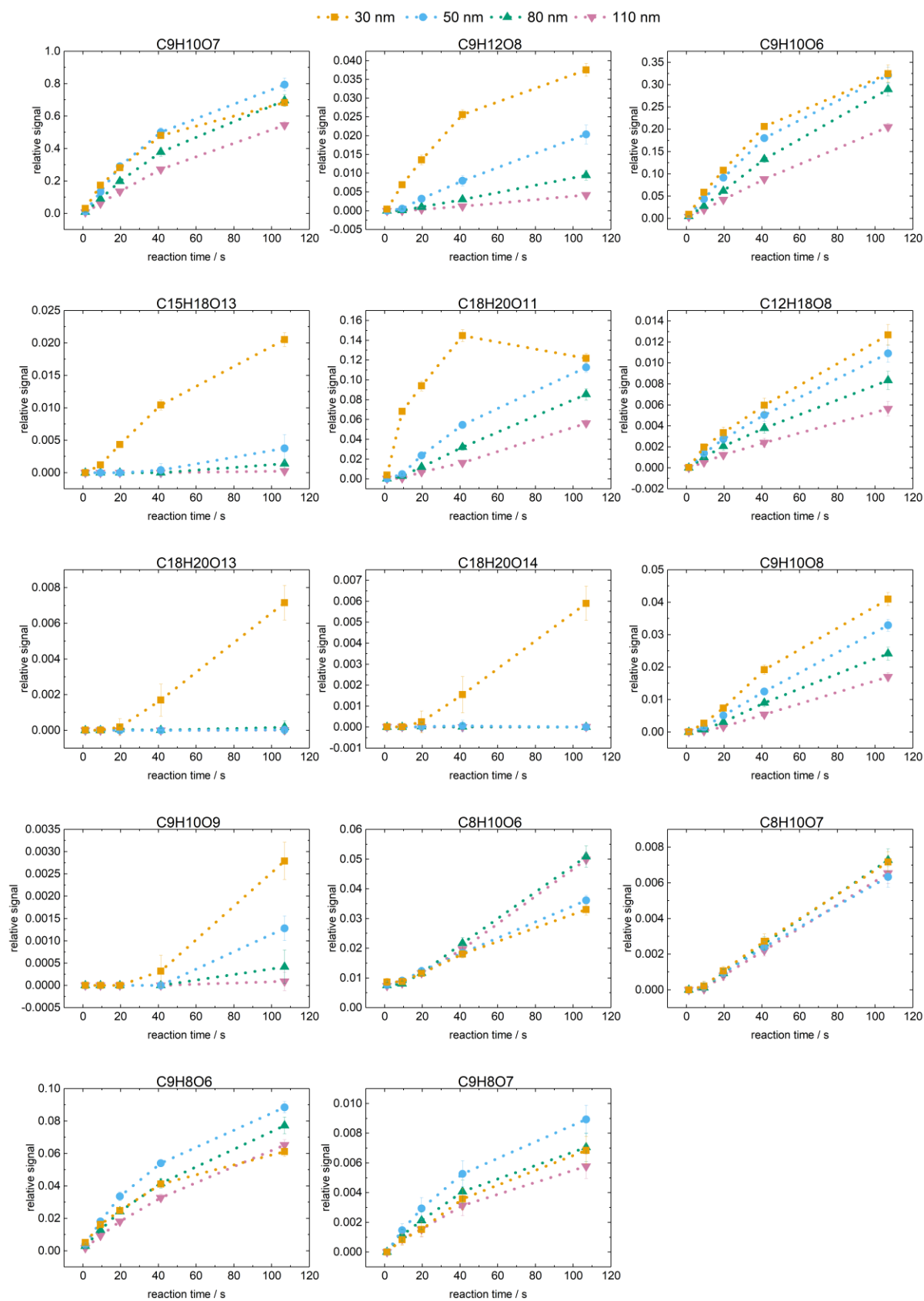


Figure 8.12: Temporal evolution of the relative intensities of the major signals assigned to NDA ozonolysis products for particles with mobility diameters of 30, 50, 80, and 110 nm at 0.1 ppm  $O_3$  and 50% relative humidity (RH).

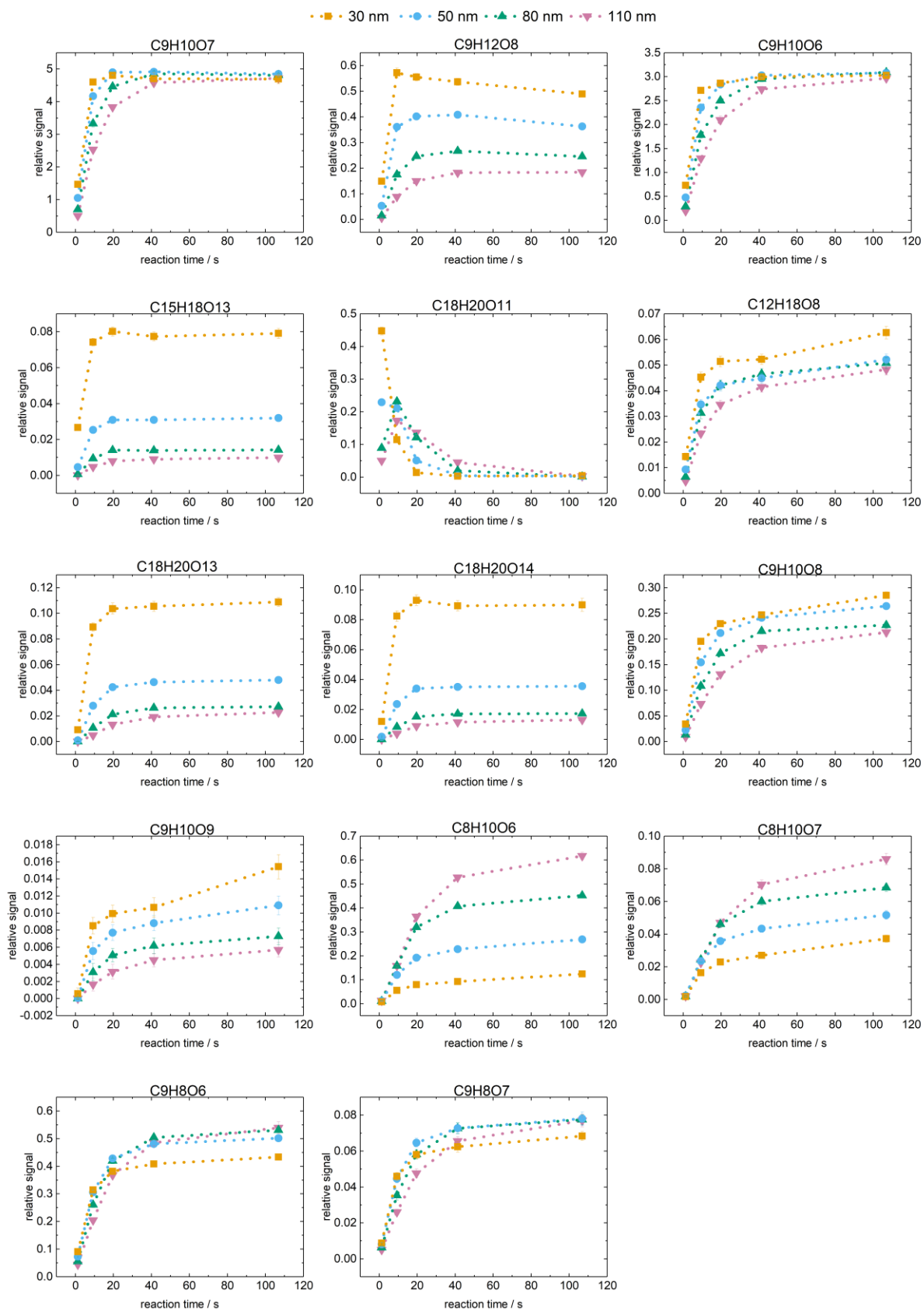


Figure 8.13: Temporal evolution of the relative intensities of the major signals assigned to NDA ozonolysis products for particles with mobility diameters of 30, 50, 80, and 110 nm at 10 ppm  $O_3$  and 85% relative humidity (RH).

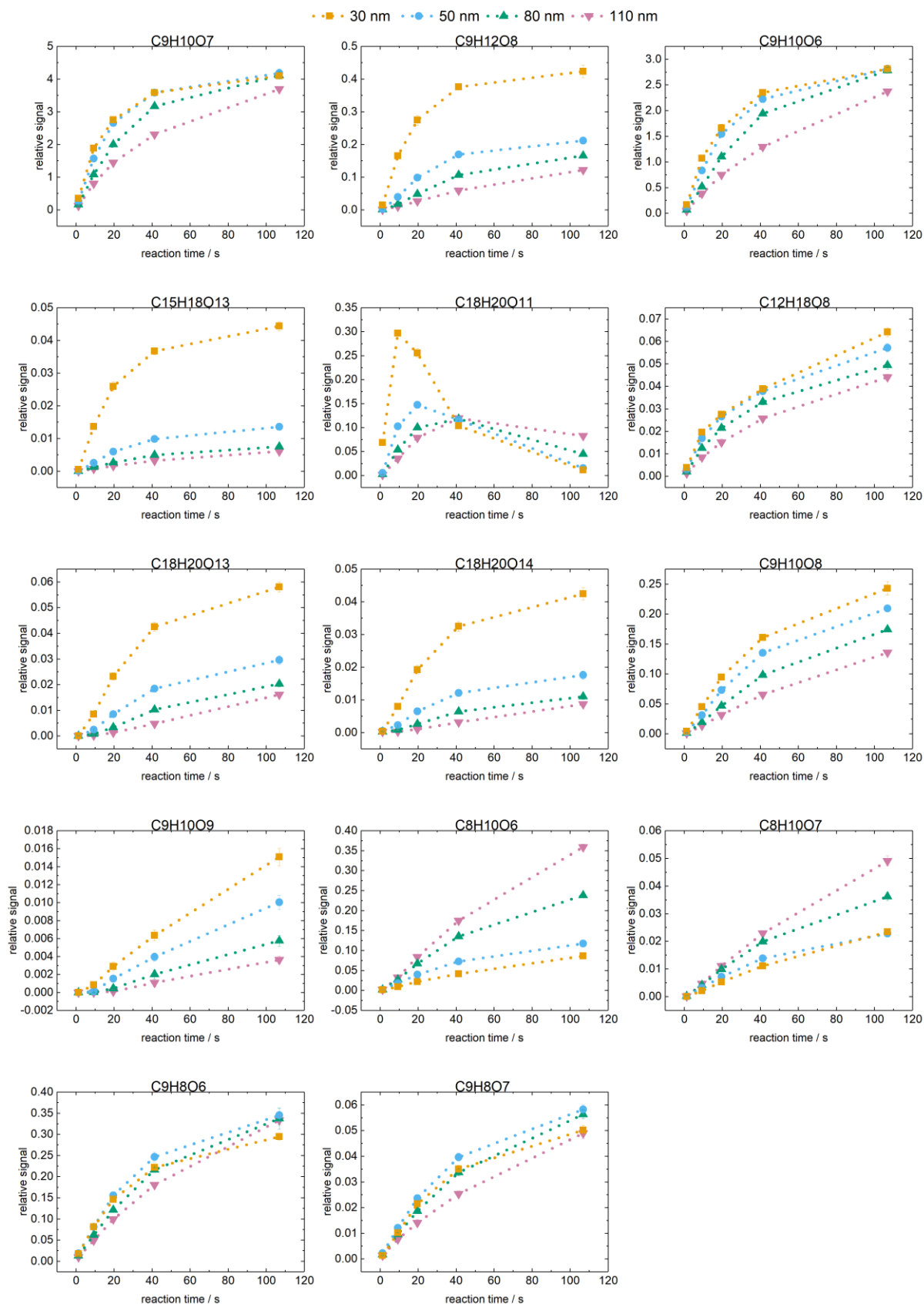


Figure 8.14: Temporal evolution of the relative intensities of the major signals assigned to NDA ozonolysis products for particles with mobility diameters of 30, 50, 80, and 110 nm at 1 ppm  $O_3$  and 85% relative humidity (RH).

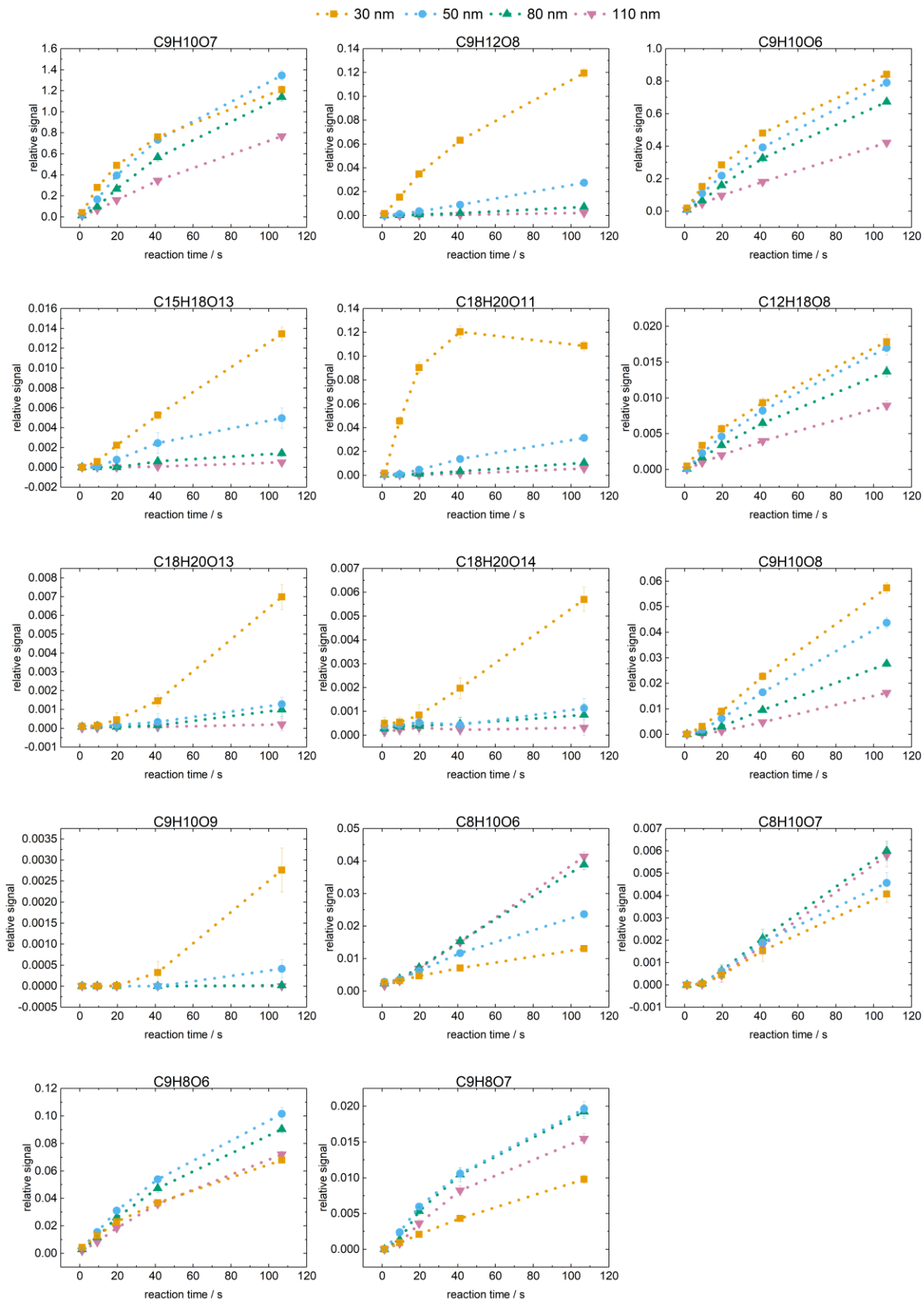


Figure 8.15: Temporal evolution of the relative intensities of the major signals assigned to NDA ozonolysis products for particles with mobility diameters of 30, 50, 80, and 110 nm at 0.1 ppm O<sub>3</sub> and 85% relative humidity (RH).

## 8.3 Supplementary Materials Chapter 4

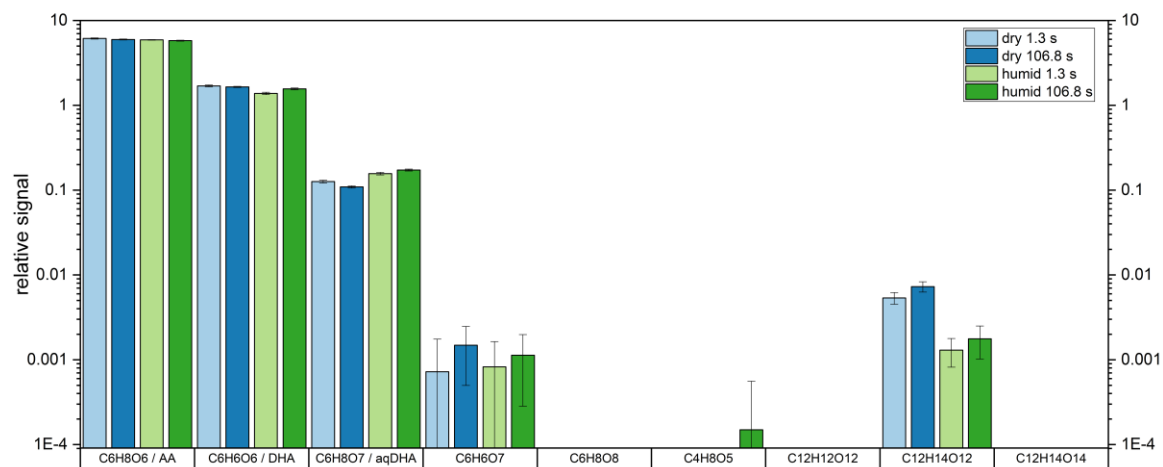


Figure 8.16: Relative  $\text{NO}_3^-$ -CI-Orbitrap signals of AA and products monitored in the AA-ozone reaction in the absence of ozone at 1.3 s and 106.8 s reaction time.

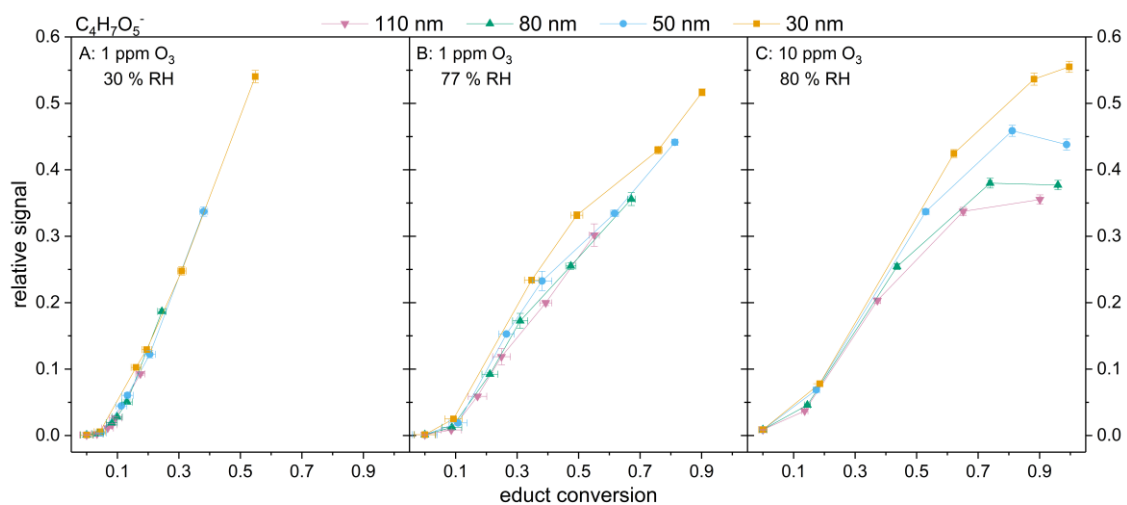


Figure 8.17: Evolution of the relative signals of the product with elemental composition  $\text{C}_4\text{H}_8\text{O}_5$  formed in the reaction of AA with ozone.

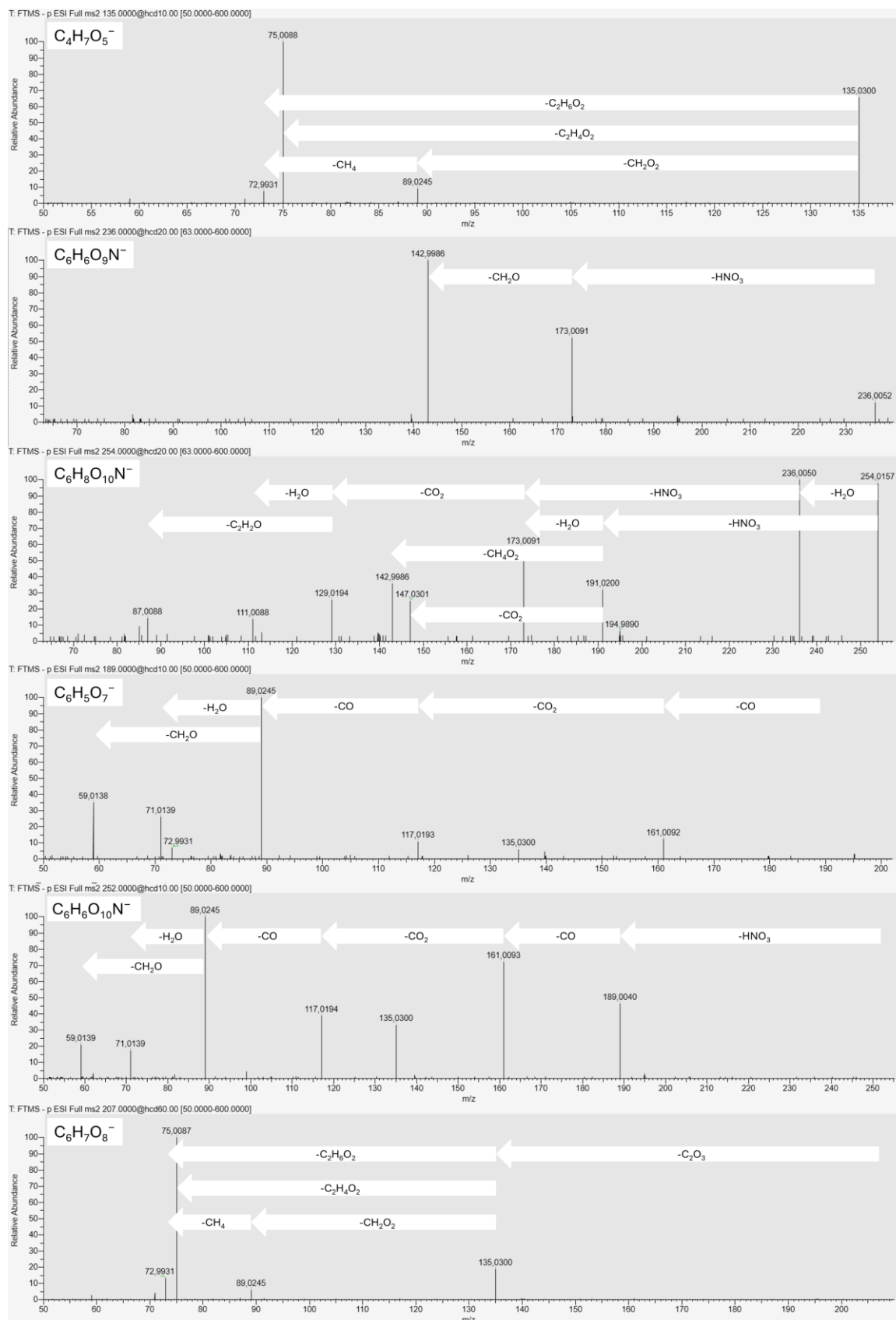


Figure 8.18: MS/MS spectra for selected  $m/z$  values assigned to major products formed in the reaction of AA with ozone.

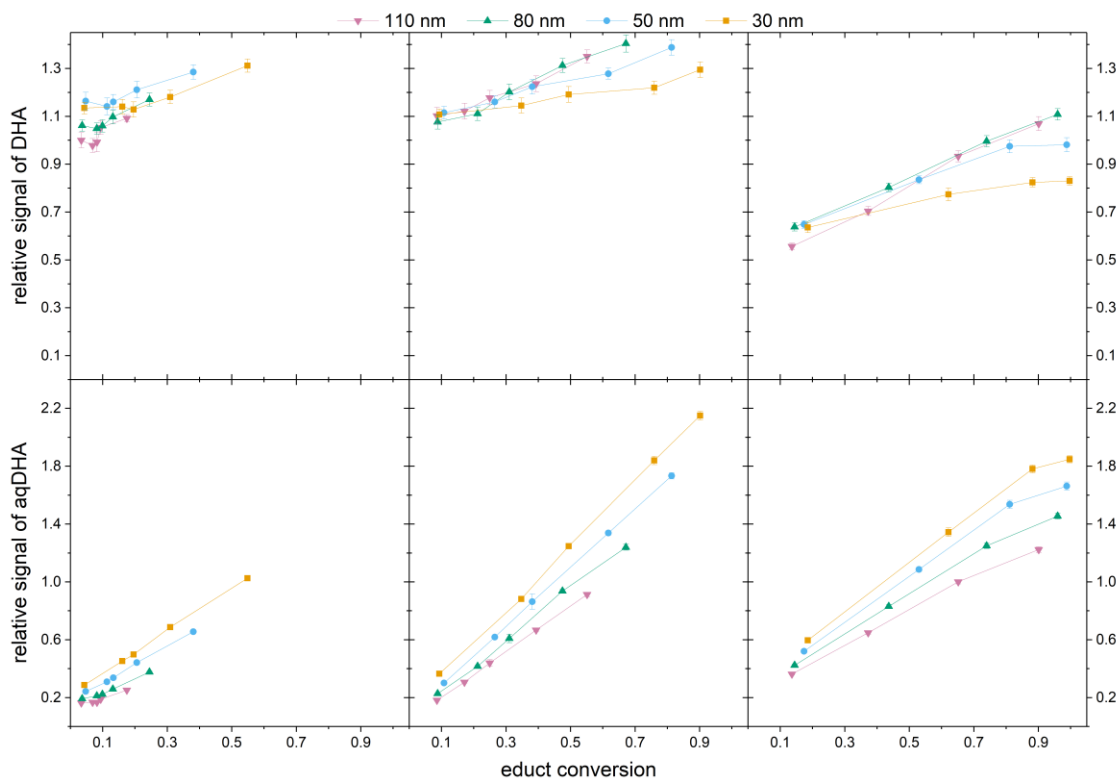


Figure 8.19: Evolution of the relative signals of the oxidation products DHA and aqDHA formed in the reaction of AA with ozone.

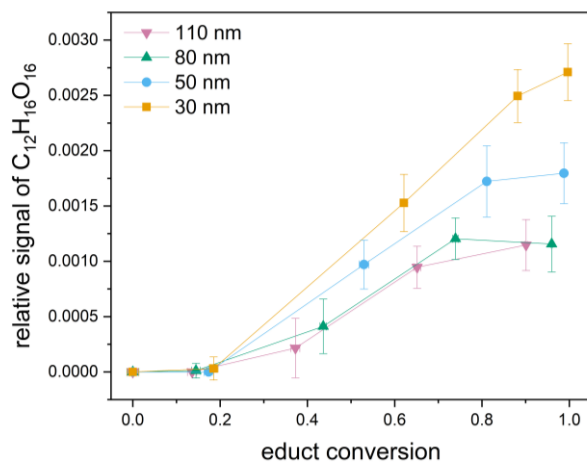


Figure 8.20: Evolution of the relative signals of the dimer with elemental composition  $C_{12}H_{16}O_{16}$  formed in the reaction of AA with ozone.

## 8.4 Supplementary Materials Chapter 5

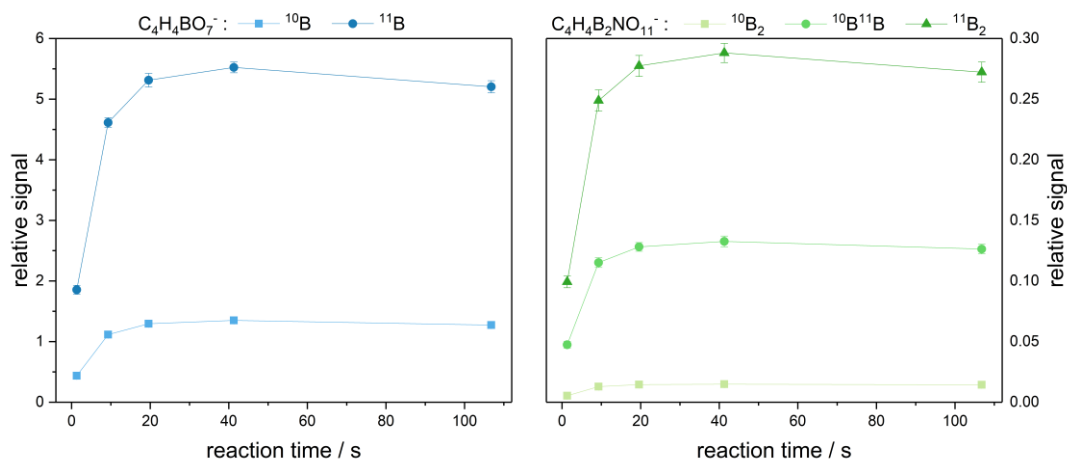


Figure 8.21: Mean relative signals of  $C_4H_4BO_7^-$  (left panel) resolved by boron isotope ( $^{10}B$ , light blue;  $^{11}B$ , dark blue) and of  $C_4H_4B_2NO_{11}^-$  (right panel) resolved by isotopologues ( $^{10}B_2$ , light green;  $^{10}B^{11}B$ , green;  $^{11}B_2$ , dark green) formed in aerosol particles, plotted versus residence time at 81% RH.

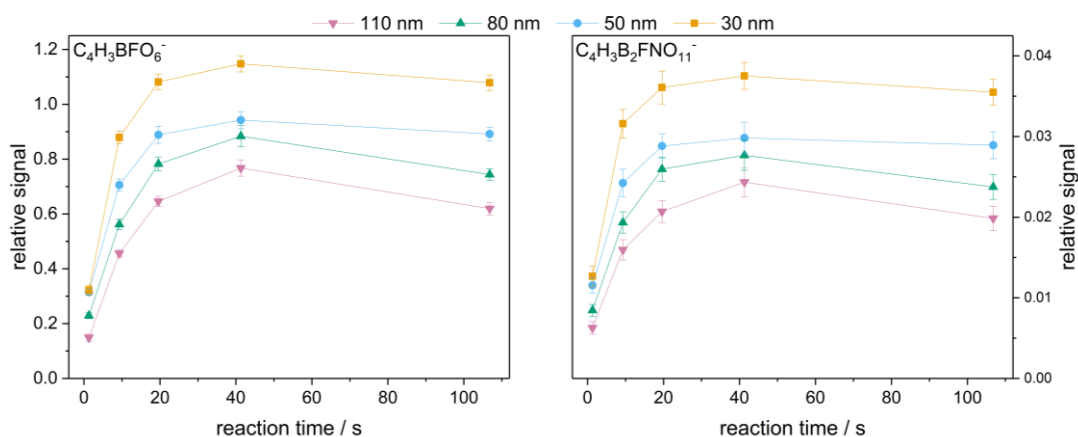


Figure 8.22: Mean relative signals of borate-tartrate ester complexes containing fluoride substituents formed in aerosol particles as a function of residence time at 81% RH:  $C_4H_3BFO_6^-$  (left) and  $C_4H_3B_2FNO_{10}^-$  (right). Particle mobility diameters were: 110 nm (pink), 80 nm (green), 50 nm (blue) and 30 nm (yellow).

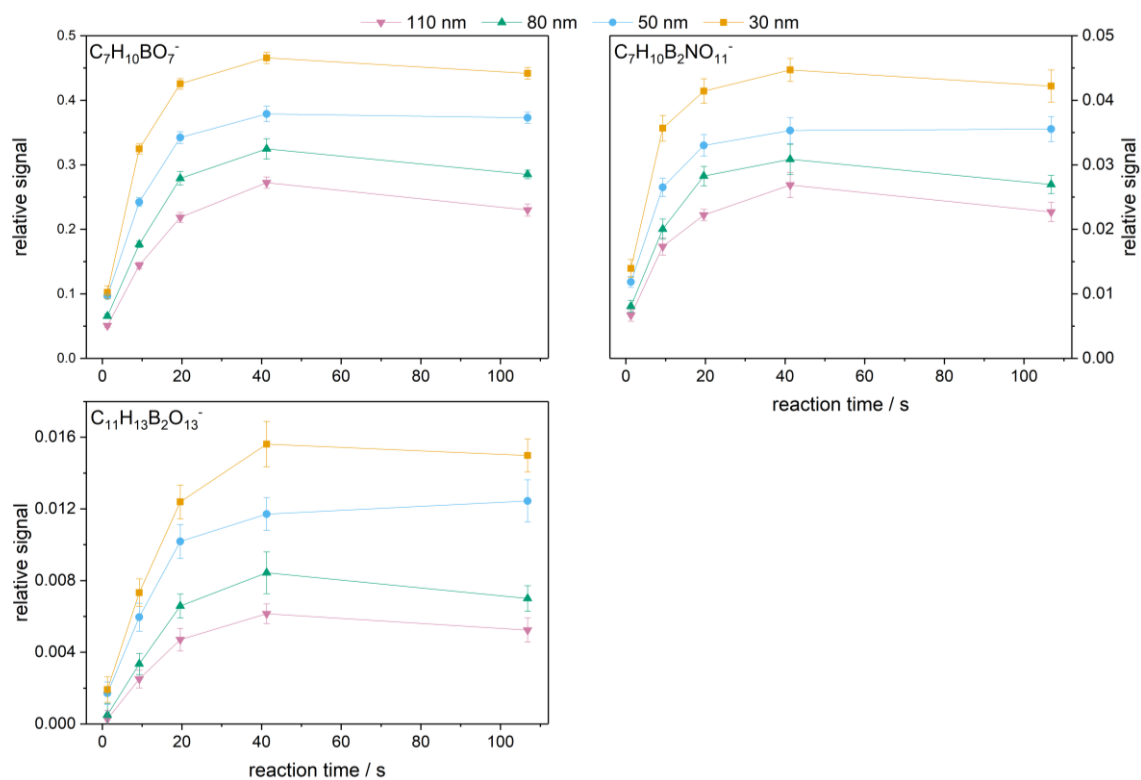


Figure 8.23: Mean relative signals of borate-tartrate ester complexes containing isopropoxy substituents formed in aerosol particles as a function of residence time at 81% RH:  $C_7H_{10}BO_7^-$  (A),  $C_7H_{10}B_2NO_{11}^-$  (B) and  $C_{11}H_{13}B_2O_{13}^-$  (C). Particle mobility diameters were: 110 nm (pink), 80 nm (green), 50 nm (blue) and 30 nm (yellow).

## 8.5 List of related publications and presentations

### Accepted publications

M. Douverne, T. Hoffmann: When Size Matters: Size-Selective Chemistry in the Heterogeneous Processing of Organic Aerosols, ACS ES&T Air 2025 2 (11), 2491-2503, DOI: <https://doi.org/10.1021/acsestair.5c00189>.

### Oral presentations

05/2022

M. Douverne, M. Böckmann, D. Thomsen, M. Riva, S. Perrier, C. George, M. Glasius, T. Hoffmann: Characterization of organic aerosols by online CI-Orbitrap MS: Laboratory studies of biogenic SOA formation and size-dependent aerosol chemistry, European Geoscience Union Assembly, Vienna, Austria, 2022, DOI: <https://doi.org/10.5194/egusphere-egu22-11038>.

### Poster presentations

09/2022

M. Douverne, M. Böckmann, M. Riva, S. Perrier, C. George, T. Hoffmann: Characterization of organic aerosols by online CI-Orbitrap MS: Laboratory studies of particle size dependent aerosol chemistry, International Aerosol Conference 2022, Athens, Greece.

09/2023

M. Douverne, M. Riva, S. Perrier, C. George, T. Hoffmann: Online measurements of particle size dependent chemistry during ozonolysis experiments via CI-Orbitrap MS, European Aerosol Conference 2023, Malaga, Spain.

## 8.6 Curriculum Vitae